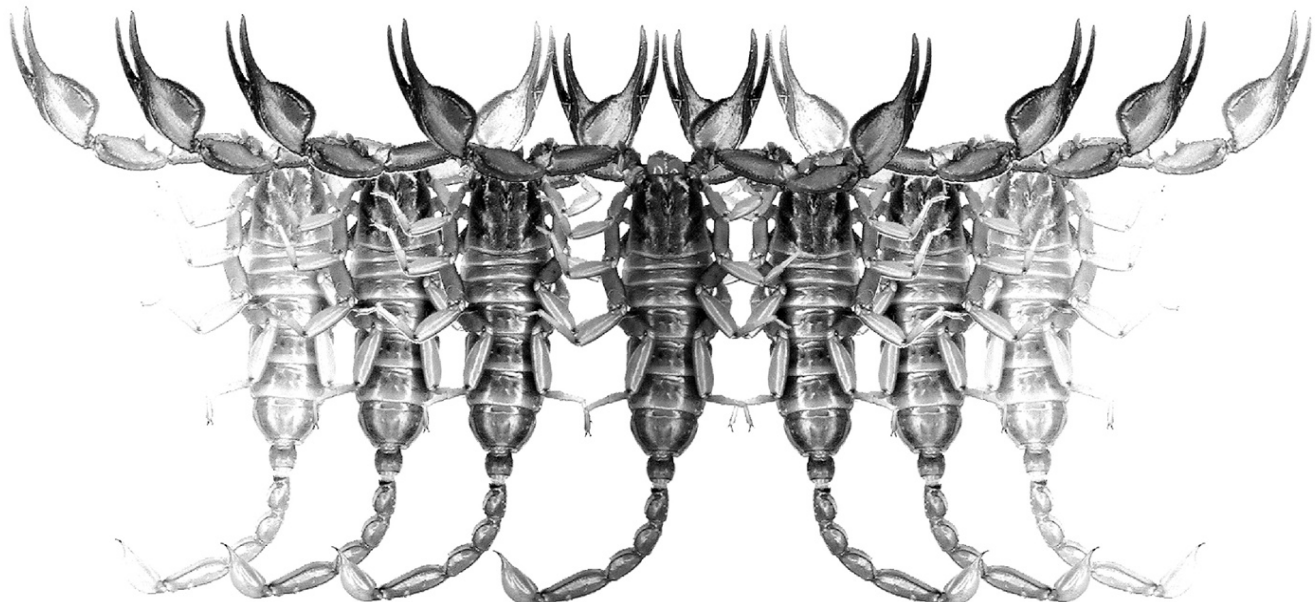


Euscorpius

Occasional Publications in Scorpiology



**Reanalysis of *Teruelius* and *Grosphus*
(Scorpiones: Buthidae)
with descriptions of two new species**

Graeme Lowe & František Kovařík

July 2022 — No. 356

Euscorpius

Occasional Publications in Scorpiology

EDITOR: Victor Fet, Marshall University, ‘fet@marshall.edu’

ASSOCIATE EDITOR: Michael E. Soleglad, ‘msoleglad@gmail.com’

TECHNICAL EDITOR: František Kovařík, ‘kovarik.scorpio@gmail.com’

Euscorpius is the first research publication completely devoted to scorpions (Arachnida: Scorpiones). *Euscorpius* takes advantage of the rapidly evolving medium of quick online publication, at the same time maintaining high research standards for the burgeoning field of scorpion science (scorpiology). *Euscorpius* is an expedient and viable medium for the publication of serious papers in scorpiology, including (but not limited to): systematics, evolution, ecology, biogeography, and general biology of scorpions. Review papers, descriptions of new taxa, faunistic surveys, lists of museum collections, and book reviews are welcome.

Derivatio Nominis

The name ***Euscorpius*** Thorell, 1876 refers to the most common genus of scorpions in the Mediterranean region and southern Europe (family Euscorpiidae).

Euscorpius is located at: <https://mds.marshall.edu/euscorpius/>

Archive of issues 1-270 see also at: <http://www.science.marshall.edu/fet/Euscorpius>

(Marshall University, Huntington, West Virginia 25755-2510, USA)

ICZN COMPLIANCE OF ELECTRONIC PUBLICATIONS:

Electronic (“e-only”) publications are fully compliant with ICZN ([International Code of Zoological Nomenclature](#)) (i.e. for the purposes of new names and new nomenclatural acts) when properly archived and registered. All *Euscorpius* issues starting from No. 156 (2013) are archived in two electronic archives:

- **Biotaxa**, <http://biotaxa.org/Euscorpius> (ICZN-approved and ZooBank-enabled)
- **Marshall Digital Scholar**, <http://mds.marshall.edu/euscorpius/>. (This website also archives all *Euscorpius* issues previously published on CD-ROMs.)

Between 2000 and 2013, ICZN **did not accept online texts** as “published work” (Article 9.8). At this time, *Euscorpius* was produced in two **identical** versions: online (ISSN 1536-9307) and CD-ROM (ISSN 1536-9293) (laser disk) in archive-quality, read-only format. Both versions had the identical date of publication, as well as identical page and figure numbers. **Only copies distributed on a CD-ROM** from *Euscorpius* in 2001-2012 represent published work in compliance with the ICZN, i.e. for the purposes of new names and new nomenclatural acts.

In September 2012, ICZN Article 8. What constitutes published work, has been amended and allowed for electronic publications, disallowing publication on optical discs. From January 2013, *Euscorpius* discontinued CD-ROM production; only online electronic version (ISSN 1536-9307) is published. For further details on the new ICZN amendment, see <http://www.pensoft.net/journals/zookeys/article/3944/>.

Publication date: 18 July 2022

<http://zoobank.org/urn:lsid:zoobank.org:pub:FB8F03EF-37AC-4462-894A-51E23F4E0A93>

Reanalysis of *Teruelius* and *Grosphus* (Scorpiones: Buthidae) with descriptions of two new species

Graeme Lowe¹ & František Kovařík²

¹ Monell Chemical Senses Center, 3500 Market St., Philadelphia, PA 19104-3308, USA; loweg@monell.org

² P. O. Box 27, CZ-145 01 Praha 45, Czech Republic; <http://www.scorpio.cz>

<http://zoobank.org/urn:lsid:zoobank.org:pub:FB8F03EF-37AC-4462-894A-51E23F4E0A93>

Summary

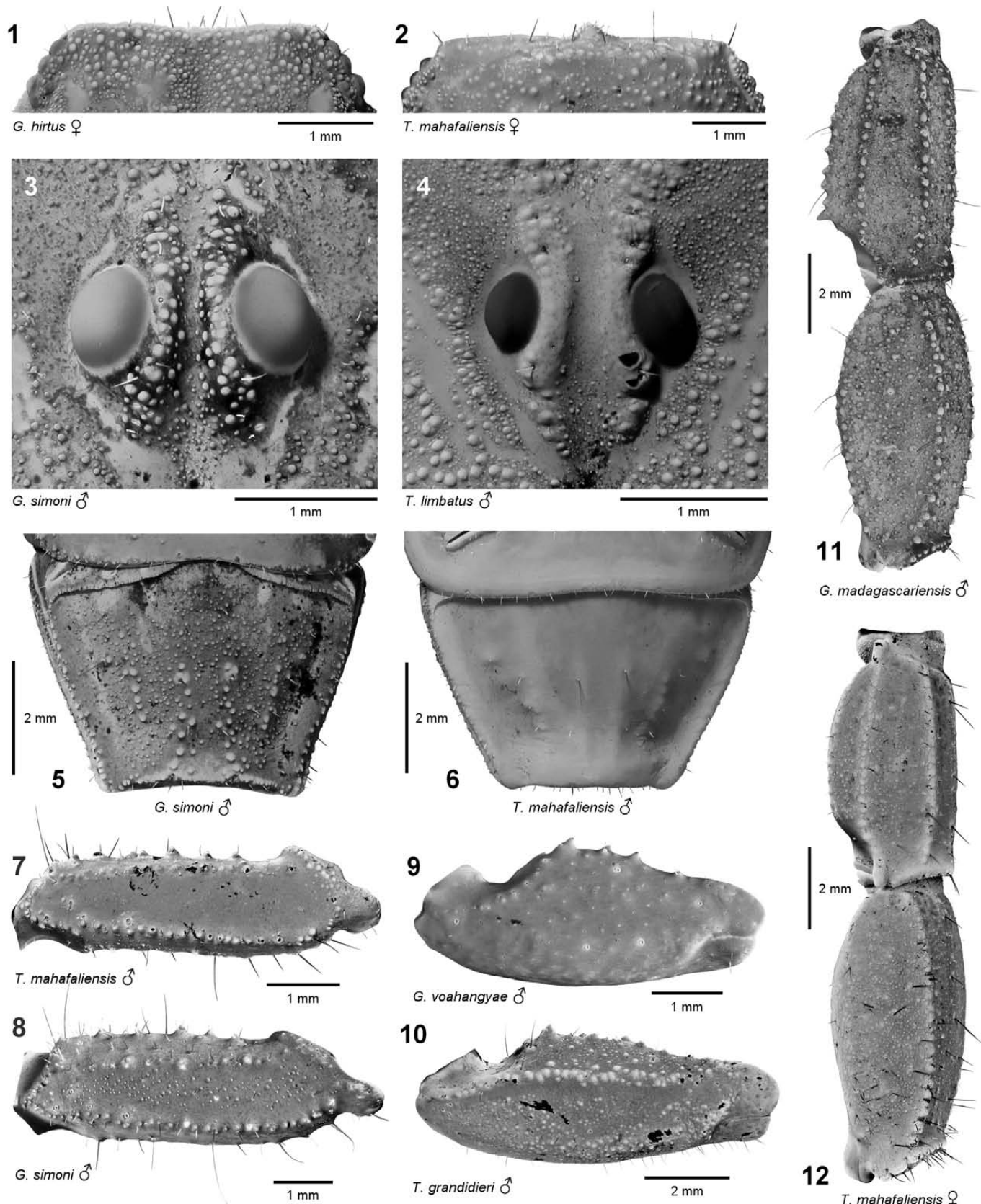
The genus *Teruelius* Lowe & Kovařík, 2019, was created for a subset of species originally included under *Grosphus* Simon, 1880, but was subsequently synonymized with *Grosphus*. We reanalyze *Teruelius* and *Grosphus* by scoring 45 discrete characters, and 32 discrete + 17 continuous characters, for all 36 included species, plus 11 related buthids as outgroup taxa. Morphometric analyses are systematically applied to quantify variation in continuous characters, including: carapace length, carapace anterior concavity, carapace preocular length, hemispermatophore posterior lobe length, tibial spur length/ tibia distal depth ratio, metasoma I length/ width ratio, pectine tooth length/ width ratio, pedipalp femur petite ‘trichobothrium’ d_2 position, pedipalp fixed finger relative position of trichobothria *db* vs. *est*, and pedipalp manus relative position of *Eb* trichobothria. Elliptic Fourier analyses and principal components analyses are applied to quantify variation in sternite IV spiracle aperture profiles, female basal pectinal tooth shapes and telson lateral profiles. Laser light scattering is applied to quantify differences in optical reflectance of sternite VII arising from cuticular lattice microstructures. Spectral image analysis is applied to quantify differences in granulation of metasoma I ventrosubmedian carinae. The use of UV fluorescence as a quantitative taxonomic character is critically reviewed. Six binary characters are proposed for differential diagnosis of *Teruelius* vs. *Grosphus*. Phylogenetic analyses rooting trees with 8 individual outgroup taxa, or with multiple outgroup taxa under morphological and molecular backbone constraints, all yield overwhelming support for the monophyly of *Teruelius*, and the genus is reinstated. The position of outgroup taxon *Microcharmus* in a separate family is not supported by any diagnostic characters or phylogenetic analysis, and Microcharmidae is synonymized with Buthidae. Two new species, *Grosphus angulatus* sp. n. and *Teruelius haekeli* sp. n. are described.

Introduction

The buthid genus *Teruelius* Lowe & Kovařík, 2019, was created to accommodate a subset of species originally included under *Grosphus* Simon, 1880. In our previous analysis, we proposed to separate *Teruelius* from *Grosphus* on the basis of nine morphological characters. Following classic Hennigian argumentation (Wiley & Lieberman, 2011), we performed a priori polarization of these characters by outgroup comparisons. We hypothesized that eight of the nine characters were synapomorphies for *Teruelius*. Subsequently, Lourenço et al. (2020) rejected *Teruelius*, synonymizing it with *Grosphus*. However, they did not test our hypothesis either by analyzing our characters or by presenting new data, and relied only on general criticisms to justify their synonymy. Here we revisit the question of the validity of *Teruelius*. We reanalyze our previous characters in greater detail and introduce numerous additional characters. Monophyly of the genus is tested by phylogenetic analyses with parsimony. Our results support recognition of *Teruelius* as a separate genus.

Methods & Materials

Methods and materials generally follow those described in Lowe & Kovařík, 2019. Additional morphometric analyses were conducted in Maxstat Pro 3.60 (<https://maxstat.de>) and NTSYSpc 2.21w (<http://www.appliedbiostat.com>). Cladistic analyses were conducted in TNT 1.5 (Goloboff & Catalano, 2016). Heuristic searches for most parsimonious trees were performed by generating 1,000 random addition sequences with tree-bisection-reconnection (TBR) branch swapping, holding 50 trees per replicate. Trees were collapsed during searches with minimum length = zero (Rule 1; Coddington & Scharff, 1994). Searches were performed under equal or prior weights, and under a series of implied weights (Goloboff, 1993) with a range of concavities to test the sensitivity of results to weighting schemes. Consistency and retention indices of trees were calculated using the macro script ‘stats.run’. Node supports were estimated by jackknife with symmetric resampling (2,000 pseudoreplicates, probability 33%) expressed as percentage group present/ contradicted (% GC) frequency differences (Goloboff et al., 2003), and



Figures 1–12. Morphological characters of *Grosphus* and *Teruelius*. **Figures 1–2.** Carapace, anterior margin, denticulate medial epistomial process (character 3): absent in *G. hirtus* (1), present in *T. mahafaliensis* (2). **Figures 3–4.** Carapace, superciliary carinae (character 6): granulate in *G. simoni* (3), smooth in *T. limbatus* (4). **Figures 5–6.** Sternite VII, submedian carinae (character 15): granulate in *G. simoni* (5), smooth or obsolete in *T. mahafaliensis* (6). **Figures 7–8.** Pedipalp femur, dorsal surface (character 30): smooth in *T. mahafaliensis* (7), granulate in *G. simoni* (8). **Figures 9–10.** Pedipalp patella (characters 31–33): dorsomedian setation dense (setae broken but sockets visible), and dorsointernal carina absent in *G. voahangyae* (9); dorsomedian setation sparse, and dorsointernal carina strong and densely granulate in *T. grandidieri* (10). **Figures 11–12.** Metasoma IV dorsosubmedian carinae, enlarged posterior terminal spiniform granule (same as for metasoma III = character 21): present in *G. madagascariensis* (11), absent in *T. mahafaliensis* (12); metasoma V dorsolateral carinae (character 22): granulate in *G. madagascariensis* (11), smooth or obsolete in *T. mahafaliensis* (12). All images acquired under UV fluorescence. Scale bars: 1 mm (1–4, 7–9), 2 mm (5–6, 10–12).

by relative Bremer support (% GC) from 50,000–90,000 suboptimal trees generated by successive TBR branch swapping of increasingly suboptimal trees. Genetic distances were calculated in MEGA11.0.13 (Tamura et al., 2021). Technical details of other methods are described in the Results and figure legends.

Nomenclature. Species nomenclature of *Grosphus* and *Teruelius* is a matter of dispute, the resolution of which lies beyond the scope of this contribution. We follow the most recently published opinion of species names (Lourenço et al., 2020) as defined by their diagnoses and descriptions, although this does not constitute an endorsement of their validity. In addition, two new species are herein described and referenced. Anatomical terminology generally follows that of Lowe & Kovařík, 2019. As before, the basal posterior marginal sclerite of the female pectines is termed the basal pectinal tooth (*bpt*), not the ‘basal middle lamella’. The so-called petite trichobothria of buthids are herein referenced as ‘trichobothria’ in quotes because they do not fit the conventional definition of trichobothria, i.e., dark, non-fluorescent setae with very long, thin shafts adapted for ultrasensitive detection of air currents (Reissland & Görner, 1985; Zhang et al., 2020). Buthid petites have much shorter, pale, fluorescent shafts similar to those of putative chemoreceptive sensillae, suggesting “*a different kind of sensory seta altogether*” (Prendini & Wheeler, 2005).

Abbreviations: 2D, two dimensional; 3D, three dimensional; AP, anterior-posterior; *bpt*, basal pectinal tooth/teeth; *bml*, basal middle lamella; CCD, charge coupled device; CI, consistency index; CMOS, complementary metal-oxide semiconductor; COI, cytochrome c oxidase subunit I gene (= *CoxI*); CV, coefficient of variation (= standard deviation/mean); DV, dorsoventral; EFA, Elliptic Fourier Analysis; EW, equal weights; GC, group present/ contradicted; IW, implied weights; LED, light emitting diode; MPT, most parsimonious tree; NIST, National Institute of Standards and Technology; OECF, opto-electronic conversion function; PCA, principal components analysis; PTC, pectinal tooth count; PW, prior weights; RBS, relative Bremer support; Ref., reference to web citation; RI, retention index; SD, standard deviation; SEM, scanning electron microscope; SR, jackknife with symmetric resampling support; UPGMA, unweighted pair group method with arithmetic mean; UV, ultraviolet; **morphometrics:** W, width; W_a , anterior width; L, length; D, depth. In citing figures, capitalized ‘Fig(s).’ cite illustrations in this paper, lower case ‘fig(s).’ cite illustrations in other papers.

Specimen repositories. FKCP: František Kovařík, private collection, Prague, Czech Republic (to be merged in future with collections of National Museum of Natural History, Prague, Czech Republic); FMNH: Field Museum of Natural History, Chicago, USA; GLPC: Graeme Lowe, private collection, Auckland, New Zealand; MHNG: Muséum d’Histoire Naturelle de la Ville de Genève, Geneva, Switzerland; MNHN: Muséum National d’Histoire Naturelle, Paris, France; NHMB: Naturhistorisches Museum, Basel, Switzerland; NZAC: New Zealand Arthropod Collection, Auckland, New Zealand; ZMUH: Centrum für Naturkunde (CeNak), Center of Natural History Universität Hamburg, Zoological

Museum, Hamburg, Germany. Online specimen data posted on institutional websites are cited in text by institutional codes and accession numbers, and listed alphanumerically with links under References.

Results

Characters

We selected for analysis a set of morphological characters that varied systematically between different species of the ingroup *Grosphus* s. lat. = *Grosphus* s. str. (hereafter referred to as ‘*Grosphus*’ for brevity) + *Teruelius*, according to either our observations or published descriptions. These are listed in Table 1 and addressed individually below. The characters were scored for 14 nominal species of *Grosphus*, 22 nominal species of *Teruelius*, and 11 buthid outgroup taxa chosen for their close relationship to *Grosphus* and *Teruelius*.

Character 0. Carapace, mean length: < 5.0 mm (0); 5.0–6.9 mm (1); > 6.9 mm (2)

Sizes of adults have been used previously in diagnoses of species. Carapace length is a morphometric character representing adult size. Fig. 13 shows the distribution of mean adult carapace lengths across both ingroup and outgroup taxa (sexes pooled). The rank ordered bar plot reveals clear segregation of *Teruelius* from *Grosphus*, with minor overlap. The three largest species, *T. ankarana*, *T. flavopiceus* and *T. grandidieri*, are segregated at the upper end of the length range. Most other species of *Teruelius* are smaller than most species of *Grosphus*, with the exception of the ‘*hirtus*’ group of *Grosphus* (defined below under Phylogenetic analysis). We discretized this character into small, medium and large ranges, separated by thresholds at apparent step changes in ranked length.

Character 1. Carapace and tergites, base color: dark, black to brown (0); brown to orange (1); orange to yellow (2)

Base color on the carapace and tergites is a diagnostic character useful for the separation some species. The majority (10/14) of *Grosphus* have darker black to brown base colors, and the majority (15/22) of *Teruelius* have lighter, orange to yellow base colors. However, there is substantial overlap as both genera include species with intermediate base colors.

Character 2. Carapace, color pattern: uniform (0); with maculate or variegated fuscosity (1)

Color patterns on the carapace are potential diagnostic characters useful for the separation some species. Variegated or mottled patterns of fuscosity on the carapace occur in some species of *Grosphus*, in particular the ‘*hirtus*’ group (e.g., Lowe & Kovařík, 2019: figs. 263, 265, 288, 290–291, 303, 352, 354; Lourenço et al., 2007a: 173–174, figs. 2, 15). They are absent in other species, including all *Teruelius*.

Character 3. Carapace, denticulate medial epistomal process: small or absent (0); well developed in either sex (1)

The anterior margin of the carapace of some species of *Teruelius* bears a blunt medial projection with fine denticulation or granulation, in one or both sexes (Fig. 2). This process is small, vestigial or absent in most species of *Grosphus* (Fig. 1).

Character 4. Carapace, anterior margin, mean concavity angle: > 8.4° (0); < 8.4° (1).

The anterior margin of the carapace varies in profile from straight or weakly convex, to emarginate and concave. To quantify this, we measured a concavity angle (Fig. 14, inset). The rank ordered bar plot in Fig. 14 reveals clear segregation of *Teruelius* (lower concavity) from *Groshus* (higher concavity), with minor overlap. The three large species, *T. ankarana*, *T. flavopiceus* and *T. grandidieri*, have higher concavity and segregated with *Groshus*. We discretized this character into low and high ranges, separated by a single threshold at a step transition in rank slope.

Character 5. Carapace, mean ratio of preocular L/Carapace L: < 0.395 (0); > 0.395 (1)

This ratio measures the relative rostrocaudal position of the median ocular tubercle on the carapace (Fig. 15, inset). The rank ordered bar plot in Fig. 15 reveals clear segregation of *Teruelius* (more posterior position of ocular tubercle) from *Groshus* (more anterior position of ocular tubercle), with minor overlap. The three large species, *T. ankarana*, *T. flavopiceus* and *T. grandidieri*, have more anterior placements of the ocular tubercle and segregated with *Groshus*. We discretized this character into anterior and posterior ranges separated by a single threshold at a minor step transition in rank slope.

Character 6. Carapace, supraciliary carinae, males: strongly or moderately granulate (0); weakly granulate or smooth (1)

Granulation of supraciliary carinae is strong in all scored males of *Groshus* (e.g., Fig. 3), and relatively weak or absent in most scored males of *Teruelius* (e.g., Fig. 4), with minor overlap. We scored this character as male specific because there is sexual dimorphism in granulation, which is typically weaker in females. The character was left unscored for taxa described only from females.

Character 7. Hemispermatophore capsule distal carina: long (0); short (1)

A long capsule and distal carina with a proximally positioned basal lobe occurs in some species of *Groshus* (cf. Lowe & Kovařík, 2019: 23, figs. 52–57); in others, including at least some members of the ‘*hirtus*’ group, the capsule is short (cf. Lowe & Kovařík, 2019: 23, figs. 58–68). In all examined species of *Teruelius*, the capsule is short with a distally positioned basal lobe (cf. Lowe & Kovařík, 2019: 25, figs. 71–85).

Character 8. Hemispermatophore capsule posterior lobe: absent (0); elongate, tapered (1); short, blunt or triangulate (2) (Lowe & Kovařík, 2019: 42, character v)

In all examined ingroup species, the posterior lobe of the capsule is present and well developed. Its shape is either elongate and tapered (*Groshus*) or short and blunt (*Teruelius*). The form of the posterior lobe and elongation of capsule distal carina (character 7) together partition the limited set of scored ingroup hemispermatophores into three disjunct clusters in bivariate morphospace (Fig. 16).

Character 9. Hemispermatophore capsule distal carina, number of lateral carinae: none (0); one (1); two or more (2)

The distal carina exhibits variable ornamentation in the form of dark creases or carinae on its convex surface (lateral surface of deposited spermatophore). Most species of *Groshus* that have been investigated bear at least a single partially developed lateral carina (cf. Lowe & Kovařík, 2019: 23, figs. 52–66; 26, fig. 86), whereas two lateral carinae occur in all investigated species of *Teruelius* (cf. Lowe & Kovařík, 2019: 25, figs. 71–85; 27, figs. 90–93).

It should be noted that the data on hemispermatophores (characters 7–9) are the most incomplete for our set of characters. Scored characters included 15/36 (42%) of nominal ingroup species. In the remaining unscored species, either adult males are unknown (8/36), or material was not available for study (13/36). Nonetheless, a 42% coverage can contribute to the phylogenetic analysis.

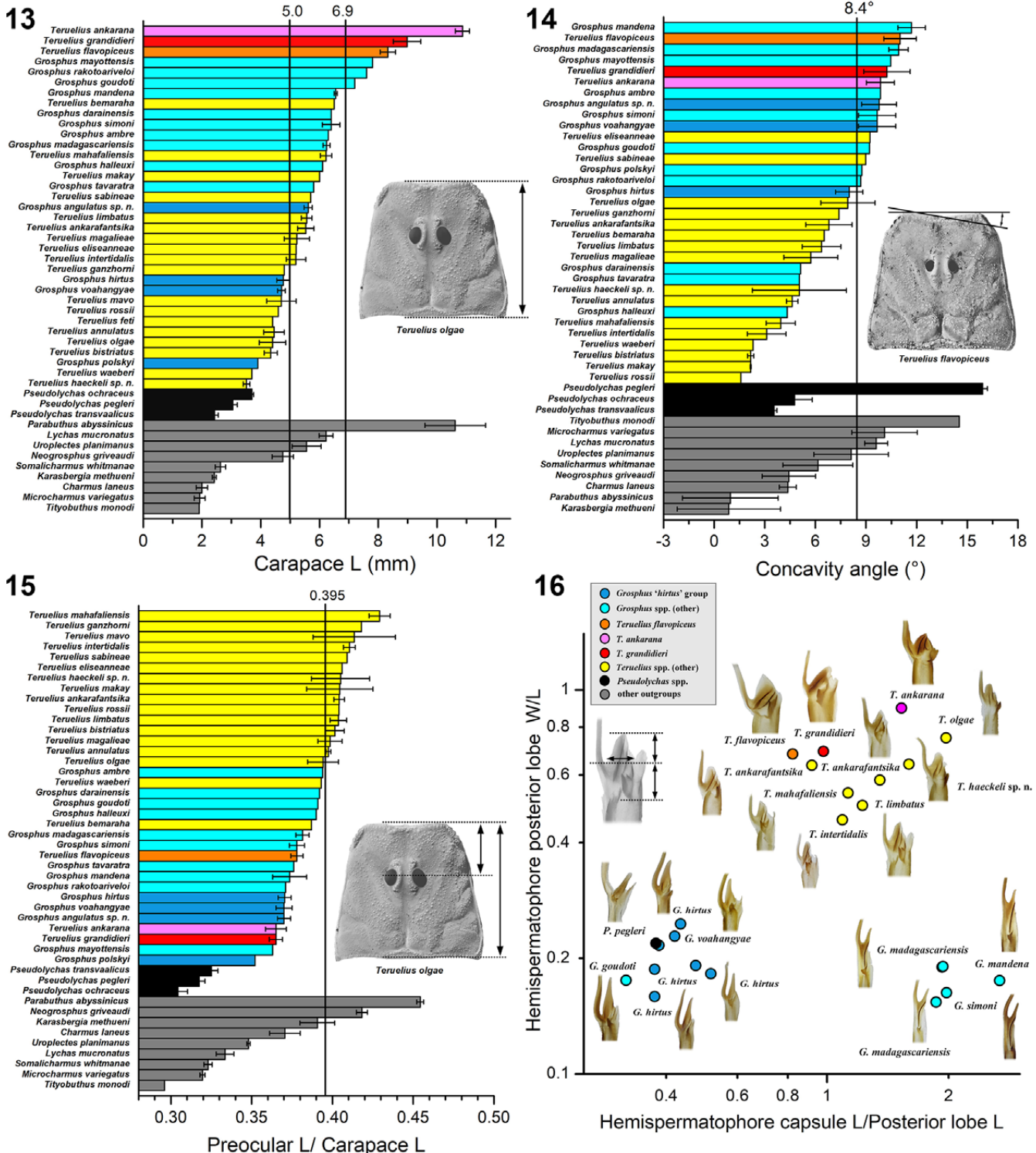
Character 10. Leg III, ratio of tibial spur L/ tibia distal D: < 0.73 (0); > 0.73 (1)

Character 11. Leg IV, ratio of tibial spur L/ tibia distal D: < 0.69 (0); > 0.69 (1)

The lengths of the tibial spurs on legs III–IV normalized to the distal depth of the tibia, varied widely across different ingroup species. Relatively short tibial spurs were characteristic of *Groshus* species (e.g., Figs. 45–46) and relatively long tibial spurs of *Teruelius* species (e.g., Figs. 47–48). Clear separation of the two genera according to tibial spur III–IV lengths is evident in rank ordered bar plots (Figs. 49–50). Discretization thresholds were placed at the largest intermediate step transitions in rank slope. The three large species, *T. ankarana*, *T. flavopiceus* and *T. grandidieri*, have the shortest tibial spurs within *Teruelius*.

Character 12. Legs I–IV, telotarsi, ventral setation: sparse, discrete with < 25 macrosetae in rows (0); dense, brush-like with > 25 irregular macrosetae (1) (Lowe & Kovařík, 2019: 43, character viii)

Ventral telotarsal setation is sparse and discrete in all scored species of *Groshus* (10/14, 71%) (e.g., Lowe & Kovařík, 2019: 39, figs. 133–137) and is dense and brush-like in all scored species of *Teruelius* (21/22, 95%) (e.g., Lowe & Kovařík, 2019: 39, figs. 138–144). Fig. 51 shows the distribution of ventral macrosetal counts on telotarsus III from a sample of $n = 50$ tarsi (*Groshus* 7 spp., *Teruelius* 11 spp.). The distribution was bimodal with a large disjunction along the logarithmic abscissa. For *Teruelius*, the mean count of 201.83 ± 45.85 (mean \pm SD; range 141–319), was about ten-fold higher than for *Groshus* (17.06 ± 3.01 ; 11–24). Macrosetae were not enumerated for some species that were scored on the basis of photographic evidence, as the images did not resolve individual macrosetae. In those cases, we implemented a forensic digital image analysis (Fig. 52). A dense macrosetal brush was detectable as a thick brown fringe along the ventral margin of the telotarsus in *Teruelius* species (Fig. 52, insets a & b; see also Figs. 47–48, ‘vs’), but not in *Groshus* species (Fig. 52, insets c & d; see also Figs. 45–46, ‘vs’). Mean blue channel values of pixels in dorsal and ventral



Figures 13–16. Morphometric analyses of carapace and hemispermatophores. **Figure 13.** Horizontal bar plot of mean carapace length (mm) (character 0) of *Groshus* (n = 46, 14 spp.), *Teruelius* (n = 70, 21 spp.), *Pseudolytchus* (n = 8, 3 spp.), and other outgroup taxa (n = 36, 9 spp.). Data from both sexes pooled. Error bars are standard errors. Discretization thresholds at step changes in ranked length. **Figure 14.** Horizontal bar plot of mean concavity angle (°) (character 4) of *Groshus* (n = 49, 14 spp.), *Teruelius* (n = 72, 19 spp.), *Pseudolytchus* (n = 8, 3 spp.) and other outgroup taxa (n = 22, 9 spp.). Data from both sexes were pooled. Error bars indicate standard errors. Discretization threshold at step transition in rank slope. Inset: angle defined by tangent line at midpoint between anterior-most lateral eye and carapace center. **Figure 15.** Horizontal bar plot of mean ratio of carapace preocular L / carapace L (character 5) of *Groshus* (n = 39, 14 spp.), *Teruelius* (n = 71, 21 spp.), *Pseudolytchus* (n = 8, 3 spp.) and other outgroup taxa (n = 23, 9 spp.). Data from both sexes pooled. Error bars are standard errors. Discretization threshold at a minor step transition in rank slope. **Figure 16.** Bivariate logarithmic scatter plot of hemispermatophore posterior lobe width/length ratio vs. hemispermatophore capsule length/posterior lobe length for *Groshus* (n = 13, 6 spp.), *Teruelius* (n = 10, 9 spp.) and outgroup *Pseudolytchus* (n = 1, 1 sp.). Color codes of symbols or bars as indicated in Fig. 16 legend: *Groshus 'hirtus'* group (*G. angulatus* sp. n., *G. hirtus*, *G. polskyi*, *G. voahangyae*), blue; other *Groshus* spp., cyan; *Teruelius flavopiceus*, orange; *T. ankarana*, magenta; *T. grandidieri*, red; other *Teruelius* spp., yellow; *Pseudolytchus* spp., black; other outgroups, gray.

regions-of-interest exhibited a disjunct bimodal distribution separating *Teruelius* from *Groshus* (Fig. 52, horizontal histogram). As controls, higher resolution images of two species, with and without brush-like setation, were resampled to match the lower resolutions of analyzed images, confirming the differences in mean pixel values.

Character 13. Mesosoma, tergites I–VI, coloration, one or more dark longitudinal stripes: absent (0); present (1)

Color patterns on tergites are potential diagnostic characters for the separation some species. Dark longitudinal stripes on a lighter orange or yellow base color occur in several *Teruelius*, some of which have been assigned to an informal ‘*limbatus/ bistrigatus*’ species group (Lourenço & Wilmé, 2016). This character is absent in *Groshus*.

Character 14. Mesosoma, sternite IV, shape of spiracles: broad, hemi-elliptic or oval, L/W < 5 (0); narrow, slit-like, L/W > 5 (1) (Lowe & Kovařík, 2019: 42, character vi)

We previously showed that the mean L/W ratios of spiracle aperture profiles of several species of *Groshus* and *Teruelius* were separated between the two genera (Lowe & Kovařík, 2019: 30, figs. 106–107; 32, fig. 116). We reanalyzed a larger sample of aperture profiles: $n = 93$ spiracles from *Groshus* (10 spp.) and *Teruelius* (18 spp.) (= 78% of ingroup taxa), and 11 outgroup taxa. Fig. 17 shows the bivariate distribution of two ratiometric descriptors of shape: (ii) circularity = $4\pi \times \text{area} / (\text{perimeter})^2$; the maximal value is 1.0 for a circle, and decreases as the shape becomes more asymmetric or elongated; and (ii) Feret’s caliper ratio = maximum width/ minimum width of parallel tangents. The distributions for *Groshus* and *Teruelius* were disjunct and separated by a wide gap. To confirm this by another method, we reanalyzed aperture profiles by Elliptic Fourier Analysis (EFA) (cf. Character 23 for method description). The upper panel of Fig. 18 shows the joint distribution of the first two principal components of 32 Fourier coefficients, explaining 41.95 % of the variance of up to 8th order harmonics. The density of points along the PC1 axis for *Groshus* and *Teruelius* is shown in the lower panel as a histogram and a collapsed series of points. The two genera were divisible into separate groups along the PC1 axis.

Character 15. Mesosoma, sternite VII submedian carinae: granulate (0); smooth or obsolete (1)

On the submedian carinae of sternite VII, granulation is present in all species of *Groshus* (e.g., Fig. 5), and absent in all species of *Teruelius* (e.g., Fig. 6) that were scored (10/14 and 15/22 species, respectively; 69.4% of ingroup taxa).

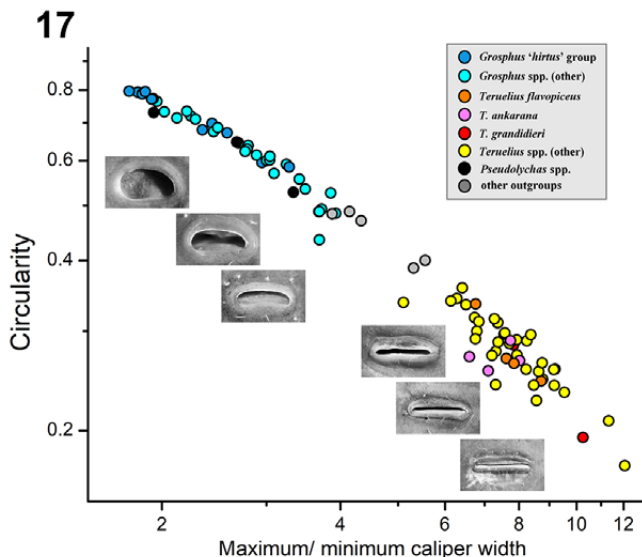
Character 16. Mesosoma, sternite VII, medial texture and optical reflectance: matte, low reflectance (0); glossy, high reflectance (1)

Figs. 53–57 show sternites IV–VII of several species of *Groshus*. Images were acquired under directional, partially diffuse white-light illumination to visualize specular reflections from glossy surfaces. Sternites IV–VI were glossy with reflections, whereas sternite VII was matte without reflections except from isolated polished granules and carinae. The ventral surface of metasoma I was also matte and non-reflective. Figs. 60–66 show sternites IV–VII of several

species of *Teruelius*. All sternites, including VII, were glossy and reflective, as were the ventral surfaces of metasoma I. Two outgroup species, *Pseudolychas transvaalicus* (Fig. 58) and *Lychas mucronatus* (Fig. 59), had matte, non-reflective surfaces on sternite VII. This character could be scored from published images by comparing the reflectance of sternite VII vs. sternite VI. Differences between matte and glossy were detectable in these adjacent sternites illuminated by a more distant photographic light source (Figs. 53–66). This allowed us to score 25/36 (69%) of ingroup species.

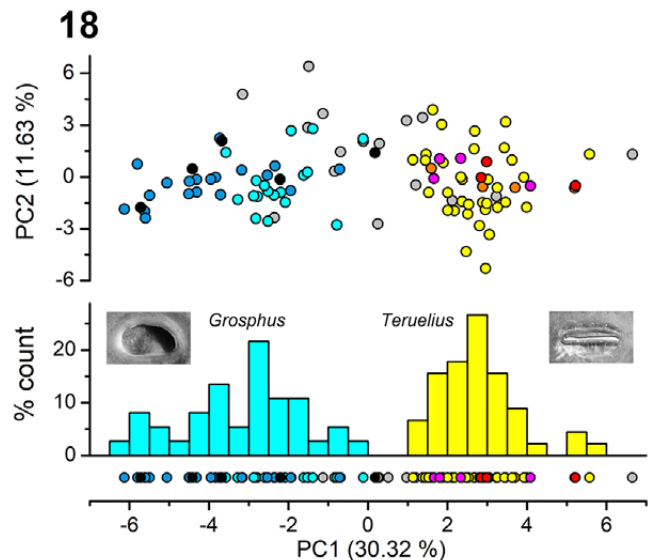
To quantify optical reflectance of sternites VI and VII, we recorded the spatial spread and intensity of reflected laser light. Sternites were dissected from the mesosoma and soft tissues were scraped off their internal surfaces to eliminate extraneous reflections and scattering. Sternites were mounted flat under a plate with a 2.25 mm diameter aperture exposing the ventromedial surface where the beam from a 650 nm laser diode was focused to a 40 µm diameter spot. The angle of incident light was +45° from normal, and reflected light at an angle of -45° from normal was viewed on a translucent projection screen. In *Groshus*, reflection from sternite VI was partially specular with a higher intensity in the center of the beam (Figs. 92, 94). Reflection from sternite VII was diffuse and widely scattered (Figs. 91, 93). Similar results were obtained for *Lychas* (Figs. 95–96). In *Teruelius*, reflection was partially specular from both sternites VI and VII (Figs. 97–102). As a measure of beam dispersion, we calculated intensity-weighted mean radii of reflected light patterns over a fixed solid angle around the beam center. For sternite VII, higher radii were obtained for *Groshus* and *Lychas*, and lower radii for *Teruelius* (Fig. 103). Radii were lower for sternite VI in all tested species. As a measure of relative reflectance, we calculated mean intensities of reflected light patterns over a fixed solid angle around the beam center. Intensities of sternite VII reflections were higher in *Teruelius*, and lower in *Groshus* and *Lychas* (Fig. 104). Intensities of sternite VI reflections were higher in all tested species.

Microscopic examination of the cuticle revealed differences in surface structure that could account for the observed differences in optical reflectance. Figs. 67 and 71 show medial intercarinal surfaces of sternite VII of two species of *Groshus* viewed in reflected light. These surfaces had rough textures which differed from the smooth textures on sternite VI shown in Figs. 68 and 72. Inspection under higher magnification by transmitted light microscopy revealed micron-scale lattice structures on the surface of sternite VII (Figs. 69, 73) that were absent on sternite VI (Figs. 70, 74). The pale spots in Figs. 68 and 72, and dark pores in Figs. 70 and 74, were identified as dermal gland openings (Farley, 1999; Shrivastava, 1954). Abundant pore canals (Filshie & Hadley, 1979) were also visible on sternite VI (Figs. 70, 74). Dermal glands and pore canals on sternite VII were obscured by the lattice microstructure. In *Teruelius*, lattice microstructures were absent on both sternite VI and VII (Figs. 79–90). In outgroup taxon *Lychas mucronatus*, cuticular surfaces of sternites VI and VII were similar to those of *Groshus* (Figs. 75–78), with lattice microstructure on sternite VII.



Figures 17–18. Morphometric analyses of spiracles. **Figure 17.** Bivariate logarithmic scatter plot of circularity vs. Feret's caliper ratio of spiracle IV aperture shapes in *Groshus* ($n = 37$, 10 spp.), *Teruelius* ($n = 45$, 18 spp.) and outgroup taxa ($n = 11$, 7 spp.). Aperture defined as margin of opening of passage leading to atrium and book lung lamellae, excluding ridges and ornamentation. **Figure 18.** Elliptic Fourier Analysis (EFA) of spiracle aperture shapes of Fig. 17. Upper panel: bivariate scatter plot of principal component PC2 (11.63% of variance) vs. PC1 (30.32% of variance) extracted from PCA of up to 8th order harmonics (32 coefficients) of spiracle profiles. Profiles oriented with long axis horizontal, anterior on top, start point at top centroid. Lower panel: frequency distributions of *Groshus* (cyan bars) and *Teruelius* (yellow bars) along PC1 axis. Color codes of symbols indicated in Fig. 16–17 legends.

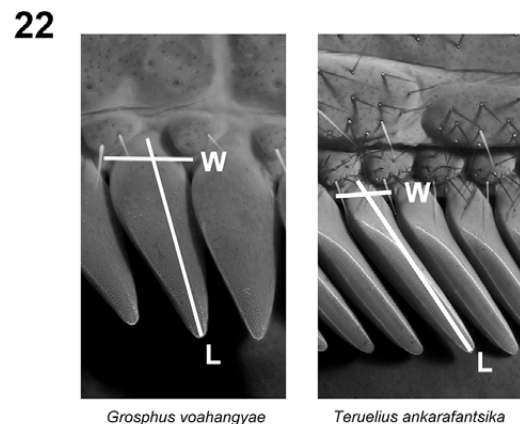
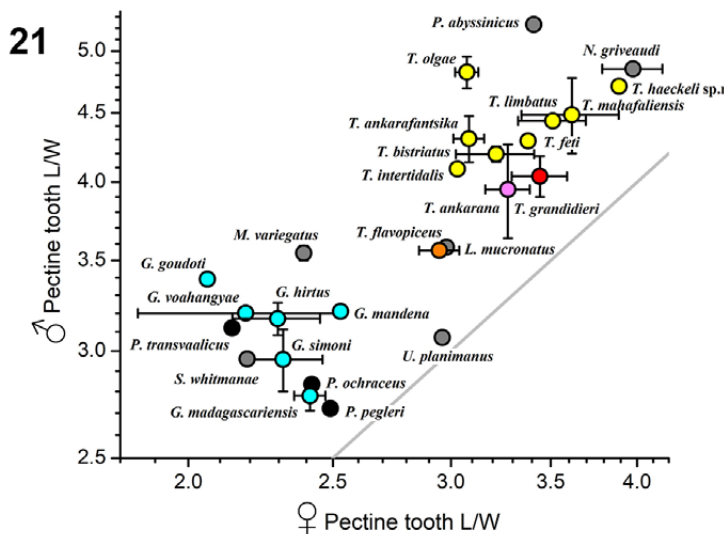
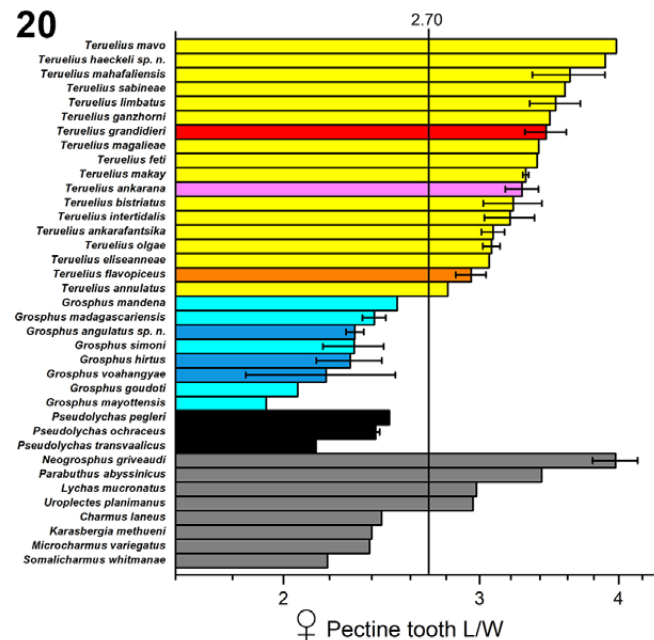
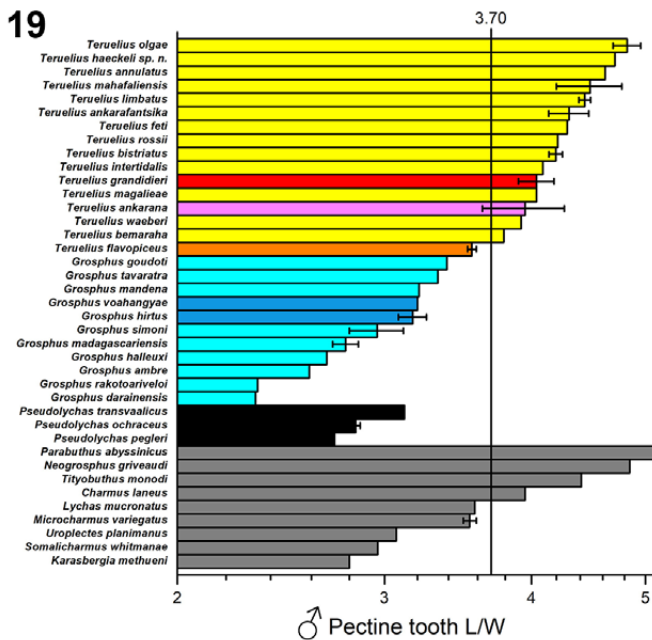
Similar lattice microstructures have been described in the scales of butterflies (Davis et al., 2020a; Dou et al., 2020; Vukusic et al., 2004; Yan et al., 2016) and snakes (Crowe-Riddell et al., 2021; Spinner et al., 2013). They suppress specular light reflection by forming multiple light scattering paths at the surface interface (structural absorption). Other antireflective microstructures with similar mechanisms have evolved independently in diverse animals, e.g., birds-of-paradise, peacock spiders, a stick insect and many bathypelagic fish (Davis et al., 2020b; Maurer et al., 2017; McCoy et al., 2018, 2019). Hypothesized functions include enhancing sexual displays and camouflage. Crypsis may be an ecological function of antireflective cuticles in scorpions. In *Groshus*, matte cuticle of lower reflectance is not restricted to sternite VII, but extends over other surfaces, e.g., ventral and lateral surfaces of metasoma and telson, and dorsal surfaces including carapace, tergites and pedipalps. These low-reflectance surfaces may be more exposed to visually guided predators. If the metasoma is coiled over the mesosoma in a resting posture, the matte ventral and lateral surfaces of the metasoma and sternite VII are visible. At the same time, the reflective surfaces of dorsal metasomal segments and telson, and sternites IV–VI are concealed. This could reduce the visibility of forest-dwelling scorpions in epigean habitats, where they may be exposed to visual detection by diurnal predators. In *Teruelius*, a smooth, higher reflectance cuticle is typically present on the surfaces that are dull and matte in *Groshus*. One exception is *T. grandidieri*, a distinctive black species with matte cuticle on some exposed surfaces (Fig. 92; Lowe & Kovařík, 2019: 100, figs. 491–494; 121–122, 600–603). However, *T. grandidieri* still possesses a reflective



sternite VII as a taxonomic character of the genus (Fig. 62). Species of *Teruelius* in more arid environments may shelter in burrows that conceal them from the view of diurnal predators. Interestingly, some other bathids in arid regions also have reflective cuticles, e.g., *Parabuthus*, *Uroplectes*, *Karasbergia*, *Somalicharmus* and many species of the ‘*Buthus*’ group. Conversely, many bathids in tropical regions have matte cuticles, e.g., *Lychas*, *Isometrus*, *Tityus* and *Ananteris*. The arid-adapted species tend to be more uniform in color, whilst many tropical species have disruptive coloration patterns suggesting stronger selective pressure from visual predators. Thermal factors could also dictate cuticular microstructure and color. In hot desert environments, a dark, light-absorbing matte cuticle increases the risk of overheating by solar radiation, compared to a pale reflective cuticle.

Character 17. Metasoma I ventrosubmedian carinae: granulate (0); costate-granulate (1); smooth (2), absent (3) (Lowe & Kovařík, 2019: 43, character vii)

Variation in the morphosculpture of ventrosubmedian carinae of metasoma I is illustrated in Figs. 105–149, for *Groshus* (9 spp.) and *Teruelius* (20 spp.) (80.5% of ingroup taxa). In most *Groshus*, carinae were marked by a series of discrete granules (Figs. 105–116, 118–119), and in most *Teruelius*, carinae were smooth (Figs. 120–129, 132–138, 141–143, 147–149). In a minority of cases, mostly *Teruelius*, the carinae appeared costate-granulate with granules connected along a continuous ridge (Figs. 117, 130, 139–140, 144–146). One exception was *T. feti* whose carinae have more discrete granules. However, the examined specimen of *T. feti* (holotype male) was a juvenile, whereas all others were adults.



Figures 19–22. Morphometric analyses of regular pectine teeth. **Figures 19–20.** Horizontal logarithmic bar plots comparing length/ width (L/W) ratios of regular pectine teeth in males (19) and females (20) of *Grosphus*, *Teruelius* and outgroup taxa. Bars are rank ordered means, error bars are standard errors; ♂ $n = 52$, 30 spp.; ♀ $n = 66$, 31 spp. **Figure 21.** Bivariate logarithmic scatter plot comparing pectinal tooth L/W ratios of males (ordinate) vs. females (abscissa) (21 spp.). Gray line is diagonal. Plotted values and error bars as in Figs. 19–20. **Fig. 22.** Regular pectine teeth (♀) of *Grosphus voahangyae* (left) and *Teruelius ankrafantsika* (right), showing measurements of length (L) and width (W). W is equal to inter-fulcral spacing. UV fluorescence. Measurements were taken at > 3 teeth away from most proximal or most distal teeth. Color codes of symbols and bars as in Fig. 16–17 legends.

Granulation is usually described in subjective terms, and we sought a quantitative method to objectively compare the carinal granulation across the ingroup taxa. Soleglad & Fet (2008: 71–74) used ‘granulation quotients’ calculated as means over multiple carinae of integer codes of granulation. However, the codes were linked to categories defined by traditional verbal descriptors, so scoring still depended on subjective judgements. More objective approaches have measured densities and size-distributions of granules on intercarinal surfaces (e.g., Lowe et al., 2014: 3, figs. 93–94;

Zambre et al., 2014: 400). We applied different methods of image analysis to analyze the carinal granulation visible in Figs. 105–149. These figures include both UV fluorescence and reflected white light images, which highlight granules by different physical mechanisms. However, in both image types, stronger granules or carinae show brighter contrast over their backgrounds. We extracted granulometric measures from this contrast by two methods. Firstly, a gray level thresholding of images was performed. A binary map of granules or carinae was then generated automatically by

a maximum entropy algorithm that computed a threshold cutoff in the gray level histogram (Kapur et al., 1985; implemented in ImageJ 1.52a). In *Groshus*, thresholded regions typically resolved into regular series of separated regions or ‘granules’ (e.g., Fig. 150); in *Teruelius* they typically coalesced into longer linear regions or ‘carinae’ (e.g., Fig. 154). The separability of granules by thresholding is determined by the magnitude of variation in gray levels of ‘granules’ vs. inter-granular integument (higher in *Groshus*, lower in *Teruelius*). Secondly, we analyzed the variation in gray levels along carinae. Piecewise linear trajectories were traced through granules of carinae (e.g., Figs. 151, 155), fluctuations in gray level along these trajectories were profiled (e.g., Figs. 152, 156), and power spectra of profiles were computed. Spectra contained one or more peaks whose heights, widths and positions were related to the strength, regularity and density of granulation, respectively. In *Groshus*, stronger granulation was correlated with larger oscillatory fluctuations in gray levels and higher peaks (e.g., Fig. 153); in *Teruelius*, weaker granulation was correlated with smaller oscillatory fluctuations and lower peaks (e.g., Fig. 157). The integrated power over a spatial frequency range of 10–26 granules/carina was calculated and compared to the mean length of granules defined as topologically disconnected domains detected by the binary thresholding method. Fig. 158 shows a bivariate logarithmic scatter plot of these two variables. A segregation of *Groshus* from *Teruelius* is evident. The sole exception was the juvenile male of *T. feti*, which had more pronounced granulation on the ventrosubmedian carinae (Fig. 131). The juvenile condition may be plesiomorphic, which would be consistent with our previous polarization of this character as granulate = primitive (Lowe & Kovařík, 2019: 43).

Character 18. Metasoma I, mean ratio L/W: ♂ < 1.02, ♀ < 0.97 (0); ♂ 1.02–1.7, ♀ 0.97–1.3 (1); ♂ > 1.7, ♀ > 1.3 (2) (♂ priority)

Morphometrics of metasomal segments varied across species of the ingroup. In particular, there was high variation in the elongation of metasomal segment I, as quantified by the L/W ratio. A rank ordered bar plot of this ratio in males (Fig. 168) revealed partial segregation of *Groshus* vs. *Teruelius*, dividing *Groshus* into several clusters. Discretization thresholds were placed at step changes in ranked ratio. Females exhibited a similar trend, but their thresholds differed slightly from those of males due to sexual dimorphism in metasomal morphometrics. Metasomal elongation and its variation were more pronounced in males. For the purpose of discrete character coding, male ratios were given priority when there was a conflict (in a minority of cases).

Character 19. Metasoma III ventral intercarinal surface: granulate (0); very weakly granulate or smooth (1)

Granulation of metasomal segments varied across species of the ingroup. To represent this variation, granulation on the ventromedial surface of metasoma III was scored. Granulation was present on all species of *Groshus*, and 12/22 species of *Teruelius*.

Character 20. Metasoma III, dorsosubmedian carinae, dentate posterior subterminal granule, either sex: present (0); absent (1)

The development of granules on the dorsosubmedian carinae of metasomal segments varied across species of the ingroup. They ranged from obsolete, to weak and blunt, to strong and dentate or triangular. To represent this variation, we scored the presence or absence of a dentate posterior subterminal granule on dorsosubmedian carinae of metasoma III. A dentate subterminal granule was present in 9/14 species of *Groshus*, and absent in *Teruelius*. When present, it could be either the same size as more anterior granules, or slightly larger.

Character 21. Metasoma III, dorsosubmedian carinae, large dentate or spiniform posterior terminal granule, either sex: present (0); absent (1)

The posterior terminus of the dorsosubmedian carinae on metasoma III was furnished with an enlarged dentate or spiniform granule in some species. This granule was distinctly larger than the subterminal granule and other more anterior granules on the carina. It was present in 13/14 species of *Groshus*, and 8/22 species of *Teruelius*.

Character 22. Metasoma V, dorsolateral carinae, granulation: strong (0); weak (1); smooth or obsolete (2)

Development of a granulated dorsolateral carina on metasoma V varied widely. A granulated dorsolateral carina was present in 13/14 species of *Groshus*. In *Teruelius*, the dorsolateral carina was weak, smooth or obsolete except in *T. grandidieri*.

Character 23. Basal pectinal tooth (bpt), female, shape: unmodified (0); triangular (1); ovoid or subrectangular (2); elongated, curved (3) (Lowe & Kovařík, 2019: 41, character iv)

In all ingroup taxa, the female basal pectinal tooth (bpt) was modified, differing from regular pectinal teeth in being dilated in some species, elongated in others, and always lacking a sensorial area with peg sensillae (cf. Lowe & Kovařík, 2019: 21–22, 24, figs. 40–51; 64, figs. 196–210). Shapes of bpt vary widely and have been used previously in keys to and diagnoses of species. However, descriptions of bpt shapes were qualitative. Lowe & Kovařík (2019: 7, 12, 41) used qualitative descriptors of bpt shape in their diagnoses of *Teruelius* and *Groshus*. For a more quantitative and objective analysis, we applied geometric morphometrics to compare bpt shapes. The absence of clear landmark structures in female bpt ruled out techniques of thin-plate spline and Procrustes superimposition. We applied two methods of landmark-independent shape parametrization that yielded different measures of variation.

The first method analyzed six ratiometric shape descriptors: (i) basal tooth width ratio = width of bpt/ width of the row of regular pectinal teeth (widths were orthogonal distances relative to an axial reference line drawn through centers of fulcra); this variable expresses bpt dilation in terms of relative protrusion beyond the line of regular pectine teeth; (ii) solidity = ratio of area/ convex hull area

of the *bpt*; this variable decreases if the perimeter includes concave sections and is sensitive to curved extensions; (iii) perimeter attachment ratio = total perimeter length/ length of perimeter attached to base of comb; this variable increases if the *bpt* expands or lengthens while maintaining a fixed length of attachment to the comb; (iv) circularity (described under character 14); (v) ellipse aspect ratio = major axis/ minor axis of ellipse fitted to the perimeter; this variable increases with *bpt* elongation; and (vi) Feret's caliper ratio (described under character 14); this variable increases with *bpt* elongation. Ratios were computed for $n = 101$ female *bpt* (*Groshus*, 8 spp.; *Teruelius*, 19 spp.), including all species in which females have been described. In bivariate scatter plots (Figs. 23–26), some ratios grouped and separated *Groshus* from *Teruelius*. Ratios were linearized by logarithmic transform and analyzed collectively by PCA. The first two principal components explained 93.74% of the variance (PC1 85.31%, PC2 8.43%) (Fig. 27). *Groshus* and *Teruelius* occupied disjunct domains separated by a gap along the PC1 axis. The *Groshus* domain was relatively compact, reflecting their simpler, more homogeneous *bpt*. In contrast, the *Teruelius* domain was broader, reflecting the greater diversity of *bpt* shape. *T. flavopiceus* has a simpler, less elongated *bpt* than those of other *Teruelius*, and was positioned closer to *Groshus*. The simple *bpt* of outgroup *Pseudolychas* were associated with *Groshus*. Data of Fig. 27 are plotted as species means in Fig. 28.

Although morphometric ratios captured only a limited number of shape attributes (elongation, convexity, size relative to comb), they were sufficient to separate *Teruelius* from *Groshus*. To confirm the separation, we reanalyzed *bpt* by a second method. Elliptic Fourier analysis (EFA) was applied to dissect *bpt* profiles in finer detail (Caple et al., 2017; Kuhl & Giardina, 1982). The *x*- and *y*-components of 2-D outlines of *bpt* were decomposed into finite Fourier series:

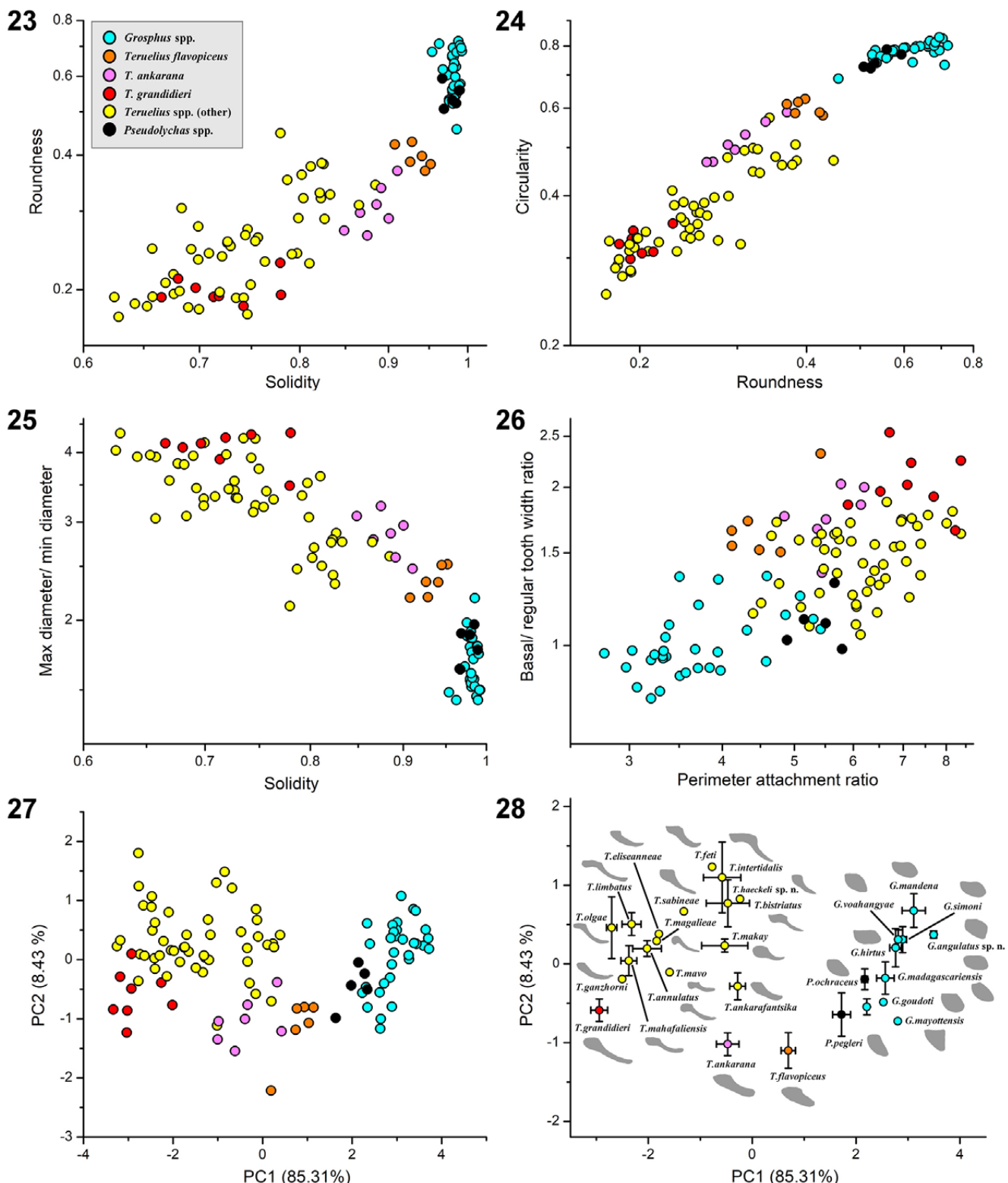
$$x(t) = \sum_{k=1}^N \left(A_k \cos \frac{2\pi k t}{T} - B_k \sin \frac{2\pi k t}{T} \right), y(t) = \sum_{k=1}^N \left(C_k \cos \frac{2\pi k t}{T} - D_k \sin \frac{2\pi k t}{T} \right)$$

where t is distance along the curve, and T the total perimeter length. The $4N$ harmonic coefficients $\{A_k, B_k, C_k, D_k\}$ contain information about progressively higher spatial frequencies with increasing k . The sum of squares of the k^{th} coefficients measured the power at each harmonic frequency (Fig. 29). The mean spectra confirmed that more complex *bpt* of *Teruelius* contained stronger high frequency content than simpler *bpt* of *Groshus*. Fourier series including up to $N = 8$ terms were sufficient to fit profiles of the most elongated *bpt* (Fig. 29, inset), so each shape was parametrized by 32 coefficients. These were converted to z-scores and analyzed by PCA. The first three principal components explained 58.36% of the variance (PC1 31.02%, PC2 19.14%, PC3 8.20%). Bivariate scatter plots of PC1 vs. PC2, and PC2 vs. PC3 show that *Groshus* and *Teruelius* occupied disjunct domains (Figs. 30–31). Data in Fig. 30 are plotted as species means in Fig. 32. *Groshus* species were again confined to a relatively compact domain, in agreement with ratiometric

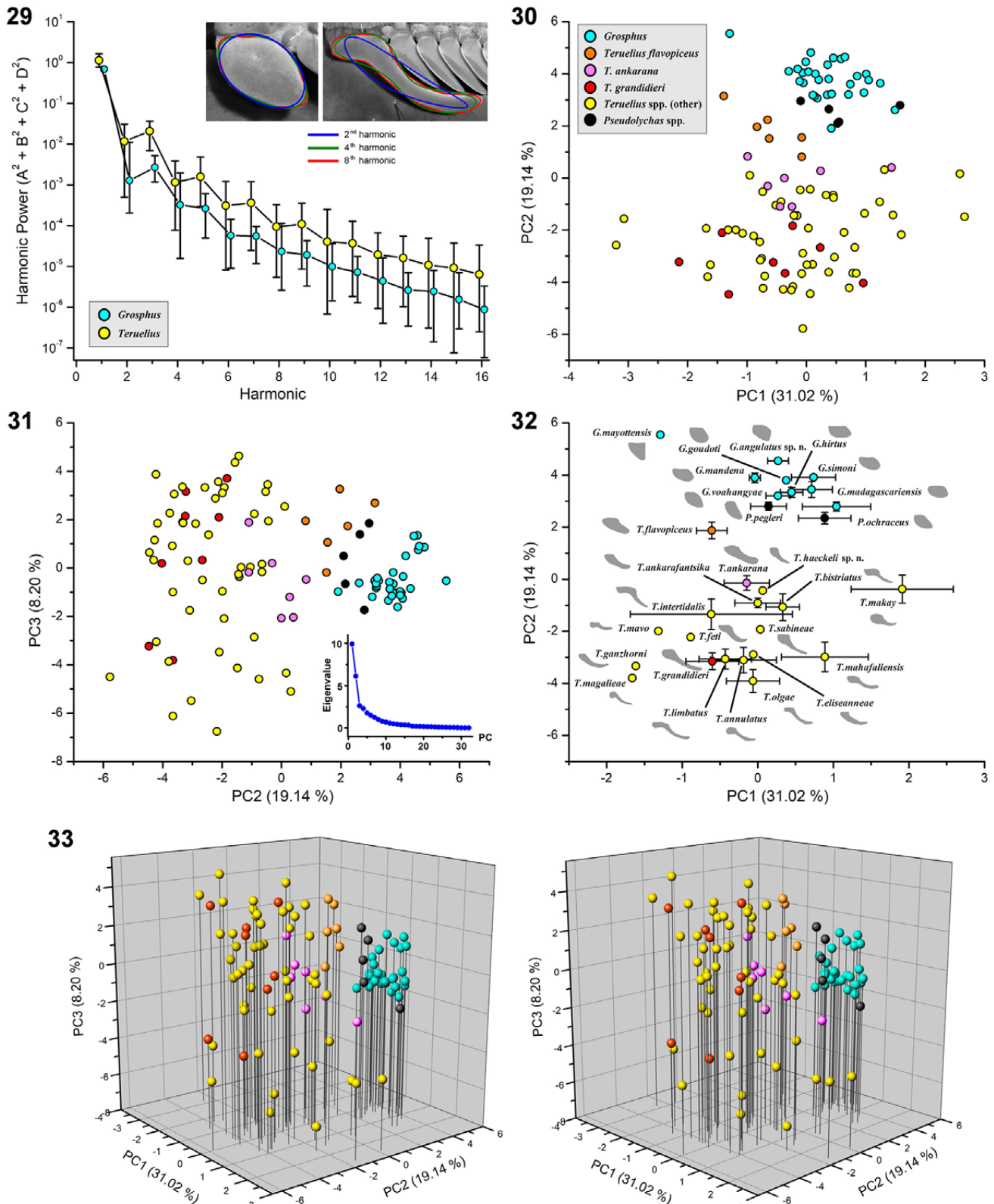
analysis. However, *Teruelius* species were more dispersed because the harmonic analysis resolved greater differences in *bpt* shape. Among *Groshus* species, *G. mayottensis* was an outlier with a subtriangular *bpt* differing from the ovoid shapes of the others. This species is known only from the Comoros Archipelago, and is geographically isolated from other *Groshus*. In the bivariate scatter plots (Figs. 30–31), some samples of *T. flavopiceus* were located closer to *Groshus*, and appeared to narrow the gap between the two genera. However, in a trivariate 3D scatter plot, these points were separated from *Groshus* along the third principal component (Fig. 33). Species of the outgroup genus *Pseudolychas* were again associated with *Groshus*. The geometric morphometric analyses provided a mathematical framework for partitioning *bpt* shapes into discrete categories for phylogenetic character coding (MacLeod, 2002).

We could also demonstrate morphometric divergence of *Teruelius* and *Groshus* *bpt* by hierarchical cluster analysis. The z-scores of harmonic coefficients were used to compute a Euclidean distance matrix between samples. The UPGMA algorithm yielded a *bpt* phenogram with nearly all *Groshus* samples clustered separately from *Teruelius* (Fig. 34). The only exception was *G. mayottensis*, which was identified as an outlier in the PCA. The position of the *Groshus* cluster does not necessarily reflect its phylogenetic relationship with *Teruelius* because the tree is constructed only from phenetic distances. A *bpt* phylogram can be assembled by neighbor-joining with *Pseudolychas* designated as an outgroup. In the resulting tree, *Groshus* was paraphyletic and *Teruelius* formed a monophyletic group (Fig. 35). Thus, both PCA and cluster analyses validated *bpt* shape as a diagnostic character for separating the genus *Teruelius* from *Groshus*.

It is evident from Figs. 34–35 that *bpt* morphometrics was insufficient to resolve species level taxonomy. Several conspecifics were scattered over different tree branches, echoing their broad dispersion in PCA morphospace (Figs. 23–28, 30–33). This indicates substantial variation in *bpt* shape for some species, contrary to the assertion that there is “little intraspecific variation” (Lourenço, 2014: 632). Below, we list several examples of potential intraspecific variation in female *bpt* shape. We define the following descriptors: *clavate*: club-shaped, divided into two distinct sections: a subrectangular or bacilliform basal section which may be mildly dilated, with its axis parallel to the comb axis, and an elongate, curved distal section arising at an angle relative to the comb axis, with the transition between the two sections marked by a bend or asymmetric constriction; *ampullate*: flask-shaped, divided into two distinct sections: a strongly dilated, rounded basal section, and a narrower, short distal section, with the transition between the two sections marked by a more or less symmetric constriction; *falcate*: more elongate, sickle-shaped, not clearly divided into distinct sections, but forming a single, curved piece nearly constant in width from base to apex; *hamate*: less elongate, ‘hook’-shaped, not clearly divided into distinct sections, but composed of a single, curved piece that tapers apically.



Figures 23–28: Ratiometric analysis of shapes of female basal pectinal teeth (*bpt*). **Figures 23–26.** Bivariate logarithmic scatter plots of six ratiometric shape variables: roundness vs. solidity (23), circularity vs. roundness (24), maximum/ minimum caliper diameter vs. solidity (25), basal tooth width/ regular tooth width vs. perimeter attachment ratio (26). **Figures 27–28.** Bivariate scatter plots of first two principal components (PC2 vs. PC1) obtained from PCA of standardized logarithms of all six ratiometric variables, accounting for 85.31% and 8.43% of variance, respectively. Individual cases plotted in Fig. 27, means and standard errors for each species in Fig. 28. Profile silhouette examples are shown for analyzed species in Fig. 28. Data from 106 *bpt* from *Grosphus* ($n = 31$, 8 spp.), *Teruelius* ($n = 70$, 18 spp.) and *Pseudolytchus* ($n = 5$, 2 spp.). Symbol colors indicated in legend of Fig. 23.



Figures 29–33: Elliptic Fourier analysis (EFA) of shapes of female basal pectinal teeth (*bpt*). **Figure 29.** Logarithmic plots of harmonic power (sums of squares of Fourier coefficients) vs. harmonic order for fits to *bpt* outlines of *Grophus* (blue symbols) and *Teruelius* (yellow symbols). Error bars indicate ranges (minimum to maximum). Upper inset: examples of EFA fits to *bpt* from *Grophus* (*G. voahangyae*) (left) and *Teruelius* (*T. olgae*) (right) by Fourier series with cumulative terms up to and including second (blue), fourth (green) and eighth (red) order harmonics. Contours of *bpt* oriented with perimeter attachment horizontal, start point at proximal vertex, area normalized. **Figures 30–31.** Bivariate scatter plots of *bpt* scores for first three principal components, PC2 vs. PC1 (Fig. 30) and PC3 vs. PC2 (Fig. 31), obtained from PCA of 32 standardized Fourier coefficients from up to eighth order harmonic terms, accounting for 31.02%, 19.14% and 8.20% of variance, respectively (total variance 58.36%). Lower inset in Fig. 31: scree plot of eigenvalue vs. PC number. **Figure 32.** Bivariate scatter plot of means and standard errors of *bpt* scores of first two principal components, PC2 vs. PC1, for each species in Fig. 30. **Figure 33.** Trivariate scatter plot of *bpt* scores of first three principal components (PC1, PC2, PC3) rendered as 3D cross stereoscopic pair. Symbol colors as in legend of Fig. 30. Analyzed data set as in Figs. 23–28.

(i) *T. bistriatus* (Kraepelin, 1900): Kraepelin (1900: 15, fig. 30), Fage (1929: 652, fig. 5) and Lourenço (1996b: 56, fig. 5) depicted a short, hamate *bpt*. According to Lourenço (2003b: 145), some material referred by Fage (1929) and Lourenço (1996b) to *T. bistriatus* belonged to a different species, *T. ankaraensiska*, which has a falcate *bpt* (Lourenço, 2003b: 149, figs. 16, 18). This raises the question of whether the hamate *bpt* illustrated in Fage (1929) and Lourenço (1996b) represent material of *T. ankaraensiska*, or *T. bistriatus*. However, the hamate *bpt* of a syntype shown in Kraepelin (1900) should represent *T. bistriatus*. For *T. bistriatus*, Lourenço (2003b: 149, figs. 15, 17) showed an ampullate *bpt* in a topotype. However, Lowe & Kovařík (2019: 64, fig. 204; 92, fig. 433) showed photographs of a second syntype in ZMUH, maybe different from the one illustrated by Kraepelin (1900), with a clavate *bpt*. Lourenço & Wilmé (2016: 54, fig. 2) showed a photograph of a topotype, also with a clavate *bpt* (Ref. MNHN-RS-RS9062).

(ii) *T. intertidalis* (Lourenço, 1999): the *bpt* of the holotype was depicted as fused with the basal middle lamella to form a single continuous structure in the original description (Lourenço, 1999a: 134, fig. 5), and subsequently (Lourenço et al., 2007b: 373, fig. 14). However, a photograph of the holotype showed a clavate *bpt* that was separated from the basal middle lamella, but with an ampullate shape different from the clavate form of the holotype *bpt*.

(iii) *T. annulatus* (Fage, 1929): Fage (1929: 656, fig. 7) depicted the *bpt* of a syntype as having a clavate shape, with proportions differing from those of the clavate *bpt* of *T. limbatus* (Fage, 1929: 654, fig. 6), a species under which *T. annulatus* was originally described as a subspecies. Lourenço (1996b: 56, fig. 9) depicted a falcate *bpt*, as did Lourenço et al. (2007b: 373, fig. 12) and Lourenço et al. (2020: 5, fig. 5, erroneously captioned as “holotype”). But, a photograph of a syntype shows a clavate *bpt* (Ref. MNHN-RS-RS1314) very similar in shape to the *bpt* illustrated by Fage (1929: 656, fig. 7).

Possible explanations for these variations that might rescue *bpt* shape as a stable species character include misidentified and mislabeled specimens, or illustration errors. However, conspicuous differences in shape can occur even within a single individual. For example:

(iv) *T. ganzhorni* (Lourenço, Wilmé & Waeber, 2016): a photograph of the holotype female (Lourenço et al., 2016: 46, fig. 2; Ref. MNHN-RS-RS9080) shows a clavate right *bpt*, and a falcate left *bpt*.

The shape of the *bpt* was previously applied as a diagnostic character in keys (Lourenço, 1996b: 8–9; Lourenço, 2003b: 153–154). Lourenço et al. (2020: 11) argued that *T. feti* was distinct from *T. makay* on the basis of *bpt* shape, shown as falcate or clavate-falcate in *T. feti* (Lourenço et al., 2020: 5, fig. 4) vs. ampullate in *T. makay* (Lourenço et al., 2020: 5, figs.

1–2). They used *bpt* shape to differentiate *T. mavo* from other species (Lourenço et al., 2020: 22). The apparent intraspecific variations cited in just the few cases listed above, and the intraspecific variation in morphometrics shown here (Figs. 23–35), call for a more extensive investigation of *bpt* shape as a diagnostic character.

COMMENTS ON TERMINOLOGY AND HOMOLOGY

Lourenço et al. (2020) criticized our use of the terminology ‘basal pectinal tooth’ for the modified female *bpt*, calling it “arbitrary”, and continued to use the term “basal middle lamella” (herein abbreviated as ‘*bml*’) for this structure. However, our choice was not arbitrary, as we already explained previously (Lowe & Kovařík, 2019: 4). From a practical standpoint, “basal middle lamella” is technically incorrect because the position of this sclerite on the comb is basal *posterior*, not basal *middle* (cf. Fig. 36: *bpt*). At the base of the comb is another distinct sclerite in the *basal middle* position (Fig. 36: *bml*), that is referred to as the ‘basal middle lamella’ in scorpions without a modified *bpt*. This *bml* is separate from the *bpt*, not fused with it. Applying the term “basal middle lamella” to a basal posterior sclerite is confusing, since the same term would then refer to two different anatomical structures.

Fig. 37 shows the homologies implied by our terminology. The proximal-to-distal series of structures along the mid-axis of the comb (m_1, m_2, m_3, \dots) are identified as middle lamellae, the most proximal being $m_1 = bml$ (basal middle lamella). The proximal-to-distal series of structures along the posterior margin of the comb (t_1, t_2, t_3, \dots) are identified as pectinal teeth, with the most proximal being $t_1 = bpt$ (basal pectinal tooth). In contrast, Fig. 38 shows the homologies implied by the terminology of Lourenço et al. (2020) (and other works of Lourenço). The proximal-distal series of structures along the mid-axis of the comb (m_2, m_3, m_4, \dots) are identified as middle lamellae, the most proximal being m_2 , and the basal posterior structure is identified as $m_1 = bml$. In this interpretation, m_1 has ‘migrated’ from its basal middle position to the basal posterior position. Such migration would justify labelling the basal posterior structure as ‘*bml*’ because it is assumed to be homologous to a posteriorly displaced m_1 . Which of these two interpretations is more plausible?

On the one hand, the basal posterior structure is similar to the middle lamellae in its broad form and laminate appearance in some, but not all, species. On the other hand, it differs from the middle lamellae in lacking (or bearing very few) macrosetae and microsetae (Lowe & Kovařík, 2019: 21, figs. 40–51). There are clear morphological differences from regular pectinal teeth: larger size, different shape and lack of a sensorial area (the angulate facet bearing peg sensillae). The shape differences are more pronounced in many *Teruelius* species which evolved elaborate, elongated, projecting structures that are presumably derived. However, in *Grosphus* the simpler, presumably plesiomorphic forms have nearly the same transverse widths as regular pectinal teeth (Lowe &

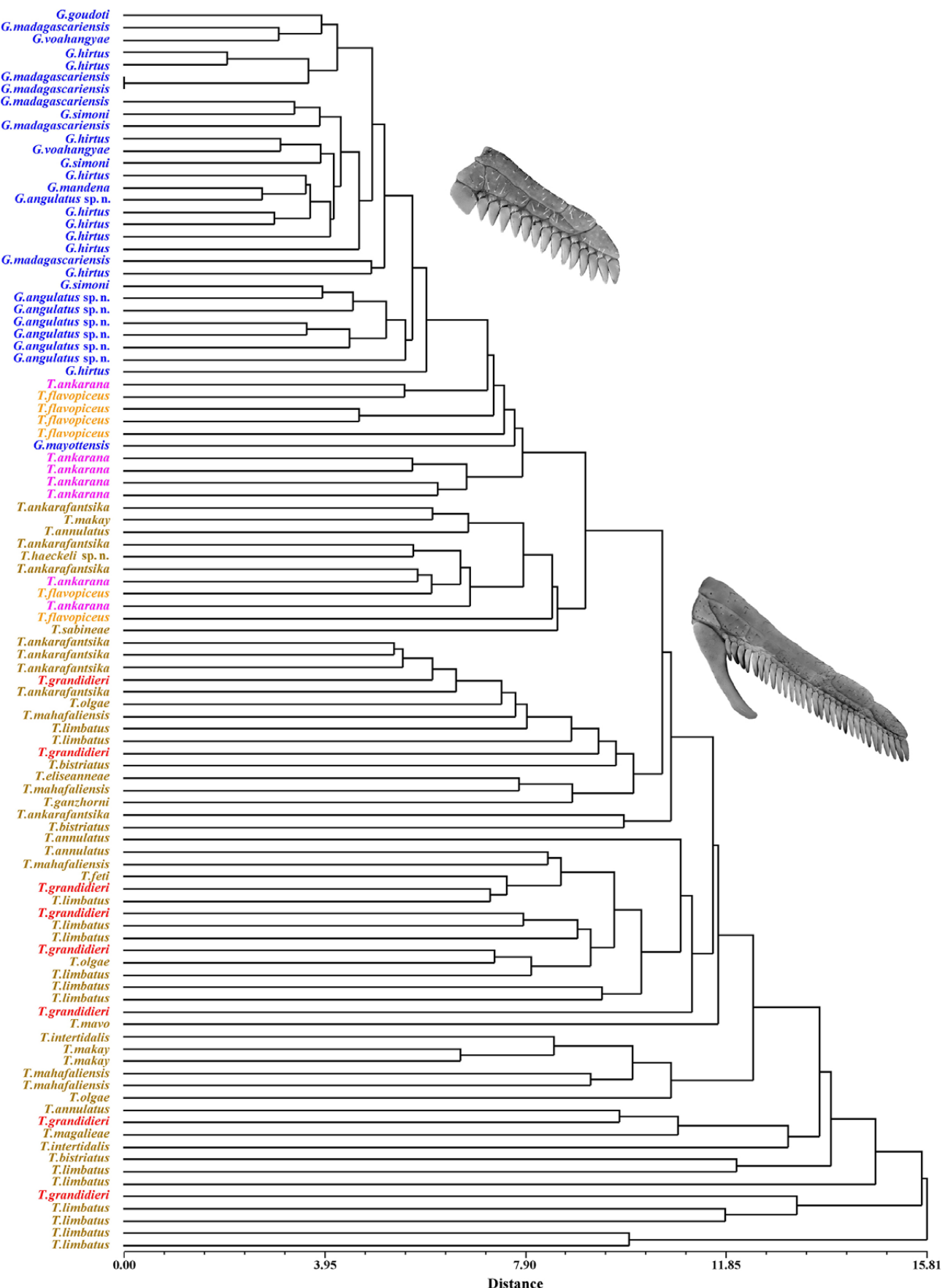


Figure 34: Phenetic analysis of shapes of female basal pectinal teeth (bpt). Ultrametric tree obtained from hierarchical cluster analysis by UPGMA of the Euclidean distance matrix of z-scores of 32 Fourier coefficients. Font colors: *Groshpus*, blue; *Teruelius flavopiceus*, orange; *T. ankaranana*, magenta; *T. grandidieri*, red; other *Teruelius* spp., dark yellow. Pectine images: *Groshpus angulatus* sp. n. (upper), *Teruelius grandidieri* (lower).

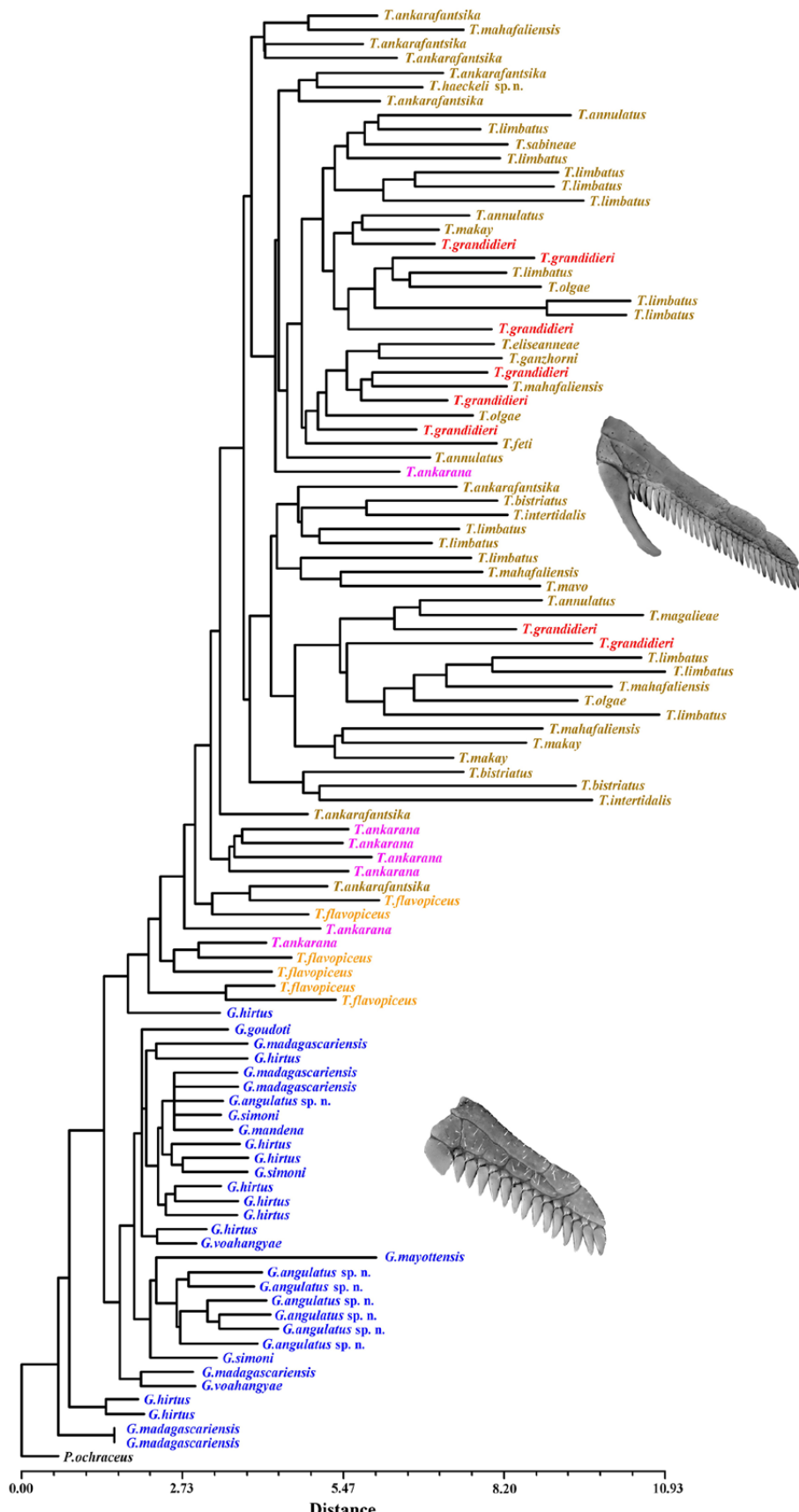


Figure 35: Phylogram of shapes of female basal pectinal teeth (bpt). Tree obtained from neighbor-joining cluster analysis of the Euclidean distance matrix of z-scores of 32 Fourier coefficients. Outgroup taxon: *Pseudolytchus ochraceus*. Font colors: as in Fig. 34, with *Pseudolytchus* black. Pectine images: *Teruelius grandidieri* (upper), *Grosphus angulatus* sp. n. (lower).

Kovařík, 2019: 21, figs. 40–43), and some show more angulate profiles reminiscent of regular teeth, e.g., *G. hirtus*, *G. angulatus* sp. n., and *G. voahangyae* (Lowe & Kovařík, 2019: 21, figs. 40, 42–43). The East African buthid genus *Uroplectes* displays a similar range of female *bpt* variation, from smaller, simpler, presumably plesiomorphic forms (Fig. 39) to larger more elongate, presumably derived forms (Fig. 40). The smaller types of *bpt* in *Uroplectes* are also more similar to the regular pectinal teeth in size and shape, with more angulate profiles (Fig. 39). The long axes of smaller *bpt* in *Groshus* and *Uroplectes* are distally inclined and roughly parallel to the long axes of regular pectinal teeth (e.g., Figs. 36, 39, 43, 310–315; Fage, 1929: 644, fig. 2; Lourenço, 1996b: 56, figs. 3–4; Lourenço & Goodman, 2009: 37, figs. 7–9; Lourenço & Wilmé, 2015a: 212, fig. 11; Lowe & Kovařík, 2019: 21, figs. 40–43; 64, figs. 196–200; Prendini, 2015b: 7, figs. 4D, 4F). In species with more elongate *bpt*, distal extensions may curve strongly and become parallel to the comb axis. However, in many cases the proximal *bpt* axis remains roughly parallel to that of regular teeth. The female *bpt* may resemble regular teeth with pale, whitish color, differing from darker marginal and middle lamellae, including the *bml*.

The interpretation of Lourenço et al. (2020) (Fig. 38) implies derivation of the simpler *bpt* of *Groshus* s. str. by a six-step transformation in which the *bml* (m_1): (i) migrated from basal middle to basal posterior position; (ii) lost macrosetae and microsetae; (iii) transformed from a large, broadly planate form to a smaller, more angulate form; (iv) adjusted its transverse width to match those of regular teeth; (v) adjusted its longitudinal axis to match the axes of regular teeth; and (vi) changed its color to match the color of regular teeth. In contrast, our interpretation (Fig. 36–37) envisages a far less convoluted two-step sequence in which a regular *bpt*: (i) lost its sensorial area, and (ii) became broader and less angulate (which may be linked to loss of sensorial area; cf. Soleglad & Fet, 2006: 14, 17). Parsimony favors our scenario. In the implied transformation sequence of Lourenço et al. (2020), the smaller, more angulate forms in *Groshus* must be derived from larger, planate intermediate forms like those in *Teruelius*. This is the opposite of the character polarity inferred from comparison with the outgroup *Pseudolychas*. Their interpretation also implies that a similarly lengthy six-step transformation sequence occurred independently in *Uroplectes*, again violating parsimony.

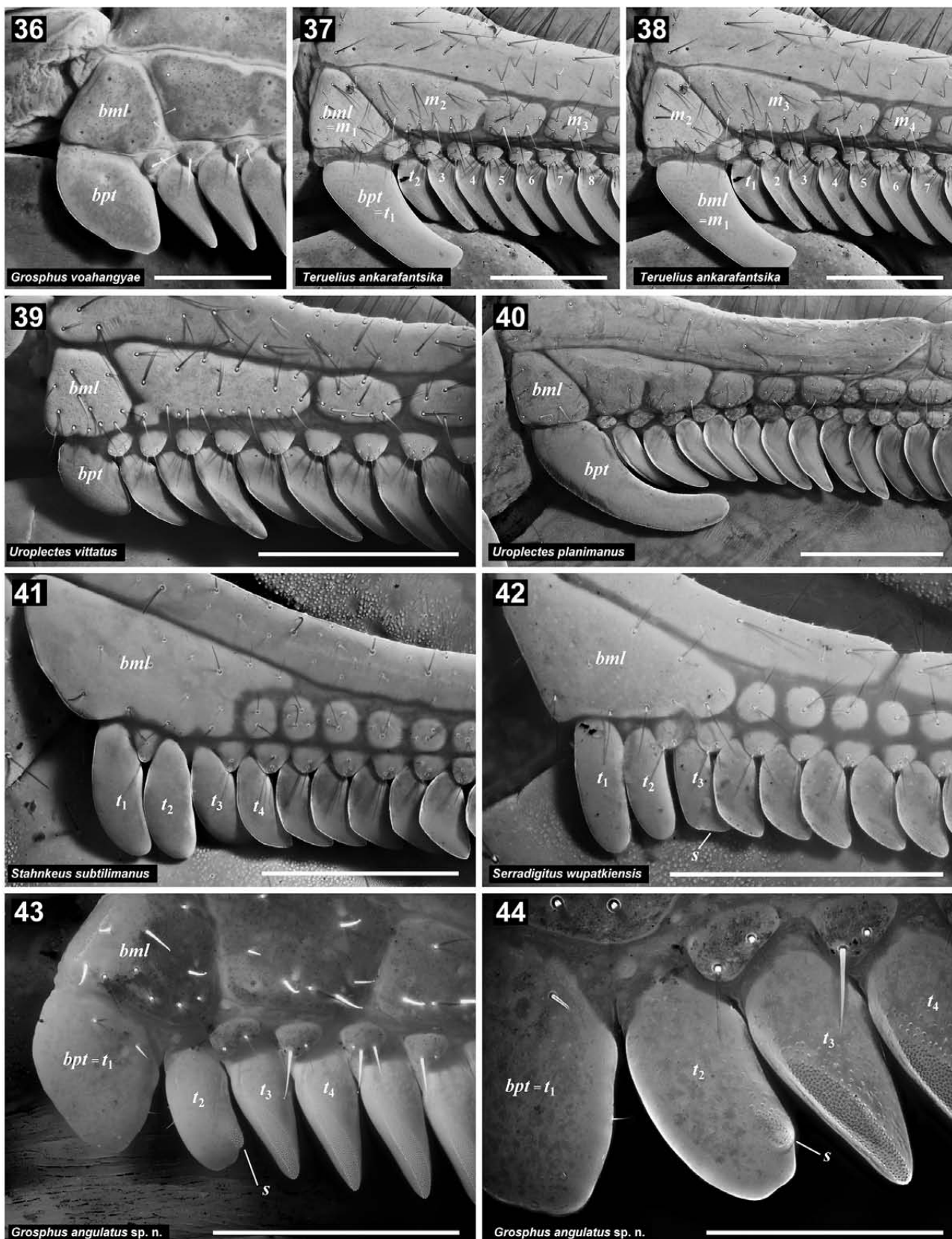
Evidence from homeotic mutations suggests that pectines were derived from abdominal limbs (Di et al., 2018; Kovařík et al., 2018a). In a developing arthropod limb, there is a strict longitudinal division of tissues into mutually separate compartments specified by regulatory gene networks controlling patterning along anterior-posterior and dorsoventral (AP/ DV) axes (cf. under Character 28 for further discussion). With respect to the AP axis, it may be supposed that pectinal teeth, and possibly fulcra, are formed in the posterior compartment, and marginal lamellae arise from the anterior compartment. The compartmental identity of middle lamellae is less clear, but their structural similarity

to marginal lamellae suggests that they may also originate from the anterior compartment. If so, relocation of the basal middle lamella to a posterior position would be difficult to reconcile with AP compartmentalization, a fundamental morphogenetic principle conserved across arthropods and other phyla (Damen, 2002; Prpic, 2019). Modification of the basal pectinal tooth is a more parsimonious model that also respects AP compartmentalization.

In *Drosophila*, the identity of cells in the posterior compartment is determined by expression of homeobox genes *engrailed* and *invected*, and in the anterior domain by *wingless*. The posterior cells secrete *hedgehog* (*hh*), a morphogen that establishes the AP boundary and midline organizing center (Brook et al., 1996). In embryos of the scorpion, *Euscorpius flavaudis* (De Geer 1776), *hh* expression was detected by *in situ* hybridization in posterior compartments of limb buds of chelicerae, pedipalps and legs (Simonnet et al., 2004). Although *hh* signal was not detected in the pectines, O3 (opisthosoma segment III, bearing the pectines) had only faint posterior staining. While it is possible that AP patterning in pectines is mediated by an entirely different gene complex than in all other limbs, a simpler explanation for their lack of *hh* signal is that expression levels in the pectinal bud were below the detection thresholds of their assays in the embryonic stages. The AP compartmentalization of limb buds along parasegment boundaries along anterior borders of *engrailed* domains is conserved across Panarthropoda (Clark et al., 2019), and probably determines the cellular organization of pectines.

A modified female *bpt* also occurs in vaejovid genera *Serradigitus* and *Stahnkeus* (Soleglad & Fet, 2006: 14–19; Soleglad, 1974: 108–109, figs. 1–6; Stahnke, 1974: 119). The female *bpt* is typically non-angulate, elongated and distally rounded without a sensorial area (Figs. 41–42, ' t_1 '). Between the *bpt* and regular teeth are several sub-basal teeth with variable intermediate morphologies (Fig. 41, t_1-t_4 ; Fig. 42, t_1-t_3). The more distal of these are more similar to regular teeth, and may be weakly angulate with reduced sensorial areas (Fig. 41, t_4 ; Fig. 42, t_3). The more proximal sub-basal teeth are more similar to the *bpt* and lack sensorial areas (Fig. 41, t_2 ; Fig. 42, t_2). These morphological gradients were already described and illustrated by Soleglad & Fet (2006: figs. 12–32, tab. 4). The intermediate morphologies may be interpreted as varying degrees of transformation of regular teeth into a modified *bpt*. A proximal-distal gradation is a sign of a morphogen diffusion gradient (Stapornwongkul & Vincent, 2021) with its source at the base of the comb. The morphogen may either instruct a developing tooth to form a modified *bpt*, or suppress developmental programs of regular teeth. Partially transformed teeth suggest a graded effect, rather than an all-or-none effect at threshold concentration. This model offers a simple explanation of the intermediate sub-basal morphologies by a known developmental mechanism.

One might argue that the vaejovid model may not generalize to buthids. Buthid genera with modified female *bpt* (e.g., *Groshus*, *Mauritanobuthus*, *Neogroshus*,



Figures 36–44. Basal pectinal teeth and basal middle lamellae of female scorpions. **Figures 36–38.** Basal pectinal structures of female *Groshus voahangyae* (36) and *Teruelius ankarafantsika* (37–38), showing basal pectinal tooth (*bpt*) and basal middle lamella (*bml*). Terminology of Lowe & Kovařík (2019) (37) is contrasted with that of Lourenço et al. (2020) (38): middle lamellae: $m_1, m_2, m_3, m_4, \dots$; pectine teeth: $t_1, t_2, t_3, t_4, \dots$. **Figures 39–40.** Basal pectinal structures of female *Uroplectes vittatus* (39) and *U. planimanus* (40), showing basal pectinal tooth (*bpt*) and basal middle lamella (*bml*). **Figures 41–42.** Basal pectinal structures of female *Stahnkeus subtilimanus* (41) and *Serradigitus wupatkiensis* (42), showing basal middle lamella (*bml*) and multiple modified basal pectinal teeth (t_1, t_2, t_3, t_4), one of which bears a sensorial area (*s*). **Figures 43–44.** Basal pectinal structures of a female *Groshus angulatus* sp. n., showing basal middle lamella (*bml*), modified basal pectinal tooth (*bpt = t₁*) regular pectinal teeth ($t_3, t_4, \text{etc.}$), and a partially modified intermediate tooth (t_2) bearing a sensorial area (*s*). Scale bars: 500 µm (36, 44), 1 mm (37–43). UV fluorescence, excitation by 395 nm LED (380–410 nm), emission filter 475 nm long pass (Edmund Optics 64633) (36–43), or Lucifer Yellow filter set (Chroma Technology 31010) (44). Figs. 43–44 show right pectines in mirror image for comparison to Figs. 41–42.

Pseudolychas, *Teruelius* and *Uroplectes*) are not known to have intermediate sub-basal teeth, and the two families are not closely related. A modified buthid *bpt* could have developed via different mechanisms, such as the debated posterior migration of the *bml*. A number of buthids have dilations or extensions of the female *bml* (e.g., *Isometrus*, *Palaeogroshus*, *Parabuthus*, *Somalicharmus*, *Thaicharmus*, *Tityopsis* and *Tityus*; Soleglad & Fet, 2006: 19; Kovářík et al., 2016: 28–30; Lourenço, 1996a). In some, the enlarged *bml* intrudes into the posterior marginal zone of regular teeth. Subdivision of this intruding sclerite along the fulcral axis, or a presumed AP boundary, could place a lamellate structure in the same position as the modified *bpt*. However, this model simply substitutes migration with sclerite fission, while retaining the undesirable aspects of a migration model, i.e., a lengthy multistep process to generate the *Groshus* s. str. phenotype, and incompatibility with AP compartmentalization. We are unaware of any cases of partial *bml* fission across the AP boundary that could be evidence for this model. This is significant because stochastic fission or fusion of pieces of middle lamellae *within* their own mid-axis longitudinal compartment occurs frequently (e.g., Fig. 37, *m*; Fig. 40; Figs. 243–248).

In the morphogen model, the absence of intermediate sub-basal teeth in buthids can be accommodated either by a transforming signal with a shorter range of diffusion and steeper concentration gradient, or by a sharp threshold dose response in developing teeth. Physiological parameters can be adjusted to produce a single modified *bpt* in a normally developed comb. This normal wild-type phenotype conceals the underlying mechanism. However, if mutations disrupt normal development, the resulting teratology may hold clues to hidden mechanisms. Fig. 43 shows an example of a developmental error in the pectine of a female *Groshus* (see also Fig. 320). The *bpt* (= t_1) displays a morphology typical of the genus, being dilated with a gently angulate profile, and lacking a sensorial area. The regular teeth, t_3 , t_4 ... also display normal morphologies with sharply angulate profiles and large sensorial areas. Of special interest is the sub-basal tooth t_2 , with a morphology intermediate between the *bpt* and regular teeth. It is partially dilated and rounded instead of angulate. Fig. 44 shows this tooth (t_2) at higher magnification. The proximal facet is swollen, rounded and more similar to the adjacent *bpt*. The distal facet resembles a partially developed, regular tooth with a pointed knob-like process and a small sensorial area (*s*). In our model, the partially transformed t_2 can be explained either by a mutation that extends the range of diffusion of the morphogen signal beyond t_1 , or one that lowers the threshold of response to the ligand. If the threshold concentration intersects the embryonic cluster of tooth progenitor cells of t_2 , it may produce a chimeric phenotype. This situation is analogous to the intermediate morphologies of vaejovid sub-basal teeth, and is further evidence that the female *Groshus* *bpt* is indeed derived by modification of a regular tooth, not by *bml* displacement. This ‘missing link’ tooth t_2 , connecting the *bpt* with regular teeth in *Groshus*, categorically refutes the assertion by Lourenço et al. (2020) that the *bpt* “has nothing in common with a tooth”.

ADDITIONAL COMMENTS ON TERMINOLOGY

Lourenço et al. (2020: 9) criticized us by writing: “... the authors seem to ignore that the term ‘basal middle lamella’ was originally coined by K. Kraepelin (1908) in his major study on the secondary characters of several groups of Arachnida”, as if invoking the authority of Kraepelin justified their usage of the term “*basal middle lamella*” for the *bpt*. However, Kraepelin (1908: 195–196) actually wrote:

“Als ausschließlich dem weiblichen Geschlecht zukommende Bildungen sind die Erweiterung der Mittellamelle des Kammgrundes wie die Vergrößerung des ersten, basalen Kammzahns selbst anzusehen. Beide Erscheinungen treten allein bei der Familie der Buthiden auf. Die Erweiterung der Kammgrundlamelle erscheint bei zahlreichen *Parabuthus* Arten (z. B. *P. abyssinicus* [Fig. 23], *villosus*, *planicauda* nsw.) in Form eines eckigen, nach unten vorspringenden und hier die Ausbildung von Kammzähnen verhindernden Lappens, wohingegen viele *Tityus* Arten (*T. crassimanus*, *obtusus*, *insignis*, *discrepans*, *androcottoides*, *cambridgei*, *macrochirus*, *forcipula*, *ecuadorensis*, *pictus*, *metuendus*, *pusillus* nsw.; Fig. 24) einen runden bläschenförmigen Lobus am kurzen Basalrande des Kammes entwickelt zeigen. Auch bei *Isometrus thwaitesi* soll nach POCOCK eine ähnliche Bildung vorkommen. Noch augenfälliger ist die Verdickung oder Verlängerung des basalen Kammzahns, wie sie bei den ♀ der Gattung *Groshus* (Fig. 25), aber auch bei manchen Arten der Gattung *Uroplectes* zu beobachten ist. Interessant ist, daß hierbei augenscheinlich größere Länge und größere Dicke des Kammzahns vikariierend für einander eintreten können, da bei den verschiedenen Arten der Zahn bald durch größere Länge, bald durch größere Dicke sicli auszeichnet. Im extremsten Fall endlich, z. B. bei *Groshus grandidieri*, kann der Zahn sowohl an Länge wie auch zugleich an Dicke den Grundzahn des ♂ um mehr als das Doppelte übertreffen.”

or, translated:

“The enlargement of the middle lamella at the base of the pectine as well as the enlargement of the first basal pectine tooth itself are to be regarded as formations belonging exclusively to the female sex. Both phenomena occur only in the family of the Buthids. The widening of the pectine basal lamella appears in numerous *Parabuthus* species (e.g., *P. abyssinicus* [Fig. 23], *villosus*, *planicauda* etc.) in the form of an angular, downwardly protruding lobe that prevents the formation of comb teeth, whereas many *Tityus* species (*T. crassimanus*, *obtusus*, *insignis*, *discrepans*, *androcottoides*, *cambridgei*, *macrochirus*, *forcipula*, *ecuadorensis*, *pictus*, *metuendus*, *pusillus* etc.; Fig. 24) show a round vesicular lobe developed on the short basal margin of the comb. According to POCOCK, a similar formation should also occur in *Isometrus thwaitesi*. The thickening or lengthening of the basal

pectine tooth, as can be observed in the female of the genus *Grosphus* (Fig. 25), but also in some species of the genus *Uroplectes*, is even more conspicuous. It is interesting that in this case, apparently greater length and greater thickness of the pectine tooth can appear independently of each other, since in the various species the tooth is sometimes characterized by greater length and sometimes greater thickness. Finally, in the most extreme case, e.g., in *Grosphus grandidieri*, the tooth can both in length and at the same time in thickness exceed the basal tooth of the male by more than double.”

We see that Kraepelin (1908) in fact restricted the term ‘basal middle lamella’ to refer only to the enlarged basal sclerite in the female comb of *Parabuthus*, some *Tityus*, and other genera, that occupies the basal middle position and may intrude into the posterior marginal zone. For the enlarged basal posterior sclerite in females of *Grosphus* and *Uroplectes*, he used the term ‘basal pectine tooth’ (“*basalen Kammzahns*”), the same terminology as ours (Lowe & Kovařík, 2019: 41–42). Furthermore, the claim that “*the term ‘basal middle lamella’ was originally coined by K. Kraepelin (1908)*” is incorrect. The term was already in use by Kraepelin 17 years earlier, cf. Kraepelin (1891: 10):

“Bei der Gattung *Heterobuthus* war es die eigenartige Entwicklung der grundständigen Mittellamelle des Kammes, die wir als ausschlaggebend für die Aufstellung einer besonderen Formengruppe bezeichneten; bei der Gattung *Grosphus* zeigt nun jene Mittellamelle keinerlei außergewöhnliche Bildung; dagegen finden wir den basalen Kammzahn selbst beim Weibchen so mächtig verbreitert oder verlängert, daß er die übrigen um mehr als das Doppelte an Größe übertrifft ...”

or, translated:

“In the case of the genus *Heterobuthus* it was the peculiar development of the basal middle lamella of the pectines which we designated as decisive for the establishment of a special group of forms; in the genus *Grosphus* that middle lamella shows no unusual formation; on the other hand, we find the basal pectine tooth itself so greatly enlarged or elongated in females that it is more than twice the size of the rest ...”

Again, we see that Kraepelin (1891) restricted the term ‘basal middle lamella’ to refer only to the enlarged basal sclerite in the female comb of *Parabuthus* (= *Heterobuthus*), reserving ‘basal pectine tooth’ (“*basalen Kammzahns*”) for the *bpt* of *Grosphus*. This was further confirmed in his dichotomous key separating the two genera (Kraepelin, 1891: 15):

“α) Von dn Mittellamellen des Kammes ist die grundständige beim Weibchen zu einem großen, breiten Lappen enteickt, der scheinbar einen verbreiterten Kammzahn darstellt (Fig. 36) *Heterobuthus* n. g.

β) Basale Mittellamelle des Kammes beim Weibchen nicht vergrößert, aber der dazu gehörige basale Kammzahn doppelt so breit oder lang, als die andern (Fig. 37) *Grosphus* Sim. (emend.).”

or, translated:

“α) Of the middle lamellae of the pectine, the basal lamella in the female is developed into a large, broad lobe that appears to be a broadened comb tooth (Fig. 36) *Heterobuthus* n. g.

β) Basal middle lamella of the pectine in the female not enlarged, but the corresponding basal pectinal tooth is twice as wide or long as the others (Fig. 37). *Grosphus* Sim. (emend.).”,

leaving no doubt that Kraepelin’s terminology was the same as ours.

Lourenço et al. (2020) further criticized us by claiming that the *bpt* was a structure that we “decided to rename in a total (sic) arbitrary way by labelling it as ‘enlarged pectine tooth’.” However, we did not rename this structure. Our terminology followed long-established conventions of all other authors in scorpion systematics and morphology (except Lourenço) who consistently referred to it as an enlarged or modified pectine tooth: i.e., Ayrey, 2011: 11–12, tab. 1; Birula, 1915: 21; Caporiacco, 1936: 139–140; Fage, 1929: 641; Farzanpay & Vachon, 1988: 138; Francke & Ponce-Saavedra, 2010: 52; Fitzpatrick, 1996: 50, 55, 60; González-Santillán & Prendini, 2013: 69; Graham & Soleglad, 2007: 1–2, 5, 8; Hewitt, 1918: 102, 117–119, 124–125; Kraepelin, 1891: 8, 10, 15; Kraepelin, 1899: 8, 32, 52; Kraepelin, 1900: 12–15; Kraepelin, 1908: 195–196; Lamoral, 1979: 619, 627, 632–633, 638, 640, 644, 647, 650; Lankester, 1883: 381; Lawrence, 1938: 292; Lawrence, 1961: 124, 126; Lawrence, 1966: 4, 6, fig. 3a, b; Monard, 1937: 259–262, 266; Newlands & Martindale, 1980: 60, 62, 65, 67; Pocock, 1889a: 348; Pocock, 1889b: 462–463; Pocock, 1890: 116–117, 123, 127–128, 134, 136; Pocock, 1896: 381–382, 384, 388–389, 393; Pocock, 1897: 118–119; Polis & Sissom, 1990: 217–218; Prendini, 2001: 17; Prendini, 2004a: 41; Prendini, 2015a: 501, 505; Prendini, 2015b: 17, 26; Purcell, 1901: 183, 185, 187–188, 192–193; Seiter, Schramm & Barthel, 2016: 85–86; Simon, 1880: 377; Soleglad & Fet, 2006: 14–19; Sissom, 1990: 95; Sissom & Stockwell, 1991: 198–199, 201, 203–205; Werner, 1934: 267; Vachon, 1950: 9, 11; Vachon, 1969: 479; Visser & Geerts, 2021: 702–704, 707; and Williams & Berke, 1986: 351.

Instead, it was Lourenço (1996b: 7–8) who renamed the basal pectinal tooth as “*lame basilaire intermédiaire*” (= basal middle lamella) “in a total (sic) arbitrary way” without offering any explanation. Subsequently, Lourenço & Goodman (2003a: 24) mistranslated from French the terminology of Fage (1929) as “*basal middle lamella*”, altering Fage’s own words of “*la dent basale du peigne*” (= basal pectinal tooth).

Character 24. Basal pectinal tooth (*bpt*), female, length: shorter than or equal to basal comb width (0); longer than basal comb width (1)

Length of the female *bpt* was measured on its longest axis, and basal width of the comb included only the basal marginal and basal middle lamella. The length was shorter in all known females of *Groshus*, and longer in most known females of *Teruelius*.

Character 25. Basal pectinal tooth (*bpt*), female: without long, narrow extension (0); with long narrow extension (1)

A long narrow extension was present in some species of *Teruelius*. It corresponds to the ‘clavate’ or ‘falcate’ shape descriptors (cf. intraspecific variation, character 23).

Character 26. Pectinal tooth count (PTC): ♂ < 24, ♀ < 22 (0); ♂ > 24 (1), ♀ > 22 (1) (♂ priority) (Lowe & Kovařík, 2019: 41, character iii)

PTC was bimodal, with *Teruelius* significantly higher than *Groshus*. The PTC distributions of the two genera were non-overlapping and the means were separated by a gap (Lowe & Kovařík, 2019: 17, figs. 28–29). The separation was more evident when body size scaling was taken into account (Lowe & Kovařík, 2019: 18, figs. 30–31). For character coding, if male and female scores conflicted the male score was prioritized.

Character 27. Pectinal tooth (regular, non-basal), mean ratio L/W, male: < 3.7 (0); > 3.7 (1)

Regular pectinal teeth (with sensorial areas) were relatively shorter and broader in *Groshus*, and relatively longer and narrower in *Teruelius* (e.g., Fig. 22). Rank ordered bar plots (Figs. 19–20) showed non-overlapping separation of the two genera in both sexes according to mean L/W ratios of their teeth. A bivariate scatter plot (Fig. 21) showed a positive correlation between male and female L/W ratios, including for the outgroup taxa ($R = 0.8468$, $P < 0.0001$). The teeth of males were more elongated than those of females in all cases (all points above gray diagonal line). To avoid including two correlated characters, we only scored males for the cladistic analysis. A discretization threshold placed at the largest mid-range step in ranked ratio was able to segregate *Teruelius* from *Groshus*, except for *T. flavopiceus*.

Character 28. Pedipalp femur petite ‘trichobothrium’ d_2 , position: dorsal (0); internal (1); absent (2) (Lowe & Kovařík, 2019: 36, character i)

In our previous work, the position of femur d_2 was scored either as ‘internal’ (= prolateral) or ‘carinal’ in *Groshus*, and either ‘carinal’ or ‘dorsal’ in *Teruelius* (Lowe & Kovařík, 2019: 7, 12). In the ‘carinal’ state, d_2 was visually judged to be straddling the dorsointernal carina. This state was scored in a minority of species of both genera, and the overlap prevented a binary division of species into mutually exclusive categories. In borderline cases, the scoring could be subjective because the position of d_2 relative to the dorsointernal carina was unclear. The dorsointernal carina is not demarcated by a continuous, raised ridge, but by a series of granules that may vary in size and spacing. At the proximal end where d_2 is located, granules may be more sparse or heterogeneous, with irregular positions, and the carinal trajectory may be unclear. For a more objective evaluation, we performed morphometric analyses of the position of d_2 relative to the dorsointernal carina. Figures 173–174 illustrate the method applied to pedipalp femora of

Groshus and *Teruelius*. On an image of the femur in dorsal view, positions of granules marking the dorsointernal carina were measured in orthogonal cartesian coordinates (x, y). The x -axis was taken as the proximal-to-distal axis of the segment, aligned with a regression line passing through the series of granules in the distal half of the segment. The proximal vertex where dorsointernal and dorsoexternal carinae converge, was fixed as the coordinate origin. The carinal trajectory defined by the granule coordinates was estimated by two different methods: (i) a cubic B-spline fit (magenta curves), and (ii) an empirical, parametric non-linear least squares fit (green curves) to the equation:

$$y = Y_{\max} \frac{x^n}{k^n + x^n} \cdot \left(1 - \frac{A}{\sqrt{2\pi}} e^{-\frac{1}{2}\left(\frac{x-m}{L}\right)^2}\right) \cdot \left(1 + \operatorname{erf}\left(\frac{b(x-m)}{L\sqrt{2}}\right)\right)$$

The B-spline is a piecewise polynomial fit that closely tracks the local granule trajectory, whereas the parametric equation yields a more global fit. The first factor in the parametric equation is a sigmoid ‘Hill’ curve that models the initial rise from the proximal vertex and the horizontal asymptote in the distal half of the segment. The second and third factors represent a skew Gaussian modulation of the sigmoid in the proximal region, to model the series of granules detouring around d_2 . Minimum distances between d_2 and the fitted curves were computed from the coordinates (d_2x, d_2y). To compare different specimens, distances were normalized against Y_{\max} as a femoral width scale.

Figure 175 shows a bivariate scatter plot of distances between d_2 and the parametric fit, vs. the distances between d_2 and the B-spline fit for $n = 83$ femora of *Groshus* (14 spp., 34 cases; blue symbols) and *Teruelius* (20 spp., 49 cases; yellow, red, orange and magenta symbols). Negative distances correspond to d_2 positions external (=dorsal) to the fitted curves, and positive distances to d_2 positions internal (= prolateral) to the fitted curves. The two distance measures were strongly correlated, indicating that the two fitting algorithms yielded similar and largely consistent estimates of dorsointernal carina trajectories. Scaled distances for *Groshus* were mostly located in the upper right quadrant (d_2 internal), whereas those for *Teruelius* were mostly located in the lower left quadrant (d_2 external). A minority of points were missorted in lower right and upper left quadrants, corresponding to cases in which the two curve fits fell on opposite sides of d_2 . The parametric fit provided better segregation of *Groshus* vs. *Teruelius* into d_2 internal vs. d_2 external groups (upper and lower halves of the plot; 90.36% success), compared to the B-spline curve (right and left halves of plot; 80.72% success). Points representing outgroup *Pseudolychas* were associated with *Teruelius*. The data from *Groshus* and *Teruelius* in Fig. 175 are plotted as species means in Fig 176.

The missorted cases included two outliers: one isolated case of *G. madagascariensis* (Lourenço & Goodman, 2006: 253, fig. 12) was positioned far into the lower left quadrant among *Teruelius* species (lower black arrow), and *T. eliseanneae* (Lourenço & Wilme, 2016: 56, fig. 15) far into the upper right quadrant with *Groshus* species (upper black

arrow). These cases seem to imply overlapping variation between the two genera. However, it is possible that the dorsointernal carinae in these cases were not accurately reconstructed by curve fits to illustrated granule positions. We therefore applied a second method to analyze d_2 position, independent of granule distributions. Relative positions of d_2 were mapped to a standard morphospace with cartesian coordinates (d_2x/L_{femur} , d_2y/Y_{max}), normalizing their coordinates by femoral length and femoral width. Femoral length, L_{femur} , was gauged along the x -axis of the coordinate system, from proximal vertex to distal limit of the segment. The result was a complete partitioning of d_2 coordinates into two domains for *Groshus* and *Teruelius* (Fig. 177). This showed that the few overlapping outlier cases in Figs. 175–176 were indeed artefacts of carinal estimation by granule tracing. The data from *Groshus* and *Teruelius* in Fig. 177 are plotted as species means in Fig. 178. The two outlier cases in the curve fitting analyses (black arrows) were segregated into their respective domains.

In the context of the cellular organization and development of arthropod limbs, our data suggest that d_2 positioning is actually a discrete binary character. It was first shown in *Drosophila* embryos that primordial limbs arise from adjacent parasegments and are subdivided into anterior-posterior (AP) and dorso-ventral (DV) longitudinal compartments through cell lineage restriction (Brook et al., 1996). Compartmental identity of cells is fixed by local expression of regulatory genes expressing developmental signaling molecules and their receptors. Similar mechanisms operate in crustaceans, arachnids and other arthropods (e.g., Damen, 2002; Janssen et al., 2008; Heingård et al., 2019). Light-sheet fluorescence microscopy and 3D tracking have directly visualized and confirmed cell lineage restrictions in AP and DV compartments of thoracic limbs of a crustacean (Wolff et al., 2018). We interpret the segregated domains in Figs. 177–178 as a phylogenetic correlate of the partitioning of d_2 into mutually exclusive cellular compartments, ‘internal’ for *Groshus* vs. ‘dorsal’ for *Teruelius*. The boundary between the morphospace domains corresponds to a morphogenetic boundary between internal and dorsal cell lineage compartments. The dorsointernal carina (or granule series) runs approximately along the boundary but may not follow it exactly. We emphasize that binary coding of this character is not merely a subdivision of points in Fig. 178 chosen to achieve separation *Teruelius* from *Groshus*. It is based on a real physical separation of d_2 locations by the granules of the dorsointernal carina (Figs. 175–176).

Character 29. Pedipalp femur trichobothrium e_1 position vs. d_5 : proximal (0), level or distal (1)

The position of e_1 was level or distal to d_5 for all ingroup taxa with the exception of *Groshus angulatus* sp. n. (proximal e_1 was diagnostic for that species).

Character 30. Pedipalp femur, dorsal surface: moderately or strongly granulate (0); weakly granulate or smooth (1)

The dorsal surface of the pedipalp femur was moderately or strongly granulate in most *Groshus* (9/11 scored) (e.g.,

Fig. 8), and weakly granulate or smooth in most *Teruelius* (17/18 scored) (e.g., Fig. 7).

Character 31. Pedipalp patella, dorsomedian surface, setation: dense, > 20 macrosetae (0); sparse, < 20 macrosetae (1); absent (2)

Macrosetae were numerous on the dorsomedian surface of the pedipalp patella in most *Groshus* (8/8 scored) (e.g., Fig. 9), and sparse in most *Teruelius* (12/12 scored) (e.g., Fig. 10).

Character 32. Pedipalp patella, dorsointernal carina development: absent (0); weak (1); moderate (2); strong (3)

Development of the dorsointernal carina of the pedipalp patella was weak to moderate in most *Groshus* (12/14) (e.g., Fig. 9), and moderate to strong in most *Teruelius* (19/21 scored) (e.g., Fig. 10).

Character 33. Pedipalp patella, dorsointernal carina granulation: sparse to absent (0); moderate (1); dense (2); costate-granulate (3)

Granulation of the dorsointernal carina of the pedipalp patella was sparse or absent in most *Groshus* (11/14) (e.g., Fig. 9), and moderate to strong in most *Teruelius* (15/21 scored) (e.g., Fig. 10).

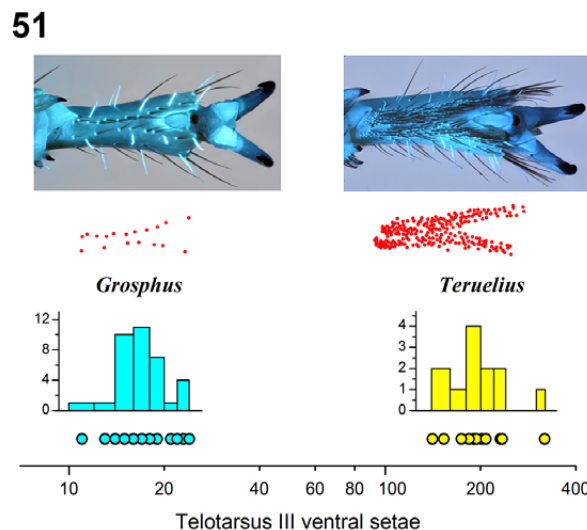
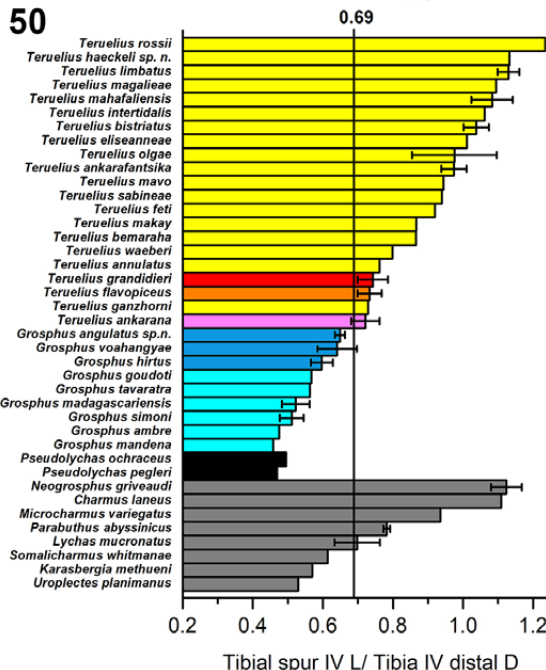
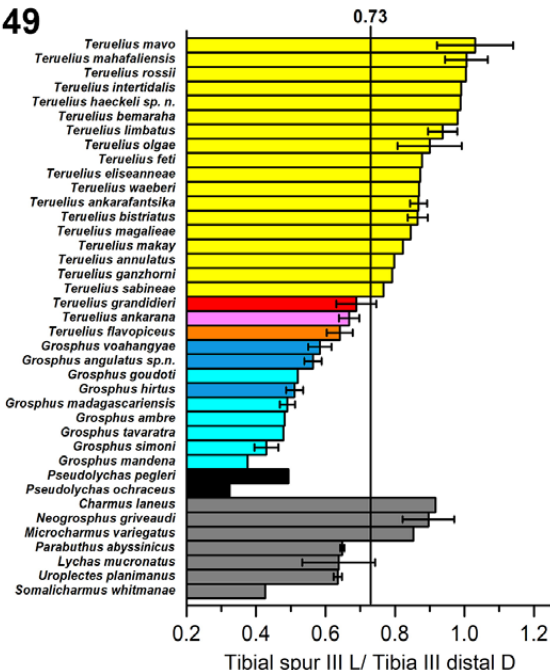
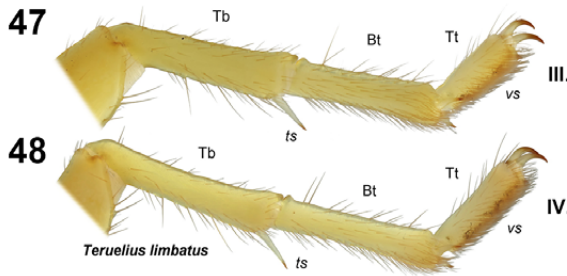
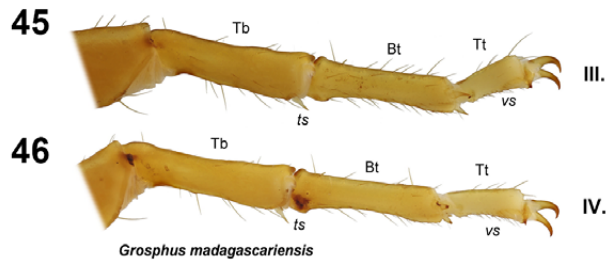
Character 34. Pedipalp chela fingers, male, proximal undulation: strong (0); moderate (1); weak or absent (2)

Undulations or scalloping on the proximal dentate margins of the pedipalp fingers in males were strong (3/11 scored) to moderate (8/11 scored) in *Groshus* (e.g., Fig. 169), and moderate (6/13 scored) to weak or absent (6/13 scored) in *Teruelius* (e.g., Fig. 170–171).

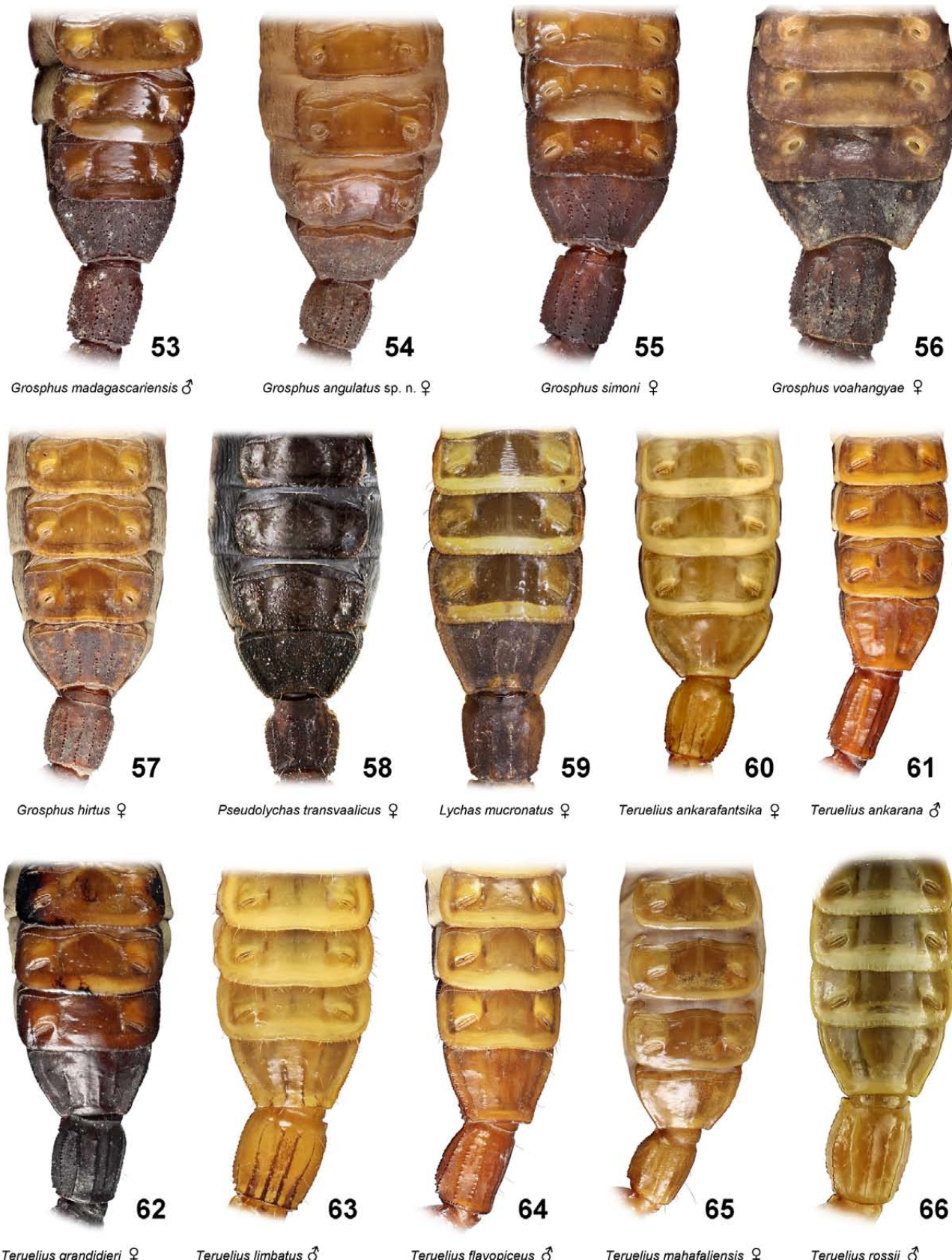
Character 35. Pedipalp chela fixed finger, relative positions of trichobothria db vs. est , mean ratio of distances from tip of finger: $db > 0.92 est$, proximal (0); $db < 0.92 est$, distal (1)

A bivariate scatter plot of raw data of relative distances of db and est from the tip of the fixed finger, normalized to the trichobothrium Et distance from the tip of the fixed finger, shows a strong segregation of *Teruelius* (db mostly proximal to est) from *Groshus* (db mostly distal to est), but with some overlap (Fig. 166). Crossover cases in *Groshus* were all from the ‘*hirtus*’ group. A rank ordered bar plot of the mean value of the ratio of db to est distances (Fig. 167) shows partial segregation of the two genera. A single discretization threshold was placed at the maximal step change in ranked values.

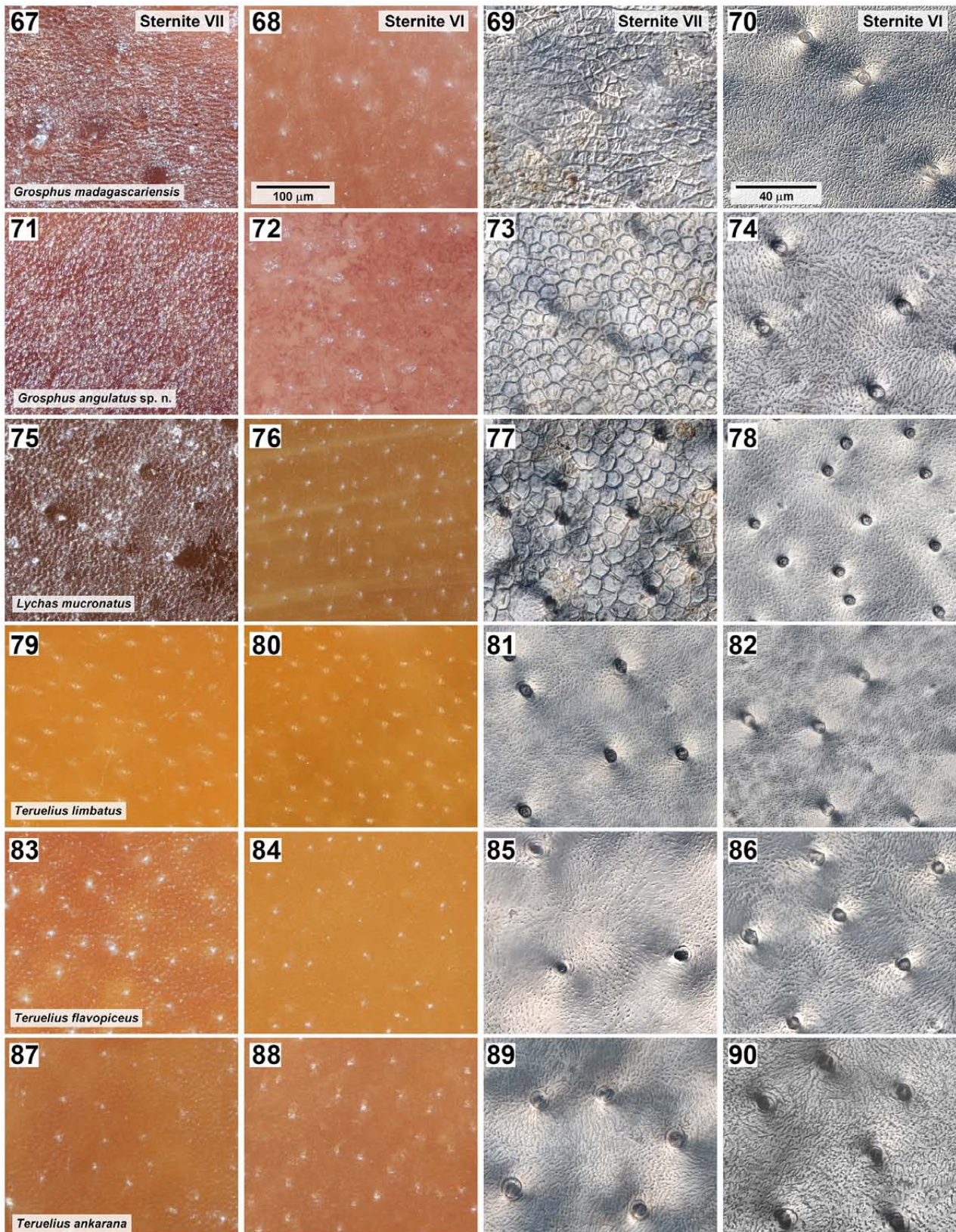
The relative position of fixed finger db vs. est has been utilized as a taxonomic character in buthids at the species level (Kovařík, 2007a; Lowe et al., 2014) and genus level (Kovařík, 2007b). Tikader & Bastawade (1983: 41) divided *Lychas* C.L. Koch, 1845 into subgenera partly based on this character, although these were later synonymized (Kovařík, 1995; Vachon, 1986). The relative positions of db vs. est may be stable in some buthid genera, but can vary in others, e.g., in *Leiurus* Ehrenberg, 1828 (Lowe et al., 2014: 117, fig. 98C) and *Buthus* Leach, 1815. It can vary intraspecifically, e.g., in *Leiurus hebraeus* and *L. macroctenus* (Lowe et al., 2014: 117, fig. 98A). Lourenço et al. (2018: 76, tab. I) used this as a diagnostic character to separate *T. bemaraha* (db proximal to est) from *T. mahafaliensis* (db distal to est). However, we found



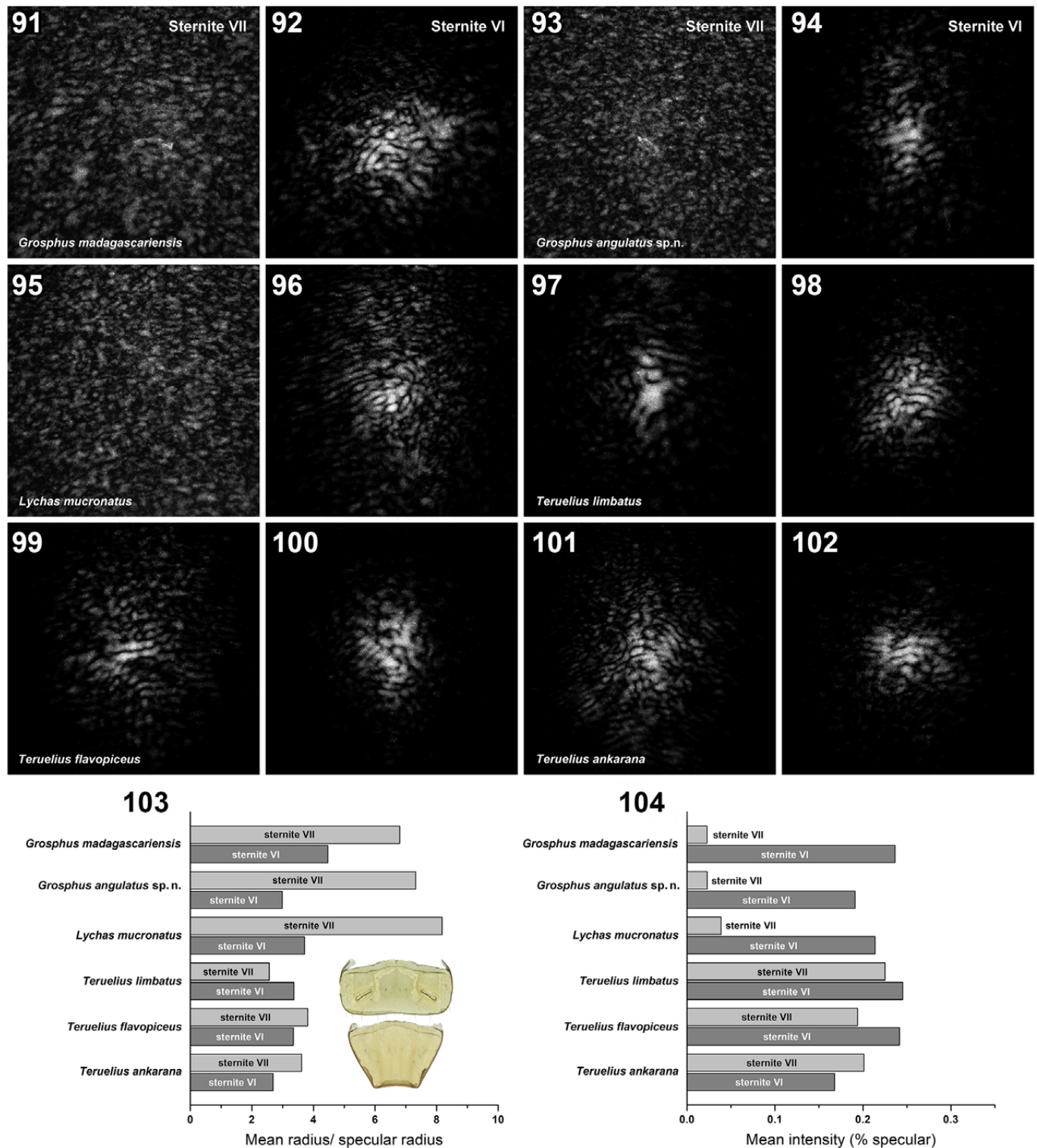
Figures 45–52. Tibial spurs and tarsal setation. **Figures 45–46.** Tibial and tarsal segments of leg III (45) and leg IV (46) of *Grophus madagascariensis* in retrolateral view. **Figures 47–48.** Tibial and tarsal segments of leg III (47) and leg IV (48) of *Teruelius limbatus* in retrolateral view. Abbreviations: Tb, tibia; Bt, basitarsus (tarsomere I); Tt, telotarsus (tarsomere II); ts, tibial spur; vs, ventral setae of telotarsus. **Figures 49–50.** Horizontal bar plots of the mean ratio of tibial spur L / tibia distal D for leg III (49) and leg IV (50) (characters 10 and 11, respectively) of *Grophus* ($n = 34$, 9 spp.), *Teruelius* ($n = 66$, 21 spp.), *Pseudolychas* ($n = 2$, 2 spp.) and other outgroup taxa ($n = 15$, 8 spp.). Data from both sexes pooled. Error bars are standard errors. Discretization thresholds shown at step changes in ranked length. Color codes of bars as indicated in Fig. 16 legend. **Figures 51–52.** Ventral telotarsal setation. **Figure 51.** Logarithmic distribution of number of macrosetae on ventral telotarsus III (character 12) in *Grophus* (cyan bars and symbols, $n = 36$, 8 spp.) and *Teruelius* (yellow bars and symbols, $n = 12$, 10 spp.). Macrosetal counts on abscissa plotted on logarithmic scale. Insets: UV fluorescence photomicrographs and maps of macroseta sockets (red dots) of ventral telotarsus III in *Grophus simoni* (left) and *Teruelius flavopiceus* (right). **Figure 52.** Horizontal bar plot of ratios of mean blue channel intensities of dorsal vs. ventral regions-of-interest (ROI) (white boxes) in telotarsal images of *Grophus* (cyan bars) and *Teruelius* (yellow bars). Insets: control images (*) of *T. haeckeli* sp. n. (a, leg III) and *G. madagascariensis* (c, leg III), original (upper) and resampled (lower); test images of *T. sabineae* (b, leg IV) and *G. ambre* (d, leg IV) (resampled from: Lourenço & Wilmé, 2016; Lourenço et al., 2018). Error bars: standard deviations of ROI pixels.



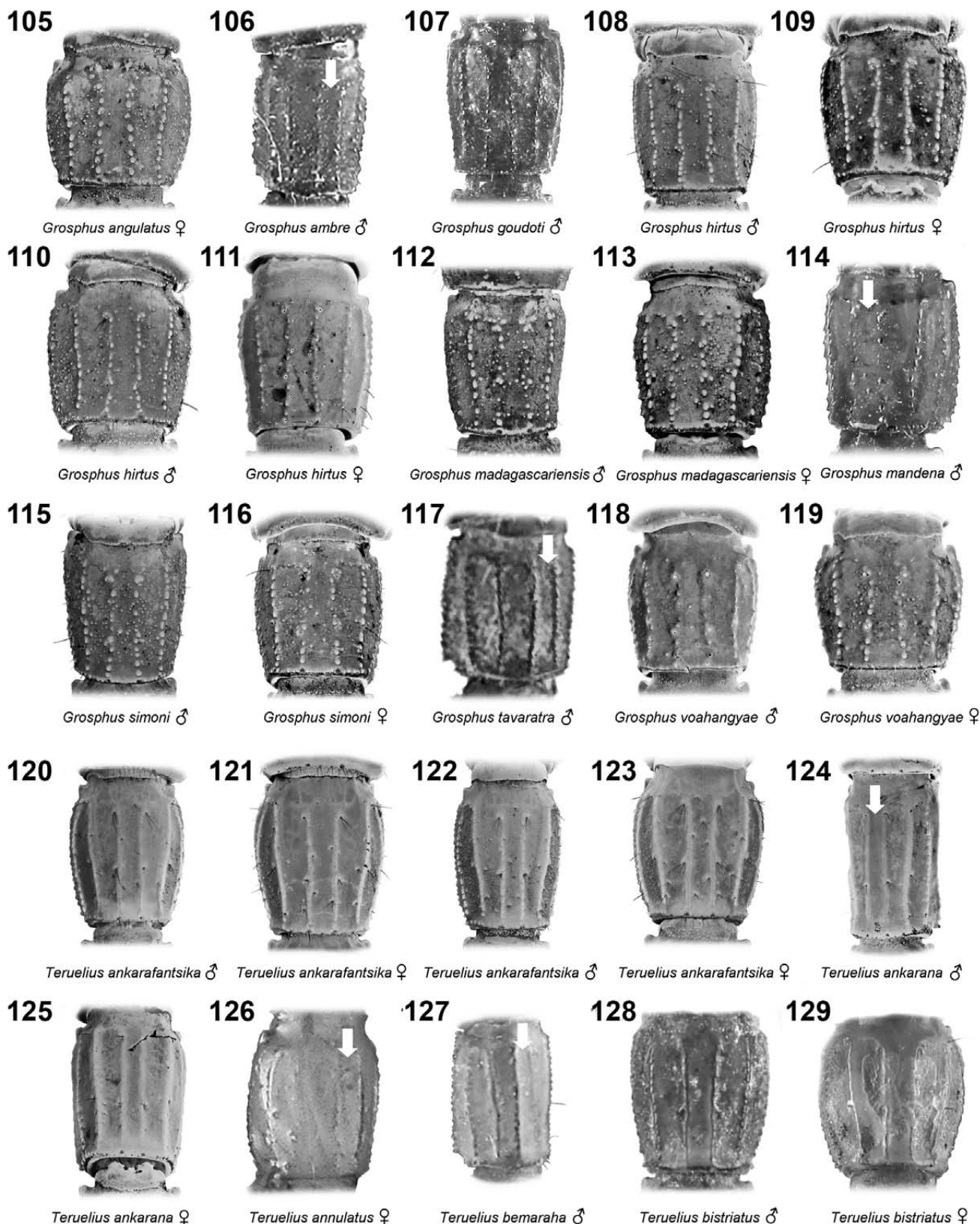
Figures 53–66. Ventral views of sternites IV–VII and metasoma I. **Figures 53–57.** *Grosphus*: *G. madagascariensis*, ♂ (53), *G. angulatus* sp. n., ♀ (54), *G. simoni*, ♀ (55), *G. voahangyae*, ♀ (56), and *G. hirtus*, ♀ (57). **Figure 58.** *Pseudolychas transvaalicus*, ♀. **Figure 59.** *Lychas mucronatus*, ♀. **Figures 60–66.** *Teruelius*: *T. ankarafantsika*, ♀ (60), *T. ankarana*, ♂ (61), *T. grandidieri*, ♀ (62), *T. limbatus*, ♂ (63), *T. flavopiceus*, ♂ (64), *T. mahafaliensis*, ♀ (65), and *T. rossii*, ♂ (66).



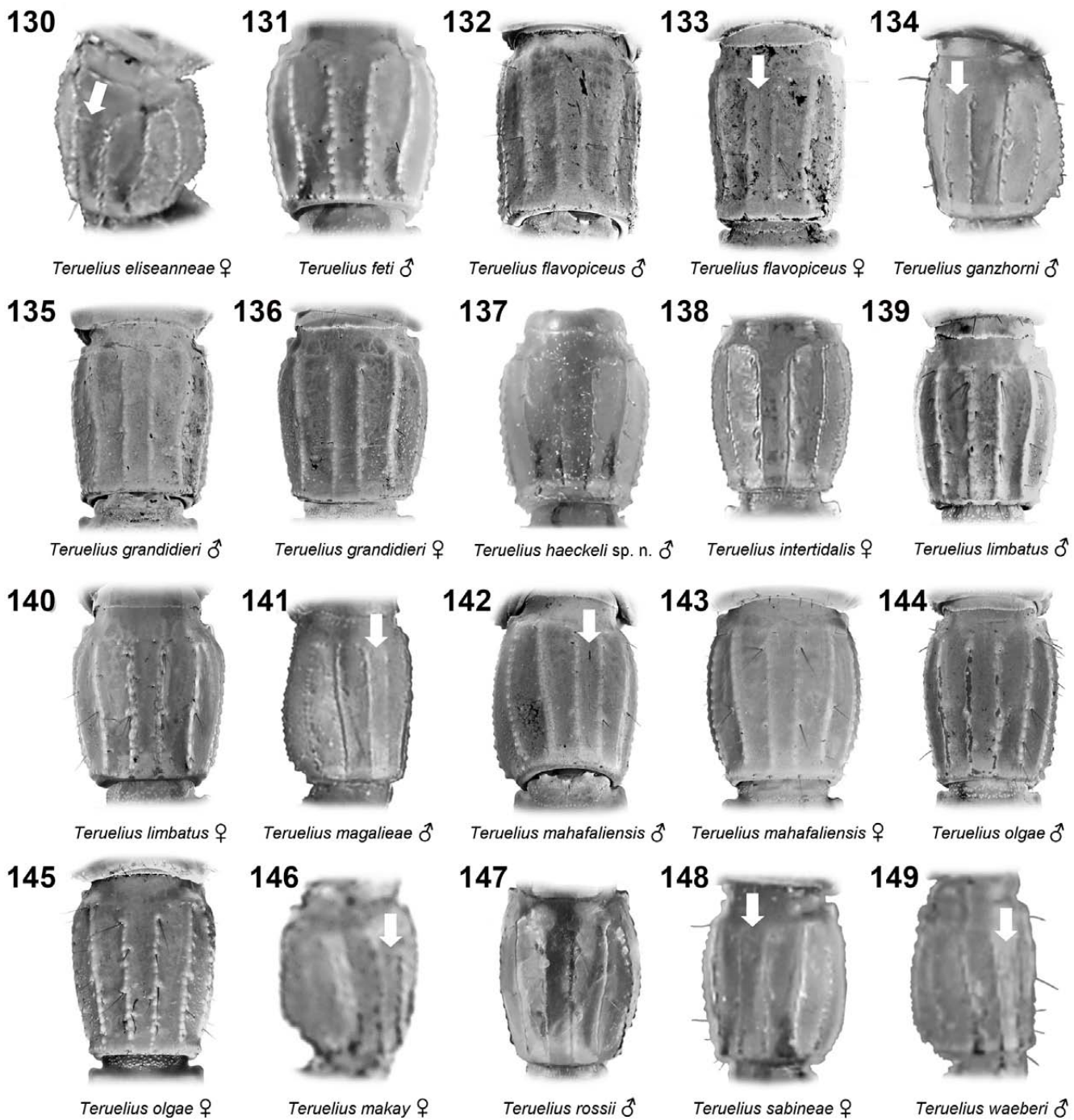
Figures 67–90. Cuticular surface microstructure of medial sternites VII and VI. **Figures 67–70.** *Groshus madagascariensis*, ♂. Sternites VII (67, 69) and VI (68, 70). **Figures 71–74.** *Groshus angulatus* sp. n., ♀. Sternites VII (71, 73) and VI (72, 74). **Figures 75–78.** *Lychas mucronatus*, ♀. Sternites VII (75, 77) and VI (76, 78). **Figures 79–82.** *Teruelius limbatus*, ♀. Sternites VII (79, 81) and VI (80, 82). **Figures 83–86.** *Teruelius flavopiceus*, ♀. Sternites VII (83, 85) and VI (84, 86). **Figures 87–90.** *Teruelius ankaranana*, ♀. Sternites VII (87, 89) and VI (88, 90). Images acquired under reflected white light epi-illumination at lower magnification (scale bar 100 µm in Fig. 68) of sternites on intact animal (67–68, 71–72, 75–76, 79–80, 83–84, 87–88), and Nomarski trans-illumination at higher magnification (scale bar 40 µm in Fig. 70) of dissected sternites after soft tissue removal (69–70, 73–74, 77–78, 81–82, 85–86, 89–90).



Figures 91–104. Light reflection properties of sternites VII and VI. **Figures 91–102.** Spatial distribution of intensity at 45° reflection angles of laser beam with 45° incidence to normal on sternites VII (odd numbered figures) and VI (even numbered figures) from *Grosphus madagascariensis* ♂ (91–92), *Grosphus angulatus* sp. n. ♀ (93–94), *Lychas mucronatus*, ♀ (95–96), *Teruelius limbatus*, ♀ (97–98), *Teruelius flavopiceus*, ♀ (99–100), and *Teruelius ankaranana*, ♀ (101–102). Illumination source: 650 nm laser diode (650MDLC-5-1235), 5 mW, focused to 40 µm diameter spot on medial areas of sternites. Imaging device: Canon EOS 7D Mark II digital camera with 100 mm f/2.8 macro lens focused on translucent white diffuser screen intercepting reflected beams. TIFF files generated by linear RAW conversion. Scale: largest circle in each bounding box subtends 0.1022 sr. **Figure 103.** Horizontal bar chart comparing mean radii of dispersion of reflected beams in Figs. 91–102. Means obtained from pixel-normalized radial density functions computed by ImageJ 1.52a Radial Profile plugin, normalized to mean radius of specular reflection off a silver front surface mirror. Inset: sternites VI and VII from *T. ankaranana*, ♀. **Figure 104.** Horizontal bar chart comparing mean intensities of reflected beams shown in Figs. 91–102. Mean intensities computed for pixels within central circle subtending 0.0637 sr, expressed as percentage mean intensity of specular reflection off a silver front surface mirror.



Figures 105–129. Ventral views of metasomal segment I showing variation in granulation and development of paired ventrosubmedian of carinae in *Grophus* and *Teruelius*. Species and sex indicated in labels under each figure. White arrows identify ventromedial intercarinal surfaces between paired ventrosubmedian carinae in figures with oblique views of the segment. Reflected white light illumination: 106–107, 114, 117, 126–129; UV fluorescence: 105, 108–113, 115–116, 118–125; resampled from published images: 106, 117, 126–127 (Lourenço et al., 2009, 2018; Ref. MNHN-RS-RS1314). Material of Figs. 110–111 determined and labeled as ‘*Grophus garciai*’ (FMNH 73434, FMNH 73436), currently a junior synonym of *G. hirtus*.



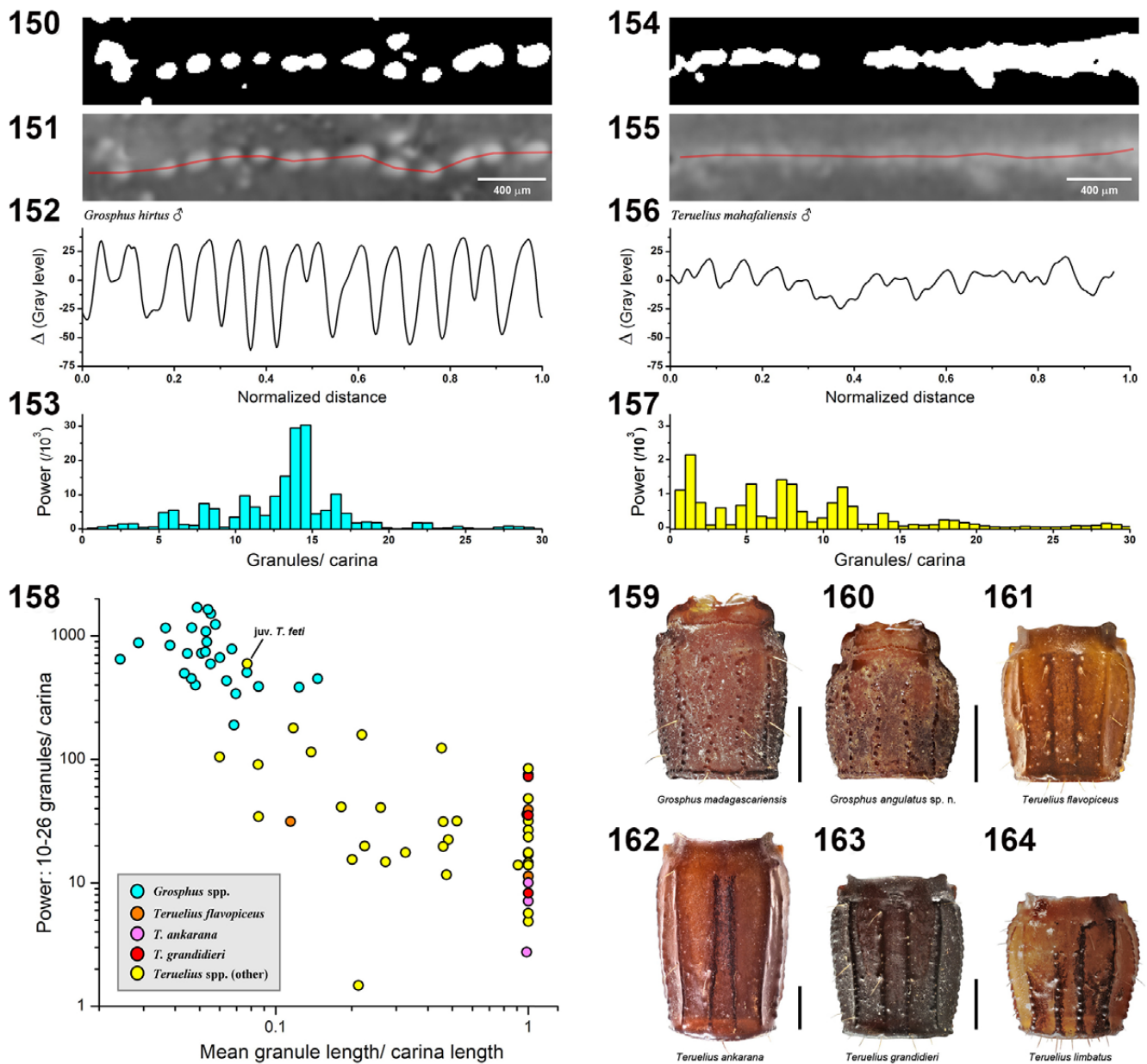
Figures 130–149. Ventral views of metasomal segment I showing variation in granulation and development of paired ventrosubmedian carinae in *Teruelius*. Labels and arrows as in Figs. 105–129. Reflected white light illumination: 130, 134, 137–138, 141, 146–149; UV fluorescence: 131–133, 135–136, 139–140, 142–145; resampled from published images: 130, 134, 141, 146, 148–149 (Lourenço & Wilmé, 2016; Lourenço et al., 2016; Lourenço, 2014; Lourenço & Wilmé, 2015b).

db to be proximal to *est* in two males and two females of *T. mahafaliensis* (e.g., Fig. 166 inset, *T. mahafaliensis* ♂ FMNH 73598). It appears that, in at least one species of *Teruelius*, the relative position of *db* vs. *est* can vary intraspecifically and is not a reliable diagnostic character.

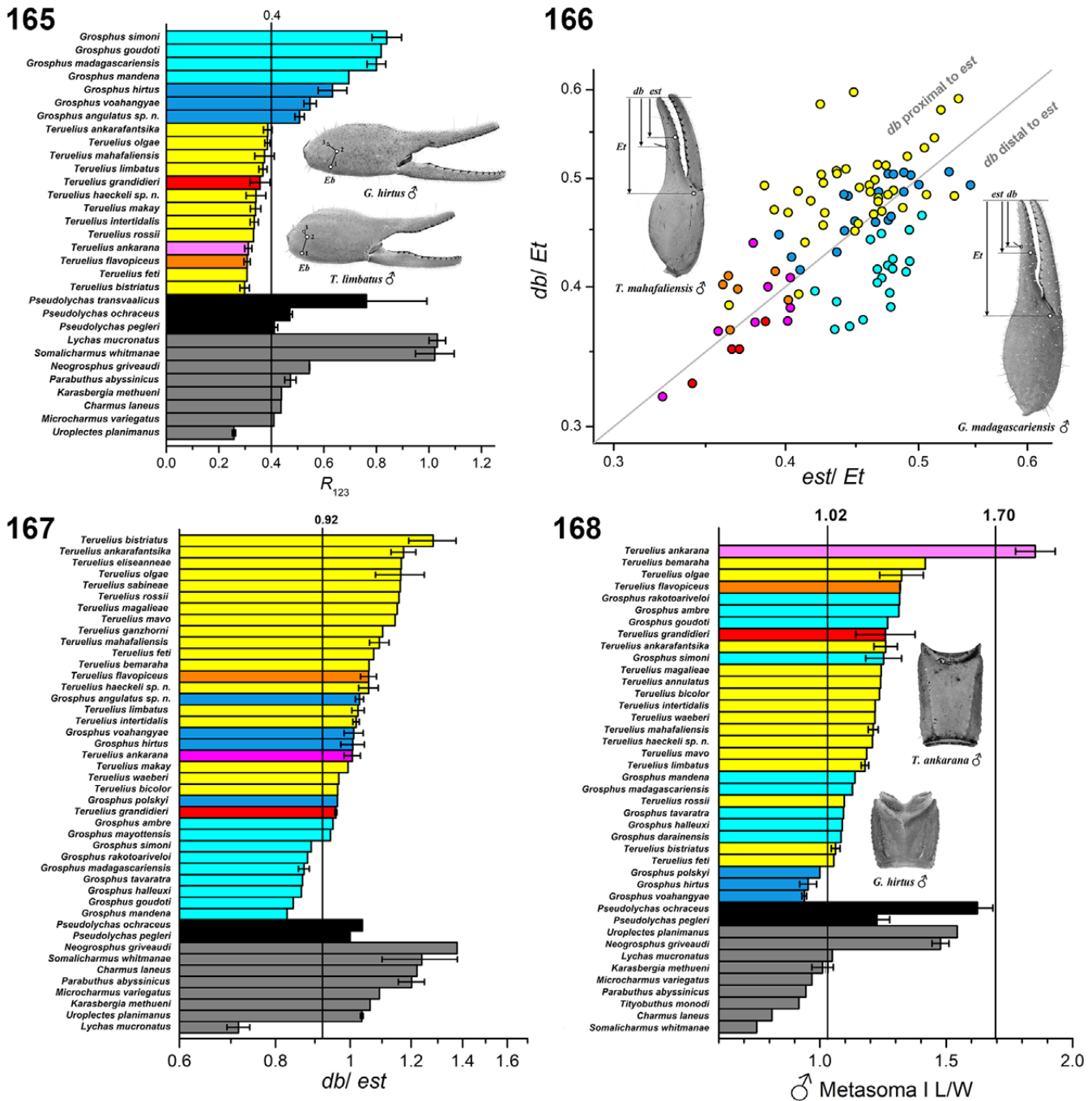
Character 36. Pedipalp manus *Eb* trichobothria, relative positions, mean ratio $R_{123} = d(Eb_2, Eb_3)/d(Eb_1, Eb_2)$: $R_{123} > 0.40$ (0); $R_{123} < 0.40$ (1) (Lowe & Kovářík, 2019: 40, character

ii)

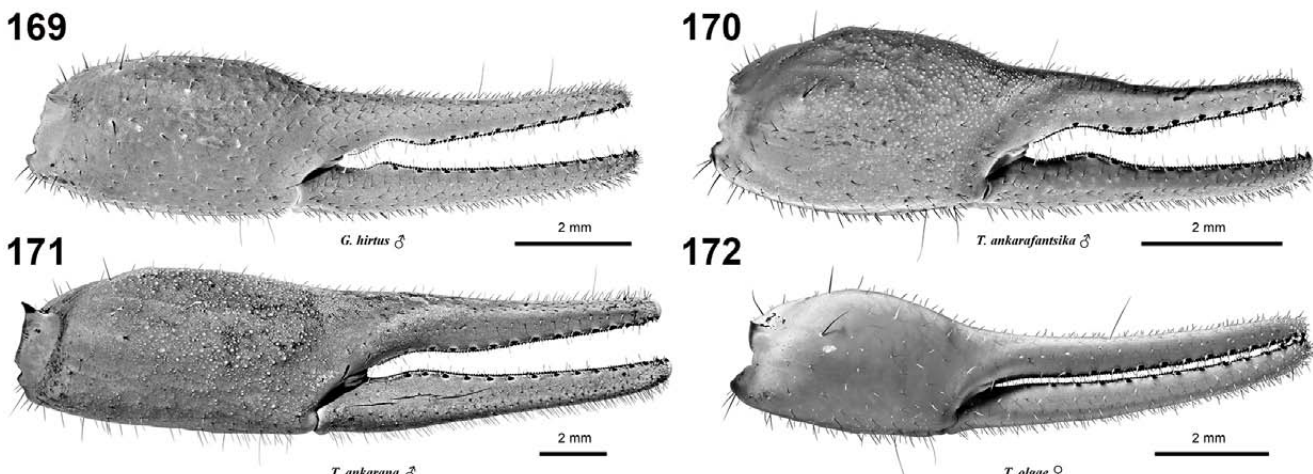
On the proximal manus of the pedipalp chela, the distance between petite ‘trichobothrium’ Eb_3 and trichobothrium Eb_2 , expressed as a ratio, R_{123} normalized to the distance between trichobothria Eb_2 and Eb_1 , was found to be smaller in *Teruelius*, than in *Grosphus* (Lowe & Kovářík, 2019: 13, figs. 21–27). In Fig. 165, mean values of R_{123} are compared in a rank ordered bar plot for an extended data set combining



Figures 150–164. Granulation of ventrosubmedian carinae of metasomal segment I. **Figures 150–157.** Optical image analysis of carinal granulation in *Groshus hirtus*, ♂ (150–153) and *Teruelius mahafaliensis*, ♂ (154–157). Granule patterns (white on black) resolved by binary thresholding of image gray level with maximum entropy algorithm (150, 154), carinae traced as piecewise linear paths following granules or ridges (151, 155, red lines, UV fluorescence), fluctuations in gray levels (8-bit) along traced carinae associated with granulation, normalized to total carinal length (152, 156), and power spectra of fluctuations after subtraction of mean gray level and linear trends (153, 157). Images resampled to 340 pixel width (bilinear down-sample, or cubic up-sample) and smoothed by Gaussian filter, radius 2 pixels (thresholding) or 1 pixel (spectral analysis). Scale bars: 400 µm (151, 155). **Figure 158.** Bivariate logarithmic scatter plot of integrated power of gray level fluctuations (spatial frequency range 10–26 granules/ carina) vs. mean length of granules along carinal axis resolved by binary thresholding for *Groshus* (cyan symbols, $n = 30$, 8 spp.) and *Teruelius* (yellow, orange, magenta and red symbols, $n = 44$, 18 spp.). *T. feti* represented by juvenile holotype male. ‘Granule’ length = 1 if thresholded regions merge into single carina. **Figures 159–164.** Ventral views of metasomal segment I showing different carinal granulation in *Groshus* vs. *Teruelius*. *G. madagascariensis*, ♂ (159), *G. angulatus* sp. n., ♀ (160), *T. flavopiceus*, ♀ (161), *T. ankarana*, ♀ (162), *T. grandidieri*, ♂ (163), and *T. limbatus*, ♀ (164). Reflected white light images. Scale bars: 2 mm.



Figures 165–168. Metasoma and pedipalp characters. **Figure 165.** Horizontal bar plot of mean ratio $R_{123} = d(Eb_2, Eb_3)/d(Eb_1, Eb_2)$, of intertrichobothrial distances on pedipalp chela manus (character 36) for *Grosphus* ($n = 50$, 7 spp.), *Teruelius* ($n = 61$, 13 spp.), *Pseudolychas* ($n = 6$, 3 spp.) and other outgroup taxa ($n = 25$, 8 spp.). Error bars are standard errors. Discretization threshold at step change in ranked ratio. **Figure 166.** Bivariate logarithmic scatter plot of positions of pedipalp fixed finger trichobothria *db* vs. *est* for *Grosphus* ($n = 40$, 13 spp.) and *Teruelius* ($n = 57$, 21 spp.). Distances of *db* and *est* to distal terminus of fixed finger normalized to corresponding distance of manus *Et* (inset diagrams). Inset diagrams show the relative positions of *T. mahafaliensis* ♂ and *G. madagascariensis* ♂. **Figure 167.** Horizontal logarithmic bar plot of mean ratio of distances of trichobothria *db* and *est* from tip of fixed finger (character 35). Data as in Fig. 166. Error bars are standard errors. Discretization threshold at step change in ranked ratio. Color codes of symbols in Fig. 166 and bars in Figs. 165, 167–168 as in Fig. 16 legend. **Figure 168.** Horizontal bar plot of mean ratio of metasoma I L/W in males (character 18) of *Grosphus* ($n = 20$, 12 spp.), *Teruelius* ($n = 28$, 18 spp.), *Pseudolychas* ($n = 5$, 2 spp.) and other outgroup taxa ($n = 12$, 9 spp.). Error bars are standard errors. Discretization thresholds at step changes in ranked ratio.



Figures 169–172. Pedipalp chela internal views of *G. hirtus* (169), *T. ankrafantsika* (170), *T. ankarana* (171) and *T. olgae* (172) showing differences in density of setation and granulation on manus (characters 37–38). Scale bars: 2 mm. UV fluorescence.

males and females. A single discretization threshold, placed at maximal step change in ranked mean values, separates the two genera of the ingroup. This character was scored for only a limited subset of ingroup species (50% of *Groshus*, 59% of *Teruelius*). Curvilinear distortion due to strong convexity of the proximal manus precluded accurate measurements of distances from published illustrations of trichobothrial maps.

Character 37. Pedipalp chela manus, internal surface, setation: sparse to absent (0); moderate to dense (1)

Denser setation on the chela manus was observed more often in *Groshus* (8/10 scored), and less often in *Teruelius* (11/12 scored). Figs. 169–172 show examples of sparse (Figs. 170–172) and dense (Fig. 169) setation.

Character 38. Pedipalp chela manus, internal surface, male or female: smooth or sparsely, weakly granulate (0); granulate (1)

The internal surface of the manus was granulate in a minority of *Groshus* species (4/14), and a majority of *Teruelius* species (14/20 scored). Figs. 169–172 show examples of smooth (Figs. 169, 172) and granulate (Figs. 171–172) morphosculptures. A granulate condition was scored if found in either sex.

Character 39. Telson aculeus, length: shorter than vesicle (0); equal to vesicle (1); longer than vesicle (2)

The aculeus was shorter than the vesicle in all species of *Groshus*, and equal to or longer than the vesicle in 10/22 species of *Teruelius*. For vesicle length, we followed Sissom et al. (1990: 452, fig. 11.1.G), for aculeus length we took the chord distance between aculeus tip and aculeus base (Kovařík & Lowe, 2022: 25, fig. 135, inset, ‘BT’).

Character 40. Telson vesicle, ventral surface: strongly to moderately granulate (0); weakly granulate (1); smooth (2)

The ventral surface of the telson was strongly to moderately granulate in all species of *Groshus* and 4/22 species of *Teruelius*, weakly granulate in 14/22 and smooth in 4/22 species of *Teruelius*.

Character 41. Telson, subaculear tubercle: strong to moderate (0); weak to vestigial (1); absent (2)

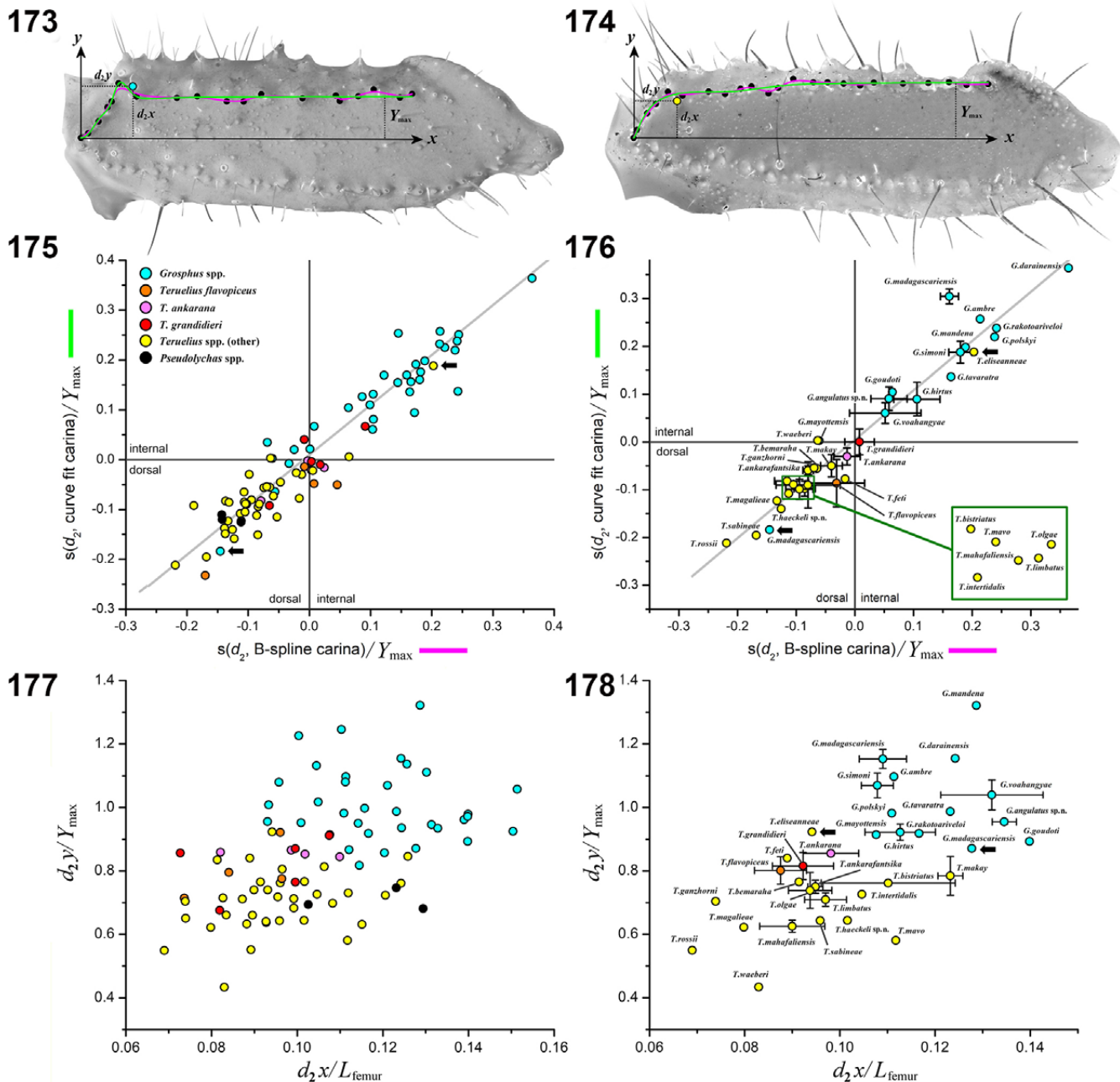
Among ingroup taxa, a small to moderately developed

subaculear tubercle was found in the ‘*hirtus*’ group of *Groshus* (Fig. 302; Lowe & Kovařík, 2019: 63, figs. 181–182, 185). In other *Groshus* species and all *Teruelius* species, the subaculear tubercle was weak, vestigial (represented only by a small granule) or absent.

Character 42. Telson lateral profile, male, elliptic Fourier analysis, mean PC1* rotated: > 0 (0); < 0 (1)

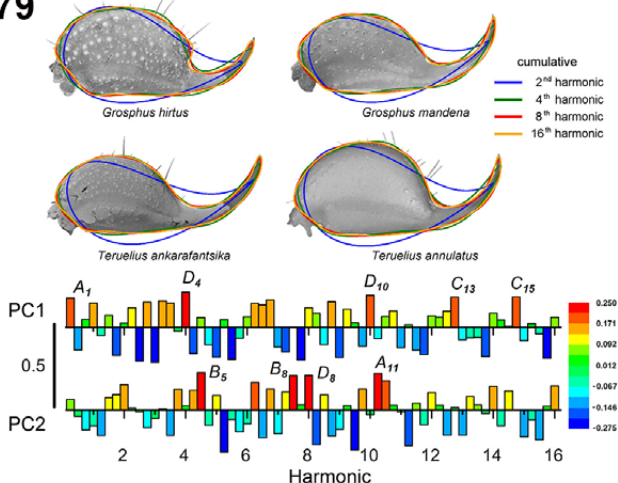
Character 43. Telson lateral profile, female, elliptic Fourier analysis, mean PC2* rotated: < 0.35 (0); > 0.35 (1)

Telson shapes have been categorized in terms of qualitative descriptors that depend on subjective judgement, such as ‘oval’, ‘bulbous’ and ‘elongate’ (e.g., Lowe & Kovařík, 2019). Recently, we conducted a quantitative analysis of telson shapes by PCA of seven variables extracted by measurement of lateral telson profiles (Kovařík & Lowe, 2022). Here, we refine our morphometric approach by applying EFA to lateral profiles. Elliptic Fourier series containing up to sixteenth order harmonics were fitted to these profiles. This yielded sufficient resolution to model the general shapes of vesicle and aculeus, as well as coarser details such as subaculear tubercles, but excluded finer surface morphosculpture such as granules (Fig. 179, upper panel). PCA was performed on 64 Fourier coefficients extracted from *Groshus* (14 spp.), *Teruelius* (21 spp.), and outgroup taxa (12 spp.) ($n = 129$ samples). The first two principal components (PC1, PC2) together accounted for 49.87% of the total variance and yielded a partial separation of *Groshus* vs. *Teruelius*. PC1 and PC2 were linearly correlated within a subgroup of *Teruelius* that excluded the 3 large species: *T. ankarana*, *T. flavopiceus* and *T. grandidieri*. The (PC1, PC2) plane was rotated 45.17° to maximize variance of the subgroup along the first axis (PC1*) and to minimize its variance along the second axis (PC2*) (yellow symbols in Fig. 180). Telson shape can be sexually dimorphic and mean values of (PC1*, PC2*) for each species were compared in separate bivariate scatter plots for males (Fig. 181) and females (Fig. 182). In both sexes, most species of the *Teruelius* subgroup were localized in a compact linear band with lower PC1* and higher PC2* z-scores, whereas *Groshus* and the large

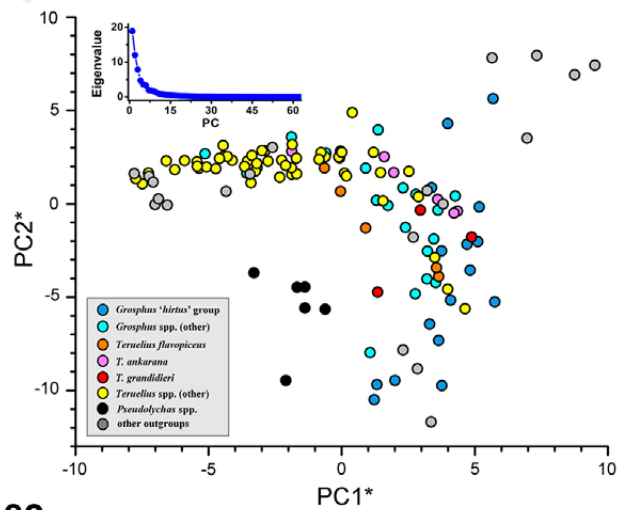


Figures 173–178: Analysis of position of petite 'trichobothrium' d_2 on pedipalp femur of *Grosphus*, *Teruelius* and *Pseudolychas*. **Figures 173–174.** Cartesian x-y coordinates for digitizing positions of d_2 and dorsointernal carina in *Grosphus madagascariensis* (173) and *Teruelius olgae* (174). Coordinates of d_2 are (d_2x, d_2y) indicated by cyan (173) or yellow (174) symbol. Positions of granules of dorsointernal carina indicated by black symbols. Granules fitted by B-spline (magenta curves) or parametric function (green curves). Y_{\max} : asymptotic value of parametric function. **Figure 175.** Bivariate scatter plot of minimum distances, s , of d_2 from parametric curve vs. d_2 from B-spline curve (both normalized against Y_{\max}) for femora of *Grosphus* ($n = 34$, 14 spp.), *Teruelius* ($n = 49$, 20 spp.) and *Pseudolychas* ($n = 3$, 3 spp.). Gray diagonal line: least squares regression for *Grosphus* and *Teruelius* data, $R = 0.8131$, $P < 0.0001$. Symbol colors indicated in legend. Black arrows mark isolated outlier points. **Figure 176.** Bivariate scatter plot of means of minimum distances for species of *Grosphus* and *Teruelius*, summarizing data of Fig. 175. Error bars are standard errors. Gray diagonal line: least squares regression, $R = 0.9700$, $P < 0.0001$. **Figure 177.** Bivariate scatter plot of normalized x-y coordinates of d_2 for data in Fig. 175. Abscissas normalized against femur length, L_{femur} , ordinates against Y_{\max} . **Figure 178.** Bivariate scatter plot of means of normalized x-y coordinates for species of *Grosphus* and *Teruelius*, summarizing data of Fig. 177. Error bars are standard errors. Data extracted from images of specimens and published figures of femur in dorsal aspect showing granules and trichobothria, in which d_2 could be identified.

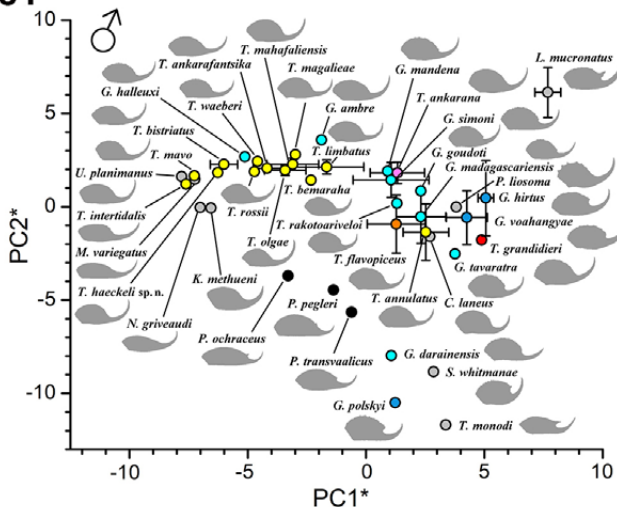
179



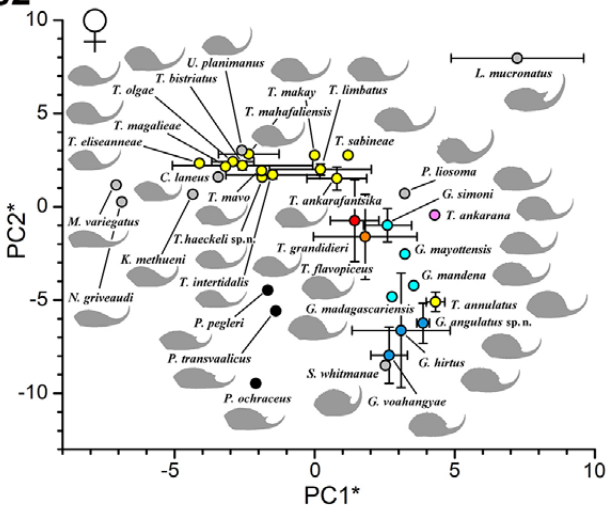
180



181



182



Figures 179–182. Morphometrics of telson lateral profiles. **Figure 179.** Elliptic Fourier analysis (EFA) of lateral profiles. Upper panel: EFA curve fits to profiles of *Groshus hirtus*, *G. mandena*, *Teruelius ankrafantsika* and *T. annulatus* by Fourier series with cumulative terms up to and including second (blue), fourth (green), eighth (red) and sixteenth (orange) order harmonics. Telson profiles oriented with dorsal surface horizontal, start point at anterior limit of vesicle, peduncle truncated, area normalized. Lower panel: Histogram plots of harmonic loadings of first two principal components, PC1 and PC2, obtained from PCA of 64 standardized Fourier coefficients from up to sixteenth order harmonic terms, accounting for 30.33% and 19.54% of variance, respectively (total variance 49.87%). Bars are heat map coded by loading values, harmonics with highest positive loadings labelled (red bars). **Figure 180.** Bivariate scatter plot of subspace of first two principal components rotated (PC1*, PC2*) to minimize variance of *Teruelius* spp. (yellow symbols) along vertical axis. Data from 117 telson profiles from *Groshus* ($n = 35$, 14 spp.), *Teruelius* ($n = 65$, 21 spp.), *Pseudolychas* ($n = 6$, 3 spp.) and other outgroup taxa ($n = 11$, 4 spp.), both males and females. Upper inset: scree plot of eigenvalue vs. PC number. Lower inset: legend for symbol colors: *Groshus 'hirtus'* group (= *G. angulatus* sp. n., *G. hirtus*, *G. polskyi*, *G. tavaratra*, *G. voahangyae*), blue; other *Groshus* spp., cyan; *Teruelius flavopiceus*, orange; *T. ankara*, magenta; *T. grandidieri*, red; other *Teruelius* spp., yellow; *Pseudolychas* spp., black; other outgroup taxa, gray. **Figure 181.** Bivariate scatter plot of mean values of PC2* vs. PC1* for male telson profiles of *Groshus* (12 spp.), *Teruelius* (16 spp.), *Pseudolychas* (3 spp.) and other outgroup taxa (4 spp.). **Figure 182.** Bivariate scatter plot of mean values of PC2* vs. PC1* for female telson profiles of *Groshus* (7 spp.), *Teruelius* (15 spp.), *Pseudolychas* (3 spp.) and other outgroup taxa (4 spp.). Profile silhouette examples shown for analyzed species in Figs. 181–182. Error bars in Fig. 182 are standard errors. Symbol colors in Figs. 181–182 as in legend of Fig. 180.

Teruelius species were more dispersed with higher PC1* and lower PC2* z-scores. Discretization thresholds were selected for PC1* (males) and PC2* (females) to reflect the separations of respective clusters along orthogonal axes.

Telsons with a shorter more ‘bulbous’ vesicle had higher PC1* scores, and those with more ‘elongate’ vesicles had lower PC1* scores. The variable PC1* serves as a quantitative

measure, substituting for the subjective shape descriptors. Telsons with longer aculei had higher PC2* scores, and those with shorter aculei had lower PC2* scores. The analysis did not identify variables capable of diagnostic separation of *Groshus* vs. *Teruelius*. The morphometric overlap suggests a degree of convergence in the evolution of telson shapes. For example, the more ‘bulbous’ vesicles of the larger species

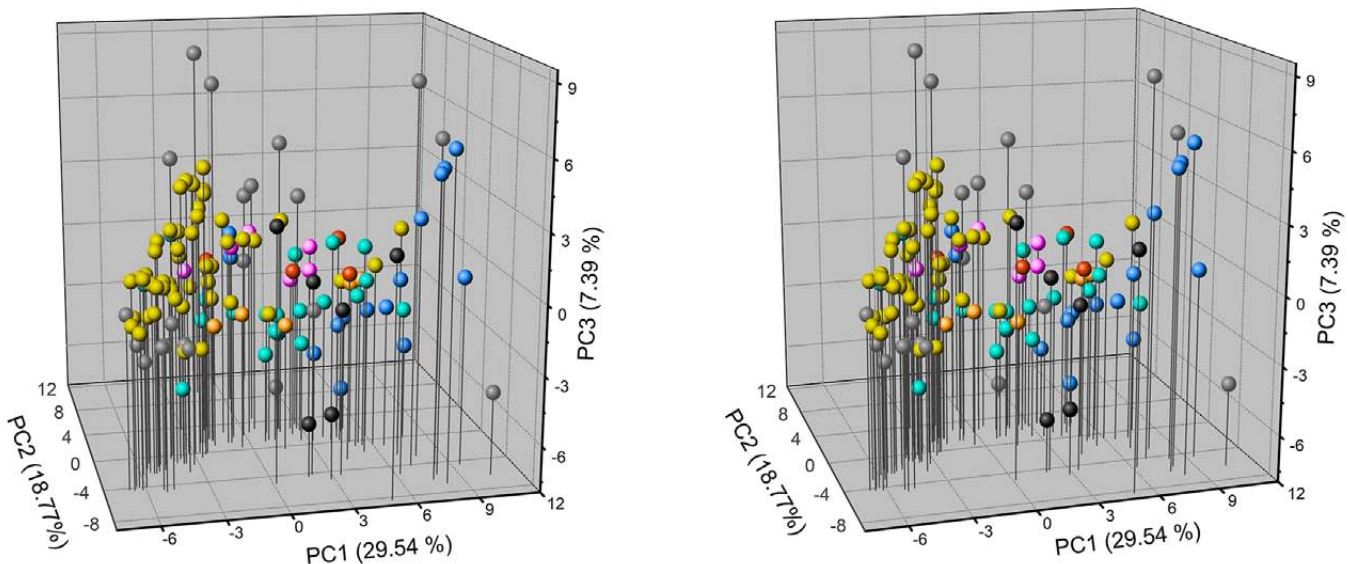


Figure 183. Morphometrics of telson lateral profiles. Trivariate scatter plot of first three unrotated principal components (PC1, PC2, PC3) of harmonics extracted by Elliptic Fourier analysis (Fig. 179), rendered as a 3D cross stereoscopic pair. Symbol colors as in legend of Fig. 180.

of *Teruelius*, and of *T. annulatus*, associated them with *Grosphus*, rather than *Teruelius*. Nonetheless, telson shapes could convey phylogenetic information, as shown by partial segregation of the two genera by PCA. The partial segregation is more evident in a trivariate 3D scatter plot including a third principal component (Fig. 183).

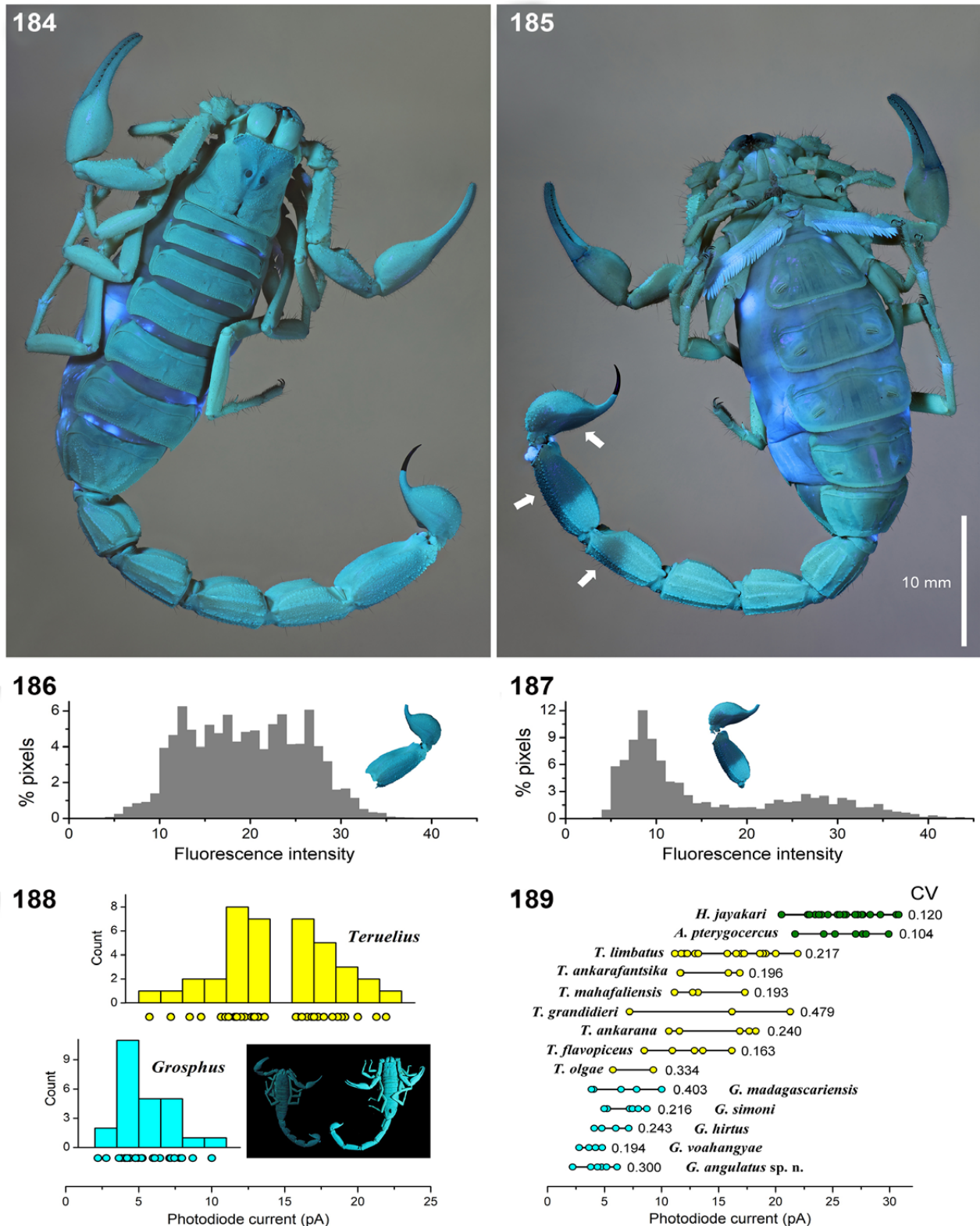
Character 44. UV fluorescence, mean intensity: weak in *Grosphus*, vs. strong in *Teruelius* (Lowe & Kovařík, 2019: 43, character ix).

We previously reported that the intensity of UV fluorescence in *Grosphus* was on average weaker than in *Teruelius*. Although our samples were limited, we found that the two genera could be segregated by mean fluorescence intensity (Lowe & Kovařík, 2019: 41, fig. 158). This permitted binary scoring of our sample. However, there was high variation in measured intensities, both within and between species. This variation caused substantial overlap between the two genera at the lower and upper ends of their ranges. The overlap is evident in grouped histogram plots (Fig. 188), and in ranked range plots of individual samples (Fig. 189). For character coding, the critical question is whether this overlap represents true phenotypic variation or measurement artefacts.

We previously discussed technical problems associated with comparative fluorescence measurements of museum specimens. A major source of systematic error is prior photobleaching (Kloock, 2009; Kloock et al., 2010). We showed this in dynamic measurements of rapid photobleaching in museum specimens of *Grosphus* and *Teruelius* under continuous UV excitation (Lowe & Kovařík, 2019: 41, figs. 159–160). The problem is further illustrated in Figs. 184–185, showing UV fluorescence of a specimen of *T. limbatus* that was stored in a bottle along with a number of other conspecific specimens (FMNH 73598, 8 ♂, 6 ♀). Fluorescence was inhomogeneous, with stronger emission from some areas of

the body and weaker emission from others. The arrows in Fig. 185 indicate localized areas on the right lateral surfaces of metasomal segments IV–V and telson vesicle where fluorescence was much weaker than in surrounding areas. On the left lateral areas of the same segments, fluorescence emission was uniform and much brighter (Fig. 184), showing that the locally weak fluorescence was not an intrinsic property. Other conspecific specimens in the same bottle did not have the same patterns of weak and strong fluorescence. We attribute the inhomogeneity of cuticular fluorescence to the cumulative effect of localized photobleaching of a specimen stored in a lighted environment. Areas directly exposed to light were strongly bleached, and areas shielded by other specimens packed into the bottle were not. Distributions of fluorescence intensity of pixels on left and right lateral surfaces of metasoma V and telson vesicle are compared in Figs. 186–187. Heavily photobleached areas correspond to the peak on the left of the histogram in Fig. 187 where fluorescence is about 3-fold lower than in surrounding areas. This provides an important context for interpreting the broad, overlapping distributions of measured fluorescence in Figs. 188–189.

The wide variations in measured intensity (CV ~16–48%) seen in some species of *Grosphus* and *Teruelius* could be caused by differential photobleaching. Measured values may not represent the intrinsic fluorescence of fresh specimens. For comparison, we acquired data from control batches of two other buthids, *Aristobuthus pterygocercus* and *Hottentotta jayakari* (Fig. 189, green symbols). Each batch included adults from one unique locality and collection date, and both batches were stored under identical conditions in the dark in single bottles of alcohol. These provided more reliable estimates of the expected variation in fluorescence. Their mean fluorescence intensity was higher, and their variation was lower (CV ~10–12%) than in the samples of *Grosphus* and *Teruelius*. The



Figures 184–189. Variation in UV fluorescence of preserved material. **Figures 184–185.** *Teruelius limbatis*, female in dorsal (184) and ventral (185) views under uniform UV Illumination (395 nm LED array). White arrows in Fig. 185 indicate areas on right lateral metasoma IV, V and telson with strong photobleaching. Scale bar: 10 mm. **Figures 186–187.** Histograms showing calculated distributions of fluorescence intensity for left lateral metasoma V and telson (186), and right lateral metasoma V and telson (187). Pixel intensities calculated from JPEG images by luminance grayscale conversion and inversion of the OECF of the camera (Canon EOS 5DsR). OECF estimated by 5th-order polynomial fit to relationship between gray values of 66 linear RAW converted vs. sRGB encoded images of a uniform test target illuminated by white light LED driven by variable current source. **Figure 188.** Distribution of measured fluorescence intensity (photodetector current) of medial sternite VI in *Grosphus* (cyan bars and symbols, $n = 25$, 5 spp.) and *Teruelius* (yellow bars and symbols, $n = 39$, 7 spp.). Inset image: *Grosphus madagascariensis* (σ) (left) and *Teruelius ankarana* (σ) (right) under UV light. **Figure 189.** Raw data of Fig. 188 plotted by species. Each symbol represents a measurement from one specimen. Horizontal lines indicate ranges of variation. Numbers on the right are coefficient of variation (CV). Cyan symbols: *Grosphus*; yellow symbols: *Teruelius*; green symbols: reference data from control batches of two buthids, *Aristobuthus pterygocercus* ($n = 7$) and *Hottentotta jayakari* ($n = 16$) stored under identical conditions in the dark.

higher mean intensities of *Apistobuthus* and *Hottentotta* could be due either to less photobleaching, or to intrinsic differences in fluorescence (e.g., higher concentrations of fluorophores). On the other hand, their lower coefficients of variation suggest that the higher variation in *Grosphus* and *Teruelius* may be caused by variable fading of fluorescence. Another possible mechanism of fading is leaching of fluorophores into preserving fluids (Lawrence, 1954; Constantinou, 1984). This introduces another uncontrolled variable that may depend on fixation methods, duration of storage, and composition of preserving fluids. It was not expected to be a factor in our control batches, which were fixed by the same methods and stored in the same bottles in identical conditions. These were preserved according to the method of Williams (1968), by heat shock and fixation in alcohol and formaldehyde, which retains more natural coloration. It is possible that this treatment was more effective at stabilizing cuticular fluorescence than fixation by alcohol alone. If the gradual leaching of fluorophores were the main cause of variation in Fig. 189, then intensity of fluorescence is predicted to be negatively correlated with time interval between collection and fluorescence measurement. However, we found no significant correlation for the *Grosphus* and *Teruelius* samples ($R = -0.08121$, $P = 0.52354$; $n = 64$, interval range 2061–9473 d). The median interval for *Grosphus* (5661 d) was not significantly longer than that for *Teruelius* (5562 d) (Mann-Whitney test, $U = 561$, $U' = 427$, $P = 0.17987$). Moreover, the *Apistobuthus* and *Hottentotta* samples exhibited the strongest fluorescence but were the oldest collected material (10,082 d), which is the opposite of the predicted trend. A third factor that could affect all samples is variable time elapsed after the most recent ecdysis. Cuticular fluorescence is weak or absent immediately after a molt, and is gradually restored over several days as tanning reactions harden the exoskeleton (Li et al., 2022; Stahnke, 1972a). Although unknown variables could introduce many systematic errors, the difference between mean intensities of *Grosphus* and *Teruelius* was still statistically significant. If each genus were assumed to be a uniform population with CV ~10%, the observed separation between the means would imply no significant overlap between the two genera.

Kloock (2009) reported that the fluorescence intensity of *Paruroctonus becki* was reduced by at least 10-fold after 32 days of exposure to UV light. After termination of UV exposure, partial recovery of fluorescence was seen in live scorpions within a week, but not in preserved specimens. Therefore, photobleaching of museum specimens is an irreversible and cumulative process. The heavy photobleaching of the metasoma and telson in Fig. 185 (arrows) probably occurred over a much longer period, maybe 20 years (collection date: 6.II.1999; imaging date: 8.II.2019). Under white light, there were no telltale signs such as color shifts in visible wavelengths to suggest localized photobleaching of UV fluorescence. To control for photobleaching or fluorophore loss, it is essential to compare multiple samples with different collection dates or histories (e.g., Lourenço, 2012; Rubin et al., 2017). Isolated observations on single specimens (Lourenço, 2020; Lourenço & Ythier, 2021) are anecdotal and inconclusive.

It is worth noting some other methodological pitfalls in scorpion fluorometry. Measurements can be compromised if a dichroic mirror or emission filter is not used to block excitation wavelengths. Rubin et al. (2017) used a 395 nm UV LED light source to excite cuticular fluorescence but did not mention using any optical filters in their detection path. Their imaging camera (Nikon D300) is sensitive to wavelengths above 400 nm (Sigernes et al., 2009: 20216, fig. 6), a range overlapping the typical output spectrum of 395 nm LEDs (380–420 nm; e.g., Zemel & Houghton, 2017: 81, fig. 2). Purple or violet reflections in images of “*non-fluorescing*” samples (Rubin et al., 2017: 248, fig. 1c,f,h) are likely to be contributions from excitation wavelengths (400–420 nm), which could add a positive offset to the fluorescence measurements.

A calibrated detector is essential for quantitative measurements. NIST-certified commercial analytical instruments can provide accurate fluorescence measurements (e.g., Frost et al., 2001; Kloock, 2008; Kloock, 2009; López-Cabrera et al., 2020; Yoshimoto et al. 2020). Measurements are simplified if detector output is a linear function of light intensity, otherwise the detector response curve must be calibrated to correct the data. We used a photodiode with a linear response to quantify scorpion fluorescence (Lowe & Kovařík, 2019). For quantitative imaging, Lowe et al. (2003) digitized the video signal from a CCD camera, disabling automatic gain control and gamma correction circuits to obtain a linear output. Quantitative fluorescence imaging is commonly performed with scientific-grade CCD or CMOS cameras with linear readouts of intensity (Berland et al., 2003; Spring, 2003). Consumer-grade digital cameras are viable alternatives, with sensitivities adequate for the brighter fluorescence of most scorpions. However, they require external calibration for photometric applications (Burggraaff et al., 2019). If writing standard formats of image files for analysis, linear RAW conversion of sensor data should be performed (Pike, 2011). JPEG files directly output from consumer digital cameras do not provide linear measures of intensity. The in-camera RAW conversion firmware applies proprietary tone curves that can distort intensity profiles. Additional non-linear distortion arises from the standard gamma encoding for sRGB color space, which selectively boosts dimmer pixels to optimize display on computer monitors (Stevens et al., 2007). The net effect is described by a device-specific, non-linear transfer function, the opto-electronic conversion function (OECF) (Garcia et al. 2013). Retrieval of intensity information requires inversion of the OECF (e.g., Figs. 186–187). López-Cabrera et al. (2020) characterized spatial distributions of scorpion fluorescence intensity by analyzing images from a camera (Nikon L320) that does not output RAW files, but did not describe how they linearized their data. Most electronically published images of fluorescent scorpions probably incorporate an OECF with gamma encoding, and it cannot be assumed that their pixel values are proportional to fluorescence intensity.

	Character
0*	Carapace length, mean: < 5.0 mm (0); 5.0–6.9 mm (1); > 6.9 mm (2)
1	Carapace and tergites base color: dark, black to brown (0); brown to orange (1); orange to yellow (2)
2	Carapace color pattern: uniform (0); maculate or variegated fuscosity (1)
3	Carapace, denticulate medial epistomal process: small or absent (0); well developed in either sex (1)
4	Carapace, anterior margin, mean concavity angle: > 8.4° (0); < 8.4° (1)
5	Carapace, preocular L/ Carapace L, mean: < 0.395 (0); > 0.395 (1)
6	Carapace, superciliary carinae, ♂: strongly or moderately granulate (0); weakly granulate or smooth (1)
7	Hemispermatophore capsule distal carina: long (0); short (1)
8	Hemispermatophore posterior lobe: absent (0); elongate, tapered (1); short, blunt or triangulate (2)
9	Hemispermatophore distal carina, number of lateral carinae: none (0); one (1); two or more (2)
10	Leg III, tibial spur L/ tibia distal D: < 0.73 (0); > 0.73 (1)
11	Leg IV, tibial spur L/ tibia distal D: < 0.69 (0); > 0.69 (1)
12	Legs I–IV, telotarsi, ventral setation: sparse, discrete, < 25 setae in rows (0); dense, brush-like, > 25 irregular setae (1)
13	Mesosoma, tergites I–VI, one or more dark longitudinal stripes: absent (0); present (1)
14	Mesosoma, sternite IV, spiracles: broad, hemi-elliptical or ovoid L/W < 5 (0); narrow, slit-like, L/W > 5 (1)
15	Mesosoma, sternite VII submedian carinae: granulate (0); smooth or obsolete (1)
16	Mesosoma, sternite VII, medial texture and reflectance: matte, low reflectance (0); glossy, high reflectance (1)
17	Metasoma I ventrosubmedian carinae: granulate (0); costate-granulate (1); smooth (2), absent (3)
18*	Metasoma I, L/W mean: ♂ < 1.02, ♀ < 0.97 (0); ♂ 1.02–1.7, ♀ 0.97–1.3 (1); ♂ > 1.7, ♀ > 1.3 (2) (♂ priority)
19	Metasoma III ventral intercarinal surface: granulate (0); very weakly granulate to smooth (1)
20	Metasoma III, dorsosubmedian carinae, dentate posterior subterminal granule, either sex: present (0); absent (1)
21	Metasoma III, dorsosubmedian carinae, large dentate posterior terminal granule, either sex: present (0); absent (1)
22	Metasoma V, dorsolateral carinae, granulation: strong (0); weak (1); smooth or obsolete (2)
23	Pectine basal tooth (<i>bpt</i>), ♀ shape: unmodified (0); triangular (1); ovoid or subrectangular (2); elongated, curved (3)
24	Pectine basal tooth (<i>bpt</i>), ♀: shorter than or equal to basal comb width (0); longer than basal comb width (1)
25	Pectine basal tooth (<i>bpt</i>), ♀: without long, narrow extension (0); with long narrow extension (1)
26	Pectinal tooth count (PTC): ♂ < 24, ♀ < 22 (0); ♂ > 24 (1), ♀ > 22 (1) (♂ priority)
27	Pectinal tooth, regular, L/W mean, ♂: < 3.7 (0); > 3.7 (1)
28	Pedipalp femur petite ‘trichobothrium’ <i>d</i> ₂ position: dorsal (0); internal (1); absent (2)
29	Pedipalp femur trichobothrium <i>e</i> ₁ position vs. <i>d</i> ₅ : proximal (0), level or distal (1)
30	Pedipalp femur, dorsal surface: strongly to moderately granulate (0); weakly granulate to smooth (1)
31	Pedipalp patella, dorsomedian surface, setation: dense, > 20 macrosetae (0); sparse, < 20 macrosetae (1); absent (2)
32	Pedipalp patella, dorsointernal carina development: absent (0); weak (1); moderate (2); strong (3)
33	Pedipalp patella, dorsointernal carina granulation: sparse to absent (0); moderate (1); dense (2); costate-granulate (3)
34	Pedipalp chela fingers, male, proximal undulation: strong (0); moderate (1); weak or absent (2)
35	Pedipalp chela fixed finger, trichobothria position, <i>db</i> vs. <i>est</i> , mean ratio : <i>db</i> > 0.92 <i>est</i> , proximal (0); <i>db</i> < 0.92 <i>est</i> , distal (1)
36	Pedipalp manus <i>Eb</i> trichobothria <i>R</i> ₁₂₃ = <i>d(Eb</i> ₂ , <i>Eb</i> ₃) / <i>d(Eb</i> ₁ , <i>Eb</i> ₂) mean value: <i>R</i> ₁₂₃ > 0.40 (0); <i>R</i> ₁₂₃ < 0.40 (1)
37	Pedipalp chela manus, internal surface, setation: sparse to absent (0); moderate to dense (1)
38	Pedipalp chela manus, internal surface, male or female: smooth or sparsely, weakly granulate (0); granulate (1)
39*	Telson aculeus, length: shorter than vesicle (0); equal to vesicle (1); longer than vesicle (2)
40	Telson vesicle ventral surface: strongly to moderately granulate (0); weakly granulate (1); smooth (2)
41	Telson, subacicular tubercle: strong to moderate (0); weak to vestigial (1); absent (2)
42	Telson lateral profile, ♂: elliptic Fourier analysis, mean PC1* rotated: > 0 (0); < 0 (1)
43	Telson lateral profile, ♀: elliptic Fourier analysis, mean PC2* rotated: < 0.35 (0); > 0.35 (1)
44	UV fluorescence: weak (0); strong (1)

Table 1. Discrete characters and character states used in phylogenetic analysis of *Teruelius*. Of 45 characters, 42 were unordered, 3 ordered*. All characters were assigned weights of 2 except characters 10, 11 which were assigned weights of 1.

TAXON	0–4	5–9	10–14	15–19	20–24	25–29	30–34	35–39	40–44
<i>Grosphus ambre</i>	11000	00???	00000	0?010	100??	?0011	00211	0?100	021??
<i>Grosphus angulatus</i> sp. n.	10000	0????	00000	00000	00020	00?10	1000?	00100	01200
<i>Grosphus darainensis</i>	11001	0????	??0?	??10	100??	?001?	??10?	??10	020??
<i>Grosphus goudotii</i>	10000	00111	00000	00010	10020	00011	0?100	10000	010??
<i>Grosphus halleuxi</i>	10001	0????	??000	0?010	000??	?00?1	0?201	1?010	021??
<i>Grosphus hirtus</i>	00101	00111	00000	00000	00020	00011	00100	00100	00000
<i>Grosphus madagascariensis</i>	10000	00011	00000	00010	00020	00011	00101	10110	01000
<i>Grosphus mandena</i>	10000	00011	00000	00010	00020	00011	00101	10100	0200?
<i>Grosphus mayottensis</i>	20000	0????	??20?	??10	10110	00?11	??11?	0?200	02?0?
<i>Grosphus polskyi</i>	01100	0????	??200	??200	110??	?0?11	0?101	0?200	000??
<i>Grosphus rakotoariveloi</i>	11000	0????	??20?	??10	000??	?0011	?2201	1?200	020??
<i>Grosphus simoni</i>	10000	00011	00000	00010	00020	00011	00110	10100	02000
<i>Grosphus tavatatra</i>	10101	0????	00000	0?110	000??	?0011	?0311	1?110	010??
<i>Grosphus voahangyae</i>	00100	00110	00000	00000	00020	00011	10001	00100	00000
<i>Teruelius ankaraensisika</i>	12011	11122	11111	11210	11130	01101	11220	01010	12111
<i>Teruelius ankarana</i>	20010	01122	01101	11221	10230	01101	11321	01010	12001
<i>Teruelius annulatus</i>	02001	11???	11101	?121?	10231	111??	1?11?	???0	2200?
<i>Teruelius bemaraha</i>	11001	0????	11101	11211	101??	?1101	1?211	0??10	221??
<i>Teruelius bicolor</i>	100??	?????	??10?	??11	101??	?1??1	?32?	0??10	0?????
<i>Teruelius bistriatus</i>	02011	11???	11111	11210	11131	11101	01321	01011	1201?
<i>Teruelius eliseanneae</i>	12010	1????	11111	?1110	11131	01?01	?22?	01?00	12?1?
<i>Teruelius feti</i>	0201?	?1???	11111	?1110	11131	11101	?1???	010?0	12??1
<i>Teruelius flavopiceus</i>	21000	01122	01101	11210	10131	01001	11321	01010	02001
<i>Teruelius ganzhorni</i>	11011	1????	11101	?1211	11131	11?01	1?21?	0?201	22???
<i>Teruelius grandidieri</i>	20000	01122	01101	11210	10031	11101	11322	01010	02001
<i>Teruelius haekeli</i> sp. n.	02011	11122	11101	11211	10230	01101	11332	01011	12111
<i>Teruelius intertidalis</i>	12011	10122	11101	11211	11131	11101	11221	01111	22111
<i>Teruelius limbatus</i>	12001	11122	11111	11110	11131	11101	11321	01011	12111
<i>Teruelius magalieae</i>	12001	1????	11101	?2210	11131	11101	1?32?	01?10	1211?
<i>Teruelius mahafaliensis</i>	11011	10122	11101	11111	11231	11101	12322	01011	12111
<i>Teruelius makay</i>	12001	1????	1111?	?2110	11130	01?01	1?21?	11?01	02?11
<i>Teruelius mavo</i>	020??	1????	11?0?	11?11	11231	11?01	?21?	01?11	1211?
<i>Teruelius olgae</i>	02001	10122	11101	11110	10231	11101	11332	01002	12111
<i>Teruelius rossii</i>	02011	11???	11101	112?1	112??	?1101	12332	01011	121??
<i>Teruelius sabineae</i>	120?0	1????	11111	?2?10	11231	11?01	1?21?	01?01	12?1?
<i>Teruelius waeberti</i>	020?1	0????	1111?	11210	111??	?1101	1?322	0?200	121??
<i>Charmus laneus</i>	00001	00001	11101	00000	11200	00100	00002	01000	22011
<i>Karasbergia methueni</i>	02001	01111	00000	11310	11200	00121	02122	01010	22101
<i>Lychas mucronatus</i>	11100	00000	01101	00000	10100	00000	12220	10010	10010
<i>Microcharmus variegatus</i>	02100	00001	11000	10000	00200	00100	11002	01000	22111
<i>Neogrosphus griveaudi</i>	01001	11122	11100	10221	11220	01101	01002	01100	22101
<i>Parabuthus abyssinicus</i>	22011	11101	01001	11201	11000	01000	01212	00102	02011
<i>Pseudolychas ochraceus</i>	00101	00?1?	00000	00120	10020	00000	01211	01010	20100
<i>Pseudolychas pegleri</i>	00110	00110	00000	00010	10020	00000	01211	00010	20100
<i>Somalicharmus whitmanae</i>	01001	01111	00000	11000	11000	00110	02212	00010	00001
<i>Tityobuthus monodi</i>	02100	01001	00010	10100	002??	?0001	1?102	?00?0	200?1
<i>Uroplectes planimanus</i>	12011	01121	00001	11211	10231	01000	12222	01011	22111

Table 2. Discrete character matrix used in phylogenetic analysis of *Teruelius*. The ingroup included 14 species of *Grosphus* and 22 species of *Teruelius* (upper two panels). Individually tested outgroup taxa (lower panel) included 10 species of the ‘*Charmus/ Uroplectes*’, and 1 species of the ‘*Ananteris/ Isometrus*’ groups of family Buthidae (Fet et al. 2005; Štundlová et al., 2022). Numbered characters and states as defined in Tab. 1. Unscored characters states indicated by ‘?’.

	Continous
0	Carapace length, mean: ♂
1	Carapace length, mean: ♀
2	Carapace, anterior margin, mean concavity angle (°)
3	Carapace, preocular L/Carapace L, mean
4	Leg III, tibial spur L/ tibia distal D
5	Leg IV, tibial spur L/ tibia distal D
6	Mesosoma, sternite IV, spiracles, shape: PC1
7	Metasoma I, L/W mean: ♂
8	Metasoma I, L/W mean: ♀
9	Pectine tooth count (PTC): ♂ (coded as deviation from buthid family regression line vs. carapace L)
10	Pectine tooth count (PTC): ♀ (coded as deviation from buthid family regression line vs. carapace L)
11	Pectine tooth L/W mean: ♂
12	Pectine tooth L/W mean: ♀
13	Pedipalp chela fixed finger, trichobothria position, db vs. est, mean ratio
14	Pedipalp manus Eb trichobothria R ₁₂₃ = d(Eb ₂ , Eb ₃) / d(Eb ₁ , Eb ₂), mean value
15	Telson lateral profile, ♂: elliptic Fourier analysis, mean PC1* rotated
16	Telson lateral profile, ♀: elliptic Fourier analysis, mean PC2* rotated
	Discrete
17	Carapace and tergites base color: dark, black to brown (0); brown to orange (1); orange to yellow (2)
18	Carapace color pattern: uniform (0); maculate or variegated fuscosity (1)
19	Carapace, denticulate medial epistomal process: small or absent (0); well developed in either sex (1)
20	Carapace, superciliary carinae, male: strongly or moderately granulate (0); weakly granulate or smooth (1)
21	Hemispermatophore capsule distal carina: long (0); short (1)
22	Hemispermatophore posterior lobe: absent (0); elongate, tapered (1); short, blunt or triangulate (2)
23	Hemispermatophore distal carina, number of lateral carinae: none (0); one (1); two or more (2)
24	Legs I–IV, telotarsi, ventral setation: sparse, discrete, < 25 setae in rows (0); dense, brush-like, > 25 irregular setae (1)
25	Mesosoma, tergites I–VI, one or more dark longitudinal stripes: absent (0); present (1)
26	Mesosoma, sternite VII submedian carinae: granulate (0); smooth or obsolete (1)
27	Mesosoma, sternite VII, medial texture and reflectance: matte, low reflectance (0); glossy, high reflectance (1)
28	Metasoma I ventrosubmedian carinae: granulate (0); carinate granulate (1); smooth (2), absent (3)
29	Metasoma III ventral intercarinal surface: granulate (0); very weakly granulate to smooth (1)
30	Metasoma III, dorsosubmedian carinae, posterior subterminal dentate granule, either sex: present (0); absent (1)
31	Metasoma III, dorsosubmedian carinae, posterior terminal large dentate or spiniform granule, either sex, present (0); absent (1)
32	Metasoma V, dorsolateral carinae, granulation: strong (0); weak (1); smooth or obsolete (2)
33	Pectine basal tooth (bpt), ♀ shape: unmodified (0); triangular (1); ovoid or subrectangular (2); elongated, curved (3)
34	Pectine basal tooth (bpt), ♀: shorter than or equal to basal comb width (0); longer than basal comb width (1)
35	Pectine basal tooth (bpt), ♀: without long, narrow extension (0); with long narrow extension (1)
36	Pedipalp femur ‘trichobothrium’ d ₂ position: dorsal (0); internal (1); absent (2)
37	Pedipalp femur trichobothrium e ₁ position vs. d ₅ : proximal (0), level or distal (1)
38	Pedipalp femur, dorsal surface: strongly to moderately granulate (0); weakly granulate to smooth (1)
39	Pedipalp patella, dorsomedian surface, setation: dense, > 20 macrosetae (0); sparse, < 20 macrosetae (1); absent (2)
40	Pedipalp patella, dorsointernal carina development: absent (0); weak (1); moderate (2); strong (3)
41	Pedipalp patella, dorsointernal carina granulation: sparse to absent (0); moderate (1); dense (2); costate-granulate (3)
42	Pedipalp chela fingers, male, proximal undulation: strong (0); moderate (1); weak or absent (2)
43	Pedipalp chela manus, internal surface, setation: sparse to absent (0); moderate to dense (1)
44	Pedipalp chela manus, internal surface, male or female: smooth or sparsely, weakly granulate (0); granulate (1)
45*	Telson aculeus, length: shorter than vesicle (0); equal to vesicle (1); longer than vesicle (2)
46	Telson vesicle ventral surface: strongly to moderately granulate (0); weakly granulate (1); smooth (2)
47	Telson, subaculear tubercle: strong to moderate (0); weak to vestigial (1); absent (2)
48	UV fluorescence: weak (0); strong (1)

Table 3. Continuous and discrete characters and character states used in phylogenetic analysis of *Teruelius*. Of 49 characters, 32 were discrete (31 unordered, 1 ordered*), and 17 continuous. All characters were assigned weights of 2 except characters 0–1, 4–5, 7–12 which were assigned weights of 1.

Taxon	Character						
	0	1	2	3	4	5	6
<i>Grosphus ambre</i>	6.3	?	9.85	0.394	0.482	0.475	-0.12
<i>Grosphus angulatus</i> sp. n.	?	5.299-5.925	7.025-12.515	0.363-0.377	0.503-0.625	0.614-0.684	-5.343- -3.834
<i>Grosphus darainensis</i>	6.4	?	5.12	0.392	?	?	?
<i>Grosphus goudoti</i>	7.2	?	9.21	0.391	0.52	0.567	-1.617
<i>Grosphus halleuxi</i>	6.1	?	4.33	0.39	?	?	?
<i>Grosphus hirtus</i>	4.039-5.653	3.974-5.436	5.6-10.413	0.361-0.38	0.434-0.588	0.514-0.679	-4.143- -2.231
<i>Grosphus madagascariensis</i>	5.795-6.555	6.056-6.691	8.943-12.912	0.369-0.394	0.432-0.548	0.435-0.61	-2.812- -2.107
<i>Grosphus mandena</i>	6.5	6.6	10.554-12.846	0.359-0.388	0.376	0.458	-2.714- -1.983
<i>Grosphus mayottensis</i>	?	7.8	10.46	0.363	?	?	?
<i>Grosphus polskyi</i>	3.9	?	8.75	0.352	?	?	?
<i>Grosphus rakotoariveloi</i>	7.6	?	8.68	0.371	?	?	?
<i>Grosphus simoni</i>	6.308-7.012	4.996-7.004	6.543-12.782	0.366-0.39	0.361-0.498	0.452-0.57	-3.326- -1.344
<i>Grosphus tavatatra</i>	5.8	?	5.05	0.376	0.479	0.563	-0.716
<i>Grosphus voahangyae</i>	4.388-5.152	4.442-4.838	6.543-12.782	0.36-0.38	0.516-0.651	0.528-0.753	-6.208- -4.458
<i>Teruelius ankarafantsika</i>	4.636-5.304	5.255-6.65	3.168-10.435	0.395-0.413	0.799-0.937	0.86-1.089	1.493-2.986
<i>Teruelius ankarana</i>	9.782-11.345	10.615-11.565	7.379-12.327	0.347-0.383	0.597-0.739	0.651-0.791	1.356-3.588
<i>Teruelius annulatus</i>	4.1	4.8	4.139-5.101	0.395-0.4	0.798	0.761	3.426-3.473
<i>Teruelius bemaraha</i>	6.5	?	6.52	0.387	0.98	0.866	2.955
<i>Teruelius bicolor</i>	?	?	?	?	?	?	?
<i>Teruelius bistriatus</i>	3.538-4.289	4.107-5.213	1.797-2.538	0.39-0.413	0.808-0.923	0.966-1.11	2.388-3.336
<i>Teruelius eliseanneae</i>	?	5.2	9.23	0.406	0.873	1.011	2.512
<i>Teruelius feti</i>	?	4.4	?	?	0.878	0.92	1.857
<i>Teruelius flavopiceus</i>	6.99-9.21	8.278-8.707	8.128-13.904	0.367-0.389	0.542-0.74	0.656-0.81	1.834-4.858
<i>Teruelius ganzhorni</i>	?	4.8	7.4	0.418	0.792	0.729	3.461
<i>Teruelius grandidieri</i>	8.348-8.702	8.113-10.757	6.348-14.127	0.354-0.376	0.589-0.788	0.667-0.818	2.353-5.015
<i>Teruelius haekeli</i> sp. n.	3.4	3.63	1.106-8.984	0.38-0.43	0.989	1.132	1.355-3.235
<i>Teruelius intertidalis</i>	4.174-5.376	5.139-6.101	1.498-4.722	0.403-0.418	0.99	1.062	3.923
<i>Teruelius limbatus</i>	4.87-8.76	5.225-6.145	2.926-9.806	0.391-0.416	0.835-1.04	1.054-1.205	1.597-4.146
<i>Teruelius magalieae</i>	4.8	5.66	3.467-7.993	0.388-0.409	0.845	1.094	2.888
<i>Teruelius mahafaliensis</i>	5.743-5.964	6.239-6.941	1.821-6.072	0.415-0.444	0.843-1.168	0.939-1.227	2.041-3.472
<i>Teruelius makay</i>	?	6	2.118-2.202	0.376-0.433	0.823	0.867	?
<i>Teruelius mavo</i>	4.2	5.2	?	0.377-0.45	0.876-1.185	0.944	?
<i>Teruelius olgae</i>	3.648-4.119	3.794-6.566	4.716-11.134	0.373-0.416	0.673-1.126	0.705-1.246	2.474-2.865
<i>Teruelius rossii</i>	4.6	?	1.58	0.404	1.005	1.235	1.463
<i>Teruelius sabineae</i>	?	5.7	8.98	0.409	0.766	0.94	1.447
<i>Teruelius waeberi</i>	3.7	?	2.3	0.393	0.869	0.798	?
<i>Charmus laneus</i>	1.8	2.19	3.498-5.228	0.357-0.384	0.917	1.109	-1.133
<i>Karasbergia methueni</i>	2.168-2.522	2.281-2.684	-4.44-6.173	0.372-0.409	?	0.57	-3.499- -1.145
<i>Lychas mucronatus</i>	5.85	5.692-6.906	8.65-10.56	0.326-0.341	0.49-0.786	0.607-0.789	-0.428-1.685
<i>Microcharrmus variegatus</i>	1.539-1.681	2.101-2.369	7.356-12.844	0.317-0.322	0.852	0.936	0.97
<i>Neogrosphus griveaudi</i>	3.321-5.925	4.423-5.33	1.256-7.594	0.411-0.425	0.791-1.002	1.062-1.185	-0.686-2.343
<i>Parabuthus abyssinicus</i>	8.65-10.7	12.5	-3.054-4.964	0.451-0.458	0.639-0.656	0.769-0.796	2.519-7.362
<i>Pseudolychas ochraceus</i>	3.507-3.733	3.74-3.81	2.681-6.854	0.292-0.316	0.324	0.495	-2.706-0.674
<i>Pseudolychas pegleri</i>	2.9	3.2	15.526-16.304	0.313-0.322	0.493	0.469	-5.718
<i>Somalicharrmus whitmanae</i>	2.8	2.45	2.557-9.736	0.319-0.327	0.426	0.614	-1.512
<i>Tityobuthus monodi</i>	1.9	?	14.53	0.296	?	?	-2.894-0.79
<i>Uroplectes planimanus</i>	4.07-5.57	5.876-6.724	4.995-11.245	0.347-0.349	0.618-0.652	0.529	-0.891-0.489

Table 4. Continuous and discrete character matrix used in phylogenetic analysis of *Teruelius*. Continuous characters 1–6. Lower and upper limits are mean ± SD. Numbered characters and states as defined in Tab. 3. Unscored character states indicated by '?'. Ingroups and outgroups as described under Table 2.

Taxon	Character						
	7	8	9	10	11	12	13
<i>Grosphus ambre</i>	1.313	?	17	?	2.59	?	0.95
<i>Grosphus angulatus</i> sp. n.	?	0.942	?	14-16	?	2.214-2.423	0.985-1.072
<i>Grosphus darainensis</i>	1.083	?	17-18	?	2.33	?	?
<i>Grosphus goudotii</i>	1.268	1.103	19-22	?	3.39	2.06	0.843
<i>Grosphus halleuxi</i>	1.088	?	16-19	?	2.68	?	0.864
<i>Grosphus hirtus</i>	0.878-1.029	0.828-0.86	17-19	14-16	2.995-3.345	1.95-2.642	0.929-1.087
<i>Grosphus madagascariensis</i>	1.128-1.129	0.984-1.129	15-20	12-17	2.681-2.879	2.312-2.514	0.824-0.918
<i>Grosphus mandena</i>	1.139	1.171	18-20	14-17	3.21	2.53	0.828
<i>Grosphus mayottensis</i>	?	1.17	?	17-18	?	1.93	0.943
<i>Grosphus polskyi</i>	1	?	18-19	?	?	?	0.963
<i>Grosphus rakotoariveloi</i>	1.316	?	18-19	?	2.34	?	0.88
<i>Grosphus simoni</i>	1.151-1.353	1.002-1.063	15-17	14-15	2.686-3.228	2.11-2.52	0.89
<i>Grosphus tavatatra</i>	1.094	?	22-23	?	3.33	?	0.867
<i>Grosphus voahangyae</i>	0.925-0.952	0.864-0.884	15-19	14-16	3.2	1.711-2.659	0.97-1.052
<i>Teruelius ankarafantsika</i>	1.18-1.34	1.126-1.168	27-31	24-27	4.014-4.599	2.938-3.232	1.087-1.26
<i>Teruelius ankarana</i>	1.741-1.964	1.276-1.47	36-41	31-35	3.404-4.496	3.025-3.527	0.937-1.076
<i>Teruelius annulatus</i>	1.24	1.097	32-34	24-29	4.62	2.81	?
<i>Teruelius bemaraha</i>	1.417	?	29-30	?	3.79	?	1.058
<i>Teruelius bicolor</i>	1.235	?	?	?	?	?	0.963
<i>Teruelius bistriatus</i>	1.037-1.087	1.037-1.072	27-32	24-27	4.117-4.273	2.829-3.606	1.154-1.41
<i>Teruelius eliseanneae</i>	?	1	?	24	?	3.06	1.165
<i>Teruelius feti</i>	1.055	?	30	25	4.29	3.38	1.073
<i>Teruelius flavopiceus</i>	1.316-1.319	1.028-1.333	27-32	24-30	3.518-3.602	2.764-3.131	0.995-1.119
<i>Teruelius ganzhorni</i>	?	1.133	?	25-28	?	3.47	1.102
<i>Teruelius grandidieri</i>	1.093-1.426	1.108-1.146	34-40	30-34	3.842-4.238	3.149-3.736	0.952-0.964
<i>Teruelius haeckeli</i> sp. n.	1.208	1.195	37-39	27-28	4.71	3.89	1.003-1.111
<i>Teruelius intertidalis</i>	1.219	1.25	32-34	28-30	4.09	2.962-3.428	1.004-1.032
<i>Teruelius limbatus</i>	1.158-1.2	1.01-1.106	25-32	23-28	4.369-4.511	3.102-3.922	0.964-1.084
<i>Teruelius magalieae</i>	1.242	?	36	27	4.04	3.39	1.151
<i>Teruelius mahafaliensis</i>	1.176-1.245	0.998-1.163	34-40	31-33	3.989-4.985	3.147-4.086	1.028-1.155
<i>Teruelius makay</i>	?	1.05	?	25-28	?	3.272-3.328	0.994
<i>Teruelius mavo</i>	1.185	1.111	40	32-35	?	3.98	1.144
<i>Teruelius olgae</i>	1.201-1.445	1.145-1.208	28-33	23-28	4.597-5.049	2.997-3.153	1.017-1.31
<i>Teruelius rossii</i>	1.097	?	28	?	4.21	?	1.157
<i>Teruelius sabineae</i>	?	1.108	?	25	?	3.58	1.162
<i>Teruelius waeberi</i>	1.217	?	26-30	?	3.92	?	0.966
<i>Charmus laneus</i>	0.811	0.792	15-17	13	3.95	2.45	1.221
<i>Karasbergia methueni</i>	0.937-1.084	0.866-1.131	13-17	11-13	2.8	2.4	1.061
<i>Lychas mucronatus</i>	1.049	0.955	22-23	20-23	3.58	2.98	0.674-0.758
<i>Microcharmus variegatus</i>	0.968	0.768	12	11	3.481-3.609	2.39	1.091
<i>Neogrospus griveaudi</i>	1.429-1.525	1.123-1.432	29-31	27-29	4.85	3.713-4.237	1.377
<i>Parabuthus abyssinicus</i>	0.945	0.966	41-47	37-39	5.23	3.41	1.108-1.296
<i>Pseudolychas ochraceus</i>	1.537-1.709	1.374-1.382	15-17	10-14	2.8-2.87	2.392-2.448	1.037
<i>Pseudolychas pegleri</i>	1.138-1.313	1.052-1.301	12-14	11-13	2.72	2.49	1
<i>Somalicharmus whitmanae</i>	0.75	0.778	11-14	11-12	2.96	2.19	1.042-1.435
<i>Tityobuthus monodi</i>	0.917	?	16	?	4.41	?	?
<i>Uroplectes planimanus</i>	1.543	1.274	24-28	22-26	3.07	2.96	1.03-1.041

Table 5. Continuous and discrete character matrix used in phylogenetic analysis of *Teruelius*. Continuous characters 7–13. Lower and upper limits are mean ± SD. Numbered characters and states as defined in Tab. 3. Unscored character states indicated by ‘?’’. Ingroups and outgroups as described under Table 2.

Taxon	Character									
	14	15	16	17–21	22–26	27–31	32–36	37–41	42–46	47–48
<i>Grosphus ambre</i>	?	-1.885	?	11000	00???	00000	0?010	100??	00011	00211
<i>Grosphus angulatus</i> sp. n.	0.451–0.564	?	-7.762– -4.725	10000	0????	00000	00000	00020	0?10	1000?
<i>Grosphus darainensis</i>	?	1.072	?	11001	0????	??20?	??10	100??	2001?	??10?
<i>Grosphus goudotii</i>	0.818	2.313	?	10000	00111	00000	00010	10020	00011	0?100
<i>Grosphus halleuxi</i>	?	-5.126	?	10001	0????	??000	0?010	000??	200?1	0?201
<i>Grosphus hirtus</i>	0.468–0.797	4.327–5.801	-11.937– -1.322	00101	00111	00000	00000	00020	00011	00100
<i>Grosphus madagascariensis</i>	0.677–0.923	0.233–4.408	-4.825	10000	00011	00000	00010	00020	00011	00101
<i>Grosphus mandena</i>	0.695	0.91	-4.219	10000	00011	00000	00010	00020	00011	00101
<i>Grosphus mayottensis</i>	?	?	-2.541	20000	0????	??20?	??10	10110	0?11	??11?
<i>Grosphus polskyi</i>	?	1.229	?	01100	0????	??200	??200	110??	?0?11	0?101
<i>Grosphus rakotoariveloi</i>	?	1.31	?	11000	0????	??20?	??10	000??	20011	??201
<i>Grosphus simoni</i>	0.681–0.999	-2.158–4.268	-2.263–0.27	10000	00011	00000	00010	00020	00011	00110
<i>Grosphus tavatatra</i>	?	3.759	?	10101	0????	00000	0?110	000??	20011	?0311
<i>Grosphus voahangyae</i>	0.477–0.618	3.027–5.477	-10.1– -5.817	00100	00110	00000	00000	00020	00011	10001
<i>Teruelius ankarafantsika</i>	0.34–0.433	-5.2– -3.155	0.628–2.386	12011	11122	11111	11210	11130	01101	11220
<i>Teruelius ankarana</i>	0.279–0.345	-0.98–3.627	-0.519– -0.379	20010	01122	01101	11221	10230	01101	11321
<i>Teruelius annulatus</i>	?	1.159–3.898	-5.842– -4.358	02001	11???	11101	?121?	10231	111??	1?11?
<i>Teruelius bemaraha</i>	?	-2.325	?	11001	0????	11101	11211	101??	?1101	1?211
<i>Teruelius bicolor</i>	?	?	?	100??	?????	??10?	??11	101??	?1??1	??32?
<i>Teruelius bistriatus</i>	0.273–0.323	-6.824– -5.19	1.863–2.556	02011	11???	11111	11210	11131	11101	01321
<i>Teruelius eliseanneae</i>	?	?	2.319	12010	1????	11111	?1110	11131	01?01	??22?
<i>Teruelius feti</i>	0.307	?	?	0201?	?1???	11111	?1110	11131	11101	?1???
<i>Teruelius flavopiceus</i>	0.276–0.339	-0.858–3.406	-4.838–1.603	21000	01122	01101	11210	10131	01001	11321
<i>Teruelius ganzhorni</i>	?	?	?	11011	1????	11101	?1211	11131	11201	1?21?
<i>Teruelius grandidieri</i>	0.281–0.433	4.889	-4.546–3.039	20000	01122	01101	11210	10031	11101	11322
<i>Teruelius haeckeli</i> sp. n.	0.288–0.394	-6.262	1.577	02011	11122	11101	11211	10230	01101	11332
<i>Teruelius intertidalis</i>	0.313–0.357	-7.783– -7.432	1.392–2.024	12011	10122	11101	11211	11131	11101	11221
<i>Teruelius limbatus</i>	0.3–0.436	-3.887–0.548	1.485–2.513	12001	11122	11111	11110	11131	11101	11321
<i>Teruelius magalieae</i>	?	-2.99	2.156	12001	1????	11101	?2210	11131	11101	1?32?
<i>Teruelius mahafaliensis</i>	0.291–0.457	-5.283– -0.918	2.496–3.145	11011	10122	11101	11111	11231	11101	12322
<i>Teruelius makay</i>	0.311–0.368	?	2.75	12001	1????	1111?	?2110	11130	01?01	1?21?
<i>Teruelius mavo</i>	?	-7.253	1.933	020??	1????	11?0?	11?11	11231	11?01	?11?
<i>Teruelius olgae</i>	0.371–0.399	-5.17– -1.66	2.294–2.542	02001	10122	11101	11110	10231	11101	11332
<i>Teruelius rossii</i>	0.332	-4.723	?	02011	11???	11101	112?1	112??	?1101	12332
<i>Teruelius sabineae</i>	?	?	2.758	120?0	1????	11111	?2110	11231	11?01	1?21?
<i>Teruelius waeberi</i>	?	-4.586	?	020?1	0????	1111?	11210	111??	?1101	1?322
<i>Charmus laneus</i>	0.437	2.696	1.592	00001	00001	11101	00000	11200	00100	00002
<i>Karasbergia methueni</i>	0.438	-6.554	0.66	02001	01111	00000	11310	11200	00121	02122
<i>Lychas mucronatus</i>	0.969–1.095	6.738–8.633	7.689–8.216	11100	00000	01101	00000	10100	00000	12220
<i>Microcharmor variegatus</i>	0.409	-7.241	1.161	02100	00001	11000	10000	00200	00100	11002
<i>Neogrospus griveaudi</i>	0.544–0.546	-7.009	0.26	01001	11122	11100	10221	11220	01101	01002
<i>Parabuthus abyssinicus</i>	0.435–0.51	3.809	0.702	22011	11101	01001	11201	11000	01000	01212
<i>Pseudolychas ochraceus</i>	0.456–0.484	-3.298	-9.461	00101	00?1?	00000	00120	10020	00000	01211
<i>Pseudolychas pegleri</i>	0.393–0.43	-1.376	-4.476	00110	00110	00000	00010	10020	00000	01211
<i>Somalicharmor whitmaniae</i>	0.895–1.15	2.852	-8.5	01001	01111	00000	11000	11000	00110	02212
<i>Tityobuthus monodi</i>	?	3.365	?	02100	01001	00010	10100	002??	?0001	1?102
<i>Uroplectes planimanus</i>	0.245–0.27	-7.789	3.014	12011	01121	00001	11211	10231	01000	12222

Table 6. Continuous and discrete character matrix used in phylogenetic analysis of *Teruelius*. Continuous characters 14–16, discrete characters 17–48. Lower and upper limits of continuous characters are mean ± SD. Numbered characters and states as defined in Table 3. Unscored character states indicated by "?". Ingroups and outgroups as described under Table 2.

	N _{MPT}	Steps/length	CI	RI	SR1	SR2	RBS1	RBS2	SR2 ₇₀
<i>Charmus laneus</i>									
PW	3	335	0.382	0.844	54	78	18	22	55
IW <i>k</i> = 3	1	351	0.365	0.832	45	64	25	25	23
IW <i>k</i> = 6	1	341	0.375	0.839	44	68	18	27	35
IW <i>k</i> = 10	1	341	0.375	0.839	46	72	12	21	41
IW <i>k</i> = 30	1	335	0.382	0.844	53	76	8	25	48
PW*	1	2436.066	0.580	0.873	75	60	19	31	31
IW* <i>k</i> = 3	1	2913.135	0.485	0.813	69	82	30	27	63
IW* <i>k</i> = 6	1	2862.639	0.493	0.820	73	87	37	37	75
IW* <i>k</i> = 10	1	2783.766	0.507	0.830	78	90	34	34	79
IW* <i>k</i> = 30	1	2646.278	0.534	0.847	82	85	23	29	61
<i>Karasbergia methueni</i>									
PW	36	330	0.382	0.844	60	65	10	40	51
IW <i>k</i> = 3	2	342	0.368	0.835	8	68	—	30	63
IW <i>k</i> = 6	18	338	0.373	0.838	15	70	—	20	65
IW <i>k</i> = 10	1	334	0.377	0.841	26	74	—	32	70
IW <i>k</i> = 30	1	330	0.382	0.844	49	71	3	24	59
PW*	3	2372.603	0.594	0.880	—	75	—	26	72
IW* <i>k</i> = 3	1	2805.104	0.503	0.826	70	88	23	37	74
IW* <i>k</i> = 6	1	2701.391	0.522	0.839	78	91	34	51	78
IW* <i>k</i> = 10	1	2701.391	0.522	0.839	81	90	35	40	81
IW* <i>k</i> = 30	1	2466.834	0.572	0.868	69	85	24	38	71
<i>Lychas mucronatus</i>									
PW	31256	338	0.379	0.842	62	81	33	50	69
IW <i>k</i> = 3	6	348	0.368	0.834	24	75	14	46	67
IW <i>k</i> = 6	6	348	0.368	0.834	27	77	6	51	69
IW <i>k</i> = 10	1	338	0.379	0.842	36	81	13	28	71
IW <i>k</i> = 30	1	338	0.379	0.842	53	83	13	19	71
PW*	1	2450.936	0.576	0.871	—	63	10	26	67
IW* <i>k</i> = 3	1	2982.127	0.473	0.805	35	81	33	31	36
IW* <i>k</i> = 6	1	2847.498	0.496	0.822	29	88	14	34	39
IW* <i>k</i> = 10	1	2810.615	0.502	0.826	24	92	5	28	48
IW* <i>k</i> = 30	1	2575.106	0.548	0.855	—	86	5	29	76
<i>Microcharmus variegatus</i>									
PW	10367	339	0.378	0.841	50	76	33	40	82
IW <i>k</i> = 3	3	347	0.369	0.835	41	63	27	27	63
IW <i>k</i> = 6	18	345	0.371	0.836	42	67	19	43	71
IW <i>k</i> = 10	9	341	0.375	0.839	44	72	15	27	77
IW <i>k</i> = 30	7	339	0.378	0.841	51	75	19	41	83
PW*	1	2471.522	0.571	0.868	22	46	56	56	31
IW* <i>k</i> = 3	1	2903.566	0.486	0.815	66	78	42	42	71
IW* <i>k</i> = 6	1	2841.555	0.497	0.822	73	86	40	40	82
IW* <i>k</i> = 10	1	2817.818	0.501	0.825	80	91	37	37	85
IW* <i>k</i> = 30	1	2652.099	0.532	0.846	40	86	9	32	73
<i>Neogrospus griveaudi</i>									
PW	473	329	0.383	0.845	84	12	50	4	—
IW <i>k</i> = 3	12	335	0.376	0.840	69	13	29	10	—
IW <i>k</i> = 6	1	333	0.378	0.842	73	14	23	3	—
IW <i>k</i> = 10	3	332	0.380	0.843	78	13	18	—	—
IW <i>k</i> = 30	1	329	0.383	0.845	84	7	22	4	—
PW*	2	2338.780	0.603	0.884	74	—	28	—	—
IW* <i>k</i> = 3	1	2885.494	0.489	0.816	72	57	46	31	26
IW* <i>k</i> = 6	1	2884.032	0.489	0.816	79	62	30	25	35
IW* <i>k</i> = 10	1	2672.624	0.527	0.843	86	55	29	26	36
IW* <i>k</i> = 30	1	2499.105	0.564	0.864	91	—	20	—	—
<i>Parabuthus abyssinicus</i>									
PW	250	339	0.378	0.841	79	31	60	22	11
IW <i>k</i> = 3	20	346	0.370	0.835	85	59	56	60	44
IW <i>k</i> = 6	20	346	0.370	0.835	84	55	45	50	42
IW <i>k</i> = 10	20	344	0.372	0.837	80	51	23	28	36
IW <i>k</i> = 30	3	342	0.374	0.838	80	37	43	22	22
PW*	1	2431.540	0.581	0.873	80	—	17	—	48
IW* <i>k</i> = 3	1	2949.587	0.479	0.809	71	55	37	37	21
IW* <i>k</i> = 6	1	3006.610	0.470	0.802	80	50	35	35	16
IW* <i>k</i> = 10	1	2873.463	0.491	0.818	88	35	26	22	—
IW* <i>k</i> = 30	1	2549.845	0.554	0.859	93	—	34	—	—

Table 7. Statistics of most parsimonious trees (MPTs) retrieved by cladistic analysis of the discrete character matrix of Table 2, and the continuous and discrete character matrix* of Tables 4–6, rooted by six different outgroup taxa. For outgroup taxa *K. methueni* and *N. griveaudi*, character 29 (discrete) or 37 (discrete + continuous) was phylogenetically uninformative and excluded from the analyses. PW, prior weights; IW implied weights, with concavity constant *k*; N_{MPT}: number of MPTs; Steps/length: tree lengths; CI: tree consistency index; RI: tree retention index; SR1, RBS1: jackknife with symmetric resampling and relative Bremer support for *Grospus* as a monophyletic group; SR2, RBS2: jackknife with symmetric resampling and relative Bremer support for *Teruelius* as a monophyletic group; SR2₇₀: jackknife with symmetric resampling support for *Teruelius* analyzing only characters with ≥ 70% taxa scored. Gray cells indicate symmetric resampling support ≥ 50%.

	N _{MPT}	Steps/length	CI	RI	SR1	SR2	RBS1	RBS2	SR2 ⁷⁰
<i>Pseudolychas ochraceus</i>									
PW	614	325	0.394	0.851	20	85	17	50	86
IW k = 3	9	340	0.376	0.840	6	78	15	64	75
IW k = 6	15	336	0.381	0.843	1	79	2	32	80
IW k = 10	1	328	0.390	0.849	3	81	9	22	84
IW k = 30	5	326	0.393	0.851	13	85	15	24	87
PW*	3	2440.311	0.579	0.872	—	79	—	38	74
IW* k = 3	1	2961.452	0.477	0.807	25	80	12	37	74
IW* k = 6	1	2854.008	0.495	0.821	28	88	—	24	82
IW* k = 10	1	2712.919	0.520	0.838	19	92	14	26	89
IW* k = 30	1	2628.587	0.537	0.849	—	93	—	40	89
<i>Pseudolychas pegleri</i>									
PW	10276	326	0.393	0.851	11	87	11	50	88
IW k = 3	9	338	0.379	0.842	—	79	14	37	73
IW k = 6	15	334	0.383	0.845	—	82	1	19	79
IW k = 10	20	328	0.390	0.849	—	86	5	23	84
IW k = 30	1	326	0.393	0.851	6	88	14	23	88
PW*	3	2419.511	0.584	0.875	—	77	—	24	77
IW* k = 3	1	2929.151	0.482	0.811	21	80	—	32	71
IW* k = 6	1	2852.434	0.495	0.821	17	89	—	39	82
IW* k = 10	1	2759.990	0.512	0.832	11	93	6	37	89
IW* k = 30	1	2594.808	0.544	0.853	—	91	—	41	87
<i>Somalicharmus whitmanae</i>									
PW	2782	328	0.390	0.849	11	82	14	14	86
IW k = 3	3	340	0.376	0.840	—	71	—	36	71
IW k = 6	6	336	0.381	0.843	—	76	—	40	77
IW k = 10	2	332	0.386	0.846	—	79	—	33	82
IW k = 30	3	328	0.390	0.849	—	83	8	17	86
PW*	1	2421.014	0.583	0.875	—	79	—	32	79
IW* k = 3	1	3007.117	0.469	0.802	—	85	—	33	78
IW* k = 6	1	2842.031	0.497	0.822	—	89	4	43	85
IW* k = 10	1	2775.794	0.509	0.831	—	92	4	16	91
IW* k = 30	1	2614.322	0.540	0.851	—	89	—	29	86
<i>Tityobuthus monodi</i>									
PW	19152	332	0.380	0.843	—	84	—	—	87
IW k = 3	9	348	0.362	0.830	—	80	9	34	73
IW k = 6	12	336	0.375	0.840	—	83	—	40	81
IW k = 10	2	334	0.377	0.841	—	86	—	23	85
IW k = 30	3	332	0.380	0.843	—	88	—	18	88
PW*	3	2364.407	0.596	0.881	—	71	6	43	68
IW* k = 3	1	2848.414	0.495	0.821	59	75	38	42	72
IW* k = 6	1	2703.211	0.522	0.839	65	85	40	40	78
IW* k = 10	1	2620.543	0.538	0.849	63	89	39	39	82
IW* k = 30	1	2546.491	0.554	0.858	13	90	14	60	82
<i>Uroplectes planimanus</i>									
PW	178	326	0.393	0.851	90	—	75	—	—
IW k = 3	6	344	0.372	0.837	74	23	33	17	26
IW k = 6	1	336	0.381	0.843	80	1	32	4	2
IW k = 10	1	328	0.390	0.849	84	—	23	—	—
IW k = 30	1	326	0.393	0.851	89	—	36	—	—
PW*	1	2412.00	0.585	0.876	64	8	21	—	24
IW* k = 3	1	3077.686	0.459	0.793	81	10	27	—	—
IW* k = 6	1	2928.100	0.482	0.812	86	5	20	—	—
IW* k = 10	1	2739.174	0.515	0.835	90	3	17	—	11
IW* k = 30	1	2523.551	0.559	0.862	85	6	28	—	27

Table 8. Statistics of most parsimonious trees (MPTs) retrieved by cladistic analysis of the discrete character matrix of Table 2, and the continuous and discrete character matrix* of Tables 4–6, rooted by five different outgroup taxa. For outgroup taxon *T. monodi*, character 29 (discrete) or 37 (discrete + continuous) was phylogenetically uninformative and excluded from the analyses. See Table 7 for abbreviations.

	N _{MPT}	Steps/length	CI	RI	SR1	SR2	RBS1	RBS2	SR2 ⁷⁰
11 outgroup taxa (morphological backbone)									
PW	7,939	576	0.222	0.662	58	67	33	50	63
IW k = 3	1	586	0.218	0.654	39	58	18	25	48
IW k = 6	1	580	0.221	0.659	41	65	12	27	56
IW k = 10	1	578	0.221	0.66	45	71	21	28	65
IW k = 30	1	576	0.222	0.662	56	72	20	25	64
PW*	1	4820.225	0.293	0.577	71	55	21	31	28
IW* k = 3	1	5458.837	0.259	0.497	71	79	26	35	62
IW* k = 6	1	5346.218	0.264	0.511	72	79	27	27	62
IW* k = 10	1	5346.218	0.264	0.511	75	81	25	31	62
IW* k = 30	1	4975.517	0.284	0.557	87	87	26	30	65
7 outgroup taxa (molecular backbone)									
PW	37	487	0.263	0.673	57	48	60	60	40
IW k = 3	12	500	0.256	0.662	32	57	14	27	48
IW k = 6	2	492	0.260	0.669	36	61	13	30	54
IW k = 10	2	492	0.260	0.669	42	60	12	26	51
IW k = 30	3	488	0.262	0.672	57	50	15	32	42
PW*	1	3721.928	0.348	0.63	63	64	14	29	50
IW* k = 3	1	4324.791	0.300	0.538	69	74	24	29	54
IW* k = 6	1	4324.791	0.300	0.538	72	75	3	21	54
IW* k = 10	1	4228.486	0.306	0.552	73	78	13	15	57
IW* k = 30	1	3865.822	0.335	0.608	76	82	15	20	57

Table 9. Statistics of most parsimonious trees (MPTs) retrieved by cladistic analysis of the discrete character matrix of Table 2, and the continuous and discrete character matrix* of Tables 4–6, rooted by multiple outgroup taxa under backbone constraints. See Figs. 206–209 for outgroup taxa and backbone constraints, Table 7 for abbreviations.

Phylogenetic analysis

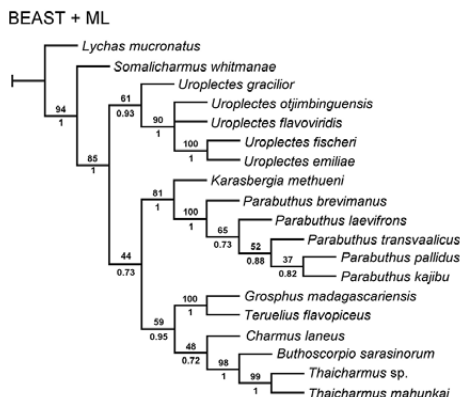
We tested the monophyly of *Teruelius* by phylogenetic analysis with parsimony. Our ingroup of 36 terminals consisted of all currently named species of *Groshus* s. lat. (*Groshus* 14 spp., *Teruelius* 22 spp.) (Table 2). The 45 discrete morphological characters listed above (summarized in Table 1) were scored for as many terminals as possible, based on data available to us (1,315/1,620 states, or 81.2% of the 45 × 36 ingroup data matrix). Of 305 unscored states, 85/305 (27.9%) were sex-specific characters in which the relevant sex was either unknown or undescribed. Characters 10 and 11 describing tibial spur morphometrics on legs III–IV were correlated. To compensate, they were assigned half the weight of other characters (prior weighting scheme). All characters were unordered except for three multistate biometric characters (0, 18 and 39). In our analysis, we made the implicit assumption that the ingroup itself, *Groshus* s. lat., is monophyletic, and asked if it contains two lineages that are sufficiently divergent to warrant classification as separate genera.

The most closely related sister genus of *Groshus* s. lat. has not been determined. We individually tested 11 potential sister taxa as outgroups to root MPTs, polarize characters and compute node supports (Table 2, lower panel). Candidate outgroup genera were mainly selected from the ‘*Charmus/ Uroplectes*’ group of buthids, where *Groshus* s. lat. has been placed by trichobothrial (Fet et al., 2005) and DNA (Štundlová et al., 2022) analyses of buthids. The tree in Fig. 190 shows the relationships of exemplar species representing several genera of the ‘*Charmus/ Uroplectes*’ group, inferred from the results of the latter study. Single exemplars of *Groshus*

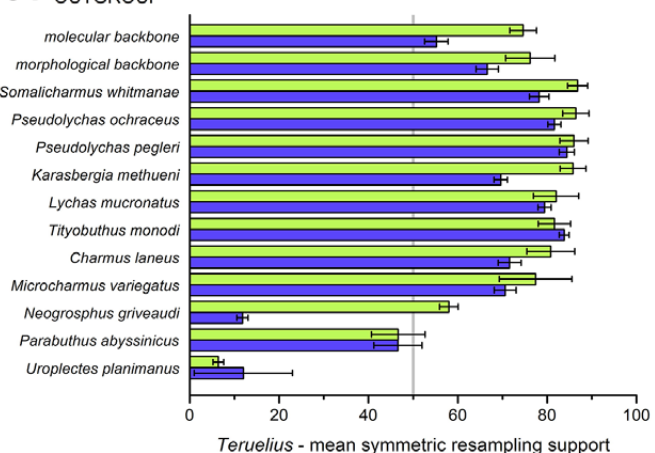
and *Teruelius* were grouped together, and exemplars of other genera of the ‘*Charmus/ Uroplectes*’ group were resolved as sister genera, including *Charmus*, *Karasbergia*, *Parabuthus*, *Uroplectes* and *Somalicharmus*. The latter five genera were included in our outgroup test set, along with *Lychas*, *Pseudolychas*, *Microcharmus*, *Neogroshus* and *Tityobuthus*. *Lychas* was included to represent the ‘*Ananteris/ Isometrus*’ group, which may be the sister clade of the ‘*Charmus/ Uroplectes*’ group (Fet et al., 2005; Štundlová et al., 2022). *Pseudolychas* was sister to a clade including *Groshus madagascariensis* in the analysis of Prendini (2004a: 42, fig. 1), and was the hypothetical outgroup genus in our previous study (Lowe & Kovařík, 2019). Although *Microcharmus* is placed in a separate family (Lourenço et al., 2019), it has been regarded as a buthid (Volschenk et al., 2008), and analyses of trichobothrial (Fet et al., 2005) and other characters (see below) associate it with the ‘*Charmus/ Uroplectes*’ group.

A number of characters in Table 1 were coded by discretization of continuous morphometric characters. Discretization thresholds were set to values that were judged to coincide with step changes in values or slopes of rank ordered mean morphometric values of each species. These judgements may be affected by noise in the data, and may be susceptible to bias as subjective values of choice for separating *Teruelius* from *Groshus* (e.g., Figs. 13–15). Discretization can also exaggerate differences between values close to either side of a threshold, particularly in the absence of a large disjunction in simple gap coding (Almeida & Bisby, 1984). To control for these potential biases, we also analyzed a combination of 32 discrete and 17 non-discretized (continuous) characters (Table 3) (Goloboff et

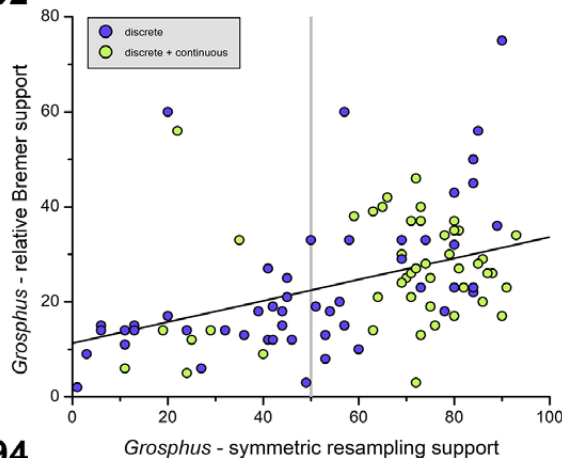
190



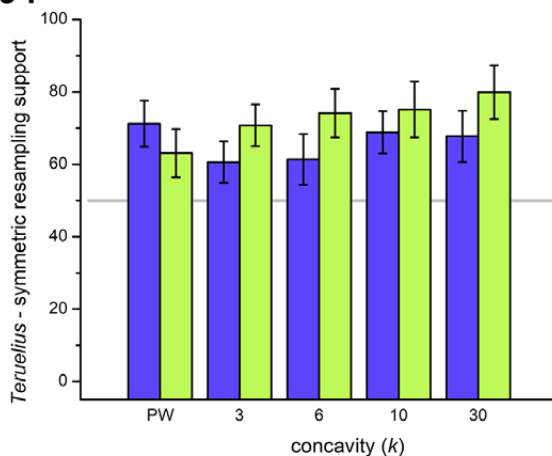
191 OUTGROUP



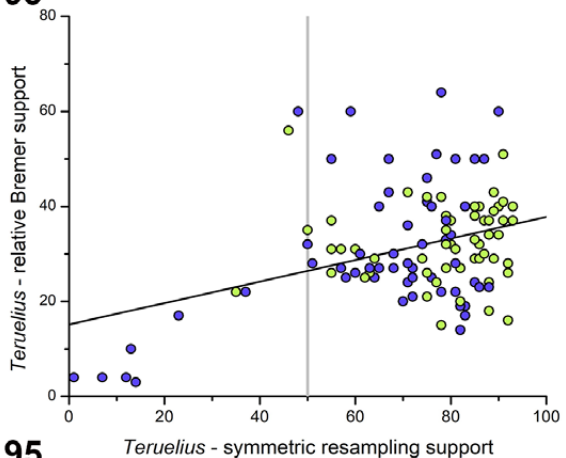
192



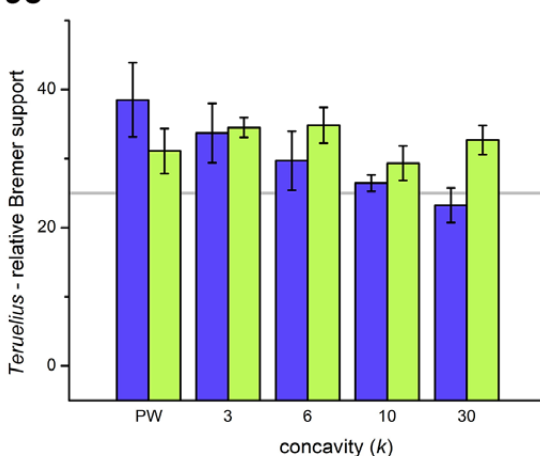
194



193

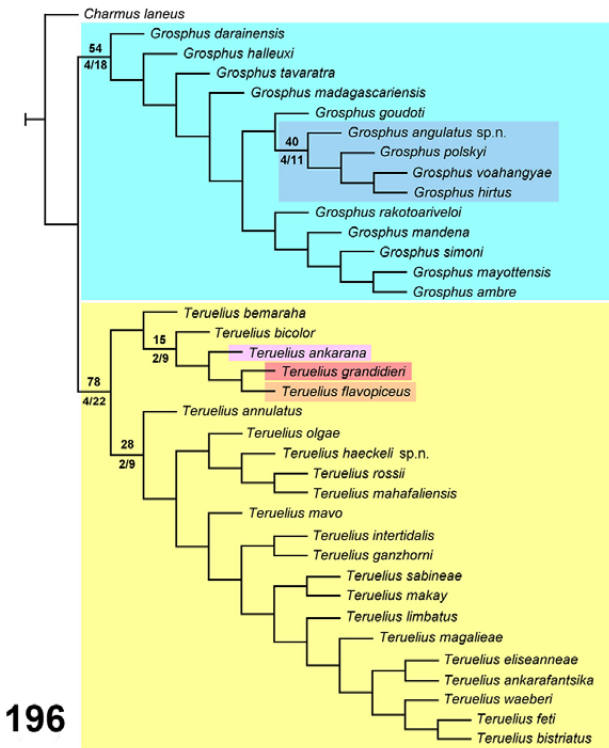
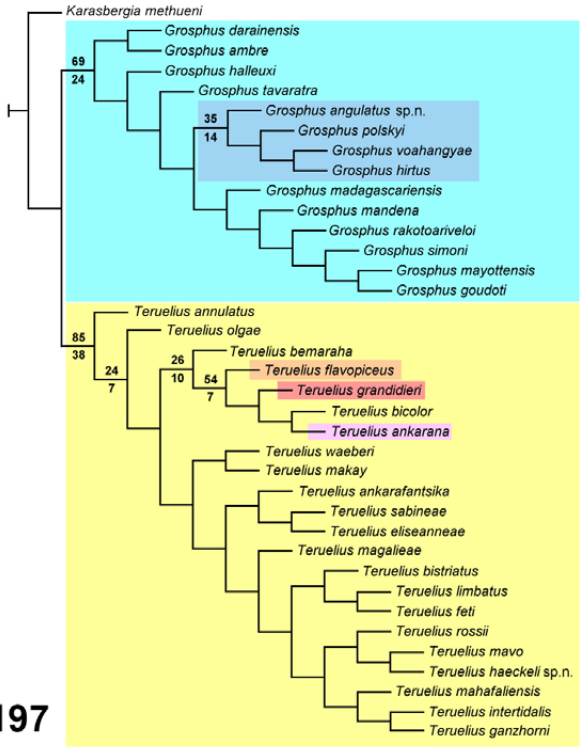
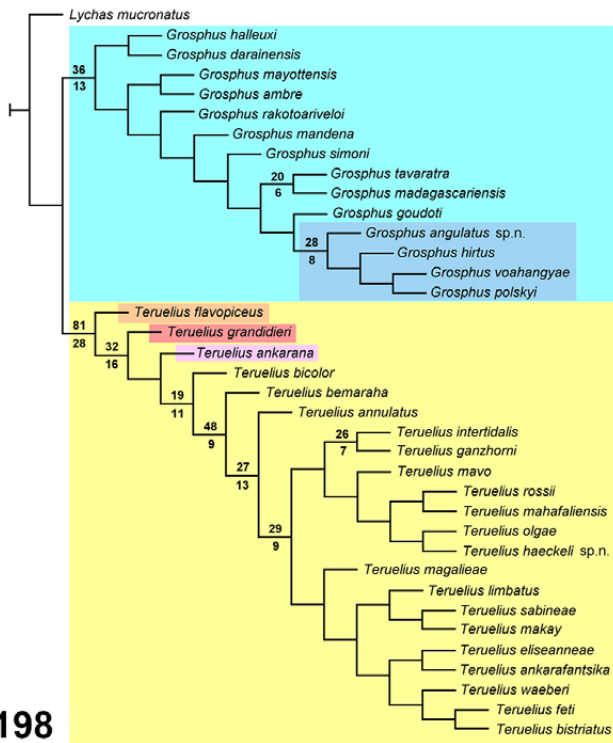
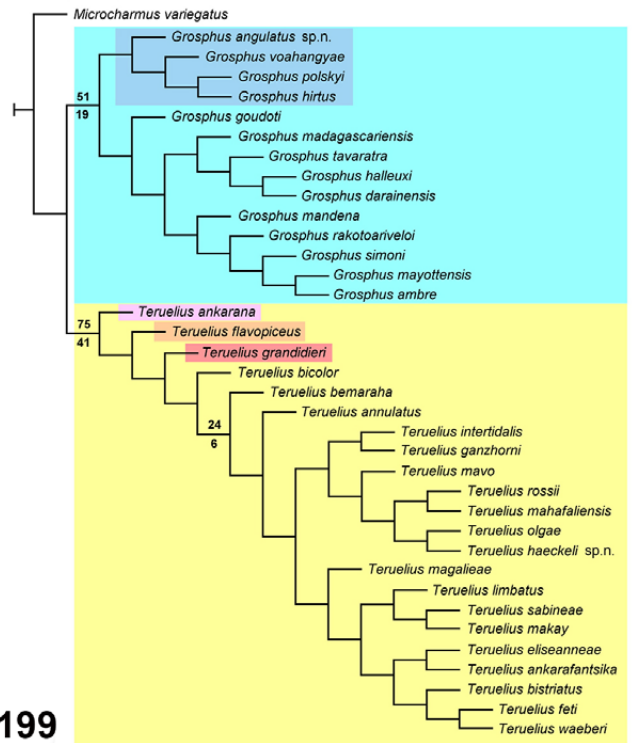


195



Figures 190–195. Phylogenetic analysis of *Teruelius*. **Figure 190.** Relationships of exemplar species of *Grosphus*, *Teruelius* and outgroup genera *Charmus*, *Karasbergia*, *Lychas*, *Parabuthus* and *Uroplectes*. Strict consensus of two trees inferred from buthid molecular phylogenies of Štundlová et al. (2022) reconstructed by Bayesian inference (BEAST) and maximum likelihood (ML) analyses of multilocus DNA sequence data. Supports in original trees are indicated below and above corresponding nodes, respectively. **Figure 191.** Horizontal bar plot showing mean GC supports from jackknife by symmetric resampling for the recovery of *Teruelius* as a monophyletic group, obtained from analyses with 11 different outgroup taxa and two backbone constraints. Means calculated over 5 weighting schemes. Error bars are standard errors. **Figure 192.** Bivariate scatter plot of relative Bremer support vs. symmetric resampling support for the recovery of *Grosphus* as a monophyletic group, with 11 different outgroup taxa, two backbone constraints and 5 weighting schemes. Dark line: least squares linear regression ($R = 0.4367$, $P < 0.0001$). **Figure 193.** Bivariate scatter plot of relative Bremer support vs. symmetric resampling support for recovery of *Teruelius* as a monophyletic group, with the same variables as in Fig. 192. Dark line: least squares linear regression ($R = 0.3678$, $P < 0.0001$). Vertical gray lines: node support thresholds of 50% (191–193). **Figures 194–195.** Mean support from symmetric resampling (194) and relative Bremer support (195) for recovery of *Teruelius* as a monophyletic group under different weighting schemes (PW, IW $k = 3, 6, 10, 30$). Means calculated over 11 outgroup taxa and two backbone constraints. Error bars are standard errors. Horizontal gray lines: node support thresholds of 50% (194) and 25% (195). Symbol and bar colors (191–194): blue, discrete characters; green, continuous + discrete characters.

PW

IW* $k = 30$ IW $k = 10$ IW $k = 30$ 

Figures 196–199. Examples of MPTs retrieved by phylogenetic analyses of *Grophus* and *Teruelius*, rooted by 4 different outgroup taxa: *Charmus laneus* (196), *Karasbergia methueni* (197), *Lycas mucronatus* (198) and *Microcharmus variegatus* (199). Weighting schemes and data matrices indicated above each tree (see Table 7). Numbers above nodes are jackknife by symmetric resampling supports, those below relative Bremer supports. Color coding of groups according to legend in Fig. 16.



Figures 200–203. Examples of MPTs retrieved by phylogenetic analyses of *Grosphus* and *Teruelius*, rooted by 4 different outgroup taxa: *Pseudolytachas ochraceus* (200), *P. pegleri* (201), *Tityobuthus monodi* (202) and *Somalicharmus whitmanae* (203). Weighting schemes and data matrices indicated above each tree (see Table 7). Numbers above nodes are jackknife by symmetric resampling supports, those below relative Bremer supports. Color coding of groups according to legend in Fig. 16.

al., 2006; Parins-Fukuchi, 2018). The latter were coded as numeric ranges of morphometrics for each taxon (Tables 4–6). Measurements of L, W and D, or their ratios, were linearized by logarithmic transforms (Mongiardino Koch et al., 2015). Pectinal tooth counts (PTC) from either sex were coded as positive or negative deviations from sex-specific linear regression fits of log(PTC) vs. log(carapace L) for samples encompassing the entire bathid family ($n = 757 \delta$, $n = 760 \varphi$). This compensated for the scaling of PTC with carapace length ('Soleglad's Law'). Principal components from EFA of male and female telson lateral profiles were coded directly (Smith & Hendricks, 2013). Ranges of continuous characters were mapped by linear transforms onto the interval [0, 65] (Goloboff et al., 2008). In the prior weighting scheme, correlated pairs of characters were assigned half the weight of other characters to offset redundancy. Sensitivity of results to weighting scheme was tested by analyzing data under prior weights, and implied weights with strong, moderate and weak concavities ($k = 3, 6, 10, 30$). In all, 130 cladistic analyses were conducted with single outgroup taxa and multiple outgroups under backbone constraints.

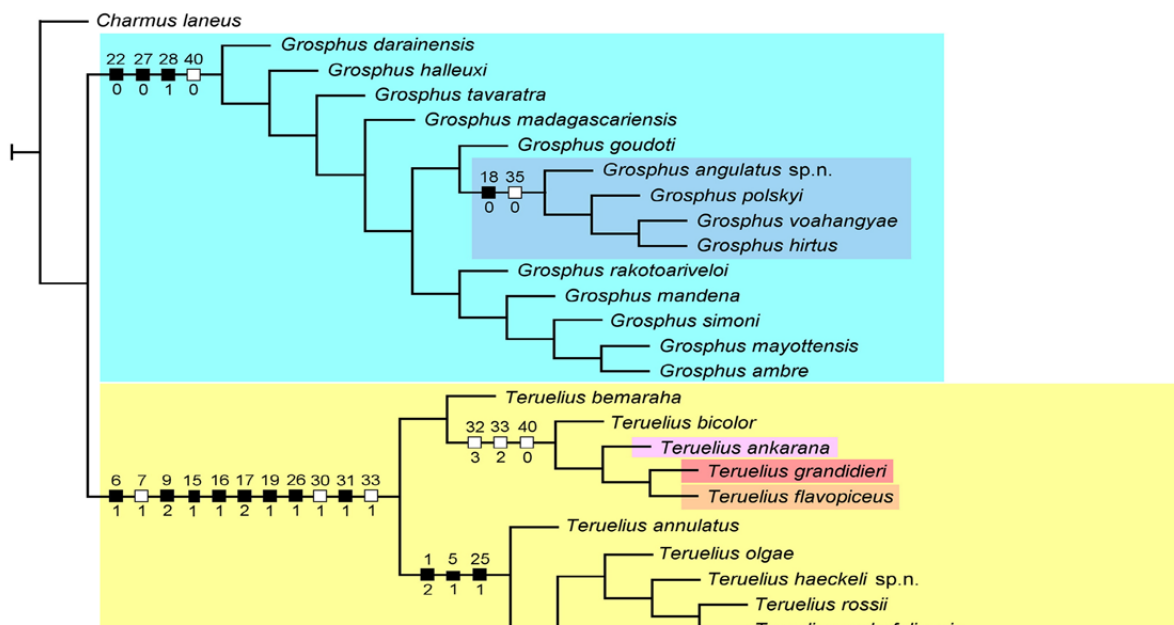
The numbers of MPTs recovered and their statistics are summarized in Tables 7–9. Node supports from jackknife by symmetric resampling (SR) (Goloboff et al., 2003) and relative Bremer support (RBS) for monophyletic groupings of *Grosphus* and *Teruelius* are tabulated. *Teruelius* was retrieved as a monophyletic group with moderate to strong SR support (50–93%) in 79/80 (98.75%) of single outgroup taxon analyses with 8/11 outgroup taxa, including *Lychas mucronatus* (Tab. 7–8). On the other hand, the support was moderate with outgroup *Parabuthus abyssinicus* (31–59%), moderate to weak with *Neogrospus griveaudi* (7–62%), and weak with *Uroplectes planimanus* (1–23%). In some of the MPTs retrieved with these three outgroup taxa, *Teruelius* was paraphyletic. *Grosphus* was retrieved as a monophyletic group with strong SR support (50–93%) in 52/110 (47.3%) of analyses with single outgroups. In particular, support was strong with the 3 outgroup taxa: *P. abyssinicus*, *N. griveaudi* and *U. planimanus*, the opposite of the result for *Teruelius*. Apparently these 3 outgroup taxa share more of the scored characters with *Teruelius* than with *Grosphus*. However, DNA analysis excludes *Parabuthus* and *Uroplectes* from the ingroup (Fig. 190), indicating that many of their morphological similarities to *Teruelius* are due to convergence. Characters shared between *Teruelius* and *Neogrospus* may also be homoplasious, although the possibility that *Neogrospus* belongs to the ingroup is not excluded (but was disputed by Lourenço et al., 2020). *Grosphus* was paraphyletic in 22/110 (20.0%, mainly with *Somalicharmus* and *Tityobuthus* outgroups), and *Teruelius* paraphyletic in 7/110 (6.3%, with *Neogrospus*, *Parabuthus* and *Uroplectes* outgroups) of analyses with single outgroups. *Teruelius* and *Grosphus* were reciprocally monophyletic with mutually strong SR supports (>50%) in 30/110 (27.3%) of these analyses. The highest incidence of strongly supported reciprocal monophyly occurred with outgroup *Charmus*, the closest sister genus in the molecular phylogeny.

To further test the monophyly of *Teruelius*, we conducted analyses including multiple outgroup taxa. Combined analyses with all 11 outgroup taxa invariably yielded MPTs that could not be rooted with a monophyletic ingroup. This was the consequence of our specific choice of characters that were focused on differentiating between ingroup taxa, rather than on resolving relationships of the outgroup taxa. These characters associated *Parabuthus* and *Uroplectes* with *Teruelius*, in conflict with molecular phylogeny. To enforce monophyly of the ingroup, relationships of the outgroup taxa were constrained on the basis of independent analyses of bathids. We imposed two backbone constraints, inferred from either morphological or molecular phylogenetic trees. A morphological backbone of 11 outgroup taxa was based on one of several MPTs retrieved from cladistic analyses of the microcharmid and bathids (see below; Fig. 280). A molecular backbone of 7 outgroup taxa was based on relationships inferred from the DNA phylogeny of Štundlová et al., 2022 (Fig. 190). MPTs were rooted with *Lychas mucronatus* as primary outgroup. In both series of combined analyses, monophyly of *Teruelius* was moderately to strongly supported (Table 9). *Teruelius* and *Grosphus* were reciprocally monophyletic with mutually strong SR supports.

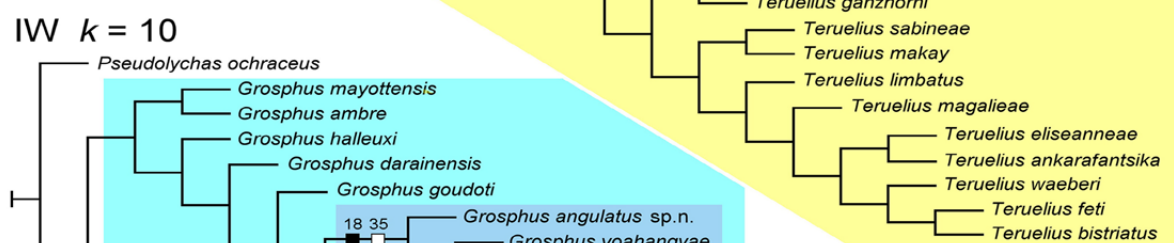
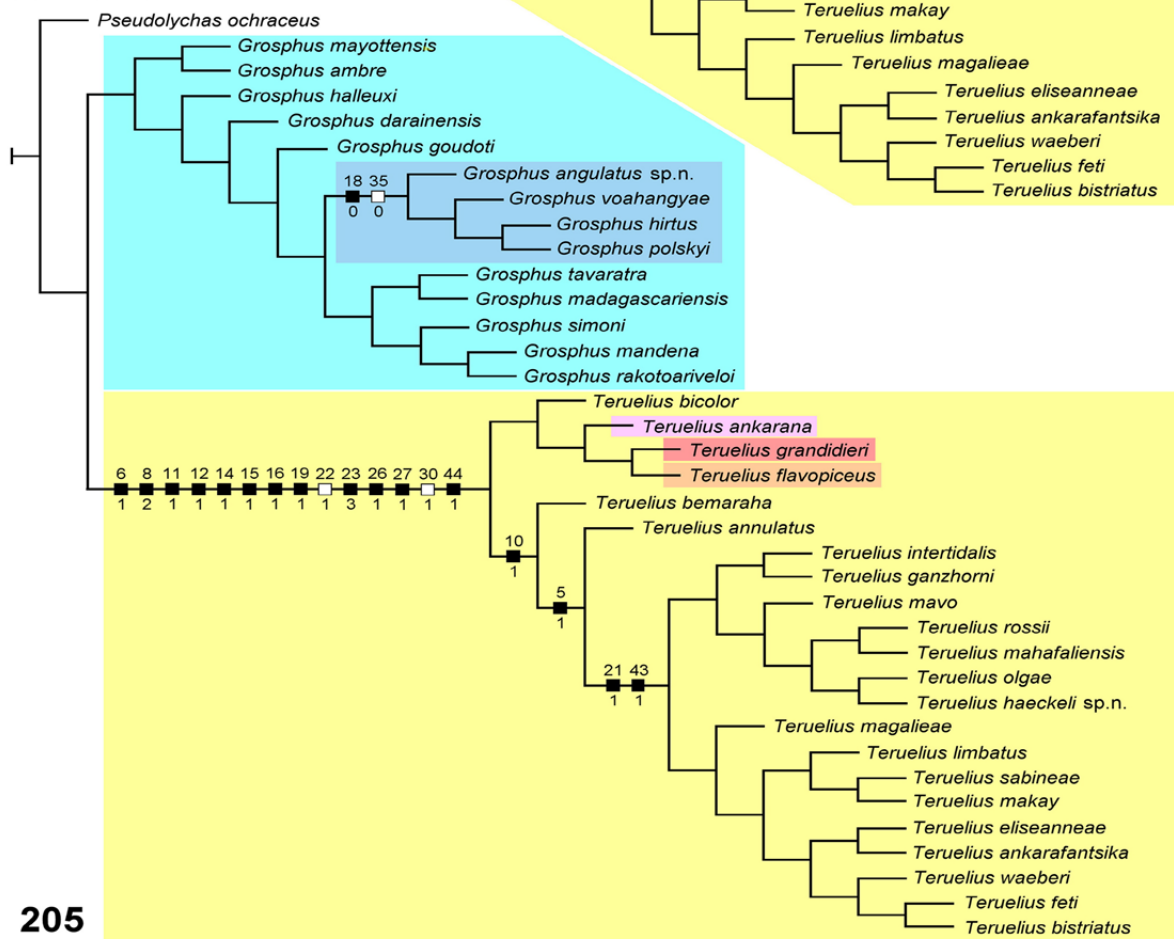
Mean SR supports of *Teruelius* for discrete, and discrete + continuous characters, obtained with different outgroups, are summarized in Fig. 191. In most outgroups that yielded moderate to strong support, SR values were higher for discrete + continuous characters. This strengthens the case for monophyly of *Teruelius* because continuous characters encode more information and avoid discretization bias. SR supports were positively correlated with RBS values, although the two metrics could have rather different values, as seen in the scatter plots in Figs. 192–193. In the scatter plots, an SR threshold of 50% was roughly equivalent to an RBS of around 25%. Fig. 193 shows that both SR and RBS provided support for *Teruelius*, and that continuous characters improved the support of both metrics. The improvement is also evident in Figs. 194–195, which show mean SR and RBS for different weighting schemes. *Teruelius* received strong support both under PW and under IW over a range of concavities.

Figs. 196–203 show examples of MPTs retrieved from various analyses with different outgroup taxa. Examples of MPTs retrieved under the two backbone constraints, for discrete and discrete + continuous characters, are shown in Figs. 206–209. *Teruelius*, and often *Grosphus*, were consistently recovered as monophyletic groups, but relationships of species within those genera were not consistent. The aim of our analysis was not to resolve phylogeny at the species level, only to test the monophyly of the genus *Teruelius*. High numbers of MPTs retrieved under PW in some cases were generated by branch shuffling at the species level that maintained monophyly of *Teruelius*. However, two recurring results at the subgeneric level were the recovery a monophyletic *Grosphus* 'hirtus' group (*G. angulatus* sp. n., *G. hirtus*, *G. polskyi* and *G. voahangyae*), and the basal placement within *Teruelius* of the larger species *T. flavopiceus*, *T. ankarana* and *T. grandidieri*, along with *T. bicolor* and *T. bemaraha*.

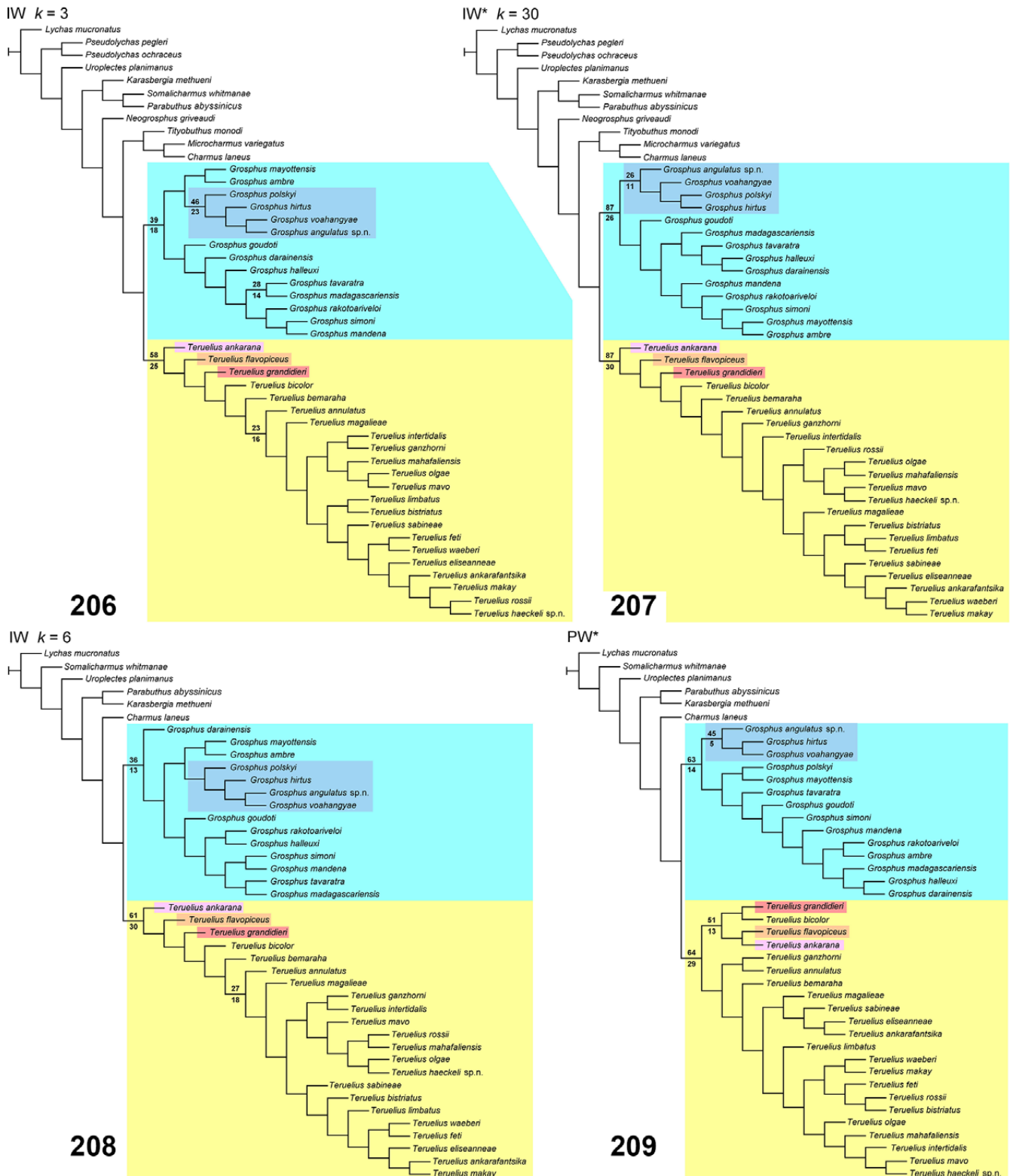
PW



204

IW $k = 10$ 

Figures 204–205. Mapping of unambiguous synapomorphies in two example MPTs retrieved by phylogenetic analyses of *Grosphus* and *Teruelius*, rooted by 2 different outgroup taxa: *Charmus laneus* (204) and *Pseudolychas ochraceus* (205). Numbers above nodes are discrete characters (Table 1), those below are discrete character states (Table 2).



Figures 206–209. Examples of MPTs retrieved by phylogenetic analyses of *Grosphus* and *Teruelius*, with multiple outgroup taxa in topologies fixed by backbone constraints. **Figures 206–207.** MPTs retrieved with 11 outgroup taxa in constrained topologies determined by the buthid MPT of Fig. 276, from discrete characters (206) or discrete and continuous characters (207), analyzed under implied weights. **Figures 208–209.** MPTs retrieved with 7 outgroup taxa in constrained topologies determined by molecular phylogenetic analyses of buthids (Fig. 190), from discrete characters (208) or discrete and continuous characters (209), analyzed under prior (209) or implied (208) weights. Numbers above nodes are jackknife by symmetric resampling supports, those below relative Bremer supports. Color coding of groups according to legend in Fig. 16.

In Figs. 204–205, unambiguous synapomorphies are mapped to nodes with moderate to strong support in two example MPTs retrieved from analyses of the discrete character matrix, with two outgroup taxa. With *Charmus laneus* as outgroup, *Teruelius* was supported by 11 unambiguous synapomorphies, 8 of them unique; with *Pseudolychas ochraceus* as outgroup, *Teruelius* was supported by 14 unambiguous synapomorphies, 12 of them unique.

The 45×36 discrete character matrix for the ingroup (Table 2) included 1,315 scored character states (81.2%) and 305 unscored character states (18.8%). The 49×36 discrete + continuous ingroup data matrix (Tables. 4–6) included 1,397 scored character states (79.2%) and 367 unscored character states (20.8%). Missing data included male-specific characters in species only known or described from females, female-specific characters in species only known or described from males, adult-specific characters in species only known or described from juveniles, and characters that could not be scored either from available material or from published information. Of the 14 synapomorphies supporting *Teruelius* in Fig. 205, 12 included at least one unscored taxon. What was the impact of incompletely scored characters on the results of our analysis? How sensitive is support for monophyly of *Teruelius* to these characters? To gauge the sensitivity, we repeated all analyses after excluding characters in which over 30% of taxa were unscored (range 31%–58%). From the discrete character set we excluded 12 such characters {6–9, 15–16, 31, 34, 36–37, 43–44}, yielding a 33×36 ingroup data matrix with 90.9% of entries scored. From the discrete + continuous character set we excluded 15 such characters {1, 8, 10, 14, 16, 20–23, 26–27, 39, 42–43, 48}, yielding a 34×36 ingroup data matrix with 88.5% of entries scored. When the reduced data matrices were analyzed, *Teruelius* was still consistently retrieved as a monophyletic group with moderate to strong SR support (50–91%) in 86/130 (66.2%) of all analyses, (Tables 7–9, rightmost columns). The general pattern of support across different outgroup taxa was consistent with the result from analysis of the full character set. This demonstrated the stability of *Teruelius* as a monophyletic group, relatively insensitive to the characters with missing entries. In 115 analyses, SR support for *Teruelius* from the full character set was increased relative to the reduced character set in 89 cases, unchanged in 6 cases, and decreased in 20 cases. In a paired t-test, support from the full set was significantly higher than from the reduced set ($P = 7.66 \times 10^{-14}$). This is consistent with modeling predictions that addition of incomplete characters generally increases phylogenetic resolution relative to excluding them (Wiens, 2006).

For some of the ingroup taxa (15 species), a minority of characters {23–25, 28–29, 34–35} in the discrete data matrix were scored from published illustrations of bpt, trichobothrial maps and pedipalp chelae (59 of 1,315 scored characters). There exists a possibility that some of these illustrations may not be entirely accurate, due to errors (e.g., Kovařík, 2018) or anomalies (e.g., the issues discussed below under *Microcharmus* character 6). Could such inaccuracies invalidate

our results supporting monophyly of *Teruelius*? We tested this by reanalyzing the data assuming the worst-case scenario in which all 59 of these illustrated characters were unreliable, and substituting them with missing data entries ("?"). *Teruelius* was still consistently retrieved as a monophyletic group for the same set of eight outgroup taxa, although node supports were somewhat lower. Node supports were higher for all analyses conducted under prior weights, and under implied weights with weak concavities (SR = 50–74%). They were more modest under implied weights with strong concavities (SR = 28–49%). Actual supports were probably higher because it is unlikely that all 59 characters were incorrectly illustrated. Comparisons of examined types of six other ingroup taxa with their published illustrations by the same author did not identify any discrepancies. Comparisons of materials of ten other ingroup taxa with similarly published illustrations of the same taxa by the same author also did not identify any discrepancies.

The overwhelming support for monophyly of *Teruelius* in our phylogenetic analyses, the addition of several new characters separating *Teruelius* from *Grosphus*, and the strengthening of our previous diagnostic character set by morphometric analyses, together justify restoration of the genus *Teruelius*.

Phylogenetic position of *Microcharmus*

We included *Microcharmus variegatus* in our set of buthid outgroup taxa to test the monophyly of *Teruelius*. At first glance this appears to be a questionable choice, because *Microcharmus* is placed in a separate family (Microcharmidae). To justify this choice, we reevaluated the status of Microcharmidae. The family was originally conceived by Lourenço (1996b) as a subfamily of the buthids, Microcharminae, for the genus *Microcharmus*. Lourenço (1998a) elevated it to family rank and included the genus *Akentrobuthus*, transferred from the buthids. Subsequently, Lourenço (2000a) removed *Akentrobuthus* and added the genus *Neoprotobuthus*. Lourenço (2004) added a third genus, *Ankaranocharmus*, but this was soon synonymized under *Microcharmus* (Lourenço et al., 2006). Currently, two genera are included in the family: *Microcharmus* with 16 species, and the monotypic *Neoprotobuthus*.

Soleglad & Fet (2003b) associated *Microcharmus* with *Grosphus*, *Uroplectes* and the New World buthids, which all share the α-pattern of femoral trichobothria. They expressed doubts about Microcharmidae, writing “*A diagnosis cannot be provided as justifying a separate family ... the given features are not diagnostic even at subfamily level*”, but continued to formally recognize the family. Fet et al. (2005) placed *Microcharmus* in their ‘*Uroplectes*’ group of buthids according to a cladistic analysis of femoral and patellar trichobothria, but included a disclaimer: “*this placement does not indicate that we endorse here the formal synonymy of Microcharmidae with Buthidae*”. Volschenk et al. (2008) reported two characters shared by *Microcharmus* and buthids, a complex open form of 8-celled ovariouterus and a lack of lateral lymphoid organs, and added that *Microcharmus* also

	Character
0	Carapace anterior margin: straight to weakly concave (0); moderately to strongly concave (1)
1	Carapace antero-submedian carinae: present (0); absent (1)
2	Carapace, median ocular tubercle position: anterior 1/3 (0); posterior 2/3 (1)
3	Chelicera fixed finger, ventral accessory denticles: ≥ 2 (0); 1 (1); 0 (2)
4	Pedipalp femur ‘trichobothrium’ d_2 : dorsal (0); internal (1)
5	Pedipalp femur trichobothria $d_1-d_3-d_4$ non-reflex angle: prolateral (beta) (0); retrolateral (alpha) (1)
6	Pedipalp femur trichobothrium e_1 position vs. d_5 : proximal or level (0), distal (1)
7	Pedipalp patella trichobothrium d_3 position vs. dorsomedian carina: external (0); internal (1)
8	Pedipalp patella trichobothrium eb_2 vs. eb_1 : absent (0); close to eb_1 (< 0.18 em) (1); distal to eb_1 (> 0.18 em) (2)
9	Pedipalp patella dorsoexternal carina: distinct, granulate (0); weak, obsolete or absent (1)
10	Pedipalp manus trichobothrium Eb_2 position relative to Eb_1 : proximal (0); distal (1)
11	Pedipalp manus trichobothrium V_2 position: external (0); medial (1); internal (2)
12	Pedipalp manus D1, V1 carinae: distinct (0); reduced or obsolete (1)
13	Pedipalp fixed finger trichobothrium db vs. est : proximal (0); level (1); distal (2)
14	Pedipalp fixed finger trichobothrium db position: proximal 30% (0); middle 30-60% (1); distal > 60% (2)
15	Pedipalp fixed finger trichobothrium it position: basal (0); mid-finger (1); distal (2)
16	Pedipalp movable finger, number of median denticle subrows: 6–7 (0); 8–10 (1); 11–16 (2)
17	Pedipalp movable finger, median denticle subrows: non-imbricated (0); imbricated (1)
18	Pedipalp movable finger, external accessory denticles per subrow: 0 (0); 1 (1); 2 (2)
19	Pectines, fulcra: present (0); absent (1)
20	Pectines, female basal middle lamella: normal (0); dilated (1)
21	Pectines, female basal pectinal tooth: normal (0); dilated (1)
22	Hemispermatophore capsule: short, basal lobe distal (0); long, basal lobe proximal (1)
23	Hemispermatophore basal carina vs. distal carina: fused (0); split (1)
24	Hemispermatophore distal carina lobes: 1 (0); 2 (1)
25	Hemispermatophore basal lobe shape: stalked lobe (0); hook (1); scoop (2)
26	Hemispermatophore distal flagellum: absent (0); filiform (1); thickened (2)
27	Hemispermatophore distal flagellum: absent (0); folded (1); coiled (2)
28	Legs III or IV, tibial spurs: present (0); absent (1)
29	Legs I–IV, telotarsi, ventral setation: absent (0); sparse, < 25 setae (1); dense, brush-like tuft, > 25 setae (2)
30	Tergite III–VI carination: absent (0); monocarinate (1); tricarinate (2)
31	Sternite VII medial surface: matte (0); glossy (1)
32	Sternites, spiracles: ovoid or elliptic (0); narrow, slit-like (1)
33	Metasomal segments I–III and tergite VII, posterior microsetal fringes: absent (0); present (1)
34	Metasoma V dorsolateral carinae: granulate (0); smooth (1); obsolete (2)

Table 10. Discrete characters and character states used in phylogenetic analysis of Microcharmidae vs. Buthidae. All 35 characters unordered. Characters 0–4, 6–34 assigned weights of 1, character 5 assigned a weight of 1 or 2.

had “numerous external morphological characters” in common with buthids (but cited only the type-A trichobothrial pattern). They pointed out that “continued recognition of Microcharmidae renders Buthidae paraphyletic” and proposed a formal synonymy, but omitted details of their character analysis. Lourenço et al. (2019) criticized the omission, writing “What, however is not acceptable is the fact that Volschenk et al. (2008) globally ignore all the characters used by Lourenço (2002a) and Lourenço et al. (2006) to justify the family Microcharmidae”, and restored the family.

The characters used to diagnose and justify Microcharmidae were as follows (Lourenço, 1998a: 846; Lourenço, 2000a: 878): **1.** Small size (7–16 mm). **2.** Two or three pairs of lateral eyes. **3.** Pentagonal sternum. **4.** Oval or round stigmata (= spiracles). **5.** Pectines with distal-most tooth and lamella rounded. **6.** Metamerization of pectine basal piece. **7.** Absence of fulcra. **8.** Lack of tibial spurs. **9.** Cheliceral movable finger with two basal teeth small, fused; distal external tooth smaller than distal internal tooth. **10.** Pedipalp patella without ventral trichobothria. **11.** Telson

TAXON	0–4	5–9	10–14	15–19	20–24	25–29	30–34
<i>Pseudochactas ovchinnikovi</i>	00000	00000	00000	00000	00000	00000	00000
<i>Hottentotta trilineatus</i>	00100	00110	00101	22010	00111	11101	20110
<i>Androctonus crassicauda</i>	00100	00110	01101	22010	00111	11101	20110
<i>Barbaracurus exquisitus</i>	11001	01010	11122	21010	00110	21201	11000
<i>Ananteris dorae</i>	01010	00011	11112	20011	00110	11201	10000
<i>Isometrus maculatus</i>	11011	00010	01122	20010	00000	11212	10100
<i>Lychas mucronatus</i>	11011	00010	01122	20010	00000	11202	10100
<i>Isometroides vescus</i>	11111	00010	02021	20010	00000	11202	10101
<i>Reddyanus melanodactylus</i>	11011	00010	01121	20010	00000	11211	10000
<i>Somalicharmus whitmanae</i>	01021	10011	00100	01010	10110	12101	11000
<i>Uroplectes planimanus</i>	01020	10021	12101	21010	01110	11101	21001
<i>Pseudolychas ochraceus</i>	01010	10010	12111	20020	01110	11201	20000
<i>Charmus laneus</i>	01000	10021	12101	21020	00000	22102	10001
<i>Buthoscorpio sarasinorum</i>	01001	10021	12102	21120	00000	22101	11101
<i>Butheoloides maroccanus</i>	11001	10021	12101	21020	00000	22100	11001
<i>Neogrosphus griveaudi</i>	01101	11011	12101	21020	01100	11102	10001
<i>Grosphus madagascariensis</i>	01101	11021	11111	22120	01000	12101	10000
<i>Grosphus hirtus</i>	01101	11021	11101	22120	01100	12101	10000
<i>Teruelius flavopiceus</i>	11100	11021	11101	22120	01100	12102	11100
<i>Microcharmus variegatus</i>	01000	10021	11101	20011	00000	22101	10001
<i>Karasbergia methueni</i>	0112?	10011	12100	10000	00110	12101	11001
<i>Parabuthus abyssinicus</i>	01100	10021	12101	22010	10110	12101	11100
<i>Tityobuthus monodi</i>	11001	11020	12101	21020	00000	11102	10001
<i>Zabius fuscus</i>	1011?	10010	00011	21110	00010	11111	20000
<i>Tityus dedoslargas</i>	10111	11020	10022	22110	10010	11112	10100
<i>Tityus ocelote</i>	10111	11020	10022	22110	00010	11112	10001

Table 11. Discrete character matrix used in phylogenetic analysis of Microcharmidae vs. Buthidae. The ingroup included one species of Microcharmidae and 24 species of Buthidae (2 ‘Buthus’ group, 6 ‘Ananteris/ Isometrus’ group, 13 ‘Charmus/ Uroplectes’ group, 3 ‘Tityus’ group), the outgroup 1 of Pseudocheactidae. Numbered characters and states as defined in Tab. 10. Unscored characters states indicated by “?”.

vesicle small, long, without subaculear tubercle. Additional characters introduced by Lourenço (2002) and Lourenço et al. (2006) (see also Lourenço et al., 2019) were: **12.** Sensillar pegs on pectine teeth round in cross section, subcylindrical or bottle-shaped. **13.** Hemispermatophore with trunk wider at base, lacking a truncal flexure, hook and flagellum. Below, we review all of these characters.

1. Small size, < 18 mm (Lourenço et al., 2006, 2019). This character also occurs in the buthid genera *Akentrobuthus*, *Ananteris*, *Microtityus*, *Microbuthus*, *Picobuthus*, *Femtobuthus*, *Charmus* and *Thaicharmus*.

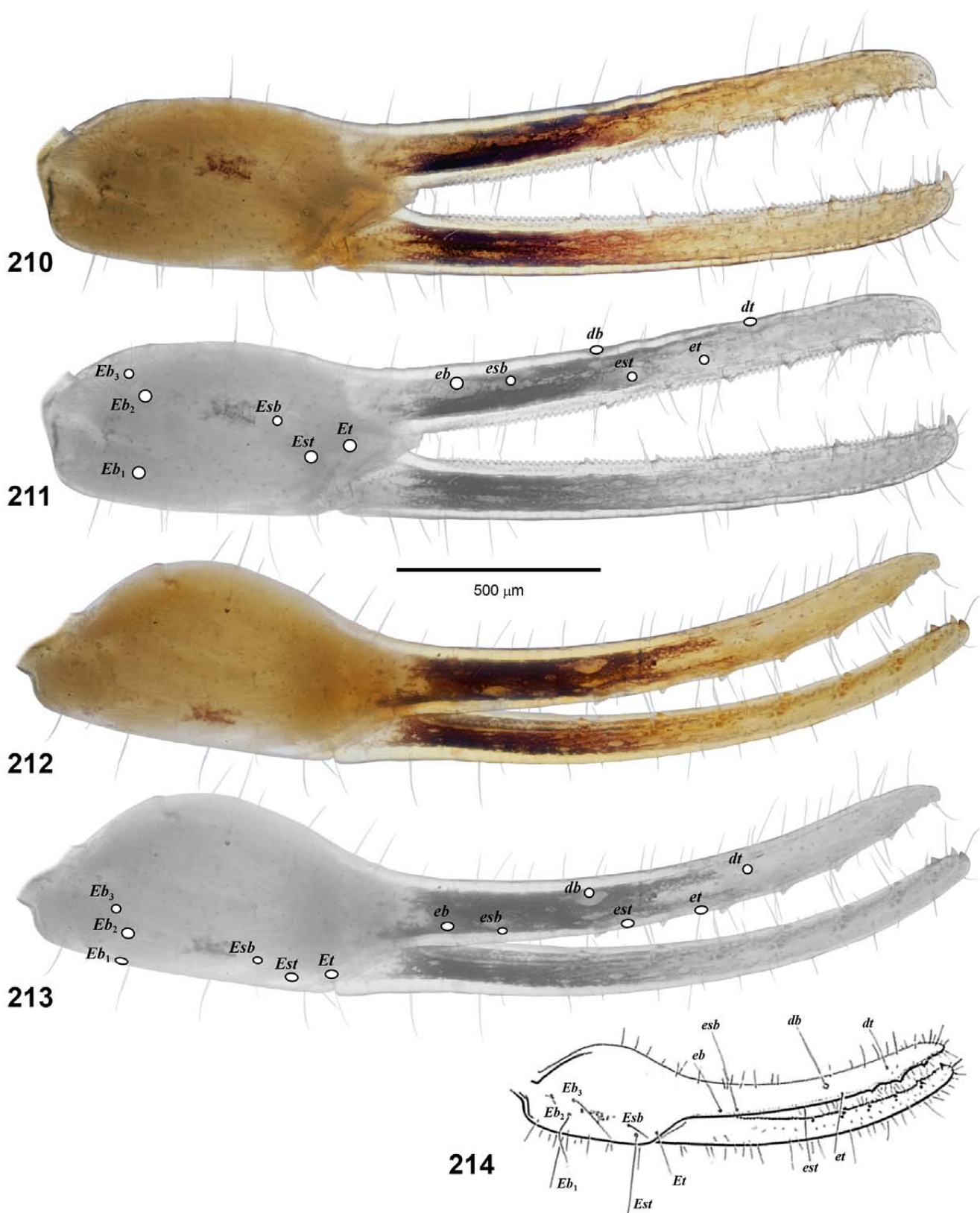
2. Two or three pairs of lateral eyes. This character also occurs in the buthid genera *Afroisometrus*, *Akentrobuthus*, *Alayotityus* and *Karasbergia* (Loria & Prendini, 2014).

3. Pentagonal sternum. A pentagonal (or ‘subpentagonal’) sternum shape also occurs in the buthid genera *Akentrobuthus*, *Butheoloides*, *Charmus*, *Karasbergia*, *Microananteris*, *Microtityus* and *Thaicharmus*. Shape of the sternum was shown to be a superficial character by Soleglad & Fet (2003a), who identified two fundamental structural types of sternum in Recent Scorpiones, i.e., type 1 and type 2. The type 1 sternum is found in pseudocheactids, chaerilids, buthids and *Microcharmus*, while

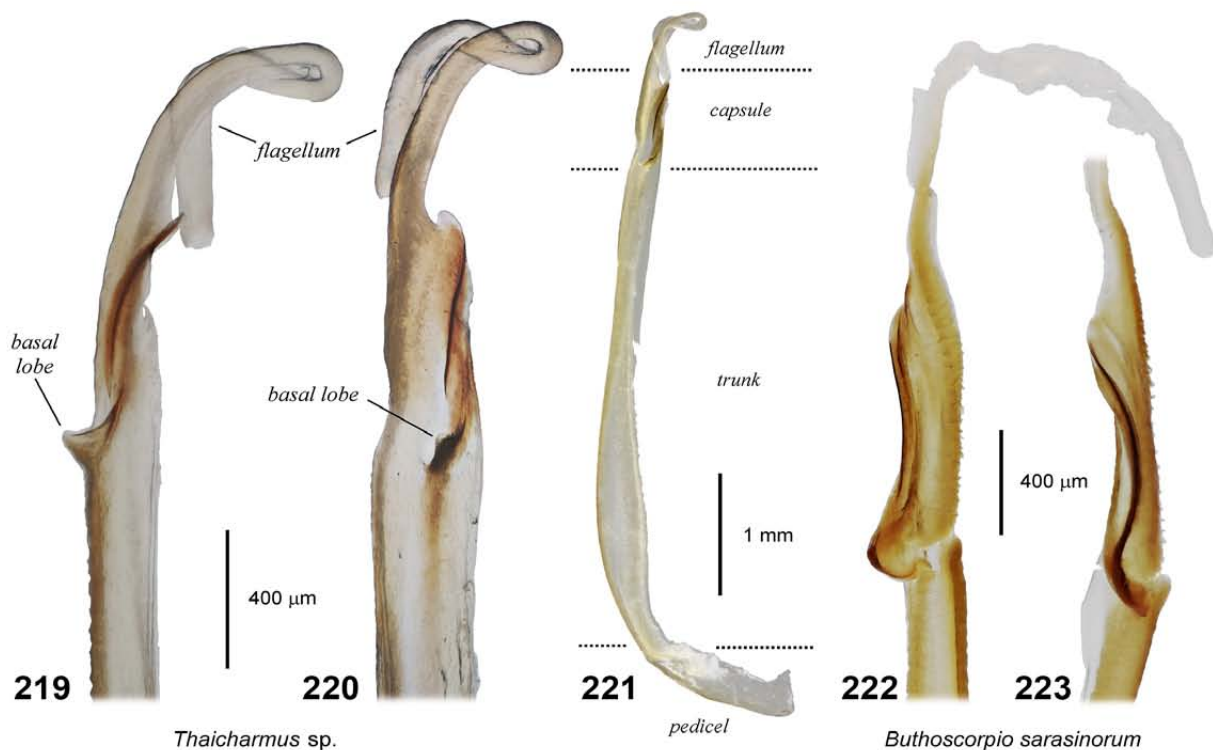
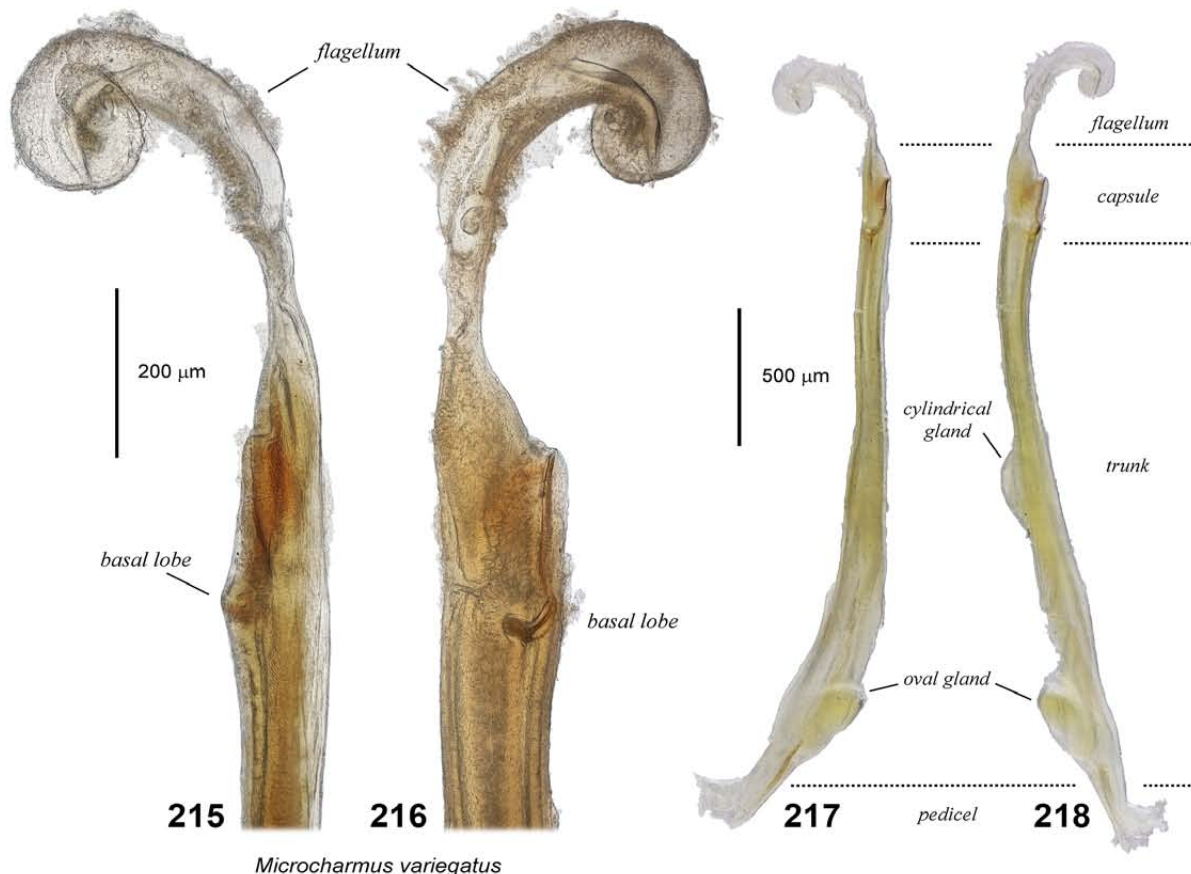
the type 2 sternum is found in all other extant scorpion families. In both buthids and *Microcharmus*, the type 1 sternum exhibits horizontal compression, a putative synapomorphy.

4. Oval or round stigmata. This character also occurs in the buthid genera *Akentrobuthus*, *Charmus*, *Somalicharmus*, *Thaicharmus*, *Grosphus*, *Alayotityus*, *Chaneke*, *Ischnotelson*, *Mesotityus*, *Microananteris*, *Microtityus*, *Tityopsis*, *Tityus* (*Archaeotityus*) spp., *Troglorhopalurus* and *Zabius*. Lowe & Kovařík (2019) discussed the ecophysiological aspects of oval spiracles (= stigmata) and their possible association with humid microhabitats. The addition to the microcharmid family of *Neoprotobuthus*, which has more elongated “semi-slit-like” spiracles (Lourenço, 2000a), reduced this to a genus level character inapplicable to the whole family.

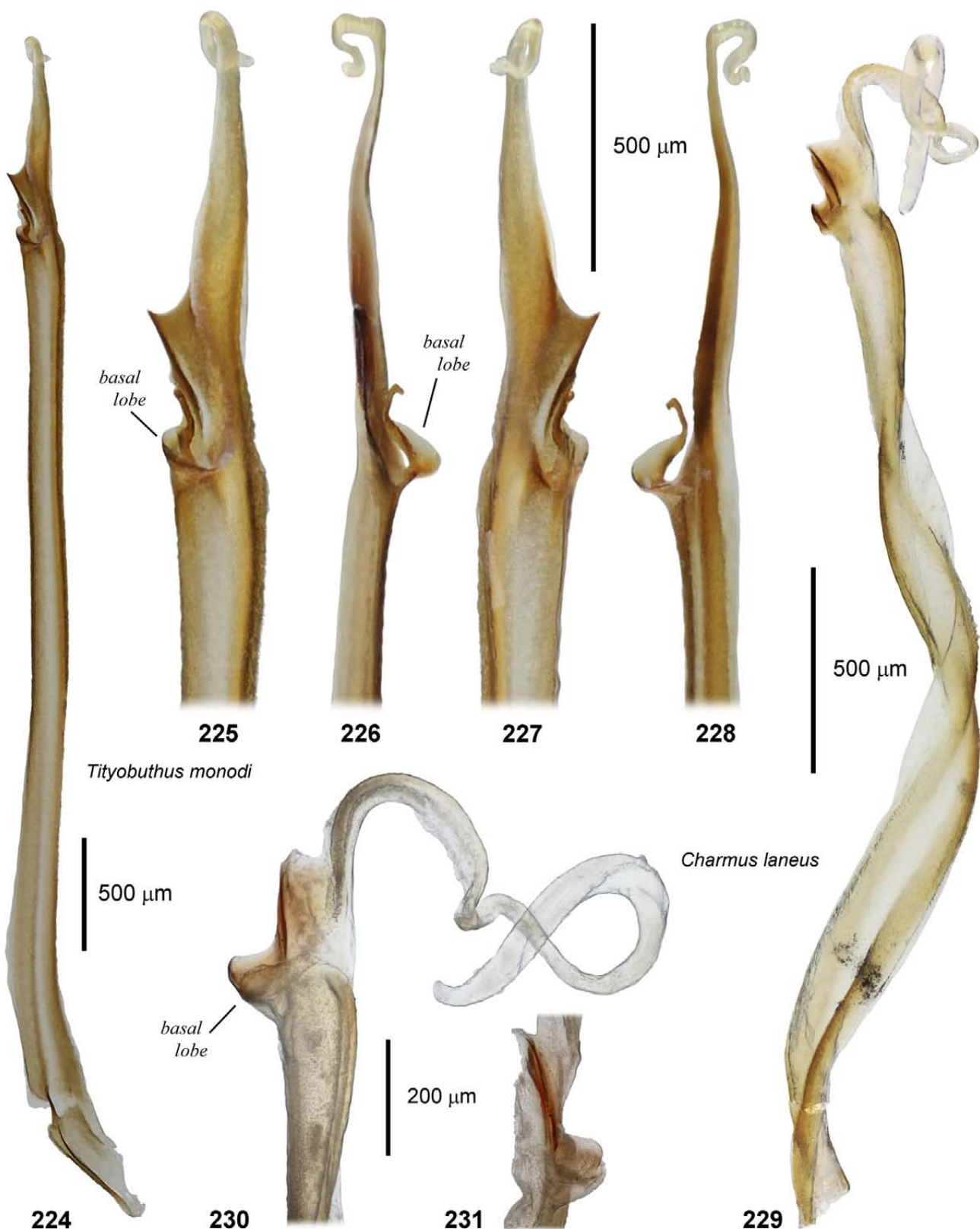
5. Pectines with distal tooth and lamella rounded. This character also occurs in the buthid genera *Lychasioides* and *Microananteris* (cf. Lourenço, 2003c). The distal tooth of the pectines of scorpions is generally shorter and more rounded than non-distal teeth, being the terminal article of a series, not nested between other teeth. The difference in shape may be exaggerated in small buthids with short pectines. To test this, we analyzed the outer marginal curvature (a measure



Figures 210–214. *Microcharmus variegatus*, right pedipalp chela. **Figures 210–211.** Paratype male, external view in color (210) and gray scale with mapped trichobothria (211). **Figures 212–213.** Paratype male, dorsoexternal view in color (212) and gray scale with mapped trichobothria (213). Scale bar: 500 µm. **Figure 214.** Holotype female illustrated by Lourenço et al. (2006: 760, fig. 27). Trichobothrial labels added for comparison to Figs. 211, 213.



Figures 215–223. Hemispermatoophores of *Microcharmus* and the buthids *Thaicharmus* and *Buthoscorpio*. **Figures 215–218.** Right hemispermatoophore of paratype male of *Microcharmus variegatus*. Distal region including capsule and flagellum (215–216), and whole hemispermatoophore (217–218) in anterior (215, 217) and convex (216, 218) views. **Figures 219–221.** Left hemispermatoophore of *Thaicharmus* sp. (shown as mirror image for comparison). Distal region including capsule and flagellum (219–220), and whole hemispermatoophore (221) in anterior (219) and convex (220–221) views. **Figures 222–223.** Left hemispermatoophore of *Buthoscorpio sarasinorum*, distal region including capsule and flagellum in posterior (222) and convex (223) views. Scale bars: 200 µm (215–216), 400 µm (219–220, 222–223), 500 µm (217–218), 1 mm (221).



Figures 224–231. Hemispermophores of the buthids *Tityobuthus* and *Charmus*. **Figures 224–228.** Left hemispermophore of *Tityobuthus monodi*. Whole hemispermophore (224) and distal region including capsule and flagellum (225–228) in convex (225), anterior (226), concave (227) and posterior (228) views. **Figures 229–231.** Left hemispermophore of *Charmus laneus*. Whole hemispermophore (229) and distal region including capsule and flagellum (230–231) in convex (229–230) and anterior (231) views. Scale bars: 200 µm (230–231), 500 µm (224, 225–228, 229).

of ‘roundness’) of the distal tooth in 186 species of buthids, sampling 61 genera from all four main groups (‘*Buthus*’, ‘*Ananteris/ Isometrus*’, ‘*Charmus/ Uroplectes*’ and ‘*Tityus*’) and 7 species of microcharmids (both genera). We found that there was indeed an inverse correlation between tooth curvature and body size as represented by carapace length (Fig. 265). Tooth curvatures of microcharmids were distributed towards the high end of the range, but overlapped broadly with those of the buthids (Fig. 266). The rounded shape of the distal pectine tooth does not separate microcharmids from buthids.

6. Metamerization of pectine basal piece. Differences in metamerized segmentation of animals reflect major bauplan transformations often associated with deeper phylogenetic divisions. A metamerized basal piece would be a major departure from the anatomy of all other Recent scorpions and could be justification for creating a separate family. The spider family Liphistiidae was introduced for species having a primitive segmented opisthosoma, among other characters. Cladistic and molecular analyses confirmed that they belonged to an ancient lineage placed in its own suborder Mesothelae (Platnick & Gertsch, 1976; Platnick & Goloboff, 1985; Wheeler et al., 2017).

Lourenço (1995: 99, fig. 10; reproduced here in Fig. 232) illustrated the basal piece of the holotype female of *Microchasmus cloudsleythompsoni* as being divided longitudinally and transversely into two pairs of sclerites, although this unusual segmentation was not mentioned in either the diagnosis of the genus, or the description of the species. Although the holotype was listed as female, the figure was captioned “holotype mâle” (likely an editorial error). Lourenço (1996d) described *M. hauseri*, comparing it to *M. cloudsleythompsoni*, but did not describe a metamerized basal piece. Lourenço (1996b: 63, fig. 31) republished the 1995 figure of the metamerized basal piece of *M. cloudsleythompsoni*, created the subfamily Microcharminae, and described two new species (*M. sabineae* and *M. jussarae*). However, the metamerized basal piece was not mentioned in either the subfamily diagnosis or the species descriptions. Such a structure was not clearly visible in photographs of the sternopectinal areas of *M. cloudsleythompsoni*, *M. sabineae* and *M. jussarae* (Lourenço, 1996b: 99, figs. 148–150, 154). Lourenço (1998a) raised the subfamily to the rank of a family, Microcharmidae, and for the first time listed the metamerized basal piece as a diagnostic character for the family (“Pièce basale présentant une métamérisation, qui la divise en plusieurs pièces”), republishing again the 1995 figure of the divided basal piece of *M. cloudsleythompsoni* (Lourenço, 1998a: 846, fig. 2). The genus *Akentrobuthus* Lamoral, 1976 was included in the family, although Lamoral did not report a metamerized basal piece for the genus, and his pectine illustration (Lamoral, 1976: 688, fig. 19) showed the basal piece of *A. leleupi* as a single undivided sclerite. Lourenço (1998b) described *M. fisheri*, and illustrated the basal piece of the holotype male as divided along the midline into two sclerites (Lourenço, 1998b: 70, fig. 4; reproduced here in Fig. 238). Lourenço (1999d) described

another species, *M. madagascariensis*, and distinguished it from *M. cloudsleythompsoni* in part by having an undivided basal piece composed of a single sclerite, implying that metamerization was not diagnostic for all members of the family. Lourenço (2000a) transferred *Akentrobuthus* back to the Buthidae, thus removing a species that contradicted this diagnostic character, and added the genus *Neoprotobuthus*. The metamerized basal piece was listed as diagnostic for the family, and the basal piece of *Neoprotobuthus* was characterized as being “less divided”. The latter condition was not defined and seems unclear, considering that division of an arthropod sclerite is binary – a piece of chitin is either divided (topologically disconnected) or not (topologically connected). “Less divided” could also be interpreted to mean divided into fewer sclerites, e.g., two, instead of four, as illustrated for *M. fisheri*. However, an illustration of the holotype female of *Neoprotobuthus intermedius* showed the basal piece as a single, undivided sclerite (Lourenço, 2000a: 881, fig. 5), contradicting the family diagnosis. An undivided basal piece can also be seen in a photograph of a paratype (Ref. MNHN-RS-RS9031). Lourenço (2002: 38) again listed basal piece metamerization as a character for *Microchasmus*, and the basal piece of *Neoprotobuthus* as “moins divisée”. However, in the same publication, SEM images of the pectines of a male paratype of *M. fisheri* (Lourenço, 2002: 43, figs. 5, 7; republished in Lourenço et al., 2006: 756, figs. 8, 10) did not show division of the basal piece. This again conflicts with the family and genus diagnoses, and with the illustration of the medially divided basal piece in the original description of *M. fisheri* (Lourenço, 1998b: 70, fig. 4). The divided basal pieces shown for the holotypes of *M. cloudsleythompsoni* and *M. fisheri* could be either atypical teratological structures, or observation errors. Lankester (1885: pl. 82, fig. 7) labeled as pectine basal piece (“c”) what appear to be pieces of a medially divided sclerite in “*Androctonus hottentotus*”, but are more likely to be a pair of dilated basal middle lamellae of a species of *Parabuthus*.

Lourenço et al. (2006) revised *Microchasmus*, updated the diagnosis of the genus, and described six new species. They did not mention the metamerized basal piece, either in the generic diagnosis, or in species descriptions. Illustrations of the sternopectinal area of two species, *M. variegatus* and *M. duhemi*, show an undivided basal piece (Lourenço et al., 2006: 759, 762, figs. 23–24, 33). At this point, one might suppose that the metamerized basal piece was no longer considered a valid character of microcharmids. However, a metamerized basal piece reappears in an illustration of the sternopectinal area of a female *M. variegatus* in Lourenço & Goodman (2013: 56, fig. 22; reproduced here in Fig. 233). This contrasted with illustrations in Lourenço et al. (2006: 759, figs. 23–24) which showed undivided basal pieces of the female holotype and a male paratype of *M. variegatus*. We examined male and female paratypes of *M. variegatus* and also found no traces of metamerization (Figs. 236–237). Could the 2013 illustration of *M. variegatus* represent another teratological case, in a third species of the genus?

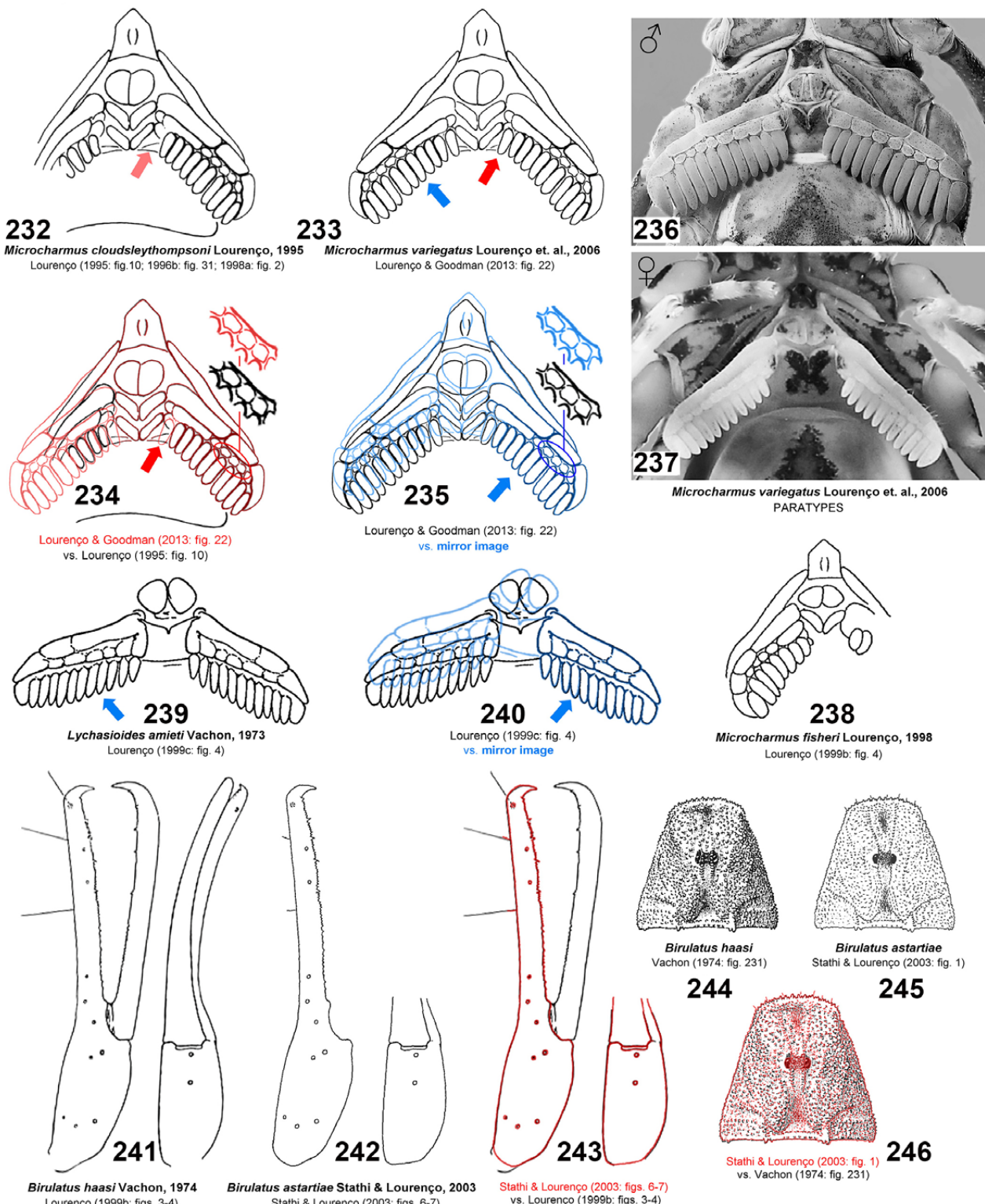
Comparison of Figs. 232 and 233 reveal close similarities between the 1995 illustration of *M. cloudsleythompsoni* and the 2013 illustration of *M. variegatus*. In Fig. 234, superimposition of the two illustrations shows the left comb of *M. variegatus* (traced in red) to be identical to that of *M. cloudsleythompsoni* (traced in black). The two combs are precisely matched in their finest details, with middle lamellae showing the same small gaps in rendered outlines (cf. expanded insets, red vs. black). The sternites, genital opercula and metamerized basal pieces of the two species are also precisely superimposable. However, sternites, genital opercula and combs typically show some variation even among conspecifics. As an example, pectines of five adult females of the small buthid, *Alayotityus sierramaestrae* are shown in Figs. 247–251. The marginal and middle lamellae of different individuals show strong variations in shape that should be resolvable in line drawings like those of Figs. 232–233. The middle lamellae vary not only in shape, but also in number ($n = 4$ –6). In pseudochactids, the number of middle lamellae is relatively stable and equal, or nearly equal, to the number of pectinal teeth, whereas in buthids the middle lamellae are “variously fused, and many fewer in number than the pectinal teeth” (Prendini et al., 2021). The variable fusion leads to intraspecific variation in middle lamellar shapes and counts. Variation occurs even within the same individual, between left and right combs (e.g., Figs. 247–252), which often have different lamellar shapes and counts (e.g., Fig. 251). In contrast, Fig. 233 of *M. variegatus* shows perfect bilateral symmetry of left and right combs. This is evident in Fig. 235, in which a mirror image of the right comb (traced in blue; blue arrow in Figs. 233 and 235) is superimposed upon the original (traced in black). Fine details of left vs. right middle lamellae are identical, including the same small gaps in rendered outlines (cf. expanded insets, blue vs. black). Microcharmid pectines are distinctive in having low PTCs and lacking fulcra, and it is possible that they are also unusual in having more stable middle lamellar fusions. However, *A. sierramaestrae* has similarly low PTCs but has variable middle lamellar fusion. An SEM image of *M. fisheri* (Lourenço et al., 2006: 756, fig. 8) shows symmetric segmentation of the combs, but the shapes of some lamellae on left and right combs are different. Moreover, Figs. 236–237 show left vs. right variation of lamellar shapes and counts in both sexes of *M. variegatus*. One conspicuous difference between Fig. 233 and Fig. 232 is the presence of an added tooth at the base of the comb (positions indicated by red arrows). The extra tooth is highlighted in Fig. 234 (red arrow); it allows Fig. 233 to comply with the recorded female PTC of 11 in *M. variegatus*, rather than the female PTC of 10 in *M. cloudsleythompsoni*.

The 2013 illustration of *M. variegatus* implies that this specimen has: (i) identical shapes of sternum, genital opercula, middle/ marginal lamellae and the distal 10 pectine teeth of the left comb, as the holotype of *M. cloudsleythompsoni*; (ii) identical basal piece metamerization with 4 sclerites of the same shapes in the same positions as in the holotype of *M. cloudsleythompsoni*; (iii) perfect bilateral symmetry of left and right combs. In light of normal intra- and interspecific

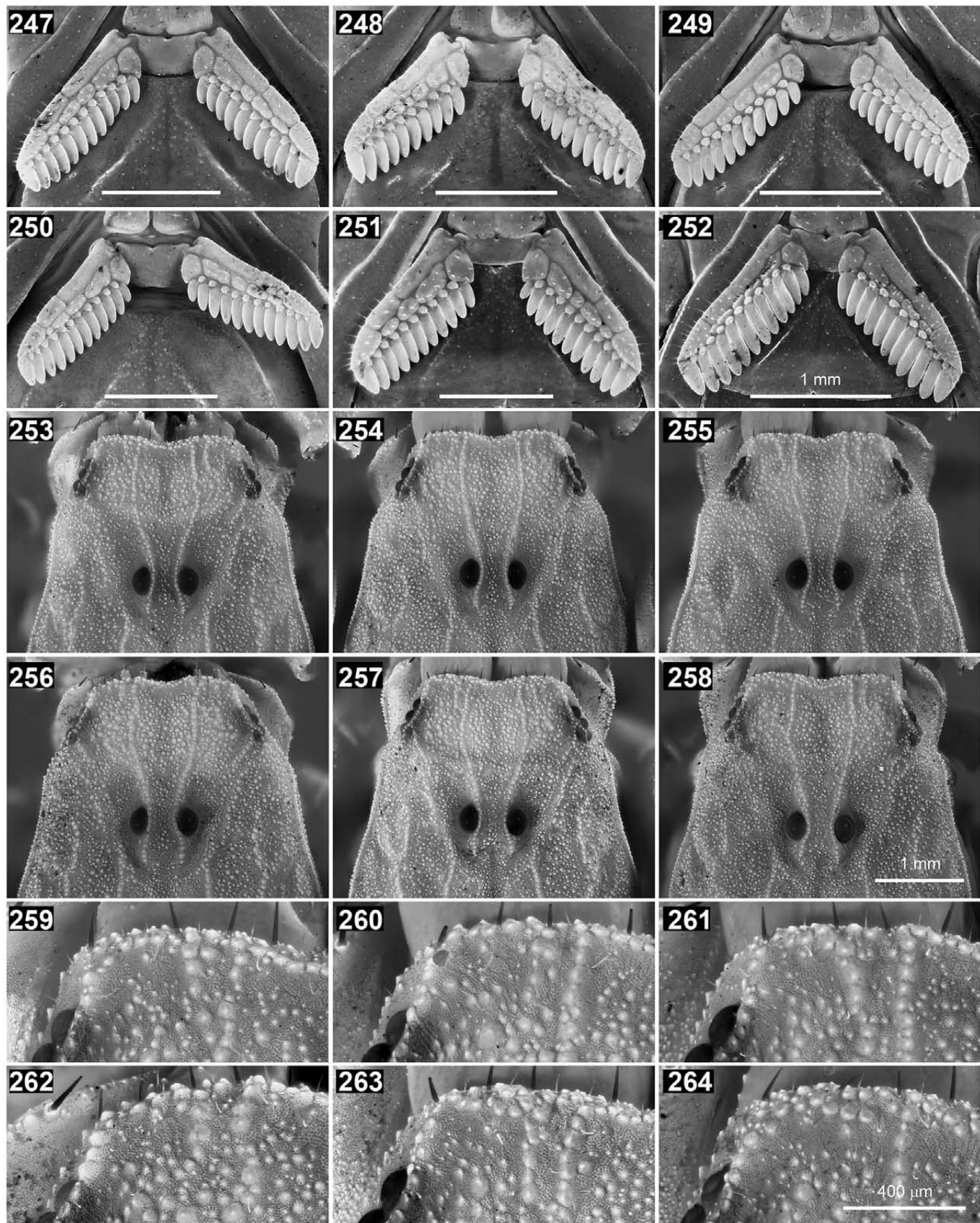
variation, this is an improbable series of coincidences. If the metamerized basal piece of the *M. cloudsleythompsoni* holotype were a rare teratology, what is the likelihood that the 2013 specimen of *M. variegatus* expressed an identical malformed phenotype? A more credible explanation is that the ‘*M. variegatus*’ pectine illustration in Fig. 233 is a composite that was fabricated by duplicating the medial and left parts of the *M. cloudsleythompsoni* pectine illustration, doctoring it by adding an extra tooth, and mirror image cloning the left comb to generate a perfectly symmetrical right comb.

COMMENTS ON IMAGE DUPLICATION

Is the 2013 figure of *M. variegatus* legitimate evidence of a metamerized basal piece, or is it a duplicated image? We argue the latter because it is not an isolated case of duplication. Figs. 239–240 show a second example of apparent image manipulation and duplication by one of the authors. In an illustration of *Lychasioides amieti*, the left and right combs are exact mirror images (Lourenço, 1999c: 11, fig. 4). As noted above, perfect bilateral symmetry seldom, if ever, occurs in scorpion pectines, and this image raises the same concerns about its fidelity. Figs. 241–243 show another example where an image published as one species appears duplicated in the description of a different species. The buthid *Birulatus haasi* was described by Vachon (1974), who illustrated the pedipalp chela of the female holotype (Vachon, 1974: 949, figs. 232–234; labeled as male, probably an editorial error). In his redescription of *B. haasi*, Lourenço (1999b: 109, figs. 2–5) republished the illustrations of Vachon (1974) with appropriate source citation (reproduced here in Fig. 241). Stathi & Lourenço (2003) described a new species, *B. astartiae*, illustrating its pedipalp chela (Stathi & Lourenço, 2003: 107, figs. 6–7; reproduced here in Fig. 242). Fig. 243 shows a superimposition of the 2003 chela illustration of *B. astartiae* (traced in red) over the 1999 chela illustration of *B. haasi* (traced in black). The manus and fixed finger are exactly matched. This implies that the holotype female of *B. astartiae* has: (i) a chela manus and fixed finger external profile, and manus ventral profile, identical to those of the holotype female of *B. haasi*; (ii) positions of all 15 chelal trichobothria in the same positions as corresponding trichobothria in the holotype female of *B. haasi*; and (iii) visible enlarged denticles on the fixed finger in the same positions as in the holotype female of *B. haasi*. However, chela shapes, trichobothrial positions and finger dentition typically exhibit variation even among conspecifics. The variation is expected to be greater between different species. In light of normal intra- and interspecific variation, this is an improbable series of coincidences. Even if (i)–(iii) were true, the illustration in Fig. 238 further requires that the chela be held in the same orientation and distance in 3D space, relative to the optical axis of a camera or microscope, to record a 2D projection identical to that recorded by Vachon (1974). Specifying the orientation of a rigid body in 3D space requires defining three body axes, and three orientation parameters relative to the laboratory frame of reference, e.g., the Euler angles (Goldstein, 1950). We doubt that Vachon (1974) recorded all of these underlying geometric

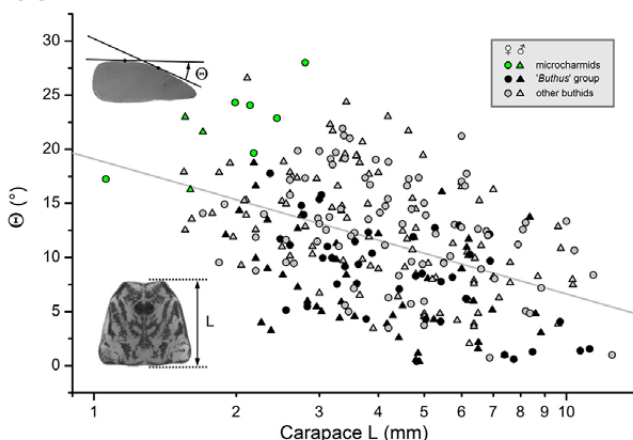


Figures 232–246. The microcharmid metamerized basal piece and other anomalies in the literature. **Figure 232.** Original illustration of metamerized basal piece of pectines of *Microcharmus cloudsleythompsoni* Lourenço, 1995. Lourenço (1995: 99, fig. 10; republished in Lourenço, 1996: 63, fig. 31, and Lourenço, 1998a: 846: fig. 2). **Figure 233.** Illustration of metamerized basal piece of pectines of *Microcharmus variegatus* Lourenço & Goodman (2013: 56, fig. 22). **Figure 234.** Superimposition of Fig. 233 (red) over Fig. 232 (black). Magnified insets: details of middle lamellae. Red arrows (232–234): site of added pectine tooth. **Figure 235.** Superimposition of mirror image of Fig. 233 (blue) over itself (black), mirrored right comb aligned with left comb (blue arrow). Magnified insets: details of right and left middle lamellae. **Figures 236–237.** Sternopectinal regions of male (236) and female (237) paratypes of *Microcharmus variegatus*. UV fluorescence. **Figure 238.** Illustration of basal piece of pectines of *Microcharmus fisheri* Lourenço, 1998b. Lourenço (1999b: fig. 4). **Figure 239.** Illustration of sternopectinal region of *Lychasiooides amieti* Vachon, 1973 (Lourenço, 1999c: 11, fig. 4). **Figure 240.** Superimposition of mirror image of Fig. 239 (blue) over itself (black), mirrored right comb aligned with left comb (blue arrow). **Figures 241–243.** Illustrations of right pedipalp chela and trichobothria of *Birulatus haasi* Vachon, 1973, from Lourenço (1999b: 109, figs. 3–4) (241); of *B. astartiae* Stathi & Lourenço, 2003, from Stathi & Lourenço (2003: 107, figs. 6–7) (242); and superimposition of Fig. 242 (red) over Fig. 241 (black) (243). **Figures 244–246.** Illustrations of carapace of *B. haasi* from Vachon (1974: 949, fig. 231) (244); of *B. astartiae*, from Stathi & Lourenço (2003: 107, fig. 1) (245); and superimposition of Fig. 245 (red) over Fig. 244 (black) (246).

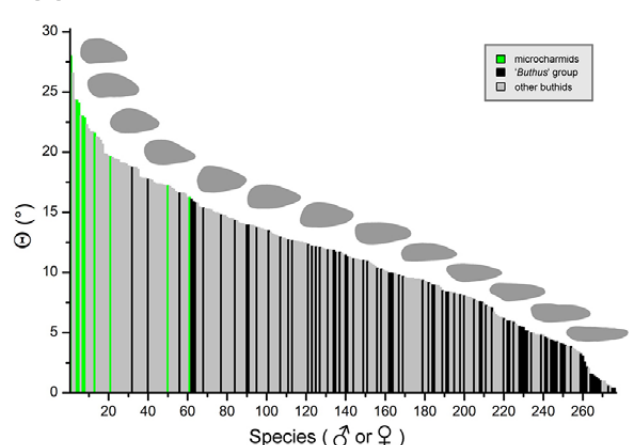


Figures 247–264. Examples of intraspecific variation in pectine morphology and carapace granulation in buthids. **Figures 247–252.** *Alayotityus sierramaestrae* Armas, 1973, pectines of five adult females (247–251) and one adult male (252). **Figures 253–258.** *Compsobuthus maindroni* (Kraepelin, 1900), anterior portions of carapaces of six adult males. **Figures 259–264.** *Compsobuthus maindroni* (Kraepelin, 1900), left anterolateral margins of carapaces of six adult males, showing granulation detail (magnified views of Figs. 253–258). UV fluorescence. Scale bars: 1 mm (247–252), 1 mm (253–258), 400 µm (259–264).

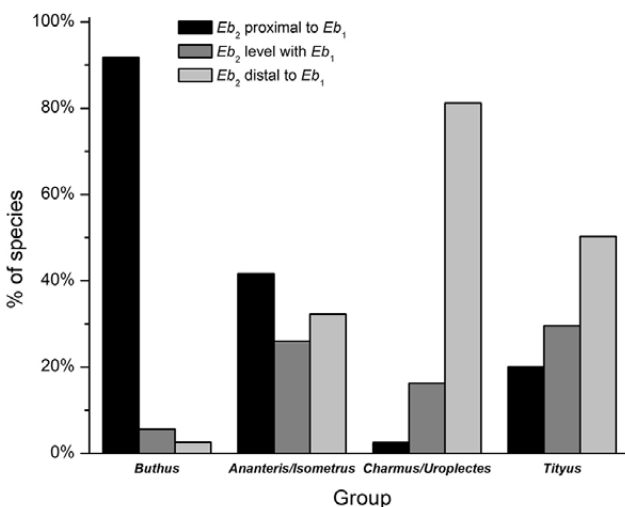
265



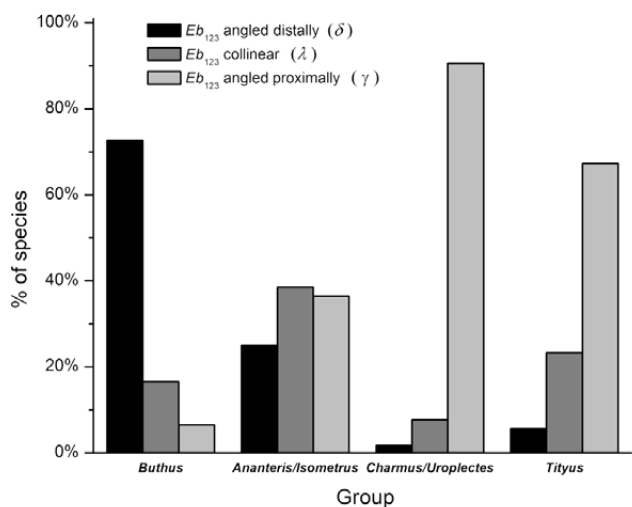
266



267



268

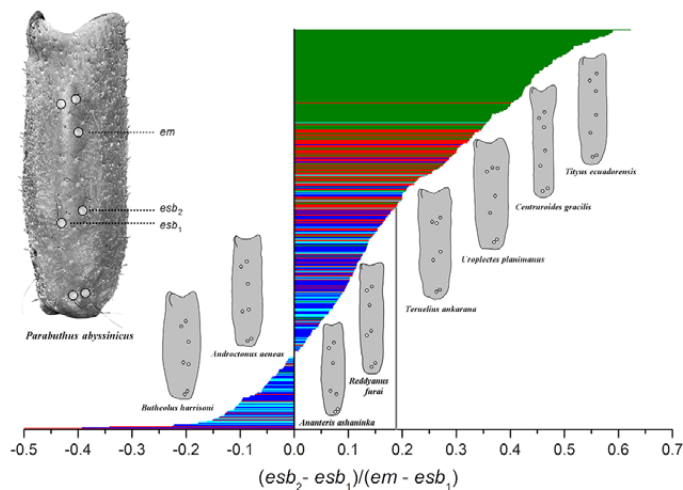


Figures 265–268. Analysis of distal pectinal tooth shape and pedipalp chela manus basal trichobothriotaxy in microcharmids and buthids. **Figure 265.** Bivariate scatter plot of outer curvature angle Θ of distal pectinal tooth vs. carapace L in buthids (black and gray symbols; $n = 267$; 142 ♂, 125 ♀; 61 genera) and microcharmids (green symbols: $n = 9$; 3 ♂, 6 ♀; 2 genera). All four main clades of buthids represented: ‘*Buthus*’, ‘*Ananteris/Isometrus*’, ‘*Charmus/Uroplectes*’ and ‘*Tityus*’ groups. Members of ‘*Buthus*’ group are plotted as black symbols. Males plotted as triangles, females as circles. Intersecting lines subtending Θ are tangent on the outer (distal) margin at 1/3 and 2/3 along the longitudinal axis of the tooth. Gray line: linear least squares regression ($R = -0.44$, $P < 0.0001$). Abscissa with logarithmic scale. **Figure 266.** Ranked vertical bar plot of data for outer curvature angle Θ in Fig. 265. Color codes as in Fig. 265. Silhouettes are examples of distal tooth profiles. **Figures 267–268.** Distributions of configurations of basal trichobothria (Eb_1 , Eb_2 and Eb_3) on pedipalp chela manus among four main clades of buthids. Relative position of Eb_1 and Eb_2 along proximal-distal axis of manus (267), and direction of opening of non-reflex angle formed by (Eb_1 , Eb_2 , Eb_3) triad (268). Data from $n = 604$ buthids, and $n = 3$ microcharmids (classified under ‘*Charmus/Uroplectes*’ group).

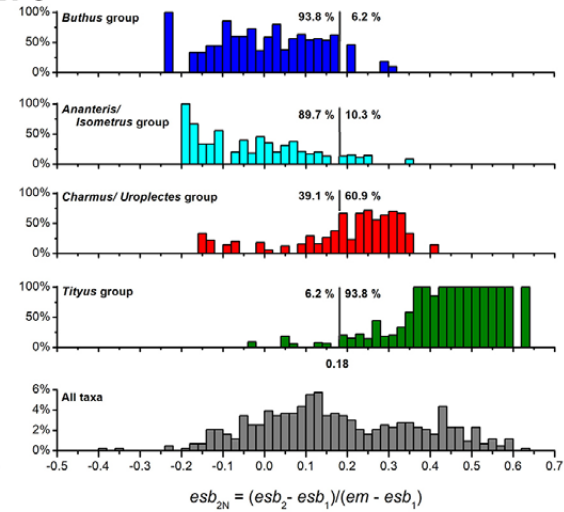
parameters for his illustration of the chela of *B. haasi*, to be reused by Stathi & Lourenço 29 years later to replicate the exact same view of the chela of the holotype of *B. astartiae*, which coincidentally also happens to have a chela identical to that of the holotype of *B. haasi*. A more credible explanation is that Vachon’s *B. haasi* illustration (Fig. 241) was recycled and relabeled as *B. astartiae* (Fig. 242). Indeed, the authors’ own measurement data show that the chela of *B. astartiae* is longer than illustrated: chela L/W = 4.0/0.6 = 6.67 for *B. astartiae*, 3.9/0.6 = 6.50 for *B. haasi* (Stathi & Lourenço, 2003: 108, tab.1), vs. chela L/W = 6.47 for Fig. 242 (matching *B. haasi*, not *B. astartiae*).

A fourth example of apparent image duplication is the carapace illustrated in the description of *B. astartiae* (Stathi & Lourenço, 2003: 107, fig. 1; reproduced here in Fig. 245), which is very similar to the carapace illustration of *B. haasi* published by Vachon (1974: 949, fig. 231; reproduced here in Fig. 244). Fig. 246 shows a superimposition of the 2003 carapace illustration of *B. astartiae* (traced in red) over the 1974 carapace illustration of *B. haasi* (traced in black). The outlines and many features of the two illustrations are in exact or very close alignment. Although the rendered granulation patterns are not precisely superimposable, in some areas there is a one-to-one match of red and black granules with only

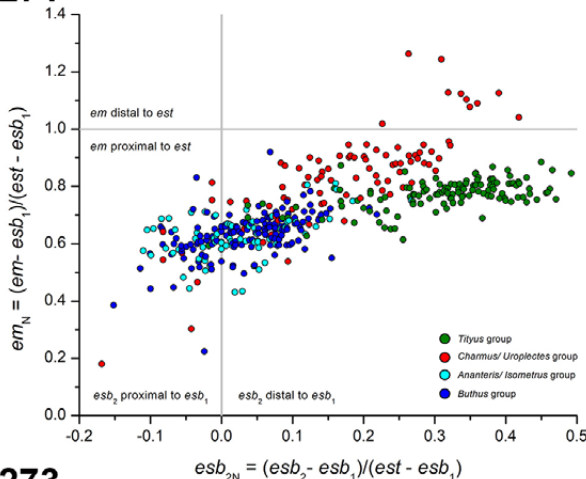
269



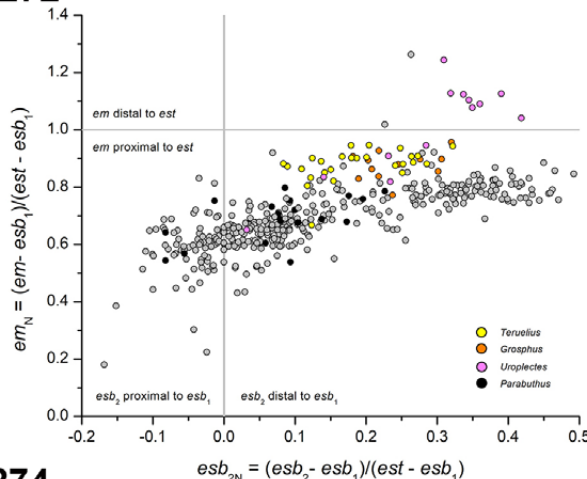
270



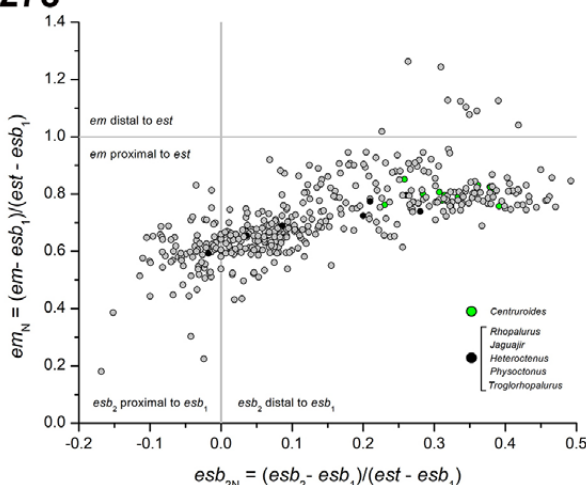
271



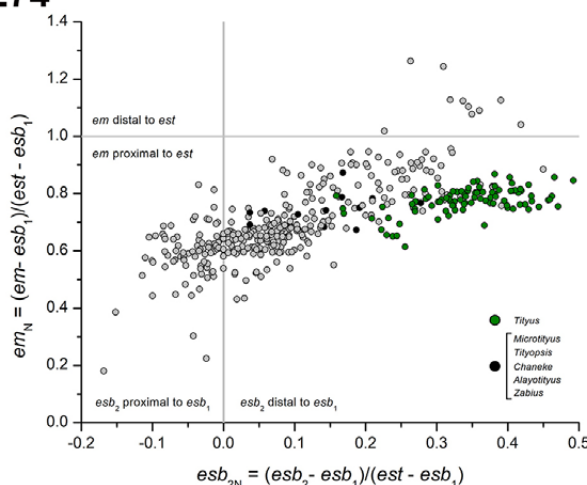
272



273



274



Figures 269–274. Analysis of position of patellar trichobothrium *esb*₂ relative to *esb*₁ and *em* in buthids. **Figure 269.** Ranked horizontal bar plot of axial position of *esb*₂ relative to *esb*₁, normalized to axial distance between *em* and *esb*₁ ($n = 435$ patellae, representing 395 species in 75 genera; 77% of recognized genera). Color codes: blue, ‘*Buthus*’ group ($n = 146$); cyan, ‘*Ananteris/ Isometrus*’ group ($n = 68$); red, ‘*Charmus/ Uroplectes*’ group ($n = 92$, including *Microcharmus variegatus*); green, ‘*Tityus*’ group ($n = 129$). Gray line: threshold ratio of +0.18 selected for character discretization. Insets: trichobothrial patterns of selected species and trichobothrial nomenclature in *Parabuthus abyssinicus* (external views, right patellae). **Figure 270.** Distributions of normalized axial positions of *esb*₂ relative to *esb*₁ in four main clades of buthids (color codes as in Fig. 269). Indicated are percentages of each group falling below and above discretization threshold. **Figure 271.** Bivariate scatter plot of normalized axial position of *em* relative to *esb*₁ vs. normalized axial position of *esb*₂ relative to *esb*₁ in buthids (sample and group color codes as in Fig. 269). Normalization by *est-esb*₁ distance. **Figures 272–274.** Bivariate scatter plots of data in Fig. 271 showing distributions of selected genera from ‘*Charmus/ Uroplectes*’ group (272) and ‘*Tityus*’ group (273–274).

small relative displacements. Along the carapace margins, red and black granules are precisely aligned, which is most easily seen along the anterior margin. However, fine details of granulation always show variation even among conspecifics. As an example, granule patterns on the anterior carapace of six adult males of the buthid *Compsobuthus maindroni* (Kraepelin, 1900) are compared in Figs. 253–258. No two specimens bear the same granulation patterns. Variation along the anterior margin is more visible in magnified views (Figs. 259–264). Fine granulation patterns are like fingerprints that are unique to each individual. In light of intra- and interspecific variation of granulation, the precisely matched patterns in Fig. 246 are highly improbable. The main difference between the two figures is the addition of a pair of anterior submedian carinae in *B. astartiae*, which are lacking in *B. haasi*. A more credible explanation of the granulation matches in Fig. 246 is that the *B. astartiae* illustration (Fig. 245) was traced from Vachon's *B. haasi* illustration (Fig. 244), and doctored by the addition of anterior submedian carinae. Indeed, the authors' own measurement data show that the carapace of *B. astartiae* is shorter than illustrated: carapace L/posterior W = 2.7/3.2 = 0.84 for *B. astartiae*, 2.8/2.9 = 0.97 for *B. haasi* (Stathi & Lourenço, 2003: 108, tab.1), vs. carapace L/posterior W = 0.97 for Fig. 245 (matching *B. haasi*, not *B. astartiae*).

A fifth example of image duplication was identified recently by Kovařík (2018). The pedipalp movable finger dentition of *Compsobuthus andresi* illustrated by Lourenço (2004: 159, fig. 1) is identical to the pedipalp movable finger dentition of *Compsobuthus williamsi* illustrated by Lourenço (1999: 86, fig. 2). All 82 illustrated median and subterminal denticles are located in the same positions. The only differences are a slight editing to erase part of the large terminal denticle, and the alteration of the scale bar to match the size of a different species (Kovařík, 2018: 3–4, figs. 1a, 1b, 6). However, numbers and positions of median denticles of pedipalp chelae normally show variation even among conspecifics. This appears to be another case of recycling an illustration of one species, to be reused in the description of another species. Considering the multiple similar cases of image duplication that we have deconstructed above, we reject the evidence of a metamerized basal piece shown in the 2013 figure of *M. variegatus*. Finally, in their most recent review of microcharmid family, Lourenço et al., (2019) again omitted mention of this character. Thus, there appears to be no credible evidence to support the validity of the metamerized basal piece as a character for the family Microcharmidae.

7. Absence of fulcra. This character also occurs in the buthids *Akentrobuthus*, *Ananteris*, *Ananteroides*, *Himalayotityobuthus*, *Lychas* sp., *Lychasioides*, *Microananteris*, *Pseudouroplectes* and *Tityobuthus* spp. Lourenço (2000: 879–880) stated that *Neoprotobuthus intermedius* lacks fulcra, in both the generic diagnosis ("Peignes très petits, sans fulcres ...") and species description ("absence des fulcres"), and listed the absence as a microcharmid family character ("Fulcres absents"). This directly contradicted the figure in his own paper showing pectines with fulcra (Lourenço, 2000: 881, fig. 5). These fulcra

are also readily visible in a photograph of the paratype (Ref. MNHN-RS-RS9031). Inclusion in the microcharmid family of *Neoprotobuthus*, which possesses fulcra, weakened this to a genus level character, inapplicable to the whole family.

8. Lack of tibial spurs. This character also occurs in the buthids *Afroisometrus*, *Akentrobuthus*, *Astibothrus*, *Isometrus*, *Lanzatus*, *Liobuthus*, *Pectinibuthus*, *Plesiobuthus*, *Tityobuthus*, *Vachoniulus* and all members of the 'Tityus' group. The proposed character is inconsistent at the family level because *Neoprotobuthus* has tibial spurs reduced but not absent, and tibial spurs in several *Microcharmus* species were described as being lost on leg III, but present on leg IV (e.g., Lourenço, 2004a; Lourenço et al., 2006, 2019).

9. Cheliceral movable finger with two small basal teeth that may or may not be fused; distal external tooth smaller than distal internal tooth. Small, or small and fused basal teeth also occur in other small buthids: *Akentrobuthus*, *Butheoloides*, *Femtobuthus*, *Microbuthus*, *Picobuthus*, *Pseudolissotus*, *Pseudouroplectes* and *Tityobuthus*. A smaller distal external tooth also occurs in the buthids: *Akentrobuthus*, *Egyptobuthus* and *Somalicharmus*. In examined paratypes of *Microcharmus variegatus*, we observed that the size of the distal external tooth was similar to that of the distal internal tooth, showing that this character is variable within the genus. Addition to the microcharmid family of *Neoprotobuthus*, which has distal external and internal teeth of equal size, weakened this to a genus level character inapplicable to the whole family (Lourenço, 2000: 878).

10. Pedipalp patella without ventral trichobothria. This character is shared with all buthids and does not separate Microcharmidae from Buthidae.

11. Telson vesicle small, long, without subaculear tubercle. This character also occurs in the buthids *Anomalobuthus*, *Baloorthochirus*, *Birulatus*, *Fetilinia*, *Isometroides*, *Lanzatus*, *Neogrosphus*, *Orthochirus*, *Picobuthus* and *Pseudouroplectes*.

12. Sensillar pegs on pectine teeth subcylindrical, bottle-like (not spatulate). This character occurs also in the buthids *Ananteris* sp., *Lychasioides*, *Microananteris* and *Tityobuthus rakotondravonyi* (Botero-Trujillo & Noriega, 2011; Lourenço, 2003c; Lourenço & Goodman, 2003b).

13. Hemispermatophore with trunk wider at base, lacking truncal flexure, hook and flagellum. A basally wider trunk is a common feature that occurs in the majority of buthids, including: *Ananteris*, *Androctonus*, *Babycurus*, *Barbaracurus*, *Buthacus*, *Butheolus*, *Buthoscorpio*, *Buthus*, *Chaneke*, *Charmus*, *Centruroides*, *Compsobuthus*, *Grosphus*, *Heteroctenus*, *Hottentotta*, *Jaguajir*, *Karasbergia*, *Lanzatus*, *Leiurus*, *Lissothus*, *Mesobuthus*, *Microbuthus*, *Microtityus*, *Neobuthus*, *Neogrosphus*, *Orthochiroides*, *Parabuthus*, *Pseudolychas*, *Rhopalurus*, *Teruelius*, *Tityus*, *Trypanothacus* and *Uroplectes*. Lack of a truncal flexure is also a general character of buthids. Lack of a basal lobe (= hook) could be a primitive pre-buthid condition, as in chaerilids. Buthid hemispermatophores that have been studied all possess some form of basal lobe, although it may be reduced (e.g., in *Babycurus* sp., *Xenobuthus*; Kovařík et al., 2018b; Lowe, 2018). Lack of a flagellum would also be a major difference from all known buthid hemispermatophores.

Lourenço (2002) showed an SEM image of a hemispermatophore of *Microcharmus fisheri* (Lourenço, 2002: 45, fig. 18; republished in Lourenço et al., 2006: 757, fig. 21), and stated that both the flagellum and the hook seemed to be missing: “Deux structures importantes semblent absentes dans la portion distale: le petit crochet ou lobe basal et surtout le flagelle” (Lourenço, 2002: 37). Lourenço et al. (2019: 28) referred to “preliminary results” from examining 3–4 microcharmids (no data shown) in which “the small hook and the flagellum, appear to be absent ...” and stated that “the flagellum if present is clearly reduced”. We extracted and examined both hemispermatophores from a paratype male of *Microcharmus variegatus*. The hemispermatophore of *Microcharmus* is long, narrow and widened basally, similar to that of many buthids. It bears a ‘cylindrical gland’ halfway down its trunk, and at its base near the pedicel is an ‘oval gland’ (Figs. 217–218), both of which have been described in paraxial organs of buthids (e.g., *Centruroides*, *Leiurus*, *Parabuthus*, *Tityus* and *Uroplectes*; Abd-El-Wahab, 1957: 113, fig. 1A, 116; Alexander, 1959: 153, fig. 3; Francke, 1979: 30; Lamoral, 1979: 526, fig. 31; Pavlovsky, 1924a: 85, figs. 7–12). The distal end bears a capsule with no truncal flexure, as in buthids. The capsule is elongated, with a simple undivided sperm hemiduct, a single fold or carina, and a blunt, scoop-like basal lobe (Figs. 215–216). It is similar to those of several other genera of small buthids, including *Charmus* (Figs. 229–231), *Buthoscorpio* (Figs. 222–223; see also Kovařík et al., 2016: 10, 13, figs. 30–33, 47) and *Thaicharmus* (Figs. 219–220). The capsule tapers and connects to a short, translucent flagellum that is distally dilated and partially coiled (Figs. 211–212). Thus, the hemispermatophore of *Microcharmus* is similar in architecture to those of several buthids and the male genital apparatus appears consistent with the ‘complex’ type described in buthids (Pavlovsky, 1924a).

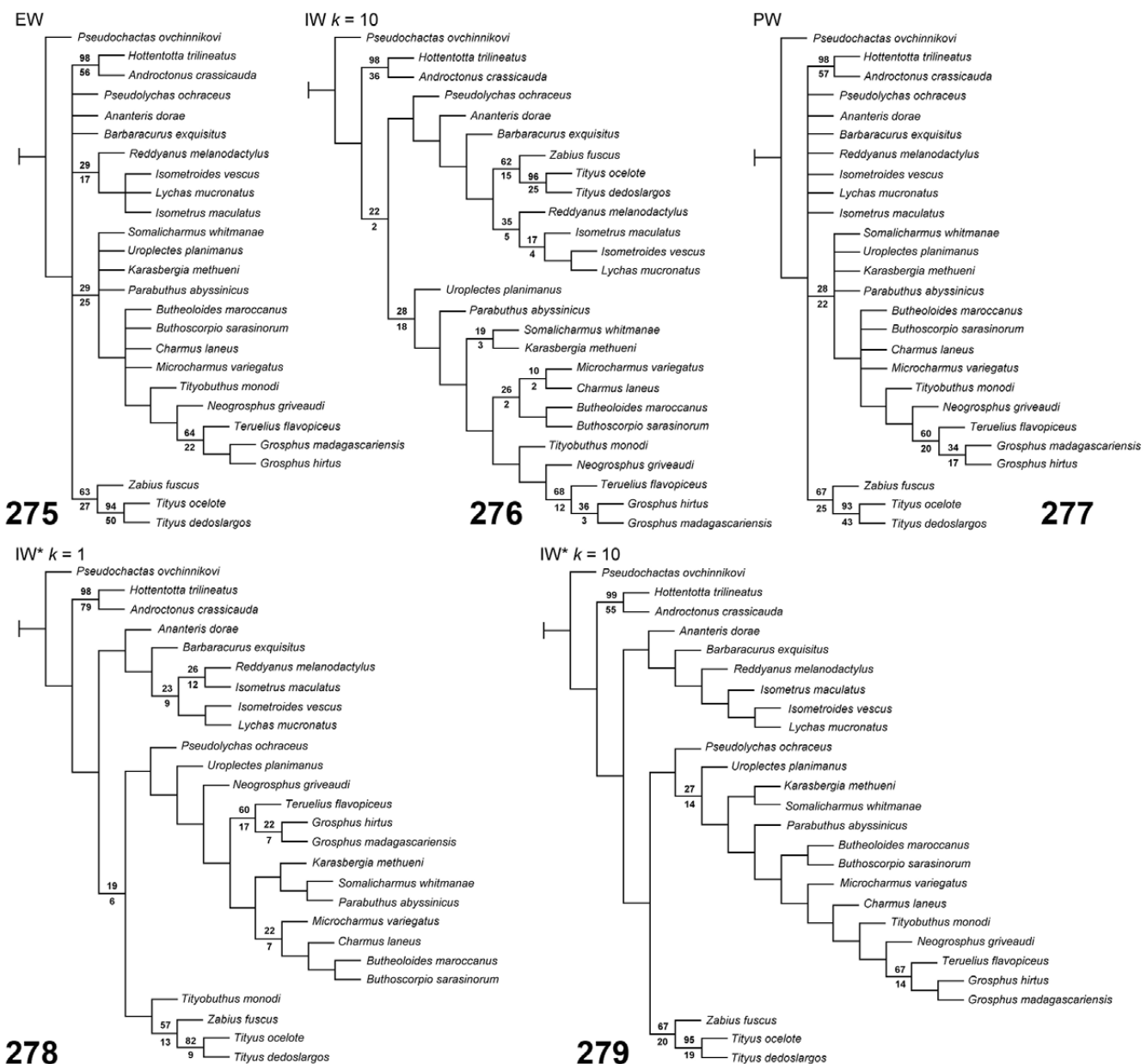
In conclusion, diagnostic characters of Microcharmidae are either invalid {5, 6, 7, 8, 9, 13}, or shared with buthids {1, 2, 3, 4, 7, 8, 10, 11, 12, 13}. The family diagnosis rests on a specific combination of characters found in buthids, not on unique characters that separate microcharmids from buthids. Applying the same logic to buthids would lead to the elevation of many buthid genera to family rank, which we can hardly recommend. However, overlap of characters does not necessarily exclude lineages of higher taxonomic rank. Characters are imperfect clues to phylogeny that can be obscured by homoplasy. Does the combination of characters found in microcharmids support their hypothesized position as a basal lineage and sister group of buthids, deserving family status? To address this question, we applied phylogenetic analysis with parsimony to explore the relationship of *Microcharmus* to buthids.

Our ingroup included *M. variegatus*, material of which we studied in detail, and 24 exemplar buthid species from 22 genera (Table 11), sampling the diversity of all four major buthid lineages resolved by molecular phylogeny and trichobothrial analysis (Fet et al., 2005; Štundlová et al. 2022): 2 species from the ‘*Buthus*’ group (*Hottentotta trilineatus*, *Androctonus crassicauda*); 6 from the ‘*Ananteris*/

Isometrus’ group (*Barbaracurus exquisitus*, *Ananteris dorae*, *Isometrus maculatus*, *Lychas mucronatus*, *Isometroides vescus*, *Reddyanus melanodactylus*), 13 from the ‘*Charmus/Uroplectes*’ group (*Somalicharmus whitmanae*, *Uroplectes planimanus*, *Pseudolychas ochraceus*, *Charmus laneus*, *Buthoscorpio sarasinorum*, *Butheoloides maroccanus*, *Neogroosphus griveaudi*, *Groosphus madagascariensis*, *Groosphus hirtus*, *Teruelius flavopiceus*, *Karasbergia methueni*, *Parabuthus abyssinicus*, *Tityobuthus monodi*), and 3 from the ‘*Tityus*’ group (*Zabius fuscus*, *Tityus dedoslargos*, *Tityus ocelote*). The ‘*Charmus/Uroplectes*’ group was emphasized because some of its genera share characters with *Microcharmus*, and because it includes all buthids endemic to Madagascar (where *Microcharmus* also resides). The outgroup taxon selected to root the tree and polarize characters was *Pseudochactas ovchinnikovi* Gromov, 1998. Pseudochactids have been hypothesized to be a sister group of buthids (Coddington et al., 2004; Prendini et al., 2006) and phylogenomic studies support such a relationship for a clade that includes pseudochactids and chaerilids (Sharma et al., 2015, 2018).

We analyzed 35 discrete morphological characters, selected either for their utility in diagnosing existing buthid genera, or for their ability to differentiate between the four major buthid lineages (Table 10). We did not include some characters well known to exhibit convergence in widely divergent taxa. Examples are bristlecombs on the tarsi, or a subaculear tubercle on the telson, both of which have evolved independently in multiple families. Since our aim was to test a family level hypothesis, we avoided certain characters which are variable at the subgeneric or species level, e.g., fine details of morphosculpture, setation and color patterns, often used to separate more closely related species. These could add noise and potentially obscure higher level relationships in our small sample of exemplar species. Our character set emphasized trichobothrial patterns (10 characters) and hemispermatophore morphology (6 characters). It included the characters analyzed by Fet et al. (2005) (coded here conventionally) that resolved the major buthid groups later supported as lineages in molecular studies (Borges & Graham, 2016; Ojanguren-Affilastro et al., 2017; Santibáñez-López et al., 2020; Štundlová et al. 2022).

The analysis of a small set of exemplar buthids and a restricted set of characters might be criticized on the grounds of poor taxon sampling and subjective choice of characters (Prendini & Wheeler, 2005). However, we selected representatives of all the major buthid lineages resolved by DNA analyses, while avoiding atypical taxa with apparently highly derived morphologies differing conspicuously from the majority of species in those lineages. Published data and keys indicate that most of our selected characters are generally conserved at lower subgeneric or species levels, while varying systematically at higher suprageneric levels (e.g., Fet et al., 2005, characters 4, 5, 7, 28; Kovařík, 2009: 21–24; Kovařík et al., 2018: 10, characters 17–18; Lowe et al., 2014: 120, fig. 9, character 13; Sissom, 1990; Stahnke, 1972b). We present new analyses showing higher level variation for two of the



Figures 275–279. Examples of MPTs of buthids and *Microchermus variegatus* retrieved by analysis of 35 discrete morphological characters (Tables 10–11), rooted by outgroup *Pseudochactas ovchinnikovi*, under equal weights (strict consensus of 20 MPTs of equal length) (275), implied weights with concavity constant $k = 10$ (276), prior weights with character 5 weight = 2, other character weights = 1 (strict consensus of 112 MPTs of equal length) (277), and implied weights with character 5 prior weight = 2, other character prior weights = 1, and with concavity constants $k = 1$ (278) and $k = 10$ (279). Numbers above nodes are jackknife by symmetric resampling supports, those below relative Bremer supports.

characters (Figs. 263–270, characters 8, 10; see below). Our aim was only to test the hypothesis that *Microchermus* resides outside the buthid family, not to resolve in finer detail the phylogeny of buthids down to the level of genera and species.

One trichobothrial character of *Microchermus variegatus* that we scored differently from the recorded literature was character 14 (relative position of chela fixed finger *db* vs. *est*). The illustration in Lourenço et al. (2006: 760, fig. 27; reproduced here in Fig. 214) appears to show *db* distal to *est* in the holotype female, contrasting with other species in

which *db* was illustrated as proximal to *est* (i.e., *M. andrei*, cf. Lourenço et al., 2019: 29, fig. 3; *M. bemaraha*, cf. Lourenço et al., 2006: 766, fig. 40; *M. confluenciatus*, cf. Lourenço et al., 2006: 772, fig. 49; *M. maculatus*, cf. Lourenço et al., 2006: 760, fig. 37; *M. pauliani*, cf. Lourenço et al., 2006: 769, fig. 44). Relative position of *db* vs. *est* can vary intraspecifically, and the illustrated position in *M. variegatus* may be atypical. We found *db* to be proximal to *est* in a male paratype of *M. variegatus* (Figs. 210–213), similar to other species of the genus, so we scored this character accordingly.

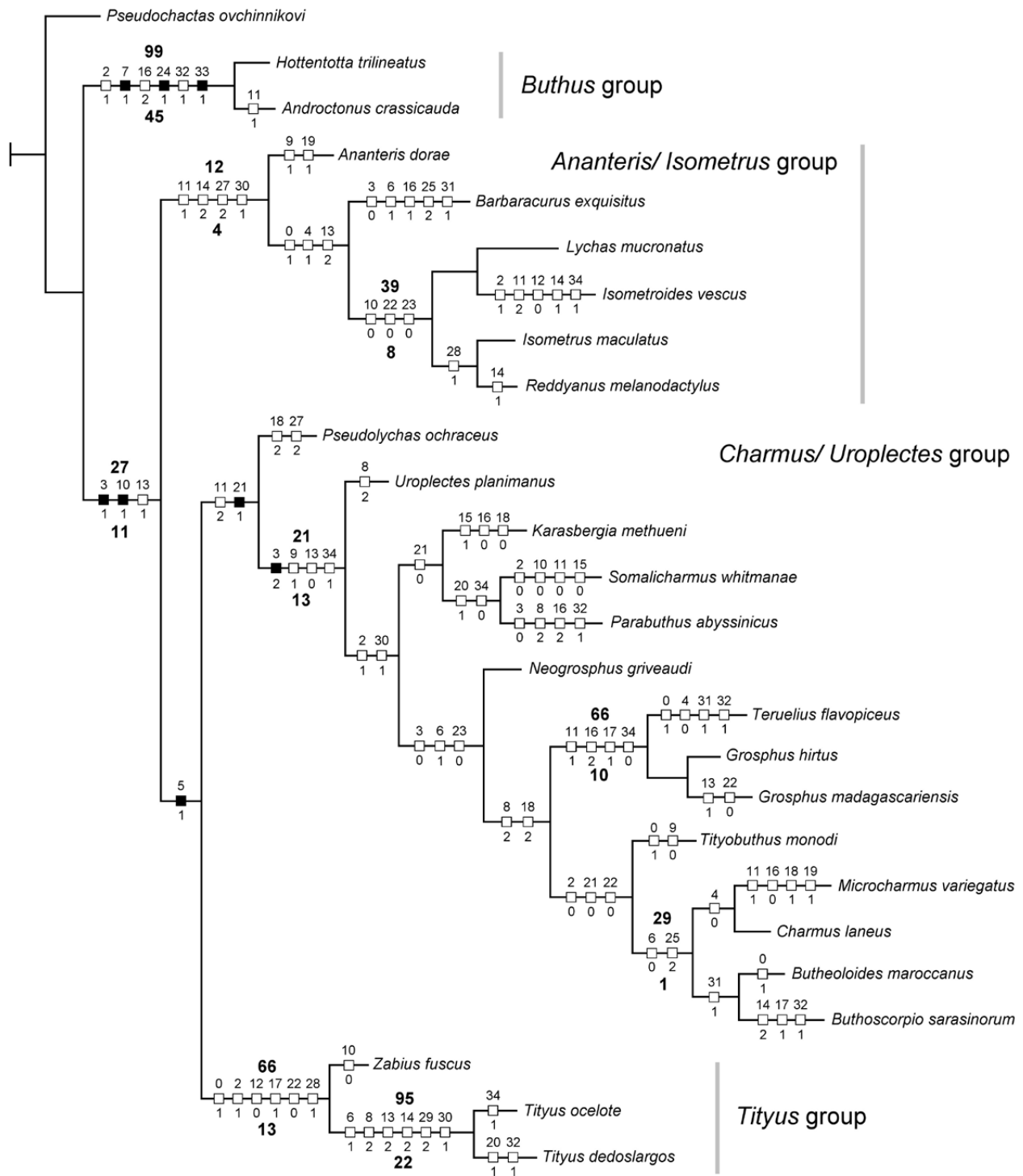
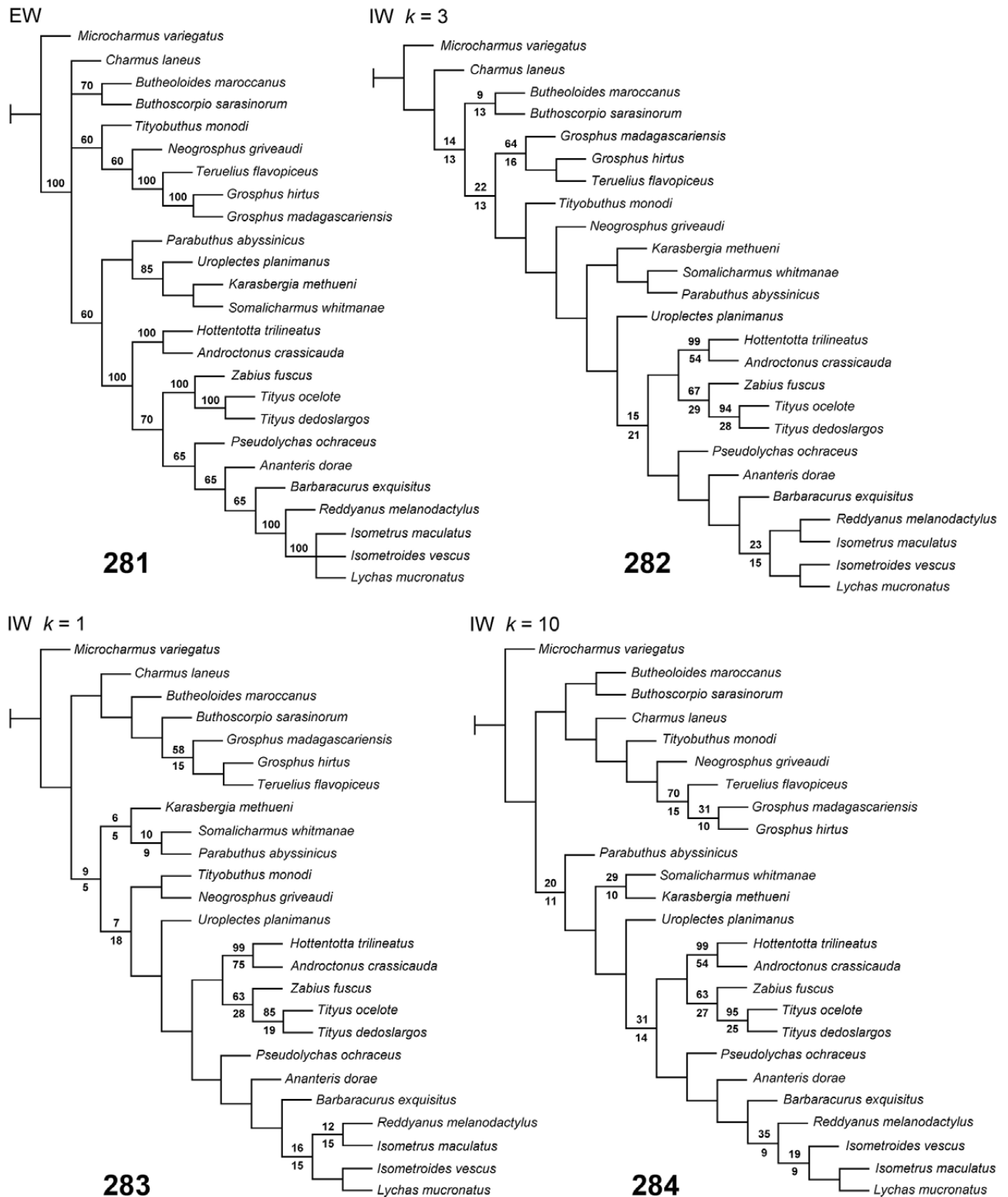
IW* $k = 6$ 

Figure 280. Example MPT of buthids and *Microcharmus variegatus* retrieved by analysis of 35 discrete morphological characters (Tables 10–11), rooted by outgroup *Pseudochactas ovchinnikovi*, under implied weights with concavity constant $k = 6$ and character 5 prior weight = 2, other character prior weights = 1. Boxes indicate unambiguous synapomorphies, filled boxes unique (derived once with reversals allowed), and open boxes homoplasious (derived more than once) synapomorphies. Numbers above boxes are character identifiers, those below boxes derived character states. Numbers above nodes are jackknife by symmetric resampling supports, those below relative Bremer supports. Vertical gray bars mark four major buthid clades resolved by previous trichobothrial and DNA analyses (Fet et al., 2005; Štundlová et al. 2022).



Figures 281–284. Examples of MPTs of buthid exemplar taxa retrieved by analysis of 35 discrete morphological characters (Tables 10–11), rooted by outgroup *Microcharmus variegatus*, under equal weights (majority rule consensus of 20 trees, 50% cut) (281), and implied weights with concavity constants $k = 1$ (282), $k = 3$ (283) and $k = 10$ (284). Numbers above nodes in Fig. 281 are percentages of MPTs. Numbers above nodes in Figs. 282–284 are jackknife by symmetric resampling supports, those below relative Bremer supports.

	N _{MPT}	Steps	CI	RI	S _{CU}
EW	20	139	0.345	0.633	29
IW k = 1	1	147	0.327	0.601	9
IW k = 2	1	142	0.338	0.621	22
IW k = 3	1	142	0.338	0.621	25
IW k = 4	1	142	0.338	0.621	26
IW k = 6	1	142	0.338	0.621	26
IW k = 8	1	142	0.338	0.621	25
IW k = 10	1	139	0.345	0.633	28
IW k = 15	1	139	0.345	0.633	31
IW k = 30	2	139	0.345	0.633	33
IW k = 60	1	141	0.340	0.625	34
PW	112	142	0.345	0.637	28
IW* k = 1	1	151	0.325	0.602	22
IW* k = 2	1	147	0.333	0.617	26
IW* k = 3	1	147	0.333	0.617	28
IW* k = 4	2	144	0.340	0.629	29
IW* k = 6	2	144	0.340	0.629	29
IW* k = 8	4	142	0.345	0.637	27
IW* k = 10	4	142	0.345	0.637	27
IW* k = 15	4	142	0.345	0.637	29
IW* k = 30	4	142	0.345	0.637	31
IW* k = 60	4	142	0.345	0.637	31

Table 12. Statistics of most parsimonious trees (MPTs) retrieved by cladistic analysis of the discrete character matrix of Table 11, rooted by outgroup *Pseudochactas ovchinnikovi*. **EW**, equal weights; **IW** implied weights; **PW**, prior weights (character 5 with weight = 2, other characters with weight = 1); **IW*** implied weights under prior weighting; **k** = concavity constant; N_{MPT}: number of MPTs; **Steps**: tree lengths; **CI**: tree consistency index; **RI**: tree retention index; **SCU**, maximum jackknife with symmetric resampling support of clade including *Microcharmus variegatus* and species from the ‘*Charmus/ Uroplectes*’ group.

We analyzed two other trichobothrial characters to justify their choice as higher level buthid characters. Character 10, the position of manus *Eb*₂ relative to manus *Eb*₁ along the proximal-distal axis, was found to be strongly correlated with membership in three of the four major buthid lineages (Fig. 267). This was related to another character, namely the orientation of the non-reflex angle formed by the *Eb*₁-*Eb*₂-*Eb*₃ triad (δ = distal, γ = proximal, λ = linear) previously used in some generic diagnoses (e.g., Lowe & Kovařík, 2019). The two characters were correlated (Fig. 268), so we included only one in the analysis. Character 8, the position of patella *eb*₂ relative to patella *eb*₁, was hypothesized by Fet et al. (2005: 10) to be diagnostic for major buthid lineages, based on a preliminary qualitative survey. We expanded the survey to include a much larger sample and undertook a quantitative analysis of *eb*₂-*eb*₁ separation. We confirmed a strong correlation of this character with membership in buthid lineages (Fig. 269). As a discretized binary character, it achieved ~90% separation of ‘*Buthus*’ and ‘*Ananteris/ Isometrus*’ groups from the ‘*Tityus*’ group, while the ‘*Charmus/ Uroplectes*’ group was internally split in a ~60%/ 40% ratio (Figs. 270–271). As a morphometric character, it was also capable of separating some genera from others within the buthid groups (e.g., Figs. 272–274).

Hemispermatophores (characters 23–28) have been described for all genera represented in our buthid ingroup with the exception of *Tityobuthus*. Figs. 224–228 show that the hemispermatophore of *Tityobuthus* has a long, narrow trunk and a short capsule with a simple, monocarinate sperm hemiduct. It was similar in its general construction to the hemispermatophores of *Charmus* (Figs. 229–231) and *Thaicharmus* (Figs. 219–221). Distinctive features included a basal lobe forming a long, bent hook, and a tapered flagellum with short distal section.

We analyzed the character matrix in Table 11 under equal weights, and implied weights with strong, moderate and weak concavities ($k = 1$ –60). Under equal weights, 20 MPTs were retrieved, for which the strict consensus tree is shown in Fig. 275. The ‘*Buthus*’ and ‘*Tityus*’ groups were consistently recovered with strong support. The ‘*Charmus/ Uroplectes*’ group was mostly recovered with modest support (except for *Pseudolychas*), and the ‘*Ananteris/ Isometrus*’ group was more fragmented. Under implied weights with strong to moderate concavity ($k = 1, 2, 3, 4, 6, 8$), all four major buthid lineages were consistently recovered, except that *Pseudolychas* was a basal member of the ‘*Ananteris/ Isometrus*’ group. Under implied weights with moderate



Figure 285. *Grosphus angulatus* sp. n., habitus. Holotype female, dorsal view. Scale bar: 5 mm.

concavity ($k = 10, 15$), the ‘*Buthus*’ group, and most of the ‘*Charmus/ Uroplectes*’ group were recovered. The ‘*Tityus*’ group, and again *Pseudolychas*, were merged with the ‘*Ananteris/ Isometrus*’ group (e.g., $k = 10$, Fig. 276). Under implied weights with weak concavity ($k = 30, 60$), only the ‘*Buthus*’ group was recovered. The higher numbers of MPTs under equal weights vs. implied weights (Table 12, upper panel), and unreliable recovery of major buthid lineages under implied weights of weak concavity, are signs of homoplasy in the character set.

The genus *Pseudolychas* has α trichobothriotaxy on the femur, but in the above analyses it was associated with the ‘*Ananteris/ Isometrus*’ group, which has β trichobothriotaxy. This conflicts with the division of buthids into mutually exclusive α vs. β lineages by a single α derivation in Fet et al., 2005. Evidence supporting division by a single α derivation comes from the molecular phylogeny of Štundlová et al. (2022) reconstructed from DNA samples of 228 buthid species representing 52 genera (although *Pseudolychas* was not included). Placement of ‘*Tityus*’ group species (with



Figure 286. *Grosphus angulatus* sp. n., habitus. Holotype female, ventral view. Scale bar: 5 mm.

α trichobothriotaxy) within the ‘*Ananteris/ Isometrus*’ group (Fig. 276), also contradicts the α vs. β division. To resolve these conflicts, we repeated the exploratory analyses allowing α vs. β (character 5) to exert a stronger influence by arbitrarily assigning it twice the weight of the other characters, thereby increasing its homoplasy cost. Under this prior weighting condition, 112 MPTs were retrieved, for which the strict consensus tree is shown in Fig. 277.

Comparison with Fig. 275 shows that recovery of the major buthid lineages was not improved. However, under implied weighting, MPT counts were reduced and unique solutions emerged under strong concavity (Table 12, lower panel). Under implied weights with strong to moderate concavity ($k = 1, 2, 3, 4, 6$), all four major buthid lineages were consistently recovered and *Pseudolychas* was resolved as the basal member of the ‘*Charmus/ Uroplectes*’ group. The

		<i>Groshus angulatus</i> sp. n.	<i>Groshus angulatus</i> sp. n.	<i>Groshus angulatus</i> sp. n.
Dimensions (mm)		♀ holotype	♀ paratype	♀ paratype
Carapace	L / W _a / W	5.97 / 3.17 / 6.56	5.93 / 3.42 / 7.05	5.85 / 3.15 / 6.54
preocular	L	2.25	2.25	2.17
Metasoma I	L / W / D	3.33 / 3.61 / 3.01	3.21 / 3.63 / 3.25	3.08 / 3.54 / 3.04
Metasoma II	L / W / D	3.88 / 3.58 / 3.42	3.96 / 3.60 / 3.17	3.83 / 3.58 / 3.08
Metasoma III	L / W / D	4.21 / 3.57 / 3.13	4.25 / 3.54 / 3.17	4.23 / 3.54 / 3.17
Metasoma IV	L / W / D	5.00 / 3.50 / 3.23	5.08 / 3.50 / 3.06	5.00 / 3.49 / 3.02
Metasoma V	L / W / D	6.19 / 3.33 / 3.00	6.17 / 3.32 / 3.08	6.05 / 3.29 / 2.92
Telson	L / W / D	– / 2.82 / 2.78	6.54 / 2.90 / 2.78	6.38 / 2.86 / 2.65
Vesicle	L	4.25	4.29	4.20
Pedipalp				
Femur	L / W	4.58 / 1.84	4.83 / 1.78	4.67 / 1.71
Patella	L / W	5.53 / 2.69	5.67 / 2.61	5.58 / 2.53
Chela	L	9.29	9.59	9.42
Manus	L / W / D	4.08 / 2.45 / 2.32	4.25 / 2.49 / 2.47	4.08 / 2.45 / 2.33
Movable finger	L	5.33	5.58	5.42
denticle subrows	left / right	10*/ 13	13 / 13	13 / 13
Fixed finger	L	4.50	4.54	4.50
denticle subrows	left / right	12 / 12	11 / 9*	12 / 12
Pectine	L	3.92	4.11	3.88
Total	L	51	48.5	50.5
PTC	left / right	14 / 15	15 / 14	14 / –

Table 13. Comparative measurements of holotype and two paratypes of *Groshus angulatus* sp. n. Abbreviations: length (L), width (W), anterior width (W_a), depth (D), pectinal tooth count (PTC). Carapace anterior width is measured between inner margins of foremost pairs of lateral eyes, carapace preocular length between middle of median eyes and anterior limit of carapace. Metasomal segment lengths are measured between posterior limit of segment and anterior limit of dorsosubmedian carinae. Pedipalp movable finger denticle subrow counts include the short subdistal subrow. Pedipalp chela manus length is ventral length from proximal limit to movable finger external articular condyle. Segment widths and depths include spiniform granules. * Malformed denticle subrows.

only disagreement with groupings of Fet et al. (2005) was association of *Tityobuthus* with the ‘*Tityus*’ group (Fig. 278) for $k = 1$, which nonetheless respects single α derivation. Under implied weights with moderate to weak concavities ($k = 8, 10, 15, 30, 60$), 4 MPTs were retrieved, half of which associated *Pseudolychas* with the ‘*Ananteris/ Isometrus*’ group, consistent with a greater influence of homoplasious characters. Fig. 279 shows an example MPT ($k = 10$) in which all four major buthid DNA lineages were recovered with single α derivation. Fig. 280 shows another such MPT retrieved under moderate concavity ($k = 6$) with unambiguous synapomorphies mapped to its nodes.

In all retrieved MPT topologies, *Microchermus* was not basal to the buthids, and was usually associated with taxa of the ‘*Charmus/ Uroplectes*’ group (e.g., Figs. 275–280). This justifies including *Microchermus* in the set of outgroup taxa used to analyze *Groshus* and *Teruelius*. Support values of nodes in the ‘*Charmus/ Uroplectes*’ group that contained *Microchermus* were modest (Table 12, right column), and the relationship of *Microchermus* to the taxa representing that group varied under different parameters. This lower

level instability was not unexpected, since our character set was focused on higher level relationships. Nevertheless, all placements of *Microchermus* in the retrieved MPTs would render Buthidae paraphyletic if Microchermidae were retained as a family. This agrees with previously reported findings (Coddington et al., 2004; Volschenk et al., 2008). Similarly, if Microchermidae were demoted to a subfamily of Buthidae, then all other buthids in the nominotypic subfamily Buthinae would be rendered paraphyletic.

The hypothesis that *Microchermus* belongs in a basal sister group of the buthids can be tested in another way. If the buthid data (Table 11) are reanalyzed with *M. variegatus* as outgroup taxon, the hypothesis predicts that we should be able to recover phylogenies that resemble to some extent the results of the buthid DNA analysis, i.e., with the four major lineages more or less intact and related to each other in similar topologies (Štundlová et al., 2022). This was not the case. Under all tested weighting schemes (EW, IW $k = 1–60$), buthid MPTs rooted on *Microchermus* failed to recapitulate the molecular phylogeny (e.g., Figs. 281–284). The ‘*Buthus*’ and ‘*Tityus*’ groups were resolved as sister clades, while the

‘*Charmus/ Uroplectes*’ group was paraphyletic and basal. The latter result reflects the association of *Microcharmorbus* with some members of the ‘*Charmus/ Uroplectes*’ group.

The absence of unique diagnostic characters separating microcharmidids from buthids, and the absence phylogenetic evidence supporting microcharmidids as a lineage separate from buthids, justify the synonymy of Microcharmididae with Buthidae.

Systematics

Family Buthidae C. L. Koch, 1837

Microcharminae Lourenço, 1996b: 6, 27; Lourenço, 1998b: 69; **syn n.**

Microcharmididae Lourenço, 1998a: 845–847; Lourenço, 1999d: 843; Fet, 2000: 421; Lourenço, 2000a: 877–879; Soleglad & Fet, 2001: 4, 18–19; Lourenço, 2002: 35–40; Lourenço, 2003a: 575, 577; Lourenço, 2003c: 1150; Soleglad & Fet, 2003a: 3, 5, 10, 25, 27, 30; Soleglad & Fet, 2003b: 1–2, 4, 8, 67, 88–91, 120; Lourenço, 2004a: 77–78; Fet et al., 2005: 4, 14–15, 26–27; Lourenço, 2005: 52; Prendini & Wheeler, 2005: 448, 465, 482; Lourenço et al., 2006: 751; Volschenk et al., 2008: 666; Kovařík, 2009: 4, 6, 17, 21, 33; Lourenço, 2009: 135; Lourenço & Goodman, 2013: 50; Lourenço et al., 2019: 26–28; Lourenço, 2021: 1, 6; **syn n.**

DIAGNOSIS. Pedipalps with type A trichobothriotaxy (Vachon, 1974); chela fixed finger with trichobothrium *it* normally positioned distally (except in *Karasbergia* and *Somalicharmus*); cheliceral movable finger with 2 basal denticles, 1 median and 1 subdistal denticle on dorsal margin, normally 2 denticles on ventral margin (Vachon, 1963); lateral eyes in 2–5 pairs (Loria & Prendini, 2014); sternum type I with horizontal compression (Soleglad & Fet, 2003a); coxapophyses of leg I not anteriorly expanded; leg coxae IV elongate; basitarsi with prolateral and retrolateral spurs; telotarsi with socketed macrosetae on ventral surface; hemispermatophore flagelliform, capsule bauplan 0-fold (Monod et al., 2017), basal lobe normally present; ovariuterus with 2-, 8- or 9-cell topology (Volschenk et al., 2008), embryonic development apoikogenic; lateral lymphoid organs absent (Pavlovsky, 1924b; Volschenk et al., 2008); metasoma V with 5 carinae, including a single ventromedian carina, lateral carinae absent; pedipalp patella normally with dorsomedian carina; dentate margins of pedipalp chela fingers with median denticles normally arranged in linear or oblique rows; venom glands thick-walled, complex, folded.

REMARKS. The above diagnosis is partly hypothetical because the internal characters have not been confirmed for all species (> 1,320) assigned to the family. A confirmed diagnosis can be selected by restriction to external characters that have been documented in published descriptions. ‘Normally present’ character states are those expressed in most taxa except for a small minority of cases.

Grosphus Simon, 1880

Grosphus Lowe & Kovařík, 2019: 7; Lourenço et al., 2020: 15 (in part). For earlier synonymies, see Lowe & Kovařík, 2019: 7.

TYPE SPECIES. *Scorpio (Androctonus) madagascariensis* Gervais, 1843.

DIAGNOSIS. Small to medium-sized buthids, adult length 25–75 mm; anterosubmedian carinae of carapace absent; median ocular tubercle located in posterior 2/3 of carapace; fixed finger of chelicera with 2 denticles on ventral surface; pedipalp femur with trichobothria d_1 - d_3 - d_4 non-reflex angle opening externally (retrolaterally) (α -configuration; Vachon, 1975); femur petite ‘trichobothrium’ d_2 position internal; pedipalp patella trichobothrium d_3 position external (retrolateral) to dorsomedian carina (DM) (Fet et al., 2005); pedipalp patella trichobothrium esb_2 distal to esb_1 (mean distance > 0.18 esb_1 -*em* distance); pedipalp chela manus with trichobothrium Eb_2 distal to Eb_1 , trichobothrium V_2 medial, located behind V_1 along proximo-distal axis of manus; chela manus with petite ‘trichobothrium’ Eb_3 usually well separated from Eb_2 , by more than half the distance between Eb_1 and Eb_2 ; pedipalp fixed finger with trichobothrium db in middle 30%–60% of finger, trichobothrium *it* distal; pedipalp chela movable finger with 11–16 imbricated subrows of median denticles, each flanked proximally by 2 enlarged external accessory denticles; chela movable finger typically with 4 external subdistal granules; pedipalp manus with weak or obsolete carination; pectines with fulcra; internal and accessory internal fulcra present, rounded, sclerotized, fluorescent; female basal middle lamella (*bml*) not dilated, female basal pectinal tooth (*bpt*) modified but not distinctly longer than other teeth, dilated, oval, subrectangular or subtriangular; pectinal tooth count (excluding ♀ *bpt*): ♂ 15–24, ♀ 12–22; hemispermatophore capsule long or short, posterior lobe with long, lanceolate extension; legs III–IV with tibial spurs present; leg IV, mean ratio of tibial spur L/tibia distal D: < 0.69; legs I–IV, telotarsi with ventral setation sparse, discrete with < 25 setae in rows; tergites III–VI monocarinate; sternites with spiracles broad, hemi-elliptical or ovoid, sternite IV spiracle L/W < 5; tergite VII, sternite VII and metasomal segments I–III without microsetal fringes on posterior margins; metasoma I ventrosubmedian carinae granulate or costate-granulate; telson with oval or bulbous vesicle, with or without subaculear tubercle in adults; cuticle with weak UV fluorescence.

REMARKS. The above standard diagnosis is partly hypothetical because some characters have not been confirmed for all 14 species assigned to the genus. For a confirmed differential diagnosis, see below under AFFINITIES.

SUBORDINATE TAXA.

Grosphus ambre Lourenço, Wilmé & Waeber, 2018

Grosphus angulatus sp. n.

Grosphus darainensis Lourenço, Goodman & Ramilijaona, 2004

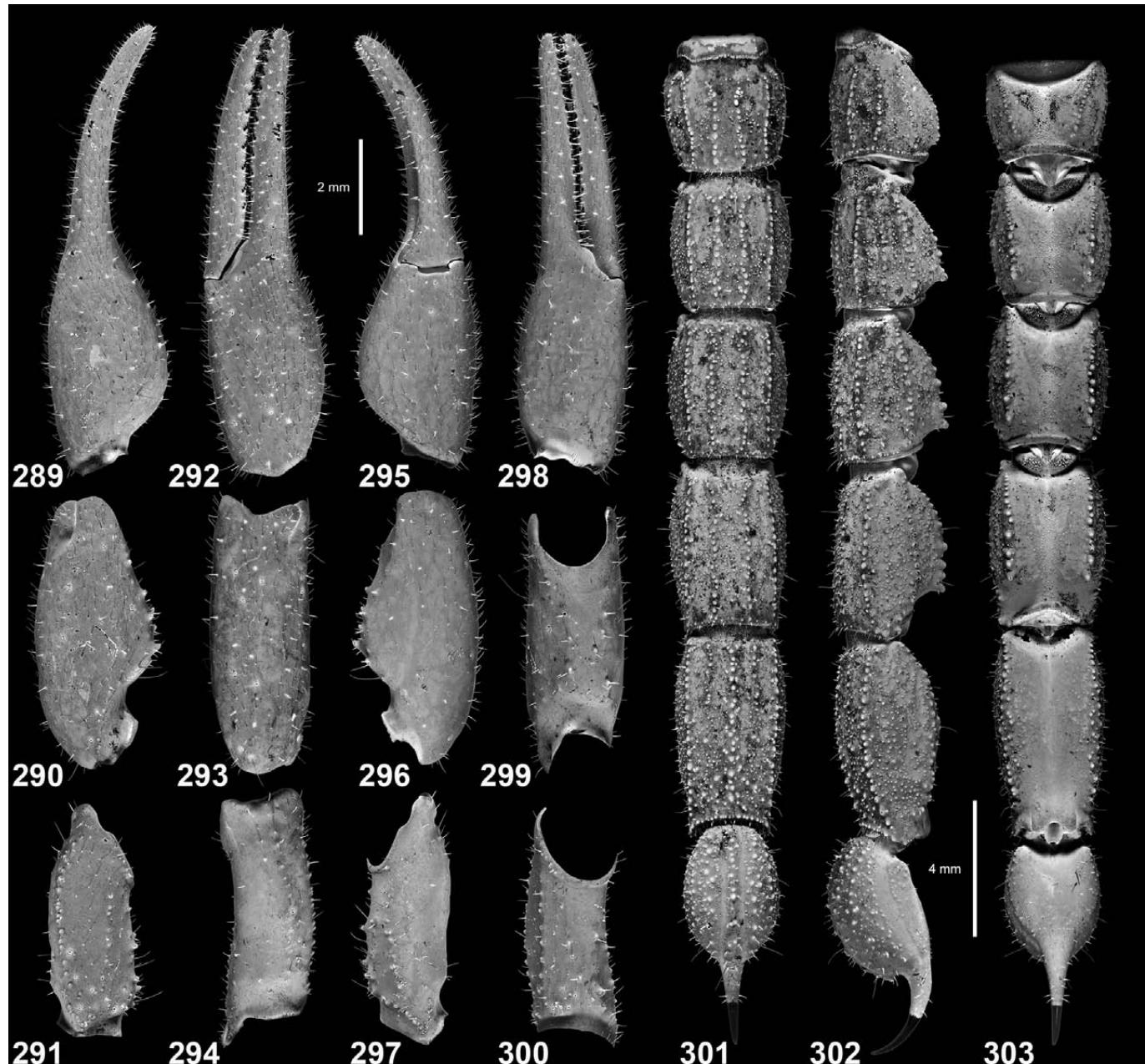
Grosphus goudoti Lourenço & Goodman, 2006



Figures 287–288. *Grosphus angulatus* sp. n., holotype female. Carapace and tergites (287) and coxosternal area and sternites (288). Scale bar: 2 mm. UV fluorescence.

Grosphus halleuxi Lourenço, Wilmé, Soarimalala & Waeber, 2017
Grosphus hirtus Kraepelin, 1900
Grosphus madagascariensis (Gervais, 1843)
Grosphus mandena Lourenço, 2005
Grosphus mayottensis Lourenço & Goodman, 2009

Grosphus polskyi Lourenço, Qi & Goodman, 2007
Grosphus rakotoariveloi Lourenço, Wilmé, Soarimalala & Waeber, 2017
Grosphus simoni Lourenço, Goodman & Ramilijaona, 2004
Grosphus tavaratra Lourenço, Soarimalala & Goodman, 2009
Grosphus voahangyae Lourenço & Wilmé, 2015



Figures 289–303. *Grosphus angulatus* sp. n. **Figures 289–300.** Left pedipalp chela (289, 292, 295, 298), patella (290, 293, 296, 299) and femur (291, 294, 297, 300) in dorsal (289–291), external (292–294), ventral (295–297) and internal (298–300) views. All are holotype female except external patella (293) from a paratype female, as the left trichobothrium *esb*₁ is missing in the holotype. Scale bar: 2 mm. UV fluorescence. **Figures 301–303.** Metasoma and telson of paratype female in ventral (301), left lateral (302) and dorsal (303) views. Scale bar: 4 mm. UV fluorescence.

AFFINITIES. The genus *Grosphus* belongs to the ‘*Charmus/Uroplectes*’ group of buthids (Fet et al., 2005; Štundlová et al. 2022). *Grosphus* is similar to *Teruelius*, and differentiated from other buthids, in the following combination of characters: pedipalp femur with trichobothria *d*₁–*d*₃–*d*₄ non-reflex angle opening externally (retrolaterally) (α -configuration; Vachon, 1975); pedipalp patella trichobothrium *d*₃ position external (retrolateral) to dorsomedian carina (DM_J) (Fet et al., 2005); pedipalp patella trichobothrium *esb*₂ distal to *esb*₁ (mean distance > 0.18 *esb*₁–*em* distance); pedipalp manus with trichobothrium *Eb*₂ distal to *Eb*₁, trichobothrium *V*₂ medial, located behind *V*₁

along proximo-distal axis of manus; pedipalp manus with weak or obsolete carination; pedipalp fixed finger with trichobothrium *db* in middle 30%–60% of finger, trichobothrium *it* distal; pedipalp chela movable finger with 11–16 imbricated subrows of median denticles, each flanked proximally by 2 enlarged external accessory denticles; pectines with fulcra; internal and accessory internal fulcra present, rounded, sclerotized, fluorescent; female *bml* not dilated, female *bpt* modified, dilated or elongated; legs III–IV with tibial spurs present; tergites III–VI monocarinate; tergite VII, sternite VII and metasomal segments I–III without microsetal fringes on posterior margins.

		<i>Grosphus angulatus</i> sp. n.	<i>Grosphus angulatus</i> sp. n.	<i>Grosphus angulatus</i> sp. n.
Dimensions (mm)		♀ paratype	♀ paratype	♀ paratype
Carapace	L / W _a / W	5.85 / 3.08 / 6.54	5.68 / 3.25 / 6.42	5.16 / 2.67 / 6.02
preocular	L	2.25	2.08	1.83
Metasoma I	L / W / D	3.13 / 3.58 / 3.08	3.17 / 3.56 / 3.25	2.75 / 2.77 / 3.21
Metasoma II	L / W / D	3.83 / 3.50 / 3.00	3.83 / 3.50 / 3.00	3.42 / 3.21 / 2.75
Metasoma III	L / W / D	4.21 / 3.48 / 3.08	4.17 / 3.50 / 3.08	3.75 / 3.13 / 2.65
Metasoma IV	L / W / D	4.92 / 3.43 / 3.08	4.92 / 3.46 / 2.98	4.42 / 3.04 / 2.71
Metasoma V	L / W / D	6.02 / 3.26 / 3.04	6.02 / 3.25 / 2.92	5.46 / 2.88 / 2.67
Telson	L / W / D	6.54 / 2.87 / 2.73	6.28 / 2.83 / 2.69	5.68 / 2.48 / 2.36
Vesicle	L	4.29	4.17	3.71
Pedipalp				
Femur	L / W	4.58 / 1.67	4.60 / 1.82	4.11 / 1.67
Patella	L / W	5.63 / 2.64	5.67 / 2.53	4.83 / 2.33
Chela	L	9.12	9.37	8.08
Manus	L / W / D	4.00 / 2.37 / 2.25	4.25 / 2.43 / 2.29	3.67 / 2.17 / 2.10
Movable finger	L	5.33	5.29	4.71
dentine subrows	left / right	13 / 13	13 / 13	13 / 13
Fixed finger	L	4.50	4.27	3.96
dentine subrows	left / right	12 / 11	12 / 12	12 / 12
Pectine	L	3.88	4.00	3.58
Total	L	52	52	48
PTC	left / right	14 / 14	15 / 16	15 / 16

Table 14. Comparative measurements of three paratypes of *Grosphus angulatus* sp. n. Abbreviations: length (L), width (W), anterior width (Wa), depth (D), pectinal tooth count (PTC). Measurements as defined in Table 13. *Subadult.

DIFFERENTIAL DIAGNOSIS. *Grosphus* is differentiated from *Teruelius* by any combination of two or more of the following characters: leg IV, mean ratio of tibial spur L/tibia distal D < 0.69; legs I–IV, telotarsi with ventral setation sparse, discrete with < 25 setae in rows; sternite IV spiracles broad, hemi-elliptical or ovoid, L/W < 5; metasoma I ventrosubmedian carinae granulate or costate-granulate; PTC: ♂ < 24, ♀ < 22; and pedipalp femur petite ‘trichobothrium’ d_2 position internal.

ETYMOLOGY. The species name refers to the angulate distal vertex of the modified basal pectinal tooth (*bpt*) in females.

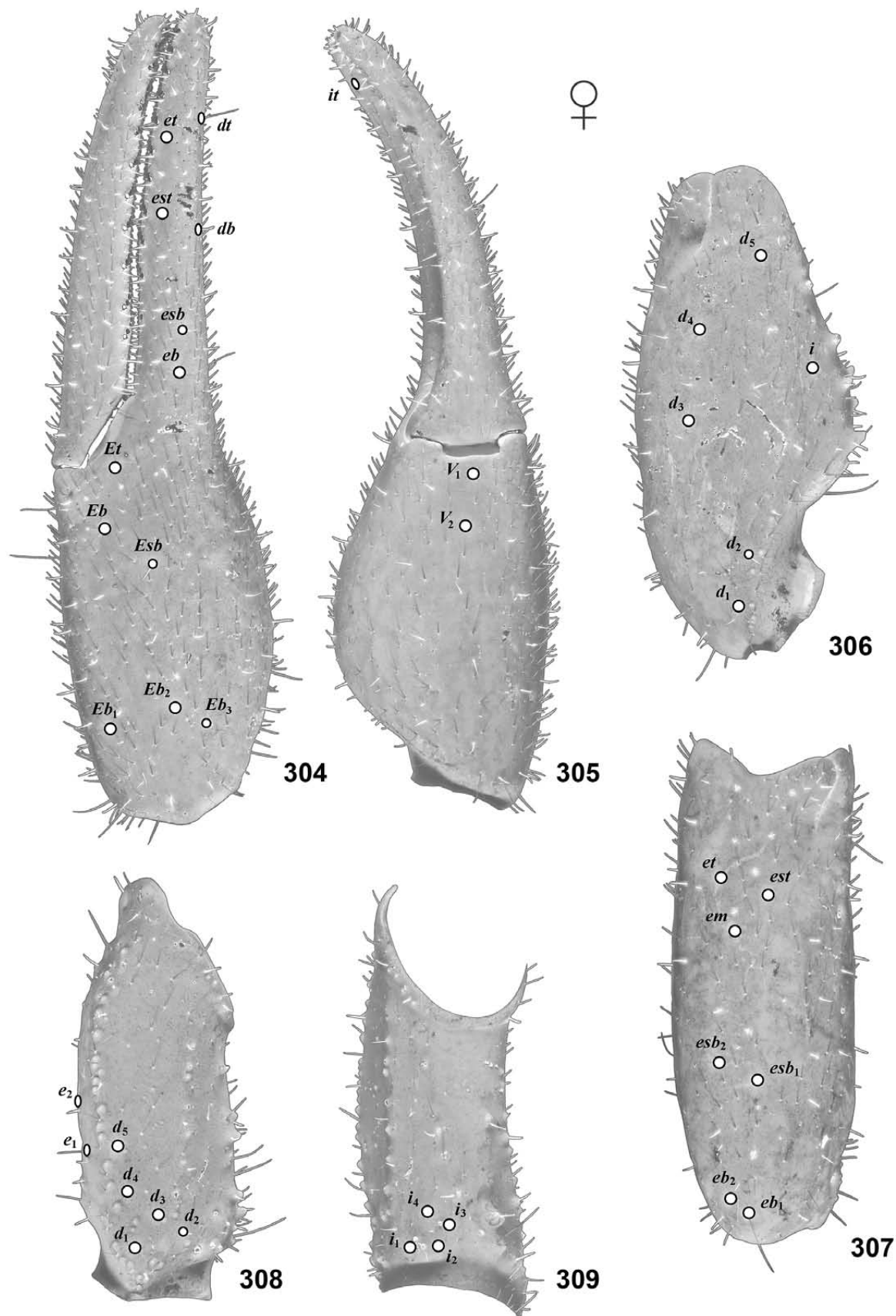
DIAGNOSIS (ADULT FEMALES). Medium-sized member of the genus, total length of adults around 50 mm; base color dark reddish-brown, carapace with weak variegated fuscous pattern; pedipalp patella with obsolete dorsointernal carina; femoral trichobothrium e_1 level with or slightly proximal to d_5 ; pedipalp chela movable finger with 11–12 median denticle subrows, fixed finger with 13; female *bpt* with angulate distal vertex; PTC 14–16; spiracles wide, ovoid in profile; metasoma II–IV with 3–4 robust, dentate granules on posterior dorsosubmedian carinae; telson vesicle hemielliptic in lateral profile, with small subaculear tubercle; morphometrics, L/W ratios ($n = 6$): metasoma I 0.86–0.92, metasoma II 1.06–1.10, metasoma III 1.18–1.20, metasoma IV 1.42–1.45, metasoma V 1.84–1.90, pedipalp chela 3.72–3.86, pedipalp femur 2.45–2.74, pedipalp patella 2.06–2.24.

DESCRIPTION (FEMALE). **Coloration** (Figs. 285–286, 310, 312, 314–317). Base color dark reddish-brown; carapace with weak variegated fuscosity; coxosternal area and sternites III–VI dark orange-brown; pectines yellow; legs dark-reddish brown to orange-brown, with more pale telotarsi; chelicerae dark reddish-brown, dorsal manus with fuscous anterior margin and reticulation.

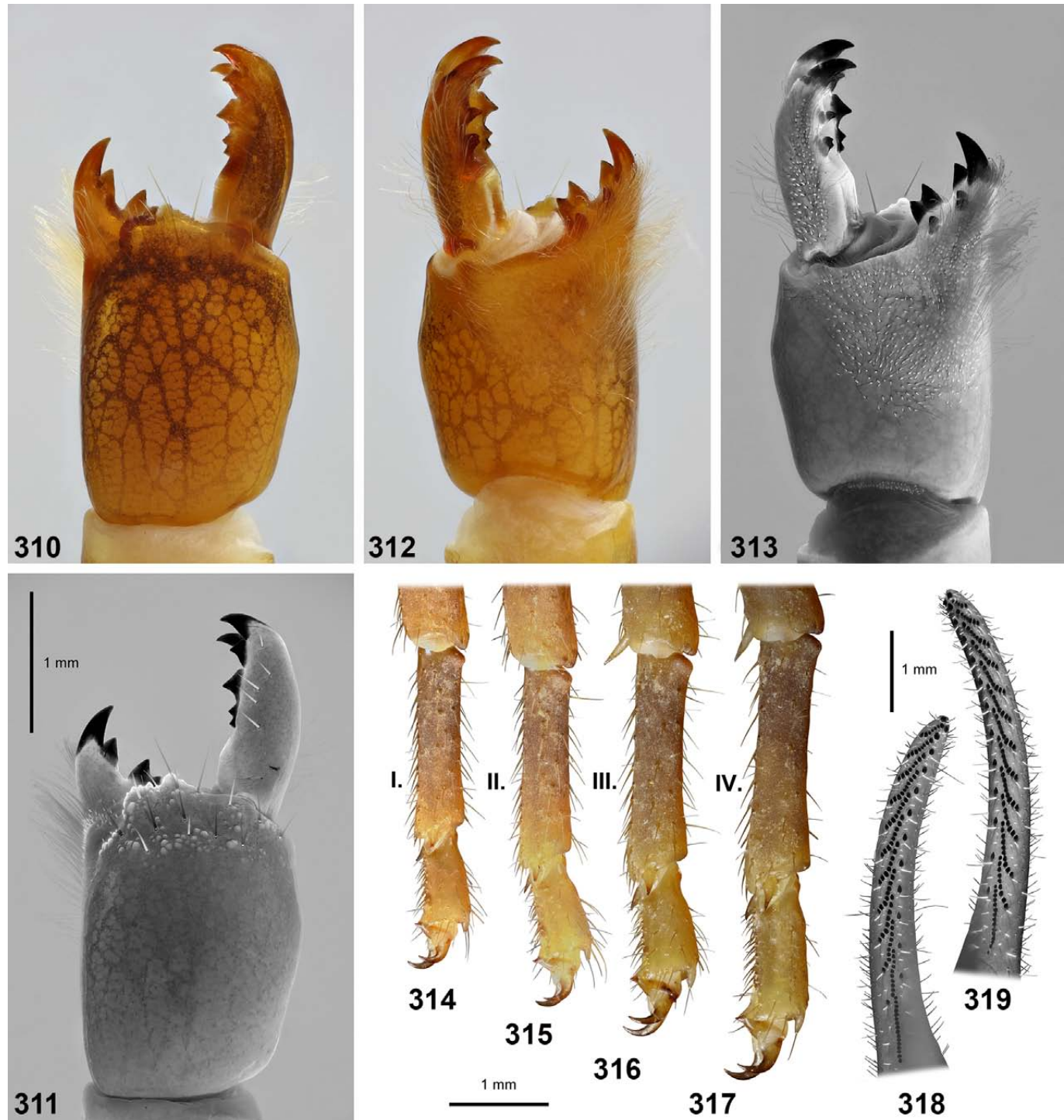
Grosphus sp. nr *hirtus* Lowe & Kovařík, 2019: 13, 19, 21, 30–31, 41, 43–44, 54, 60; figs. 26, 36, 40, 107, 111, 158.

TYPE LOCALITY AND TYPE REPOSITORY. Madagascar: Moramanga env., Anjyro, 1995; NZAC, GLPC.

TYPE MATERIAL. Madagascar: Moramanga env., Anjyro, 10.II.1995, 1♀ (holotype), 4♀ (paratypes) NZAC; 1♀ (paratype) GLPC.



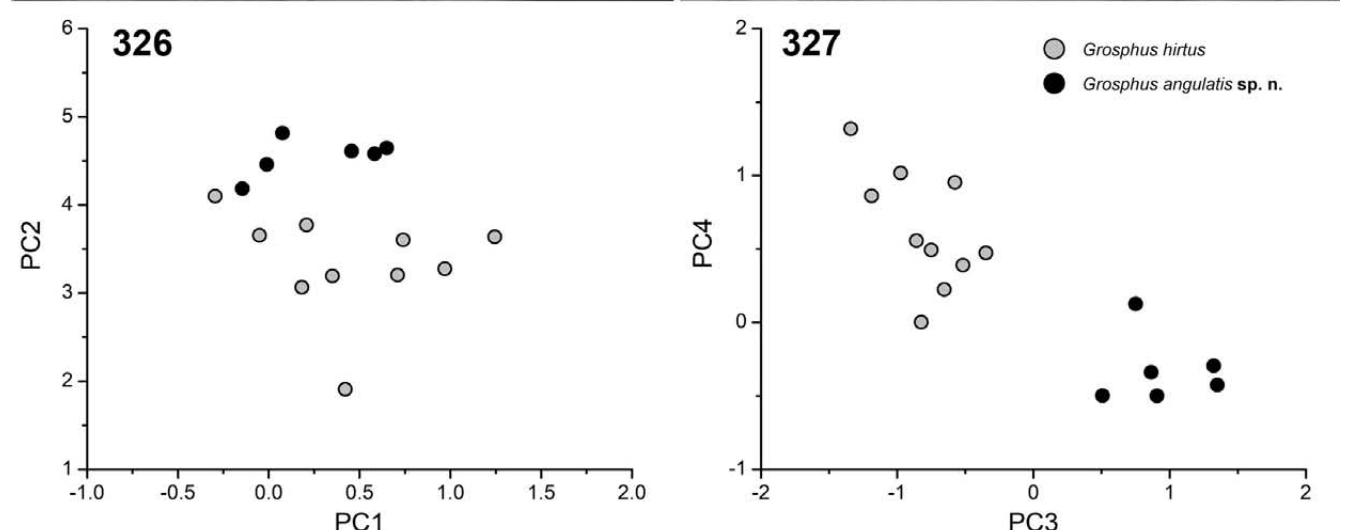
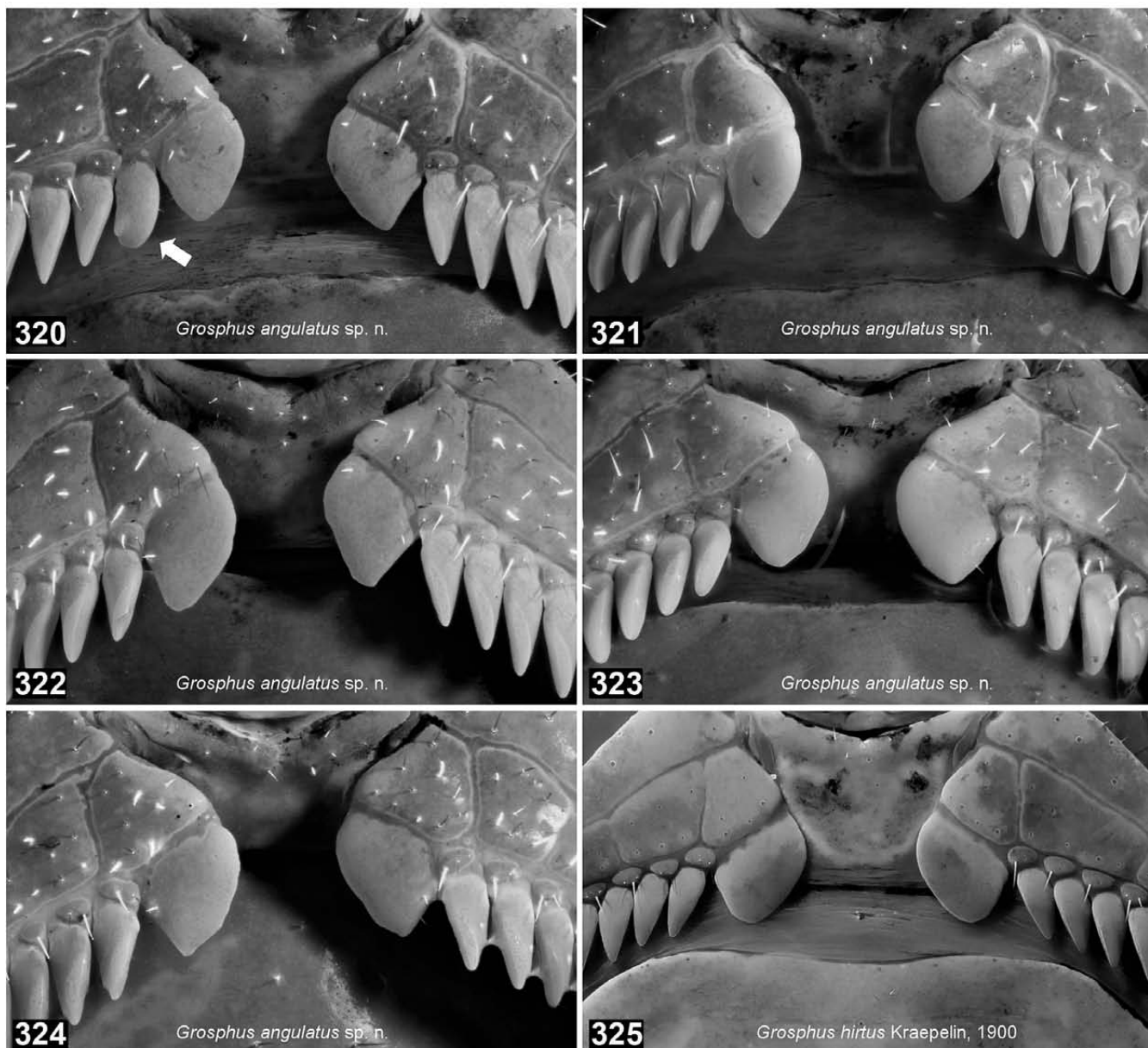
Figures 304–309. *Grophus angulatus* sp. n., pedipalp segments of female holotype (304–306, 308–309) and female paratype (307) with trichobothrial pattern indicated. Chela in external (304) and ventral (305) views. Patella in dorsal (306) and external (307) views. Femur in dorsal (308) and internal (309) views.



Figures 310–319. *Grosphus angulatus* sp. n. **Figures 310–313.** Paratype female, right chelicera in dorsal (310–311) and ventral (312–313) views, under white light (310, 312) and UV fluorescence (311, 313). Scale bar: 1 mm. **Figures 314–317.** Paratype female, right basitarsi and telotarsi in retrolateral views, legs I (314), II (315), III (316) and IV (317). Scale bar: 1 mm. **Figures 318–319.** Holotype female, right chela dentition, fixed finger (318), movable finger (319). UV fluorescence. Scale bar: 1 mm.

Carapace (Figs. 285, 287). Subrectangular, W/L 1.10–1.19; medial surface level along its entire length; anterior margin slightly concave with small epistomal process; preocular L/carapace L 0.36–0.38; surface mostly bearing fine granules of moderate density, except in some bilateral smooth strips and areas around central median, posterior median, posterior

transverse and posterior marginal furrows; granulation more coarse and dense on preocular triangle; superciliary carinae granulate; macrosetae absent; lateral eye groups composed of either 3 large + 2 small ocelli (8/12 groups), or 2 large + 2 small ocelli (4/12 groups), i.e., type 5 or type 4B, respectively (Loria & Prendini, 2014); 4 carapaces with type 5/5 pattern, 2



Figures 320–327. *Groshus angulatus* sp. n., variation in female bpt. **Figures 320–324.** Basal pectines showing bpt shapes of holotype (322) and four paratypes (320–321, 323–324). White arrow (320) indicates partially modified intermediate tooth bearing a sensorial area (cf. Figs. 43–44). **Figure 325.** Basal pectines of female *G. hirtus* showing typical bpt shape. UV fluorescence (320–325). **Figures 326–327.** Bivariate scatter plots of bpt scores of *G. angulatus* sp. n. (black circles) and *G. hirtus* (gray circles) for principal components PC2 vs. PC1 (326) and PC4 vs. PC3 (327) obtained from PCA of 32 Fourier coefficients from up to eighth order harmonic terms in EFA of bpt shapes of *Groshus* and *Teruelius* (cf. Figs. 29–33).

carapaces with type 4B/5 pattern, 1 carapace with type 4B/4B pattern (left group/right group); median eyes of moderate size, eye diameter/ carapace L 0.086.

Chelicerae (Figs. 310–313). Dorsal surface of manus granulate on anterior 1/5, smooth on posterior 4/5; anterior granulate area with 8–9 macrosetae, 4–5 pale, fluorescent microsetae; dorsointernal carina strong, granulate; fingers with typical buthid dentition (Vachon, 1963), movable finger dorsal margin with two large subdistal denticles and two small basal denticles, ventral margin with subdistal and basal denticles (notched basal denticle in Figs. 312–313 is atypical or worn, and not present in the holotype and other paratypes), fixed finger with large subdistal denticle and proximal bicusp, two denticles on ventral surface; dorsal surface of movable finger smooth, with dorsal row of 5–7 pale, fluorescent microsetae.

Coxosternal area (Figs. 286, 288). All coxae smooth with sparse macrosetae and fluorescent microsetae; sternum smooth, subtriangular, with narrow slit-like posteromedial depression, bearing 2 macrosetae; genital opercula smooth, divided.

Pectines (Figs. 28, 32, 34–35, 43–44, 286, 288, 320–335). Basal piece smooth, with concave anterior margin, surface flat without groove or pit, pectines with 3 marginal lamellae, 4–6 middle lamellae, extending to distal end of coxa IV; marginal and middle lamellae with sparse cover of macrosetae and pale, fluorescent microsetae; fulcra with 2 fluorescent microsetae; *bpt* with angulate distal vertex.

Hemispermatophore. Unknown.

Mesosoma (Figs. 54, 71–74, 93–94, 285–288, 393). *Tergites*: pretergites smooth, with microsulcate posterior margins; tergites densely, finely granulated, with narrow, smooth transverse lateral strips on tergites II–VI; tergite I without discernible carinae, tergites II–VI with single weak, granulate median carina, tergite VII with medial hump and 2 pairs of granulate carinae; all tergites lacking macrosetae. *Sternites*: sternites III–VI smooth, acarinate; sternite VI smooth with two pairs of weak, granulate carinae; posterior margins of all sternites smooth; spiracles broad, hemi-elliptic; sternite III–VI macrosetae: one submedian pair, one lateral pair, two posterior marginal pairs; sternite VII macrosetae: one submedian carinal pair, one lateral pair; sternites III–VI glossy, sternite VII matte.

Metasoma (Figs. 105, 160, 285–286, 301–303). Segments of uniform width, robust. *Carination*: segments I–III with 10 complete carinae, IV with 8 complete carinae (lateral median carinae indistinct posteriorly), V with 5 complete carinae; all carinae granulate; dorsosubmedian carinae on II–VI with enlarged dentate posterior granules; ventrolateral carinae on V strongly, uniformly granulate; dorsolateral carinae on V irregularly, coarsely granulate; lateral anal margin with 2 small granules, ventral anal margin with up to 18 granules. *Intercarinal surfaces*: moderately dense, fine granulation on lateral, ventrolateral and ventral surfaces of all segments; I–VI with dorsomedian surfaces finely granulated or shagreened, with decreasing density on more posterior segments, dorsolateral surfaces with sparse fine granules, mostly smooth;

V with dorsomedian surface smooth, dorsolateral surfaces with sparse fine granules, mostly smooth. *Setation*: dorsal surfaces without setae; other surfaces with numerous short macrosetae and fluorescent microsetae, mostly associated with carinae.

Telson (Figs. 285–286, 301–303). Vesicle dorsal surface smooth, lateral and ventral surfaces covered with numerous coarse and fine granules, except along lateral and paramedian longitudinal strips which are smooth; vesicle hemi-elliptic in lateral profile, with distinct subaculear tubercle; numerous short macrosetae and fluorescent microsetae on lateral and ventral surfaces; dorsal surface with posterior patch of short macrosetae; aculeus shorter than vesicle.

Pedipalps (Figs. 289–300, 304–309, 318–319). Segments robust (see DIAGNOSIS for morphometrics). *Femur*: dorsointernal, dorsoexternal and ventrointernal carinae distinct, granulate; other carinae indistinct; intercarinal surfaces smooth; sparse short macrosetae and fluorescent microsetae present, mostly associated with granules and carinae. *Patella*: all carinae obsolete, smooth except for isolated granules on internal surface; numerous short macrosetae and fluorescent microsetae present. *Chela*: all carinae obsolete, surfaces smooth, with dense cover of short macrosetae and fluorescent microsetae; 11–12 median denticle subrows on fixed finger, 13 on movable finger including short subdistal row (excluding malformations), all subrows except proximal flanked by one mid-row internal and two proximal external accessory denticles. *Trichobothriotaxy*: orthobothriotaxic, type Aα (Vachon, 1974), femur d_2 internal, e_1 level with or slightly proximal to d_5 ; chela fixed finger db proximal to est .

Legs (Figs. 285–286, 314–317). Femora and patellae with granulate carinae, prolateral surfaces sparsely granulate and matte, retrolateral surfaces smooth, glossy; tibial spurs present on legs III–IV; retrolateral tarsal spurs simple, prolateral tarsal spurs with very small basal bifurcation; basitarsi with 2 axial rows of macrosetae on ventral surface, irregular macrosetae on lateral and dorsal surfaces; telotarsi with 2 axial rows of up to 8 short macrosetae on ventral surface, lateral apices with 4–6 macrosetae; tarsal ungues stout.

Measurements. See Tables 13–14.

Affinities. *G. angulatus* sp. n. is similar to three other species of the genus: *G. hirtus*, *G. polskyi* and *G. voahangyae*. The four species share the following characters: metasoma I stout, mean L/W ratio ♀ < 0.97, ♂ < 1.02 (Fig. 168); dorsointernal carina of pedipalp patella with granulation sparse or absent; pedipalp chela fixed finger with trichobothrium db level with or proximal to 0.92 est (Fig. 167); leg IV tibial spur L/ tibia distal D, mean ratio 0.60–0.65 (Fig. 50). These four species were often recovered as a monophyletic ‘*hirtus*’ group in cladistic analyses (e.g., Figs. 196–200, 203–209).

G. hirtus differs from *G. angulatus* sp. n. as follows: lighter base color of yellowish to reddish-yellow, with more distinct variegated fuscous patterns on body, pedipalps and legs; pedipalp patella with weakly granulate dorsointernal carina; femoral trichobothrium e_1 distal to d_5 ; female *bpt* rounded distally (Fig. 325 vs. Figs. 320–324), z-scores of

Fourier harmonics clustered separately (Figs. 34–35), non-overlapping in PC1-PC2 plane (Fig. 326), disjunct in PC3-PC4 plane (Fig. 327); metasoma II–IV with smaller dentate granules on posterior dorsosubmedian carinae; more elongate pedipalp patella, L/W ♀ 2.21–2.42. *G. voahangyae* differs from *G. angulatus* sp. n. as follows: smaller size, adult female total length around 40 mm; more distinct variegated fuscous patterns on body, pedipalps and legs; femoral trichobothrium e_1 distal to d_5 ; female *bpt* ovoid, rounded distally, z-scores of Fourier harmonics clustered separately (Figs. 34–35); more elongate pedipalp patella, L/W ♀ 2.22–2.30. Only the male is known for *G. polskyi*, but the following differences from *G. angulatus* sp. n. do not exhibit strong sexual dimorphism in species of *Groshus* for which both sexes are known: smaller size, adult male total length around 33 mm; lighter base color of reddish-yellow, with more distinct variegated fuscous patterns on body; femoral trichobothrium e_1 distal to d_5 ; metasoma II–IV without enlarged dentate granules on posterior dorsosubmedian carinae; telson with larger subaculear tubercle. The species *G. tavaratra* is also similar, but only the male is known. However, *G. tavaratra* differs in having a granulate dorsointernal carina on the pedipalp patella, femoral trichobothrium e_1 distal to d_5 , and narrower spiracles, traits that do not exhibit strong sexual dimorphism in species of *Groshus* for which both sexes are known.

Teruelius Lowe & Kovařík, 2019

Teruelius Lowe & Kovařík, 2019: 12.

Groshus Lourenço et al., 2020: 15 (in part).

TYPE SPECIES. *Buthus limbatus* Pocock, 1889.

DIAGNOSIS. Medium- to large-sized bathids, adult length 35–120 mm; anterosubmedian carinae of carapace absent; median ocular tubercle located in posterior 2/3 of carapace; fixed finger of chelicera with 2 denticles on ventral surface; pedipalp femur with trichobothria d_1 - d_3 - d_4 non-reflex angle opening externally (retrolaterally) (α -configuration; Vachon, 1975); femur petite ‘trichobothrium’ d_2 position dorsal; pedipalp patella trichobothrium d_3 position external (retrolateral) to dorsomedian carina (DM_J) (Fet et al., 2005); pedipalp patella trichobothrium esb_2 distal to esb_1 (mean distance > 0.18 esb_1 -em distance); pedipalp chela manus with trichobothrium Eb_2 distal to Eb_1 , trichobothrium V_2 medial, located behind V_1 along proximo-distal axis of manus; chela manus with petite ‘trichobothrium’ Eb_3 usually near Eb_2 , closer than than half the distance between Eb_1 and Eb_2 ; pedipalp fixed finger with trichobothrium db in middle 30%–60% of finger, trichobothrium it distal; pedipalp chela movable finger with 11–16 imbricated subrows of median denticles, each flanked proximally by 2 enlarged external accessory denticles; chela movable finger typically with 4 external subdistal granules; pedipalp manus with weak or obsolete carination; pectines with fulcra; internal and accessory internal fulcra present, rounded, sclerotized, fluorescent; female basal middle lamella (*bml*) not dilated, female basal pectinal

tooth (*bpt*) modified with elongate, tapering distal extension, distinctly longer than other teeth; pectinal tooth count (excluding ♀ *bpt*): ♂ 25–42, ♀ 23–35; hemispermatophore capsule short, posterior lobe rounded without long, lanceolate extension; legs III–IV with tibial spurs present; leg IV, mean ratio of tibial spur L/ tibia distal D: > 0.69; legs I–IV, telotarsi with ventral setation dense, irregular with broad, brush-like strips of > 25 long filiform macrosetae; tergites III–VI monocarinate; sternites with spiracles narrow, slit-like, sternite IV spiracle L/W > 5; tergite VII, sternite VII and metasomal segments I–III without microsetal fringes on posterior margins; metasoma I ventrosubmedian carinae costate-granulate, smooth or absent; telson with oval or bulbous vesicle, without subaculear tubercle in adults; cuticle with strong UV fluorescence.

REMARKS. The above standard diagnosis is partly hypothetical because some characters have not been confirmed for all 22 species assigned to the genus. For a confirmed differential diagnosis, see below under AFFINITIES.

SUBORDINATE TAXA.

Teruelius ankaraensiska (Lourenço, 2003)

Teruelius ankarana (Lourenço & Goodman, 2003)

Teruelius annulatus (Fage, 1929)

Teruelius bemaraha (Lourenço, Wilmé & Waeber, 2018)

Teruelius bicolor (Lourenço, 2012)

Teruelius bistriatus (Kraepelin, 1900)

Teruelius eliseanneae (Lourenço & Wilmé, 2016)

Teruelius feti (Lourenço, 1996)

Teruelius flavopiceus (Kraepelin, 1900)

Teruelius ganzhorni (Lourenço, Wilmé & Waeber, 2016)

Teruelius grandidieri (Kraepelin, 1900)

Teruelius haeckeli sp. n.

Teruelius intertidalis (Lourenço, 1999)

Teruelius limbatus (Pocock, 1889)

Teruelius magalieae (Lourenço, 2014)

Teruelius mahafaliensis (Lourenço, Goodman & Ramilijaona, 2004)

Teruelius makay (Lourenço & Wilmé, 2015)

Teruelius mavo (Lourenço & Rossi, 2020)

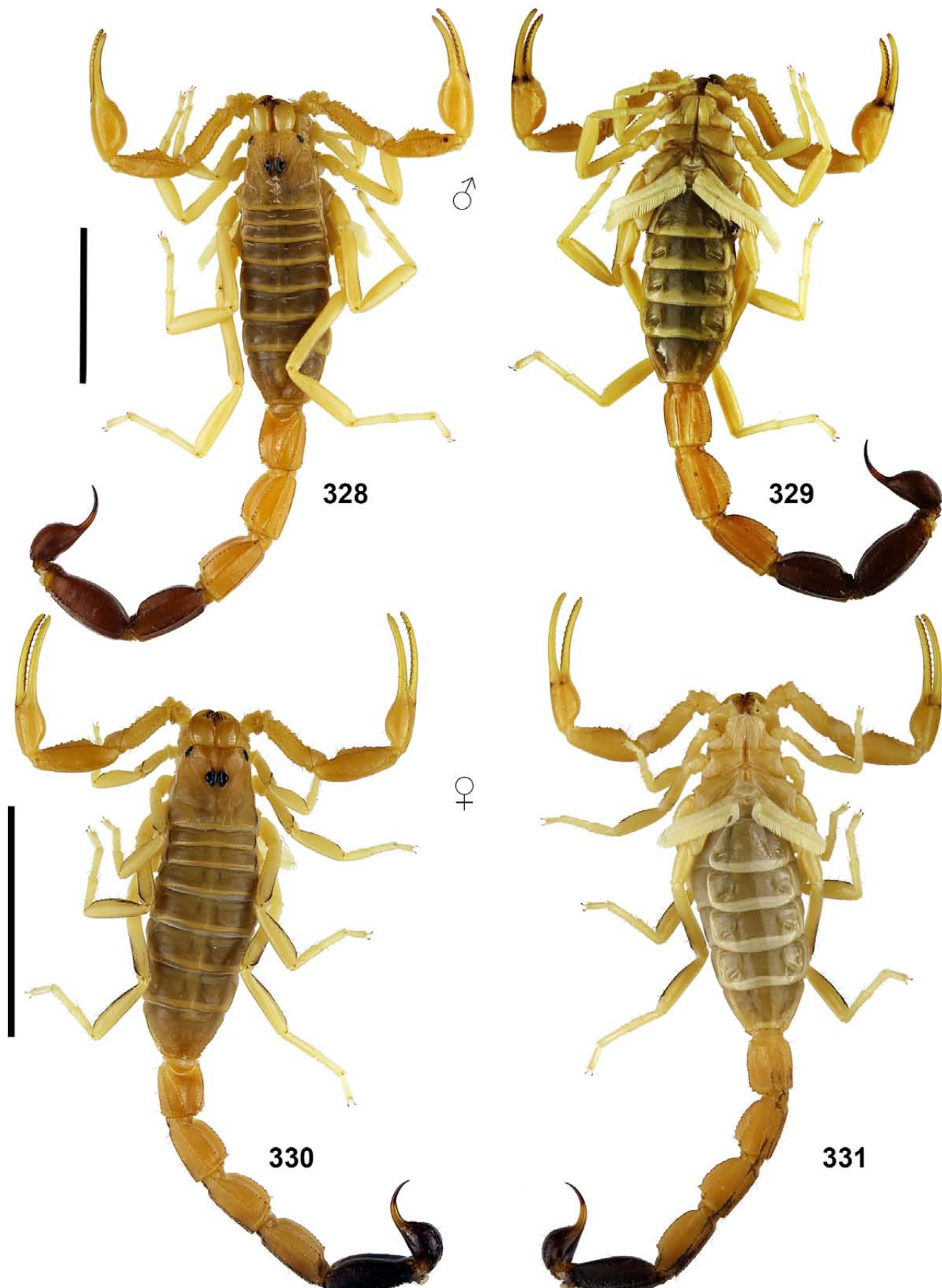
Teruelius olgae (Lourenço, 2004)

Teruelius rossii (Lourenço, 2013)

Teruelius sabineae (Lourenço & Wilmé, 2016)

Teruelius waeberi (Lourenço & Wilmé, 2016)

AFFINITIES. The genus *Teruelius* belongs to the ‘*Charmus/Uroplectes*’ group of bathids (Fet et al., 2005; Štundlová et al. 2022). *Teruelius* is similar to *Groshus*, and differentiated from other bathids, in the following combination of characters: pedipalp femur with trichobothria d_1 - d_3 - d_4 non-reflex angle opening externally (retrolaterally) (α -configuration; Vachon, 1975); pedipalp patella trichobothrium d_3 position external (retrolateral) to dorsomedian carina (DM_J) (Fet et al., 2005); pedipalp patella trichobothrium esb_2 distal to esb_1 (mean distance > 0.18 esb_1 -em distance); pedipalp manus with trichobothrium Eb_2 distal to Eb_1 , trichobothrium V_2 medial, located behind V_1



Figures 328–331. *Teruelius haeckeli* sp. n., habitus. **Figures 328–329.** Holotype male in dorsal (328) and ventral (329) views. **Figures 330–331.** Paratype female in dorsal (330) and ventral (331) views. Scale bars: 10 mm.

along proximo-distal axis of manus; pedipalp manus with weak or obsolete carination; pedipalp fixed finger with trichobothrium *db* in middle 30%–60% of finger, trichobothrium *it* distal; pedipalp chela movable finger with 11–16 imbricated subrows of median denticles, each flanked proximally by 2 enlarged external accessory denticles; pectines with fulcra; internal and accessory internal fulcra present, rounded, sclerotized, fluorescent; female *bml* not dilated, female *bpt* modified, dilated or elongated; legs III–IV with tibial spurs present; tergites III–VI monocarinate; tergite VII, sternite VII and metasomal segments I–III without microsetal fringes on posterior margins.

DIFFERENTIAL DIAGNOSIS. *Teruelius* is differentiated from *Grosphus* by any combination of two or more of the following characters: leg IV, mean ratio of tibial spur L/ tibia distal D > 0.69; legs I–IV, telotarsi with ventral setation dense, brush-like with > 25 irregular setae; sternite IV spiracles narrow, slit-like, L/W > 5; metasoma I ventrosubmedian costate-granulate, smooth or absent; PTC: ♂ > 24, ♀ > 22; and pedipalp femur petite ‘trichobothrium’ *d*₂ position dorsal.

Teruelius haeckeli sp. n.

(Figs. 13–16, 19–21, 23–28, 30–35, 49–50, 52, 137, 165, 167–168, 175–178, 180–183, 196–209, 328–392, Tab. 15)
<http://zoobank.org/urn:lsid:zoobank.org:act:7CBD4E06-8D6C-47CB-BBD4-F068D262DF50>

Teruelius annulatus Lowe & Kovařík, 2019: 25, 61, 64–65, 91–92; figs. 77, 203, 218, 422–432 (misidentification).

TYPE LOCALITY AND TYPE REPOSITORY. Madagascar: Toliara Province, Tsimanampetsotsa National Park, Andranovao camp, FKCP.

TYPE MATERIAL. Madagascar: Toliara Province, Tsimanampetsotsa National Park, Andranovao camp, 15 m a. s. l., 24°01.505'S 43°44.306'E, 1♂(holotype), 3♂1♀1juv♂ (paratypes), 2014, FKCP, GLPC (1 hemispermatophore).

ETYMOLOGY. The species is named in honor of Czech entomologist, physician Martin Häckel.

DIAGNOSIS. Small to medium-sized member of the genus, total length of adults 30–53 mm; body and appendages uniformly yellow, metasoma IV–V (or only V) and telson dark, black-brown; carapace of males with granulate superciliary carinae; pedipalp patella with strong, costate-granulate dorsointernal carina in both sexes; pedipalp chela of males with internal surface of manus granulate, fingers without undulations on proximal dentate margins; leg III tibial spur L/ tibia distal D > 0.73; female *bpt* falcate, without long narrow extension, shorter than basal comb width; PTC ♂ 37–40, ♀ 27–28, regular pectine tooth L/W ♂ 4.71, ♀ 3.89; hemispermatophore posterior lobe short, apically rounded, with two lateral carinae; metasoma III ventral intercarinal surface smooth, dorsosubmedian carinae of males bearing large dentate posterior terminal granule; metasoma V with dorsosubmedian carinae smooth, obsolete; telson with aculeus length equal to

vesicle length, vesicle weakly granulate on ventral surface; morphometrics, L/W ratios (*n* = 4 ♂, 1 ♀): metasoma I ♂ 1.20–1.27, ♀ 1.195, metasoma II ♂ 1.49–1.54, ♀ 1.47, metasoma III ♂ 1.57–1.62, ♀ 1.56, metasoma IV ♂ 1.81–2.01, ♀ 1.89, metasoma V ♂ 2.03–2.19, ♀ 2.41, pedipalp chela ♂ 3.64–3.77, ♀ 5.16, pedipalp femur ♂ 2.78–3.44, ♀ 2.34, pedipalp patella ♂ 2.67–3.65, ♀ 2.64.

DESCRIPTION. Coloration (Figs. 328–333, 338–357, 372–387). Base color yellow to orange-yellow; metasoma IV either dark brown (♂) or yellow and partially black ventrally (♀); metasoma V and telson either dark brown (♂) or black (♀). Leg femora and patellae with dark ventral margins (♀).

Carapace (Figs. 328, 330, 334, 336). Subrectangular, W/L 1.06–1.08; medial surface level along its entire length; anterior margin slightly concave, male with epistomal process; preocular L/ carapace L 0.40–0.43; surface densely, finely granulate in most areas; granulation more coarse on preocular triangle; granulation much weaker in female; superciliary carinae granulate in male, weakly granulate to smooth in female; anterior margin with several macrosetae; lateral eye groups composed of 3 large and 2 small ocelli (type 5; Loria & Prendini, 2014); median eyes large, eye diameter/ carapace L 0.11 (♂), 0.15 (♀).

Chelicerae (Figs. 332, 334–337). Dorsal surface of manus of male weakly granulate near anterior margin, smooth elsewhere, of female smooth throughout; several macrosetae and pale, fluorescent microsetae near anterior margin; dorsointernal carina strong, weakly granulate in male, smooth in female; fingers with typical buthid dentition (Vachon, 1963), movable finger dorsal margin with two large subdistal denticles and two small basal denticles, ventral margin with subdistal and basal denticles, fixed finger with large subdistal denticle and proximal bicuspid, two denticles on ventral surface; dorsal surface of movable finger smooth, with dorsal row of 4–5 pale, fluorescent microsetae.

Coxosternal area (Figs. 335, 337). All coxae smooth with sparse macrosetae and fluorescent microsetae; sternum smooth, subtriangular, with long medial depression, bearing 2 macrosetae; genital opercula smooth, divided in female.

Pectines (Figs. 28, 32, 34–35, 323, 325, 327). Basal piece smooth, with deep anteromedian invagination, combs with 3 marginal lamellae, 10–12 middle lamellae; combs long, extending to distal limit (♂) or distal 2/3 (♀) of trochanter IV; marginal and middle lamellae with numerous small macrosetae, fewer fluorescent microsetae; fulcra with 4–6 short setae; female *bpt* falcate.

Hemispermatophore. (Figs. 388–392). Flagelliform; trunk narrow, elongate; capsule short, with large, robust, hook-like basal lobe; posterior lobe rounded, with two carinate folds on convex surface; flagellum with short pars recta and pars reflecta (the latter probably incomplete in the examined specimen).

Mesosoma (Figs. 332–337). **Tergites:** pretergites smooth, with microsulcate posterior margins; all tergites densely, finely granulated or shagreened, more weakly so in female; tergite I without distinct carinae, tergites II–VI with single weak, granulate median carina, VII with medial hump and 2 pairs

		<i>Teruelius haeckeli</i> sp. n.	<i>Teruelius haeckeli</i> sp. n.
Dimensions (mm)		♂ holotype	♀ paratype
Carapace	L / W	5.37 / 5.54	3.35 / 3.56
Mesosoma	L	13.86	9.71
Tergite VII	L / W	3.71 / 5.38	2.00 / 3.35
Metasoma + telson	L	33.81	18.92
Segment I	L / W / D	4.13 / 3.42 / 3.06	2.39 / 2.00 / 1.79
Segment II	L / W / D	4.90 / 3.27 / 3.16	2.73 / 1.85 / 1.75
Segment III	L / W / D	5.19 / 3.30 / 3.12	2.84 / 1.81 / 1.64
Segment IV	L / W / D	5.89 / 3.25 / 2.84	3.24 / 1.71 / 1.60
Segment V	L / W / D	7.01 / 3.20 / 2.85	3.95 / 1.69 / 1.49
Telson	L / W / D	6.69 / 2.43 / 2.27	3.77 / 1.34 / 1.27
Pedipalp	L	19.48	11.93
Femur	L / W	4.95 / 1.44	2.70 / 0.87
Patella	L / W	5.48 / 2.05	3.55 / 1.34
Chela	L	9.05	5.68
Manus	W / D	2.40 / 2.43	1.10 / 1.12
Movable finger	L	5.29	3.66
Pectine	L	4.40	3.50
Total	L	53.04	31.98
PTC	left / right	39 / 39	29 / 28

Table 15. Comparative measurements of *Teruelius haeckeli* sp. n. Abbreviations: as in Table 13.

of granulate carinae; all tergites lacking macrosetae. *Sternites*: all sternites smooth, glossy, acarinate; posterior margins of all sternites smooth; spiracles long, narrow, slit-like; sternite III–VI macrosetae: one submedian pair, one lateral pair, two posterior marginal pairs; sternite VII macrosetae: two submedian pairs, three lateral pairs; posteromedian margin of sternite V convex in female, forming a sensory patch with dense narrow, transverse band of microsetae along margin, and a wider, more sparse transverse band of microsetae slightly anterior to margin; posteromedian marginal setation on sternite V denser than on sternites IV and VI.

Metasoma (Figs. 137, 372–374, 376–378). Elongate, segments I–IV uniform in width, segment V narrower posteriorly. *Carination*: segment I with 10 complete carinae, II with 8 complete carinae (lateral median carinae anteriorly indistinct), segments III–IV with 8 carinae, V with 5 carinae; dorsosubmedian and dorsolateral carinae on segments I–IV and lateral median carinae on segments I–III granulate, crenulate or dentate-granulate in both sexes; ventrosubmedian and ventrolateral carinae on segments II–IV granulate or crenulate (♀) or smooth (♂); ventrosubmedian and ventrolateral carinae on segment I weakly crenulate to smooth in both sexes; segment V with dorsolateral carina granulate, ventrolateral and ventromedian carinae granulate with larger dentate granules in posterior half; lateral anal margin with 4 large granules, ventral anal margin with up to 20 granules. *Intercarinal surfaces*: dorsolateral, lateral, ventrolateral and ventral surfaces of segments I–VI smooth or almost smooth

with sparse fine granules; dorsomedian surfaces of all segments smooth; segment V smooth laterally, with sparse coarse and fine granules ventrally. *Setation*: carinae bear regular series of long macrosetae, 3–6 on segments I–IV, up to 10 on segment V; posterior ventral margins of segments I–IV with several long macrosetae.

Telson (Figs. 372–379). Vesicle dorsal surface smooth; lateral surfaces and ventral surface weakly granulate, with sparse, long macrosetae; vesicle hemi-elliptic or bulbous in lateral profile, without subaculear tubercle; aculeus shorter than vesicle.

Pedipalps (Figs. 338–371). *Femur*: dorsointernal, dorsoexternal and ventrointernal carinae strong, coarsely granulate; other carinae indistinct; internal surface with 7–10 large granules; intercarinal surfaces smooth; sparse short macrosetae and fluorescent microsetae present.

Patella: dorsointernal carina strong, costate-granulate in both sexes, weaker in female; dorsomedian carinae obsolete; dorsoexternal carina of male weakly granulate in distal half, obsolete in proximal half of segment, of female obsolete; ventroexternal and ventromedian carinae of male nearly obsolete, indicated by small granules, of female obsolete; ventrointernal carina granulate in both sexes, weaker in female; internal carina indicated by series of 4–5 enlarged dentate granules; sparse short and long macrosetae, and fluorescent microsetae present. *Chela*: all carinae obsolete, surfaces smooth except for finely granulate internal surface of manus in males; short macrosetae and fluorescent microsetae



332

333

Figures 332–333. *Teruelius haeckeli* sp. n., holotype male. Carapace and tergites (332) and pectinal area and sternites (333).

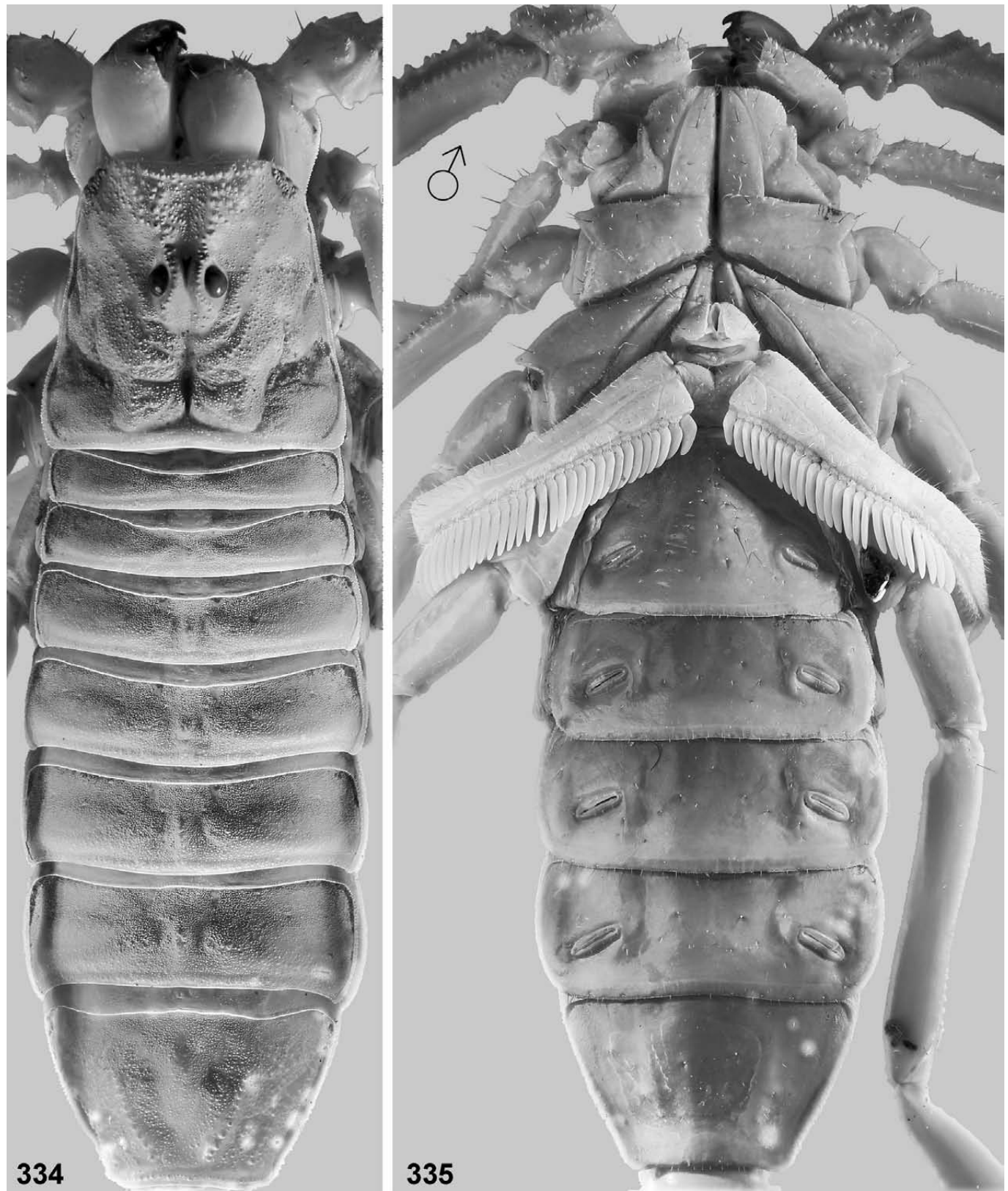
sparse on manus, dense on fingers; 11–12 median denticle subrows on fixed finger, 13 on movable finger including short subdistal row; subrows flanked by one mid-row internal and two proximal external accessory denticles (except for unfused proximal subrow). *Trichobothriotaxy*: orthobothriotaxic, type Aα (Vachon, 1974), femur d_2 dorsal, e_1 distal to d_5 ; chela fixed finger db proximal to est .

Legs (Figs. 328–331, 380–387). Femora with crenulate ventral carinae; surfaces of all segments smooth; patellae with series of long macrosetae; tibia and tarsal segments bearing numerous short macrosetae; tibial spurs present on legs III–IV; retrolateral tarsal spurs simple, prolateral tarsal spurs basally bifurcate; ventral surfaces of basitarsi with numerous macrosetae arranged roughly in two axial series;

ventral surfaces of telotarsi with dense brush of macrosetae irregularly arranged, lateral apices with conspicuous fringes of long macrosetae; tarsal unguis stout.

Measurements. See Table 15.

AFFINITIES. *Teruelius olgae* (Lourenço, 2004) is similar to *T. haeckeli* sp. n. in adult size, color pattern, and telson shape, but differs in having more slender metasomal segments, a lower range of male PTC (29–33), and a clavate female *bpt* with long curved extension. *T. mahafaliensis* is similar to *T. haeckeli* sp. n. in having a higher range of male PTC (34–40), but differs in its larger adult size (55–60 mm), reddish coloration, lack of black color on metasoma IV–V and telson vesicle, and a clavate female *bpt* with moderately long, curved extension.



Figures 334–335. *Teruelius haeckeli* sp. n., holotype male. Carapace and tergites (334) and coxosternal area and sternites (335). UV fluorescence.



336

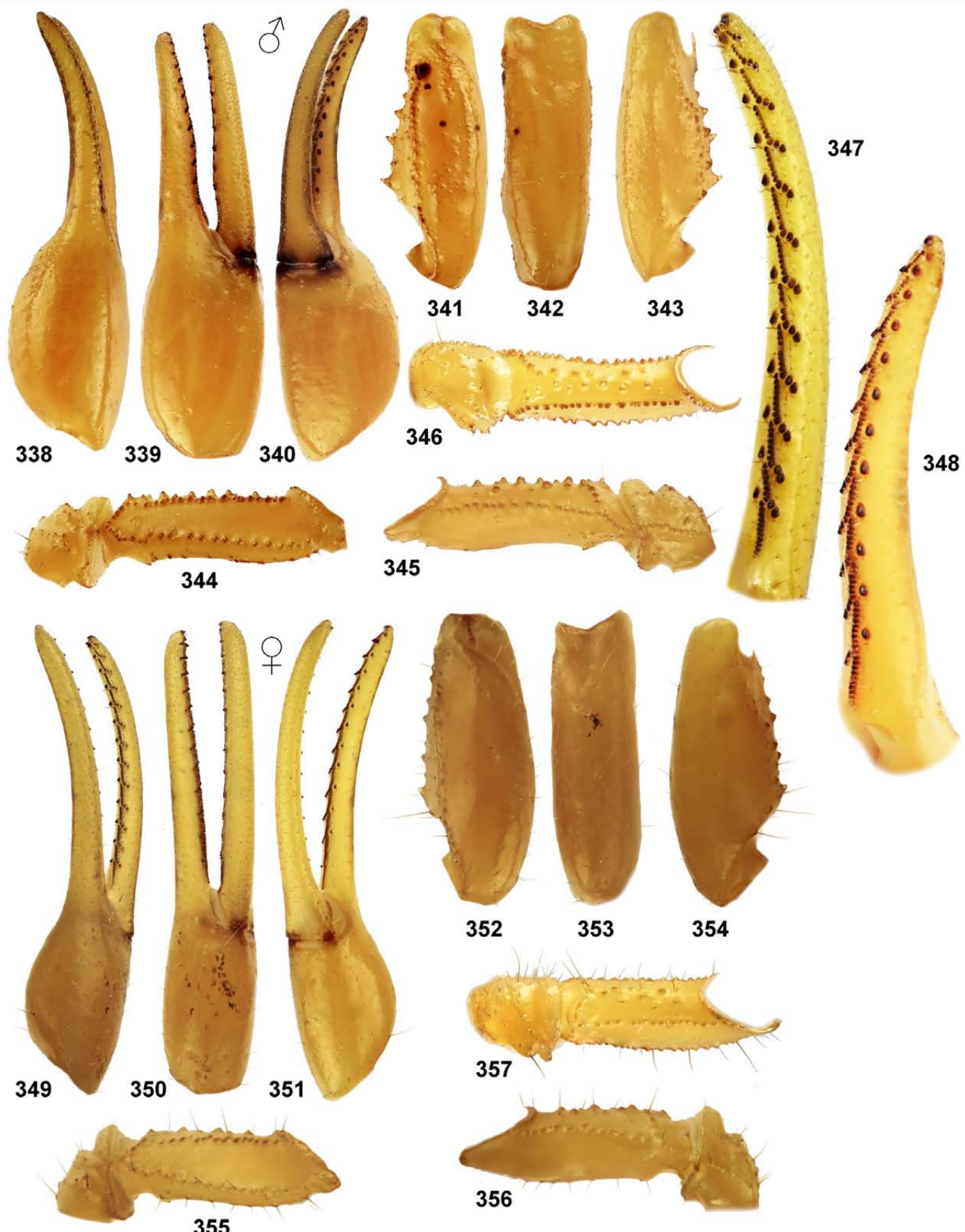


337

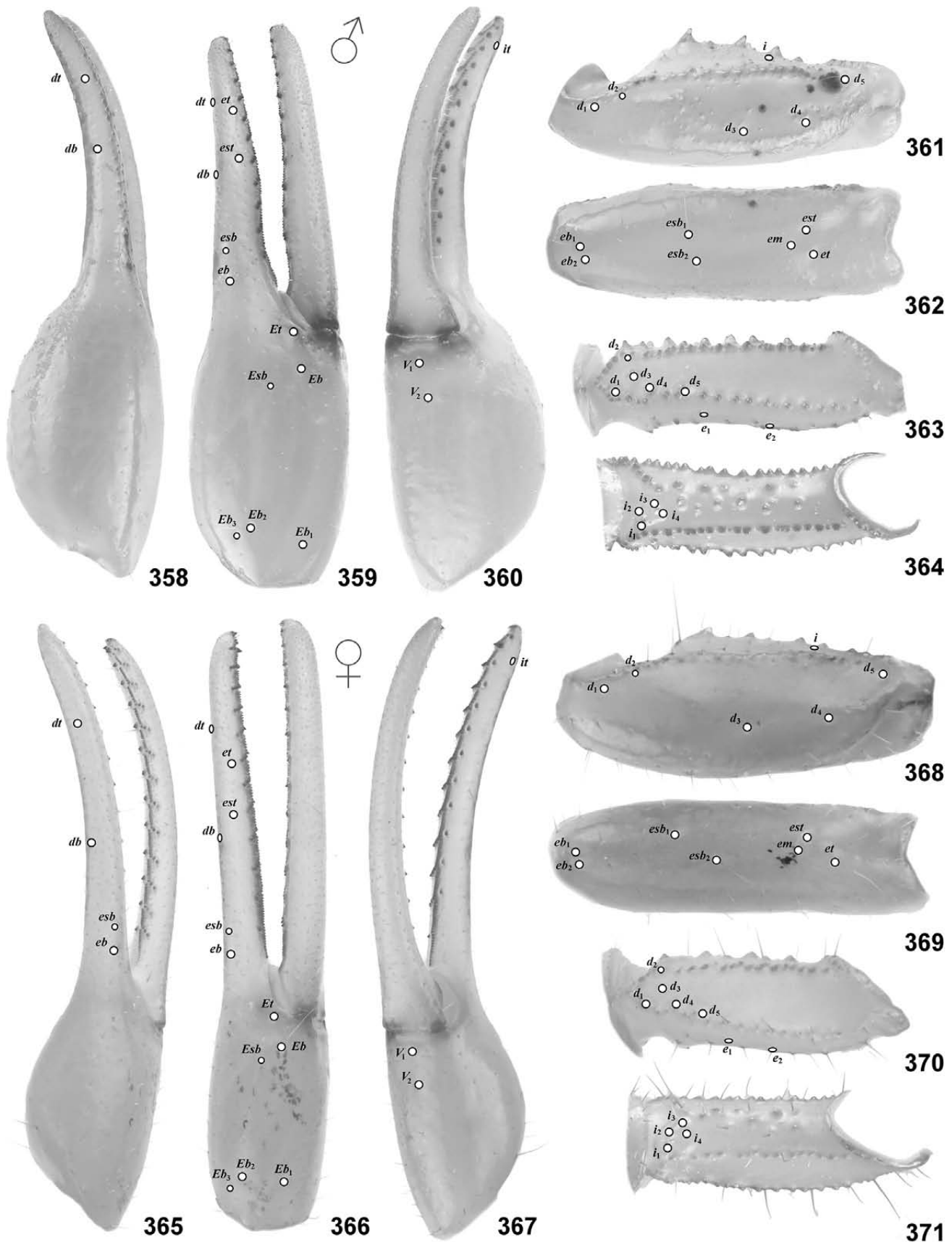
Figures 336–337. *Teruelius haeckeli* sp. n., paratype female. Carapace and tergites (336) and coxosternal area and sternites (337). UV fluorescence.

REMARKS. The convex profile of the posteromedian margin of sternite V in females (Fig. 337) differs from the almost straight posteromedian margin of sternite V in males (Fig. 335). There is also sexual dimorphism of the setation, which is strictly confined to the margin in males, but

extends slightly anterior to the margin in females. In both sexes, the posteromedian marginal setation is denser on sternite V, than on sternites IV and VI. These anatomical differences suggest functional specialization. Sternite V is also modified in various other buthids, forming a smooth,



Figures 338–357. *Teruelius haekeli* sp. n., pedipalp. **Figures 338–348.** Holotype male. Right chela (338, 339, 340) and patella (341, 342, 343) in dorsal, external and ventral views, respectively. Right femur (344, 345, 346) in dorsal, ventrointernal and internal views, respectively. Dentition of right chela, movable (347) and fixed (348) fingers. **Figures 349–357.** Paratype female. Right chela (349, 350, 351) and patella (352, 353, 354) in dorsal, external and ventral views, respectively. Right femur (355, 356, 357) in dorsal, ventrointernal and internal views, respectively.



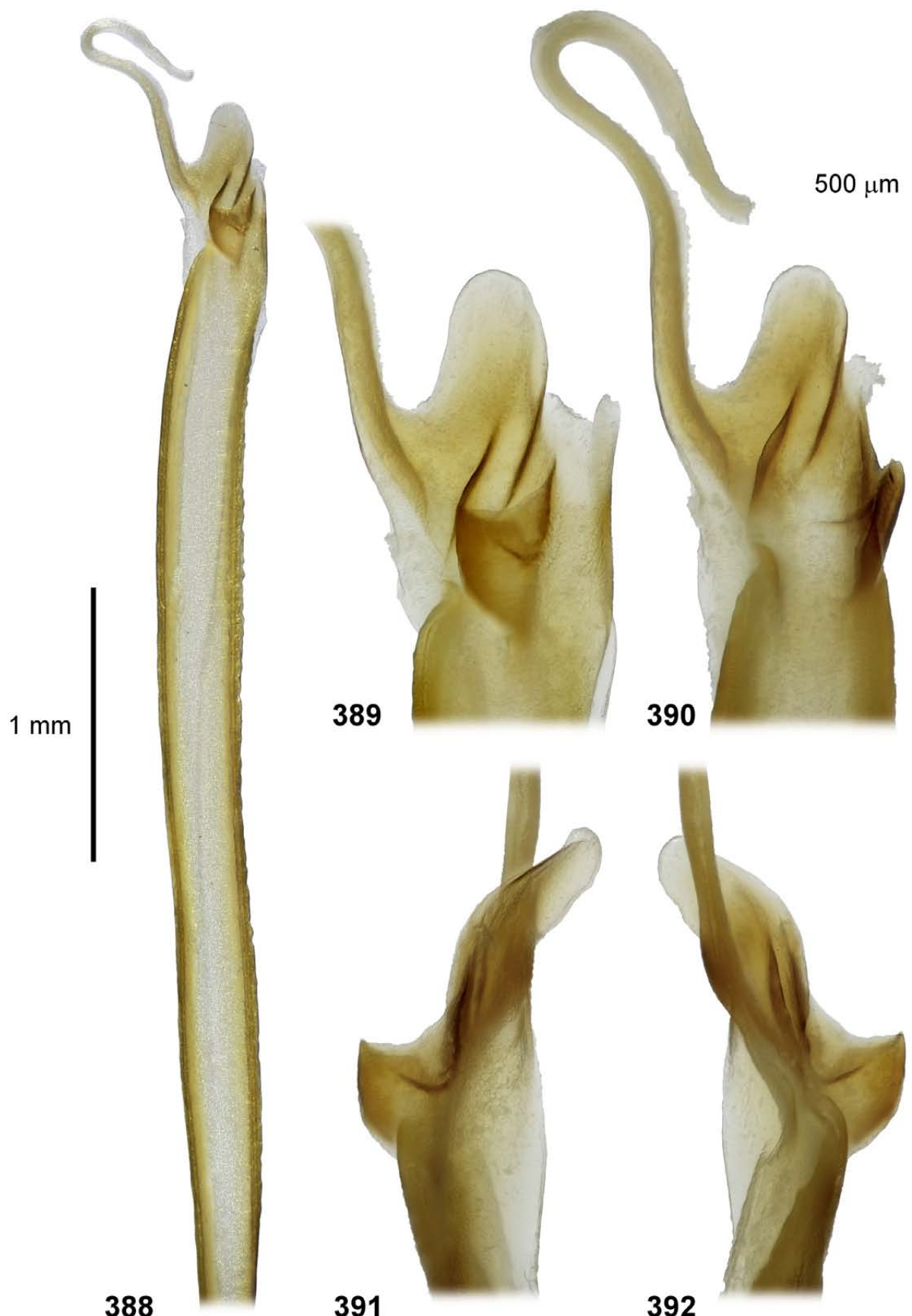
Figures 358–371. *Teruelius haeckeli* sp. n., pedipalp segments of male holotype (358–364) and female paratype (365–371) with trichobothrial pattern indicated. Chela in dorsal (358, 365), external (359, 366) and ventral (360, 367) views. Patella in dorsal (361, 368) and external (362, 369) views. Femur in dorsal (363, 370) and internal (364, 370) views.



Figures 372–379. *Teruelius haeckeli* sp. n., metasoma and telson. **Figures 372–375.** Paratype female. Metasoma and telson in right lateral (372), dorsal (373) and ventral (374) views. Telson in left lateral view (375). **Figures 376–379.** Holotype male. Metasoma and telson in right lateral (376), dorsal (377) and ventral (378) views. Telson in left lateral view (379). Scale bars: 10 mm (372–374), 10 mm (376–378).



Figures 380–387. *Teruelius haeckeli* sp. n., tarsi. Left basitarsi and telotarsi, legs I (380), II (382), III (384) and IV (386) in ventral (380, 382) and retro-lateral (384, 386) views. Left telotarsi, legs I (381), II (383), III (385) and IV (387) in proventral (381, 383) and retroventral (385, 387) views.



Figures 388–392. *Teruelius haeckeli* sp. n., right hemispermophore, paratype male. **Figure 388.** Capsule, part of flagellum and part of trunk, convex view. Pedicel truncated and lost during extraction. Scale bar: 1 mm. **Figures 389–392.** Capsule and part of flagellum, in convex compressed (389), convex (390), anterior (391) and posterior (392) views. Scale bar: 500 µm.

pale or fluorescent posteromedian patch with possible glandular or sensory functions. We found differences in the relative density of posteromedian marginal setation of sternites IV–V between *Groshus* and *Teruelius* in several examined species. In females, marginal setation on sternite V in *Groshus* was similar in density to that of sternite IV (5 spp., ♀, Figs. 393–397), and marginal setation on sternite V in *Teruelius* was denser than that on sternite IV (5 spp., ♀, Figs. 398–402). In males of these species, denser marginal setation on sternite V was absent in *G. hirtus*, *G. madagascariensis*, *G. simoni*, *G. voahangyae* and *T. mahafaliensis*, and was present in *T. ankara*santsika, *T. ankarana*, and *T. limbatus*. Other *Teruelius* with denser marginal setation on sternite V vs. IV include *T. bistrigatus* (♀) (Lowe & Kovařík, 2019: 93, fig. 437). *T. flavopiceus* (♂, ♀; modestly so), *T. intertidalis* (♀), *T. ganzhorni* (♀) (Ref. MNHN-RS-RS9080), *T. grandidieri* (♂, not ♀). These data suggest that dense marginal setation on sternite V is a potential diagnostic character or synapomorphy separating at least some *Teruelius* from *Groshus*. However, we did not include this in our analyses, due to limited taxon sampling and character variability. There was variability in posterior marginal profiles (i.e., convex, linear or concave), and in the density and arrangement of setae. The denser setation could be associated with an increase in numbers of either macrosetae, or fluorescent microsetae. Further investigation of putative glandular or sensory specializations of sternite V, and their sexual dimorphism, is needed to establish character homologies for phylogenetic analysis.

Discussion

Lowe & Kovařík (2019) analyzed nine discrete characters that were proposed to separate *Teruelius* from *Groshus* s. str. We extended the analysis to include a set of 45 discrete characters, or 32 discrete + 17 continuous characters. The nine previous characters corresponded to characters {8, 12, 14, 17, 23, 26, 28, 36, 44} of our current discrete set. Of these, we reanalyzed characters {17, 23, 28} by morphometric methods and validated their coding as discrete states. We considered four additional characters {11, 15, 16, 27} for separating *Teruelius* from *Groshus* s. str., giving a total of 13 potential binary diagnostic characters without any known overlap of scored states between the two genera. All 36 species of the ingroup (*Groshus* s. lat.) were scored for at least two of these characters, and a majority of species (30/36, 83%) were scored for at least seven of them; for the 13 character set, 74.1% of states were scored. We selected six characters {11, 12, 14, 17, 26, 28} to construct a differential diagnosis for the separation of *Teruelius* from *Groshus* s. str. via any combination of two or more of the six. For this six character set, 87.5% of states were scored. If any of the small minority (12.5%) of missing states are found to further confirm the generic separation, the diagnosis can be strengthened. If any are found to clash with it, they can be treated as homoplasious states that do not invalidate the

overall diagnosis. The remaining 32/45 discrete characters showed varying degrees of overlap between the two genera, but can still convey information about relationships among the ingroup taxa. Phylogenetic analyses of all 45 characters taken together confirmed monophyly of *Teruelius*, with strong node supports (> 70%) in 85% of analyses conducted with eight outgroup taxa. Monophyly was further confirmed by analyses of 32 discrete + 17 continuous characters, with strong node supports (> 70%) in 92.5% of analyses conducted with eight outgroup taxa. The continuous versions of the morphometric characters yielded more objective analyses and included more information about character variation.

Establishing a group of species as a monophyletic lineage is a necessary, but not sufficient condition for the definition of a genus. No generally accepted criteria govern whether a group of species should be elevated to the rank of genus. Elevation of rank could be tied to lineage age as estimated by dated molecular phylogenies, although such studies have not been conducted for *Groshus* s. str. and *Teruelius*. However, the DNA evidence presented by Štundlová et al. (2022: tab. S2) indicates a genetic divergence between *Groshus* and *Teruelius* that is similar to or greater than the genetic divergences between many other pairs of currently recognized bathid genera. For example, according to their data the uncorrected p-distance between COI coding sequences of *G. madagascariensis* and *T. flavopiceus* was 0.164. Among 48 of their analyzed genera (excluding *Teruelius*), the corresponding pairwise distances between selected representatives were ≤ 0.164 in 313 of 1,128 binary combinations (27.7%). A 16.4% difference suggests Miocene divergence, assuming a bathid COI mutation rate of ~1.4% per Myr (Gantenbein et al., 2005). This estimated divergence of *Teruelius* from *Groshus* is probably conservative because *T. flavopiceus* was consistently recovered as a more basal member of *Teruelius* in our cladistic analyses (e.g., Figs. 196–209). We argue that *Teruelius* is sufficiently distinct from *Groshus* s. str., both genetically and morphologically, to merit its own genus in accordance with generally accepted convention. Our argument is supported by consistent morphological differences, either in discrete characters {12, 15, 16, 17, 28}, or in disjunct morphometric characters {11, 14, 23, 26, 27}. Several characters suggest shared innovations in ecomorphic, ecophysiological or reproductive adaptation, e.g., dense macrosetal tufts on the tarsi, narrow slit-like spiracles, glossy cuticle on sternite VII, elongated female bpt, high PTCs and stronger UV fluorescence. Correlation between many of these characters and habitats or distribution of *Teruelius* was discussed previously (Lowe & Kovařík, 2019).

To justify their synonymy of *Teruelius*, Lourenço et al. (2020) listed several criticisms. We rebut their criticisms, taking into account new data and analyses presented here.

(i) Our diagnostic characters “represent mainly gradients inside the *Groshus* lineage and can clearly be observed in the way tables and graphs are presented” (Lourenço et al., 2020: 9).

We showed here that 32 of our 45 discrete characters have some overlap between *Teruelius* and *Groshus* s. str., and these might be described loosely as “gradient” characters. The other 13 discrete characters were binary without overlap in all scored taxa. Several characters scored for the majority of taxa were non-overlapping and disjunct (Figs. 16–17, 20–21, 23–25, 27, 30–33, 35, 49–104, 158, 166, 178). True character gradients could theoretically blur the distinction between *Teruelius* and *Groshus* s. str. However, in 116/130 (89.2%) of phylogenetic analyses, *Teruelius* was resolved as a monophyletic lineage, exclusive of *Groshus* s. str. (Figs. 191, 193–209, Tabs. 7–9).

(ii) We used “... nongeneric characters, which should mainly be restraint (sic) to the definition of species groups” (Lourenço et al. 2020: 9).

As discussed above, no generally accepted criteria govern whether a group of species should be regarded as a genus. Species groups initially defined as looser categories for organizing large, diverse genera, may later be refined and elevated to generic rank. For example, *Vaejovis* C. L. Koch, 1836 historically included several informal species groups (Sissom, 1991, 2000; Soleglad, 1972; Williams, 1970, 1971, 1980) that were later revised and elevated to generic status (González-Santillán & Prendini, 2013; Soleglad & Fet, 2006; Stahnke, 1974). By the same token, there is no universal agreement about which characters are diagnostic for genera vs. species-groups. Phylogenetic analysis reveals monophyletic groups that could merit the rank of genus, and synapomorphies supporting those groups are potential diagnostic characters.

(iii) Our work was “based on a rather incomplete number of species; less than 50% of the original types were studied,” (Lourenço et al., 2020: 9).

The reanalysis presented here and its conclusions are based on data from all 36 named species of the ingroup. In 20/36 species (56%), data were obtained and characters were scored by direct examination of types or determined material. In other species, characters were scored from published descriptions, illustrations and photographic images of the types. This approach enabled us to score 81.2% of ingroup characters for phylogenetic analyses that yielded strong support for the monophyly of *Teruelius*. The results were insensitive to the missing data, with strong support maintained after deletion of 12/45 characters with the highest percentages of unscored taxa. Examination of all original types would be more crucial for taxonomic revisions at the species level, but the aim of our reanalysis was to determine relationships at the generic level. When type material is unavailable for study, published descriptions and photographs can provide adequate information for testing higher level phylogenetic hypotheses (e.g., Prendini & Loria, 2020).

(iv) “For the non-observed species, speculative extrapolations are proposed including for internal characteristics, which could not be obtained – as claimed by the authors – from the previous publications of other authors” (Lourenço et al., 2020: 9).

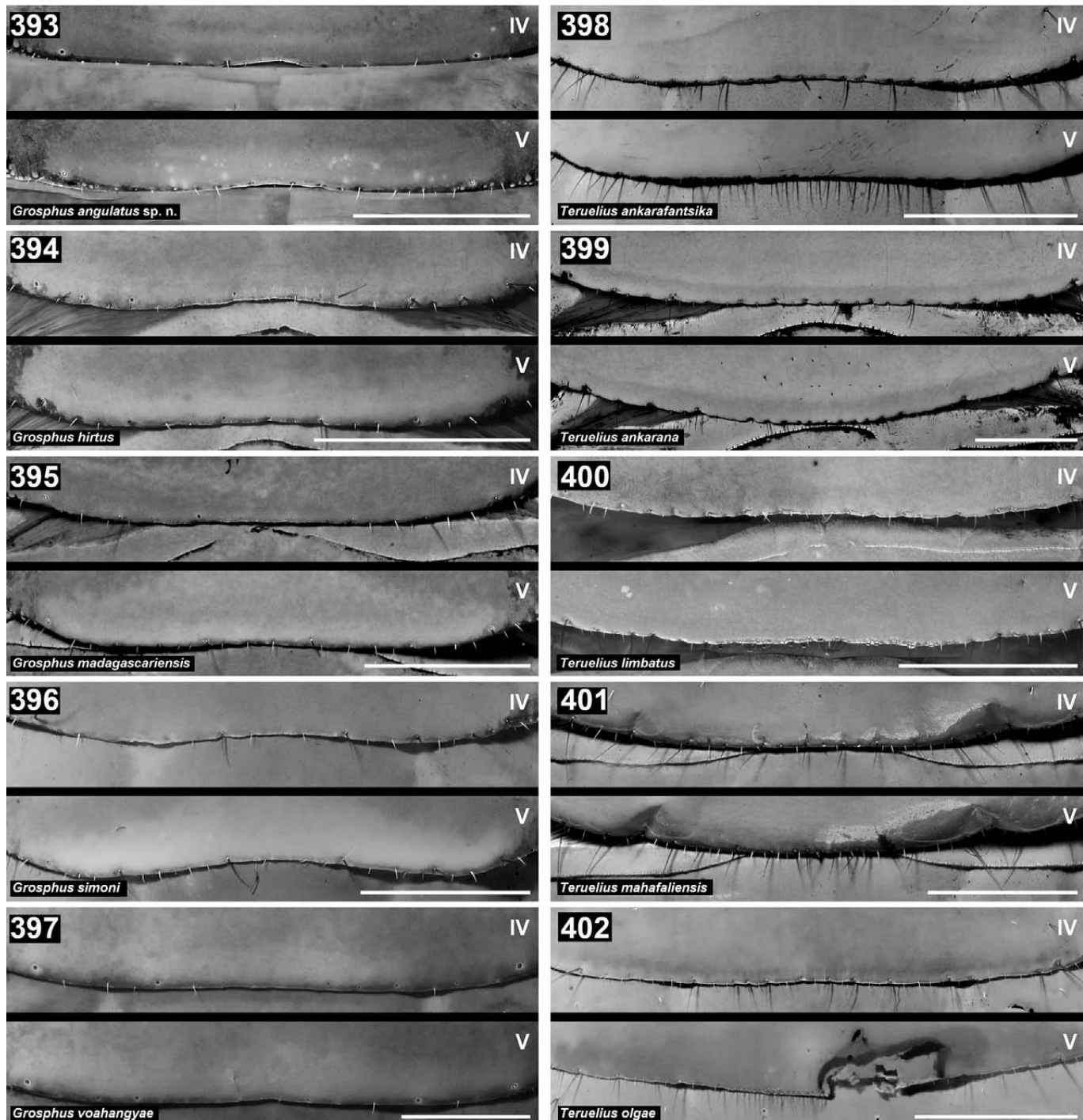
Only two internal characters were analyzed by Lowe & Kovařík (2019): the position of the hemispermatophore basal lobe, and the length of the hemispermatophore posterior lobe. These characters were scored in examined species for which adult males were available for hemispermatophore dissection (Lowe & Kovařík, 2019: 9, tab. 2, columns 2–3, rows 1–8, 11–16). They were left unscored in examined species for which adult males were unavailable for hemispermatophore dissection (Lowe & Kovařík, 2019: 9, tab. 2, columns 2–3, blank cells in rows 9–10), and in unexamined species (Lowe & Kovařík, 2019: 15, tab. 3, characters unlisted). In the latter table, a number of other unscored characters were also left as blank cells, and no claims were made about the scoring of these characters from published descriptions. The “extrapolations” may refer to proposed generic diagnoses (Lowe & Kovařík, 2019: 7, 12) which tentatively listed characters that had not been scored for all subordinate taxa. We acknowledge this logical error and submit here differential diagnoses that are valid with less than complete information about all characters, and depend only on combinations of already scored characters (cf. Systematics).

Scientific studies seldom, if ever, enjoy access to complete information. In systematics, many practical barriers can hinder and prevent scoring of all characters for all ingroup taxa. We argue that acquiring 100% of all possible comparative data should not be a prerequisite for defining a genus. The proposal that a group be treated as a genus, as a taxonomic act and as a phylogenetic hypothesis, is appropriate if a large majority of chosen descriptive characters have been scored (> 80% in our case), if the analysis of these characters yields strong support for monophyly of the group, and if most or all known diagnostic characters support the genus and few or none oppose it. In the words of Platnick & Gertsch (1976: 8–9):

“... if we insist on having all the “facts” before constructing hypotheses, we shall always have only “facts” and never hypotheses. Further, we suspect that most such objections have their root in a belief that a classification is a permanent statement of truth about the world, when it is in actuality only a hypothesis and as such is potentially testable (by studying the distributions of character states other than those used to originally construct it) and falsifiable.”

(v) Due to “lack of knowledge of the Malagasy fauna” we compared *Neogroshus* Lourenço, 1995 with *Groshus* s. lat., but “both genera have quite little in common, and *Neogroshus* is most certainly basal to *Groshus* and could even be associated to other Malagasy buthid genera such as *Pseudouroplectes* Lourenço, 1995” (Lourenço et al., 2020: 10)

The characters proposed by Lowe & Kovařík (2019) to support the separation of *Teruelius* from *Groshus* s. str. were polarized individually by outgroup comparisons with other buthid taxa. Since these comparisons were independent of characters in *Neogroshus*, any hypothesized affiliations



Figures 388–392. Variation in sternite IV–V posterior margins in *Grosphus* and *Teruelius*. Posterior margins of sternites IV (upper panels) and sternite V (lower panels) of females of *G. angulatus* sp. n. (393), *G. hirtus* (394), *G. madagascariensis* (395), *G. simoni* (396), *G. voahangyae* (397), *T. ankarafantsika* (398), *T. ankarana* (399), *T. limbatus* (400), *T. mahafaliensis* (401) and *T. olgae* (402). Sternite midlines positioned near middle of each panel. UV fluorescence. Scale bars: 2 mm (393–396, 398–402), 1 mm (397).

of *Neogrosphus* had no impact on the arguments supporting *Teruelius*. This criticism does not address the characters that we proposed for *Teruelius*, and is nothing but an ad hominem attack against us.

Lourenço et al. (2020) did not present any evidence or analysis to support their claimed phylogenetic position of *Neogrosphus*. If associating *Neogrosphus* with *Grosphus*

shows a “lack of knowledge of the Malagasy fauna”, then the same lack of knowledge was on full display in following publications: (1) Lourenço (2003a: 576): “... *Neogrosphus*, a genus that probably evolved more recently from *Grosphus*”; (2) Lourenço (2002: 39): “*Grosphus Simon* un des genres malgaches les plus caractéristiques, ainsi que *Neogrosphus* Lourenço, genre étroitement

associé à Grosphus ont certainement des affinités avec le genre africain Uroplectes Peters” (“*Grosphus Simon one of the most characteristic Malagasy genera, as well as Neogrosphus Lourenço, a genus closely associated with Grosphus certainly have affinities with the African genus Uroplectes Peters*”); (3) Lourenço (2000a: 880, fig. 1): constructed a phylogenetic tree in which *Neogrosphus* is the closest immediate sister genus of *Grosphus*, not associated with more basal genera *Palaeogrosphus*, *Tityobuthus*, *Troglotityobuthus* and *Pseudouroplectes*; (4) Lourenço (2000b: 727): “... *Neogrosphus, a genus which probably evolved more recently from Grosphus*”; (5) Lourenço (1996c: 447): “... *Neogrosphus, a genus which probably evolved more recently from Grosphus, ...*”; and (6) Lourenço (1995: 106), the paper originally diagnosing *Neogrosphus*: “*Le genre Neogrosphus est sans aucun doute associé à Grosphus, et sa différenciation a certainement eu lieu plus récemment que celle d’autres genres malgaches*” (“*The genus Neogrosphus is undoubtedly associated with Grosphus, and its differentiation has certainly taken place more recently than that of other Malagasy genera*”). All of the above citations, especially the last, directly contradict the claim by Lourenço et al. (2020: 10) that “*When Lourenço (1995) moved the species to a new genus he named it Neogrosphus only in report to its previous association with Grosphus. Nevertheless, both genera have quite little in common*”. We accept that opinions can change over time. However, if the latter claim of Lourenço et al. (2020) were true, then Lourenço (1995, 1996c, 2000a, 2000b, 2002, 2003a) published intentionally misleading statements taking positions diametrically opposed to the author’s real opinion at the time. Conversely, if the statements of Lourenço (1995, 1996c, 2000a, 2000b, 2002, 2003a) were honest expressions of opinion, then the latter claim by Lourenço et al. (2020) is a fabricated revisionist history that is easily debunked by inspection of the published record.

Lourenço et al. (2019: 27) rejected the synonymy of Microcharmidae with Buthidae by Volschenk et al. (2008) with the stern admonishment: “*What, however is not acceptable is the fact that Volschenk et al. (2008) globally ignore all the characters used by Lourenço (2002a) and Lourenço et al. (2006) to justify the family Microchrmidae*”. Yet, in the following year Lourenço et al. (2020) engaged in their own act of global character ignorance, synonymizing the genus *Teruelius* with *Grosphus* without analyzing and refuting the characters that we proposed for *Teruelius*. In doing so, they conveniently exempted themselves from the rigorous standards of scientific proof that they reprimanded other authors for neglecting. We agree with Lourenço et al. (2019), that the act of synonymizing a taxon must be validated by addressing and analyzing all characters used to define that taxon. We adhered to this principle in synonymizing Microchrmidae with Buthidae. On the other hand, the superficial synonymization of *Teruelius* with *Grosphus* by Lourenço et al. (2020) is “*not acceptable*” by the authors’ own declared standards (Lourenço et al., 2019).

MATERIAL EXAMINED.

- Alayotityus sierramaestrae* Armas, 1973: 1♂ 5♀, Cuba, leg. R. Teruel, GLPC.
- Androctonus crassicauda* (Olivier, 1807): 3♂ 13♀, Oman, Batinah Plain; 10–15 km W of Barka, Abyad pipeline road, coastal sand dunes, edge of *Acacia* woodland, UV detection, sand dunes/ flats, 23°41.16'N 57°43.61'E, 50 m a. s. l., 13.X.1993, leg. G. Lowe, A. S. Gardner, S. M. Farook, GLPC.
- Aristobuthus pterygocercus* (Finnegan, 1932): 26♂ 19♀, Oman, North Wahiba Sands, 22°28.56'N 58°44.25'E, 340 m a. s. l., 3.X.1994, leg. G. Lowe, M. D. Gallagher, GLPC.
- Barbaracurus exquisitus* (Lowe, 2000): 1♂, Oman, Jabal Akhdar hotel, Sayq plateau, 23°04'N 57°38'E, 1850 m a. s. l., 21.VI.2002, leg. G. R. Feulner, GLPC; 1♀ paratype, Jabal Shams, Jabal Akhdar, Al Hajar Al Gharbi, 23°14.29'N 57°11.62'E, 1855 m a. s. l., 2.X.1994, leg. G. Lowe, M. D. Gallagher, NHMB.
- Buthoscorpio sarasinorum* (Karsch, 1892): 1♂, Sri Lanka, North Central Province, Polonnaruwa District, near Kaudulla National Park, 08°08'40.6"N 080°51'04"E, 101 m a. s. l., 23.IV.2015, leg. Kovařík et al., FKCP, GLPC.
- Charmus laneus* Karsch, 1879: 1♂, Sri Lanka, North Central Province, Puttalam District, Eluwankulam, 08°17'15"N 079°50'38.7"E, 38 m a. s. l., 28.IV.2015, leg. Kovařík et al., FKCP, GLPC.
- Compsobuthus maindroni* (Kraepelin, 1900): 22♂ 11♀ 3juv, Oman; Jabal Bani Jabir, 22°49.6'N 59°1.59'E 1640 m a. s. l., 14.IX.1995, leg. G. Lowe, M. D. Gallagher, J. Dundon, GLPC.
- Hottentotta jayakari* (Pocock, 1985): 12♂ 19♀, Oman, Wadi Bani Auf, Salma Rd, 23°13'N 57°22'E, 900 m a. s. l., 14.X.1993, leg. A. S. Gardner, GLPC.
- Hottentotta trilineatus* (Peters, 1862): 1♂ 1♀, Kenya, S. Magadi, Lake Magadi env., 6.XII.1997, leg. M. Snižek, GLPC.
- Isometroides vescus* (Karsch, 1880): 1♀, Australia, SA, South Olary Plain, c. 32°30'S 140°10'E, X.1992, NPWS Survey, GLPC.
- Isometrus maculatus* (DeGeer, 1778): 1♂, Australia, Queensland, leg. R. V. Southcott, GLPC; 1♀, USA, Hawaii, Honolulu Co., Ka’ena Point State Park, under *Casuarina* bark, above high littoral zone, 12.I.1984, leg. G. Lowe, GLPC.
- Karasbergia methueni* Hewitt, 1913: 1♂ 1♀, RSA, 25°2'46.67"S 16°16'07.47"E, GLPC.
- Lychas mucronatus* (Fabricius, 1798): 1♂, China, GLPC; 1♀, Vietnam, 15.VII.2003, GLPC.
- Microchrmus variegatus* Lourenço, Goodman & Fisher, 2006: 1♂ 1♀, Madagascar, Antsiranana Province, Forêt d’Analabe (Sahaka) 30 km 72° ENE Daraina, 30 m a.s.l., 13°05'00"S 49°54'5"E, leg. Fisher et al., FKCP.
- Parabuthus abyssinicus* Pocock, 1901: 1♂ 1♀, Ethiopia, Sodora, 1400 m. a. s. l., IV.1994, leg. R. Lízler, GLPC.
- Pseudochactas ovchinnikovi* Gromov, 1998: Uzbekistan, Babatag Mountains, 38°01'39"N 68°14'45"E, 763 m a. s. l., 4.V.2002, leg. V. Fet, GLPC.
- Reddyanus melanodactylus* (L. Koch, 1867): 1♂, Australia, Queensland, Toowoomba, 27°34'S 151°57"E, VI.1955, leg. J. North, GLPC.

Serradigitus wupatkiensis (Stahnke, 1940): 2♀, California, Kern Co., Nine Mile Canyon, road to Kennedy Flat, 35°51.36'N 118°1.6'W, 1966 m a. s. l., UV detection, road to campsite, Juniper woodland, 2.VIII.1997; leg. G. Lowe, B. Hébert, GLPC.

Somalicharmus whitmanae Kovařík, 1998: Ethiopia, SNNPR, Turmi, 04°58'32"N 36°30'53"E, 908 m a. s. l., 14-15.IV.2016, 1♂3♀, leg. F. Kovařík, FKCP, GLPC.

Stahnkeus subtilimanus (Soleglad, 1972): 1♀, California, Riverside Co., Berdoo Canyon Road, 3-4 mi. N.E. Dillon Rd, 23.VII.1987, UV detection, rocky canyon walls, leg. G. Lowe, B. Hébert, B. Firstman, GLPC.

Teruelius ankarana (Lourenço & Goodman, 2003): 1♂2♀, Madagascar, Antsiranana Province, Ankarana National Park, 126 m a. s. l., 12°57'43.4"S 49°07'13.48"E, GLPC.

Teruelius flavopiceus (Kraepelin, 1900): 1♂2♀, Madagascar, Antsiranana Province, Diego Suarez env., E. of Ramena village, ~50 m a. s. l., 12°15'9.95"S 49°21'31.05"E, GLPC.

Teruelius grandidieri (Kraepelin, 1900): 1♂, Madagascar, Toliara Province, Tsimanampetsotsa National Park, Mitoho Camp, 10 m a. s. l., 24°02.838'S 43°45.138'E, GLPC.

Teruelius limbatus (Pocock, 1889): 1♂3♀, Madagascar, 2006, GLPC.

Thaicharmus sp.: 1♂, Vietnam, Nha Trang, FKCP, GLPC.

Tityus dedoslargos Francke & Stockwell, 1987: 1♂, Costa Rica, Quepos, III.1991, leg. S. D. Miller, GLPC; 1♀, Costa Rica, Puntarenas, S.E. Quepos, 20.IV.1994, 7 P.M., UV detection, forest floor, leg. S. D. Miller, GLPC.

Tityus ocelote Francke & Stockwell, 1987: 1♂1♀, Costa Rica, Puntarenas, Quepos, III.1991, leg. S. D. Miller, GLPC.

Tityobuthus monodi Lourenço, 2000: 1♂, Madagascar, Reserv Experimental de Vohimana, 18°55'42.2"S 48°30'55.5"E, 782 m a. s. l., 28.VIII.2012, leg. L. S. Rahamitriniaina, E. M. Rabotoson, MHNG.

Uroplectes planimanus (Karsch, 1879): 1♂1♀, Botswana, Maun, Island Safari Lodge env., 15-29.I.1997, leg. M. Snížek, GLPC; 1♂1♀, Zimbabwe, nr. National Parks Camp, Tuli Falcon College, 10.IV.1990, GLPC.

Uroplectes vittatus (Thorell, 1878): 1♂1♀, Botswana, Nata, 9-14.I.1997, leg. M. Snížek, GLPC.

Zabius fuscus (Thorell, 1876): 1♂1♀, Argentina, Cordoba Province, La Falsa, 24.IV.1975, leg. C. Césari, FKCP.

Other materials listed in Lowe & Kovařík (2019).

Acknowledgements

This work was facilitated in part by data acquired from materials made available to us in previous institutional loans (Lowe & Kovařík, 2019). We again gratefully acknowledge all participating institutions and curators: Petra Sierwald and Crystal Maier (FMNH), Peter Schwendinger and Lionel Monod (MHNG), Nadine Dupré and Danilo Harms (ZMUH), for their past generous support and open commitment to the advancement of science. We also thank numerous colleagues and collectors who, over many years, donated material that was important for comparative study. Two anonymous reviewers provided valuable comments that improved our manuscript.

References

- ABD-EL-WAHAB, A. 1957. The male genital system of the scorpion, *Butthus quinquestriatus*. *Quarterly Journal of Microscopical Science*, 98 (1): 111–122.
- ALEXANDER, A. J. 1959. Courtship and mating in the buthid scorpions. *Proceedings of the Zoological Society of London*, 133 (1): 145–169.
- ALMEIDA, M. T. & F. A. BISBY. 1984. A simple method for establishing taxonomic characters from measurement data. *Taxon*, 33 (3): 405–409.
- AYREY, R. F. 2011. *Serradigitus miscionei* (Scorpiones: Vaejovidae), a new species from southern Arizona. *Euscorpius*, 111: 1–13.
- BERLAND, K., K. JACOBSON, T. FRENCH & Z. RAJFUR. 2003. Electronic cameras for low-light microscopy. Pp. 103–132 in: SLUDER, G. & D. E. WOLF (Eds.). *Methods in Cell Biology*, 72. *Digital Microscopy: A second edition of video microscopy*. Elsevier Academic Press, San Diego.
- BIRULA, A. A. 1915. A general list of the scorpions of British East Africa. *Scientific Results of the Zoological Expedition to British East Africa and Uganda made by Prof. V. Dogiel and I. Sokolow*, 1 (9): 1–31.
- BORGES, A. & M. R. GRAHAM. 2016. Phylogenetics of Scorpions of Medical Importance. Pp. 82–104 in: GOPALAKRISHNAKONE, P. & CALVETE, J. J. (Eds.). *Venom Genomics and Proteomics*. Springer.
- BOTERO-TRUJILLO, R. & J. A. NORIEGA, 2011. On the identity of *Microananteris* with a discussion on pectinal morphology, and description of a new *Ananteris* from Brazil (Scorpiones, Buthidae). *Zootaxa*, 2747: 37–52.
- BROOK, W. J., F. J. DIAZ-BENJUMEA & S. M. COHEN. 1996. Organizing spatial pattern in limb development. *Annual Review of Cell and Developmental Biology*, 12: 161–180.
- BURGGRAAFF, O., N. SCHMIDT, J. ZAMORANO, K. PAULY, S. PASCUAL, C. TAPIA, E. SPYRAKIS & F. SNIK. 2019. Standardized spectral and radiometric calibration of consumer cameras. *Optics Express*, 27 (14): 19075–19101.
- CAPLE, J., J. BYRD & C. N. STEPHAN. 2017. Elliptical Fourier analysis: fundamentals, applications, and value for forensic anthropology. *International Journal of Legal Medicine*, 131: 1675–1690.

- CAPORIACCO, L. di. 1936. Scorpioni, Pedipalpi, Solifugi e Chernetidi di Somalia e Dancalia. *Annali del Museo Civico di Storia Naturale di Genova*, 58: 135–149.
- CLARK, E., A. D. PEEL & M. AKAM. 2019. Arthropod segmentation. *Development*, 146, dev170480. doi:10.1242/dev.170480
- CODDINGTON, J. A., G. GIRIBET, M. S. HARVEY, L. PRENDINI & D. E. WALTER. 2004. Arachnida. Pp. 296–318 in: CRACRAFT, J & M. J. DONOGHUE (Eds.) *Assembling the Tree of Life*. New York, NY: Oxford University Press.
- CODDINGTON, J. A. & N. SCHARFF. 1994. Problems with zero-length branches. *Cladistics*, 10: 415–423.
- CONSTANTINOU, C. 1984. Fluorescence of scorpion cuticle. *Newsletter of the British Arachnological Society*, 39: 2–3.
- CROWE-RIDDELL, J. M., S. DIX, L. PIETERMAN, J. H. NANKIVELL, M. FORD, A. J. LUDINGTON, B. F. SIMÕES, N. DUNSTAN & J. C. PARTRIDGE, K. L. SANDERS & L. ALLEN. 2021. From matte banded to glossy black: structures underlying colour change in the caudal lures of southern death adders (*Acanthophis antarcticus*, Reptilia: Elapidae). *Biological Journal of the Linnean Society*, 132: 666–675.
- DAMEN, W. G. M. 2002. Parasegmental organization of the spider embryo implies that the parasegment is an evolutionary conserved entity in arthropod embryogenesis. *Development*, 129: 1239–1250.
- DAVIS, A. L., H. F. NIJHOUT & S. JOHNSEN. 2020a. Diverse nanostructures underlie thin ultra-black scales in butterflies. *Nature Communications*, 11:1294; https://doi.org/10.1038/s41467-020-15033-1.
- DAVIS, A. L., K. N. THOMAS, F. E. GOETZ, B. H. ROBISON, S. JOHNSEN & K. J. OSBORN. 2020b. Ultra-black camouflage in deep-sea fishes. *Current Biology* 30, 1–7.
- DI, Z., G. D. EDGECOMBE & P. P. SHARMA. 2018. Homeosis in a scorpion supports a telopodal origin of pectines and components of the book lungs. *BMC Evolutionary Biology*, 18: 73.
- DOU, S., H. XU, J. ZHAO, K. ZHANG, N. LI, Y. LIN, L. PAN & Y. LI. 2020. Bioinspired microstructured materials for optical and thermal regulation. *Advanced Materials*, doi:10.1002/adma.202000697
- FAGE, L. 1929. Les scorpions de Madagascar, leur affinités, leur distribution géographique. Pp. 637–693 in: *Faune des Colonies Françaises*. Paris: Société d’Éditions Géographiques Maritimes et Coloniales.
- FARLEY, R.D. 1999. Scorpiones. Pp. 117–222, Chapter 3 in: HARRISON, F.W. & FOELIX, R.F. (Eds.) *Microscopic Anatomy of Invertebrates, Volume 8A: Chelicerate Arthropoda*. Wiley-Liss, Inc.
- FARZANPAY, R. & M. VACHON. 1979. Contribution à l'étude des caractères sexuels secondaires chez les scorpions Buthidae (Arachnida). *Revue Arachnologique*, 2 (4):137–142.
- FET, V. 2000. Family Microcharmidae Lourenço, 1996. Pp. 421–4236 in: FET, V., W.D. SISSOM, G. LOWE & M.E. BRAUNWALDER. *Catalog of the Scorpions of the World* (1758–1998). The New York Entomological Society.
- FET, V., M. E. SOLEGLAD & G. LOWE. 2005. A new trichobothrial character for the high-level systematics of Buthoidea (Scorpiones: Buthidae). *Euscorpius*, 23: 1–40.
- FILSHIE, B. K. & N. F. HADLEY. 1979. Fine structure of the cuticle of the desert scorpion, *Hadrurus arizonensis*. *Tissue & Cell*, 11 (2): 249–262.
- FITZPATRICK, M. J. 1996. The genus *Uroplectes* Peters, 1861 in Zimbabwe (Scorpiones: Buthidae). *Arnoldia Zimbabwe*, 10 (7): 47–70.
- FRANCKE, O. F. 1979. Spermatophores of some North American Scorpions (Arachnida, Scorpiones). *Journal of Arachnology*, 7 (1): 19–32.
- FRANCKE, O. F. & J. PONCE-SAAVEDRA. 2010. A new genus and species of scorpion (Scorpiones: Vaejovidae) From Michoacán, Mexico. *Boletín de la Sociedad Entomológica Aragonesa*, 46: 51–57.
- FROST, L. M., D. R. BUTLER, B. O'DELL & V. FET. 2001. A coumarin as a fluorescent compound in scorpion cuticle. Pp. 171–177 in: FET, V & P. A. SELDEN (eds.) *Scorpions 2001. In Memoriam Gary A. Polis*. British Arachnological Society, Burnham Beeches, Bucks. xi + 404 pp.
- GANTENBEIN, B., V. FET, I. A. GANTENBEIN-RITTER & F. BALLOUX. 2005. Evidence for recombination in scorpion mitochondrial DNA (Scorpiones: Buthidae). *Proceedings of the Royal Society B, Biological Sciences*, 272: 697–704. doi 10.1098/rspb.2004.3017.
- GARCIA, J. E., A. G. DYER, A. D. GREENTREE, G. SPRING & P. A. WILKSCH. 2013. Linearisation of RGB camera responses for quantitative image analysis of visible and UV photography: a comparison of two techniques. *PLoS ONE* 8(11): e79534. doi:10.1371/journal.pone.0079534
- GOLDSTEIN, H. 1950. *Classical Mechanics*. Addison-Wesley Publishing Company.

- GOLOBOFF, P. A. 1993. Estimating character weights during tree search. *Cladistics*, 9: 83–91.
- GOLOBOFF, P. A. & S. A. CATALANO. 2016. TNT version 1.5, including a full implementation of phylogenetic morphometrics. *Cladistics*, 32: 221–238.
- GOLOBOFF, P. A., J. S. FARRIS, M. KÄLLERSJÖ, B. OXELMAN, M. J. RAMÍREZ & C. A. SZUMIK. 2003. Improvements to resampling measures of group support. *Cladistics*, 19: 324–332.
- GOLOBOFF, P. A., J. S. FARRIS & K. C. NIXON. 2008. TNT, a free program for phylogenetic analysis. *Cladistics*, 24: 1–13.
- GOLOBOFF, P. A., C. I. MATTONI & A. S. QUINTEROS. 2006. Continuous characters analyzed as such. *Cladistics*, 22: 589–601.
- GONZÁLEZ-SANTILLÁN, E. & L. PRENDINI. 2013. Redefinition and generic revision of the North American vaejovid scorpion subfamily Syntropinae Kraepelin, 1905, with descriptions of six new genera. *Bulletin of the American Museum of Natural History*, 382: 1–71.
- GRAHAM, M. R. & M. E. SOLEGLAD. 2007. A new scorpion genus representing a primitive taxon of tribe Stahnkeini, with a description of a new species from Sonora, Mexico (Scorpiones: Vaejovidae). *Euscorpius*, 57: 1–13.
- HEWITT, J. 1918. A survey of the Scorpion fauna of South Africa. *Transactions of the Royal Society of South Africa*, 6 (2): 89–192.
- HEINGÅRD, M., N. TURETZEK, N.-M. PRPIC & R. JANSSEN. 2019. FoxB, a new and highly conserved key factor in arthropod dorsal-ventral (DV) limb patterning. *Evolution and Development*, 10: 28, 1–16.
- JANSSEN, R., N. M. FEITOSA, W. G. M. DAMEN & N.-M. PRPIC. 2008. The T-box genes H15 and optomotor-blind in the spiders *Cupiennius salei*, *Tegenaria atrica* and *Achaearanea tepidariorum* and the dorsoventral axis of arthropod appendages. *Evolution and Development*, 10: 2, 143–154.
- KAPUR, J. N., P. K. SAHOO & A. K. C. WONG. 1985. A new method for gray-level picture thresholding using the entropy of the histogram. *Computer Vision, Graphics and Image Processing*, 29 (3): 273–285. doi: 10.1016/0734-189x(85)90125-2
- KLOOCK, C. T. 2008. A comparison of fluorescence in two sympatric scorpion species. *Journal of Photochemistry and Photobiology B: Biology*, 91: 132–136.
- KLOOCK, C. T. 2009. Reducing scorpion fluorescence via prolonged exposure to ultraviolet light. *Journal of Arachnology*, 37: 368–370.
- KLOOCK, C. T., K. ABRAHAM & R. REYNOLDS. 2010. Ultraviolet light detection: a function of scorpion fluorescence. *Journal of Arachnology*, 38: 441–445.
- KOVARÍK, F. 1995. Review of Scorpionida from Thailand with descriptions of *Thaicharmus mahunkai* gen. et sp. n. and *Lychas krali* sp. n. (Buthidae). *Acta Societas Zoologicae Bohemoslovenicae*, 59: 187–207.
- KOVARÍK, F. 2007a. *Leiurus nasheri* sp. nov. from Yemen (Scorpiones, Buthidae). *Acta Societatis Zoologicae Bohemicae*, 71: 137–141.
- KOVARÍK, F. 2007b. A revision of the genus *Hottentotta* Birula, 1908, with descriptions of four new species (Scorpiones, Buthidae). *Euscorpius*, 58: 1–107.
- KOVARÍK, F. 2009. *Illustrated catalog of scorpions. Part I. Introductory remarks; keys to families and genera; subfamily Scorpioninae with keys to Heterometrus and Pandinus species*. Prague: Clairon Production, 170 pp.
- KOVARÍK, F. 2018. Notes on the genera *Buthacus*, *Compsobuthus*, and *Lanzatus* with several synonymies and corrections of published characters (Scorpiones: Buthidae). *Euscorpius*, 269: 1–12.
- KOVARÍK, F. & LOWE, G. 2022. Review of *Orthochirooides* Kovařík, 1998 with description of a new species (Scorpiones Buthidae). *Euscorpius*, 349: 1–42.
- KOVARÍK, F., G. LOWE & F. ŠŤÁHLAVSKÝ. 2016. Scorpions of the Horn of Africa (Arachnida: Scorpiones). Part IX. *Lanzatus*, *Orthochirus*, and *Somalicharmus* (Buthidae), with description of *Lanzatus somalilandus* sp. n. and *Orthochirus afar* sp. n. *Euscorpius*, 232: 1–38.
- KOVARÍK, F., G. LOWE, A. I. AWALE, H. SH A. ELMI & A. A. HURRE. 2018a. Scorpions of the Horn of Africa (Arachnida, Scorpiones). Part XVII. Revision of *Neobuthus*, with description of seven new species from Ethiopia, Kenya and Somaliland (Buthidae). *Euscorpius*, 271: 1–82.
- KOVARÍK, F., G. LOWE & F. ŠŤÁHLAVSKÝ. 2018b. Review of the genus *Babycurus* Karsch, 1886 (Arachnida, Scorpiones, Buthidae), with descriptions of *Barbaracurus* gen. n. and two new species from Oman and Yemen. *Euscorpius*, 267: 1–41.
- KRAEPELIN, K. 1891. Revision der Skorpione. I. Die Familie der Androctonidae. *Jahrbuch der Hamburgischen Wissenschaftlichen Anstalten*, 8: 1–144.

- KRAEPELIN, K. 1899. Scorpiones und Pedipalpi. In: F. DAHL (Ed.). *Das Tierreich. Herausgegeben von der Deutschen Zoologischen Gesellschaft*. Berlin: R. Friedländer und Sohn Verlag, 8 (Arachnoidea): 1–265.
- KRAEPELIN, K. 1900. Ueber einige neue Gliederspinnen. *Abhandlungen aus dem Gebiete der Naturwissenschaften. Herausgegeben vom Naturwissenschaftlichen Verein in Hamburg*, 16, 1(4): 1–17.
- KRAEPELIN, K. 1908. Die sekundären Geschlechtscharaktere der Skorpione, Pedipalpen und Solifugen. *Mitteilungen aus dem Naturhistorischen Museum (2. Beiheft zum Jahrbuch der Hamburgischen wissenschaftlichen Anstalten)*, 25: 181–225.
- KUHL, F. P. & G. R. GIARDINA. 1982. Elliptic Fourier features of a closed contour. *Computer Graphics and Image Processing*, 18: 236–258.
- LAMORAL, B. H. 1976. *Akentrobuthus leleupi*, a new genus and species of humicolous scorpion from eastern Zaïre, representing a new subfamily of the Buthidae. *Annals of the Natal Museum*, 22 (3): 681–691.
- LAMORAL, B. H. 1979. The scorpions of Namibia (Arachnida: Scorpionida). *Annals of the Natal Museum*, 23 (3): 497–784.
- LANKESTER, E. R. 1885. Notes on certain points of the anatomy and generic characters of Scorpions. *Transactions of the Zoological Society, London*, 11 (10): 372–384.
- LAWRENCE, R. F. 1938. The arachnida of the Transvaal Museum expedition to South Rhodesia, November–December, 1937. Scorpions and Solifugae. *Annals of the Transvaal Museum*, 19 (2): 289–296.
- LAWRENCE, R. F. 1954. Fluorescence in Arthropoda. *Journal of the Entomological Society of South Africa*, 17: 167–170.
- LAWRENCE, R. F. 1961. A new forest-living scorpion from the Transvaal. *Annals and Magazine of Natural History*, (13) 4: 123–126.
- LAWRENCE, R. F. 1966. New and little known scorpions and solifuges from the Namib Desert and South West Africa. *Scientific Papers of the Namib Desert Research Station*, 29: 1–11.
- LI, S., K. C. KIM, S. ZONG, Y. LIU, J. KANG, C. PAK, Z. CAO & Y. WU. 2022. Dynamic synthesis and transport of fluorescent substances from moulting scorpions. *Journal of Photochemistry & Photobiology, B: Biology*, 234, 112511. <https://doi.org/10.1016/j.jphotobiol.2022.112511>
- LÓPEZ-CABRERA, D., G. RAMOS-ORTIZA, E. GONZÁLEZ-SANTILLÁN & R. ESPINOSA-LUNA. 2020. Characterization of the fluorescence intensity and color tonality in the exoskeleton of scorpions. *Journal of Photochemistry & Photobiology, B: Biology*, 209, 111945: 1–9.
- LORIA, S. F. & L. PRENDINI. 2014. Homology of the lateral eyes of Scorpiones: a six-ocellus model. *PLoS ONE* 9 (12): e112913. doi:10.1371/journal.pone.0112913.
- LOURENÇO, W. R. 1995. Description de trois nouveaux genres et quatre nouvelles espèces de scorpions Buthidae de Madagascar. *Bulletin du Muséum National d'Histoire naturelle, Paris (Zoologie, Biologie et Écologie Animale)*, (4), 17A (1-2): 95–106.
- LOURENÇO, W. R. 1996a. Premier cas connu d'un subfossile de scorpion dans le copal de Madagascar. *Comptes Rendus de l'Academie des Sciences, Paris, Sér. IIa*, 323: 889–891.
- LOURENÇO, W. R. 1996b. *Faune de Madagascar. 87. Scorpions (Chelicerata, Scorpiones)*. Paris: Muséum National d'Histoire Naturelle. 102 pp.
- LOURENÇO, W. R. 1996c. Origins and affinities of the scorpion fauna of Madagascar. Pp. 441–455 in: LOURENÇO, W. R. (Ed.). *Biogéographie de Madagascar*. Paris, Orstom.
- LOURENÇO, W. R. 1996d. *Microcharmus hauseri*, nouvelle espèce de scorpion de Madagascar (Scorpiones, Buthidae). *Revue Suisse de Zoologie*, 103 (2): 319–322.
- LOURENÇO, W. R. 1998a. Une nouvelle famille est nécessaire pour les microscorpions humicoles de Madagascar et d'Afrique. *Comptes Rendus de l'Académie des Sciences (Paris)*, 321: 845–848.
- LOURENÇO, W. R. 1998b. Description of a new species of scorpion from the reserve Spéciale d'Anjanaharibe-Sud, Madagascar. Pp. 69–72 in: GOODMAN, S.M. (Ed.). *A floral and faunal inventory of the reserve Spéciale d'Anjanaharibe-Sud, Madagascar, with reference to elevational variation* Fieldiana Zoology, new series, 90 (1495). Chicago Natural History Museum.
- LOURENÇO, W. R. 1999a. A new species of *Grosphus* Simon (Scorpiones, Buthidae), the first record of an intertidal scorpion from Madagascar. *Entomologische Mitteilungen aus dem Zoologischen Museum Hamburg*, 12 (156): 183–188.
- LOURENÇO, W. R. 1999b. On the phylogenetic position of the genus *Birulatus* Vachon, 1973 (Scorpiones, Buthidae) and redescription of *Birulatus haasi*. *Zoology in the Middle East*, 18: 109–113.

- LOURENÇO, W. R. 1999c. Complementary notes on the phylogenetic position of the genus *Lychasiooides* Vachon, 1973, and redescription of *Lychasiooides amieti* (Chelicerata, Scorpiones, Buthidae). *Revue Arachnologique*, 13 (1): 7–13.
- LOURENÇO, W. R. 1999d. Un modèle de distribution géographique présenté par les scorpions du genre *Microcharmus* Lourenço, avec la description d'une nouvelle espèce. *Comptes Rendus de l' Académie des Sciences*, sér. 3, Sci. Vie, 322 (10): 843–846.
- LOURENÇO, W. R. 2000a. Un nouveau genre de Scorpion malgache, maillon possible entre les Microcharmidae et les Buthidae. *Comptes Rendus de l'Académie des Sciences, series III, Sciences de la vie*, 323 (10): 877–881.
- LOURENÇO, W. R. 2000b. More about the Buthoidea of Madagascar, with special references to the genus *Tityobuthus* Pocock (Scorpiones, Buthidae). *Revue Suisse de Zoologie*, 107 (4): 721–736.
- LOURENÇO, W. R. 2002. Nouvelles données sur la morphologie et la biogéographie des *Microcharmus* Lourenço avec confirmation de la validité des Microcharmidae (Chelicerata, Scorpiones). *Biogeographica*, 78(1): 35–47.
- LOURENÇO, W. R. 2003a. Scorpiones, scorpions. Pp. 575–579 in: GOODMAN, S. & BENSTEAD, J. (Eds.). *The Natural History of Madagascar*. Chicago, Illinois: The University of Chicago Press.
- LOURENÇO, W. R. 2003b. New taxonomic considerations on some species of the genus *Groshpus* Simon, with description of a new species (Scorpiones, Buthidae). *Revue Suisse de Zoologie*, 110 (1): 141–154.
- LOURENÇO, W. R. 2003c. Humicolous buthoid scorpions: a new genus and species from French Guiana. *Comptes Rendus Biologies*, 326 (12): 1149–1155.
- LOURENÇO, W. R. 2004a. Humicolous microcharmid scorpions: a new genus and species from Madagascar. *Comptes Rendus Biologies*, 327: 77–83.
- LOURENÇO, W. R. 2005. Diversity and endemism in the scorpion fauna of Madagascar. *Biogeographica*, 80: 43–64.
- LOURENÇO, W. R. 2009. A new sub-fossil scorpion of the genus *Microcharmus* Lourenço, 1995 from Malagasy copal (Scorpiones, Microcharmidæ). *Boletín Sociedad Entomológica Aragonesa*, 44: 135–137.
- LOURENÇO, W. R. 2012. Fluorescence in scorpions under UV light; can chaerilids be a possible exception? *Comptes Rendus Biologies*, 335: 731–734.
- LOURENÇO, W. R. 2014. The genus *Groshpus* Simon, 1880 in south-western Madagascar, with the description of a new species (Scorpiones, Buthidae). *Zoosystema*, 36 (3): 631–645.
- LOURENÇO, W. R. 2020. A remarkable new species of *Leiurus* Ehrenberg, 1828 from the north deserts of Mali (Scorpiones: Buthidae). *Revista Ibérica de Aracnología*, 37: 147–152.
- LOURENÇO, W. R. 2021. A further new species for the Malagasy genus *Pseudouroplectes* Lourenço, 1995 (Scorpiones: Buthidae). *Faunitaxys*, 9 (41): 1–7.
- LOURENÇO, W. R. & S. M. GOODMAN. 2003a. Description of a new species of *Groshpus* Simon (Scorpiones, Buthidae) from the Ankarana Massif, Madagascar. *Revista Ibérica de Aracnología*, 7: 19–28.
- LOURENÇO, W. R. & S. M. GOODMAN. 2003b. New considerations on the genus *Tityobuthus* Pocock (Scorpiones, Buthidae), and description of a new species from the Ankarana in northern Madagascar. *Revista Ibérica de Aracnología*, 8: 13–22.
- LOURENÇO, W. R. & S. M. GOODMAN. 2006. Further considerations regarding the status of *Groshpus madagascariensis* (Gervais) and *Groshpus hirtus* Kraepelin, and description of a new species (Scorpiones, Buthidae). *Revue Suisse de Zoologie*, 113 (2): 247–261.
- LOURENÇO, W. R. & S. M. GOODMAN. 2009. Scorpions from the Comoros Archipelago: description of a new species of *Groshpus* Simon (Scorpiones, Buthidae) from Mayotte (Maore). *Boletín de la Sociedad Entomológica Aragonesa*, 44: 35–38.
- LOURENÇO, W. R. & S. M. GOODMAN. 2013. A synopsis of the scorpion fauna of the Loky-Manambato (Daraina) region in Madagascar. *Revista Ibérica de Aracnología*, 22: 47–58.
- LOURENÇO, W. R., S. M. GOODMAN & B. L. FISHER. 2006. A reappraisal of the geographical distribution of the endemic family Microcharmidæ Lourenço (Scorpiones) in Madagascar and description of eight new species and subspecies. *Proceedings of the California Academy of Sciences*, 4th Ser., 57, 26: 751–783.
- LOURENÇO, W. R., J.-X. QI & S. M. GOODMAN. 2007a. Scorpions of south-western Madagascar. A new species of *Groshpus* Simon, 1880 (Scorpiones, Buthidae). *Boletín de la Sociedad Entomológica Aragonesa*, 40: 171–177.

- LOURENÇO, W. R., A. ROSSI, L. WILMÉ, M. J. RAHERILALAO, V. SOARIMALALA & P. O. WAEBER. 2020. The remarkable diversity of the genus *Grosphus* Simon, 1880 (Scorpiones: Buthidae) in southern Madagascar and in particular in the region of Cap Sainte Marie. *Arachnida – Rivista Aracnologica Italiana*, 6 (27): 1–35.
- LOURENÇO, W. R., V. SOARIMALALA & S. M. GOODMAN. 2007b. Scorpions of south-west Madagascar. II. The species of *Grosphus* Simon (Scorpiones, Buthidae). *Boletín de la Sociedad Entomológica Aragonesa*, 41: 369–375.
- LOURENÇO, W. R., V. SOARIMALALA & S. M. GOODMAN. 2009. The species of *Grosphus* Simon (Scorpiones, Buthidae) distributed in the northern and eastern regions of Madagascar with the description of a new species. *Malagasy Nature*, 2: 144–153.
- LOURENÇO, W. R., P.O. WAEBER & L. WILMÉ. 2019. Additions to the geographical distribution of the Malagasy family Microcharmidae Lourenço 1996 (Scorpiones: Buthoidea) and description of three new species of *Microcharmus* Lourenço 1995. *Madagascar Conservation & Development*, 14 (1): 26–36.
- LOURENÇO, W. R. & L. WILMÉ. 2015a. Species of *Grosphus* Simon, 1880, associated to the group *madagascariensis* / *hirtus* (Scorpiones: Buthidae); description of a peculiar new species from the humid eastern forests of Madagascar. *Entomologische Mitteilungen aus dem Zoologischen Museum Hamburg*, 17 (194): 207–223.
- LOURENÇO, W. R. & L. WILMÉ. 2015b. Scorpions collected in the Makay mountain range, Madagascar (Scorpiones: Hormuridae, Buthidae) and with description of a new species. *Revista Iberica de Arachnologia*, 26: 55–61.
- LOURENÇO, W. R. & L. WILMÉ. 2016. Three new species of *Grosphus* Simon 1880, (Scorpiones: Buthidae) from Madagascar; possible vicariant cases within the *Grosphus bistriatus* group of species. *Madagascar Conservation & Development*, 11 (2): 52–65.
- LOURENCO, W. R., L. WILMÉ & P. O. WAEBER. 2016. One more vicariant new species of *Grosphus* Simon, 1880 (Scorpiones: Buthidae) from Madagascar. *Revista Ibérica de Aracnología*, 29: 45–50.
- LOURENCO, W. R., L. WILMÉ & P. O. WAEBER. 2018. Two more new species of *Grosphus* Simon, 1880, associated to the ‘*Grosphus simoni* group’ (Scorpiones: Buthidae) from the regions of the Tsingy de Bemaraha and Montagne d’Ambre (Madagascar). *Revista Ibérica de Aracnología*, 32: 73–80.
- LOURENÇO, W. R. & E. YTHIER. 2021. A particular new species of *Orthochirus* Karsch, 1891 from Somalia (Scorpiones: Buthidae). *Serket*, 17 (4): 335–349.
- LOWE, G. 2018. The genera *Butheolus* Simon, 1882 and *Xenobuthus* gen. nov. (Scorpiones: Buthidae) in Oman. *Euscorpius*, 261: 1–73.
- LOWE, G., S.R. KUTCHER & D. EDWARDS. 2003. A powerful new light source for ultraviolet detection of scorpions in the field. *Euscorpius*, 8: 1–7.
- LOWE, G. & F. KOVAŘÍK. 2019. Review of *Grosphus* Simon, 1880, with description of *Teruelius* gen. n., a new buthid genus from Madagascar (Scorpiones: Buthidae). *Euscorpius*, 281: 1–128.
- LOWE, G., E. A. YAĞMUR & F. KOVAŘÍK. 2014. A review of the genus *Leiurus* Ehrenberg, 1828 (Scorpiones: Buthidae) with description of four new species from the Arabian Peninsula. *Euscorpius*, 191: 1–129.
- MACLEOD, N. 2002. Phylogenetic signals in morphometric data. Pp. 100–138 in: MACLEOD, N. & P. FOREY (Eds.). *Morphometrics, Shape and Phylogenetics*. Taylor & Francis, London.
- MAURER, D., T. KOHL & M. J. GEBHARDT. 2017. Cuticular microstructures turn specular black into matt black in a stick insect. *Arthropod Structure & Development*, 46: 147–155.
- MCCOY, D. E., T. FEO, T. A. HARVEY & R. O. PRUM. 2018. Structural absorption by barbule microstructures of super black bird of paradise feathers. *Nature Communications*, 9:1, doi:10.1038/s41467-017-02088-w.
- MCCOY, D. E., V. E. MCCOY, N. K. MANDSBERG, A. V. SHNEIDMAN, J. AIZENBERG, R. O. PRUM & D. HAIG. 2019. Structurally assisted super black in colourful peacock spiders. *Proceedings of the Royal Society, B* 286: 20190589. <http://dx.doi.org/10.1098/rspb.2019.0589>
- MONARD, A. 1937. Scorpions, solifuges et Opilions d’Angola. *Revue Suisse de Zoologie*, 44: 251–270.
- MONGIARDINO KOCH, N., I. M. SOTO & M. J. RAMÍREZ. 2015. Overcoming problems with the use of ratios as continuous characters for phylogenetic analyses. *Zoologica Scripta*, 44: 463–474.
- MONOD, L., L. CAUWET, L. E. GONZÁLEZ-SANTILLÁN & S. HUBER. 2017. The male sexual apparatus in the order Scorpiones (Arachnida): a comparative study of functional morphology as a tool to define hypotheses of homology. *Frontiers in Zoology*, 14: 51: 1–48.

- MOUSSIAN, B. & S. ROTH. 2005. Dorsoventral axis formation in the *Drosophila* embryo - shaping and transducing a morphogen gradient. *Current Biology*, 15: R887–R899.
- MNHN-RS-RS1314. *Groshus annulatus* Fage, 1929. Syntypes. Muséum National d'Histoire Naturelle, Paris, France. <http://mediaphoto.mnhn.fr/media/1400492373742T3wKjGAcaxfq4zvE> (accessed 7.VII.2022).
- MNHN-RS-RS9031. *Neoprotobuthus intermedius* Lourenço, 2000. Paratype. Muséum National d'Histoire Naturelle, Paris, France. <http://mediaphoto.mnhn.fr/media/1504178171623nAwqN29omxGXWtTD> (accessed 7.VII.2022).
- MNHN-RS-RS9062. *Groshus bistriatus* Kraepelin, 1900. Muséum National d'Histoire Naturelle, Paris, France. <http://mediaphoto.mnhn.fr/media/1504178173031N9aSGDF2CDu5GtBP> (accessed 7.VII.2022).
- MNHN-RS-RS9080. *Groshus ganzhorni* Lourenço, Wilmé & Waeber, 2016. Holotype. Muséum National d'Histoire Naturelle, Paris, France. <https://mediaphoto.mnhn.fr/media/1631629010470S60Usz3Gk8dG9RQ5> (accessed 7.VII.2022).
- NEWLANDS, G. & C. B. MARTINDALE. 1980. The buthid scorpion fauna of Zimbabwe-Rhodesia with checklists and keys to the genera and species, distributions and medical importance (Arachnida, Scorpiones). *Zeitschrift für Angewandte Zoologie*, 67 (1): 51–77.
- OJANGUREN-AFFILASTRO, A. A., R. S. ADILARDI, C. I. MATTONI, M. J. RAMIREZ & F. SARA CECCARELLI. 2017. Dated phylogenetic studies of the southernmost American buthids (Scorpiones; Buthidae). *Molecular Phylogenetics and Evolution*, 110: 39–49.
- PAVLOVSKY, E. N. 1924a. [On the morphology of the male genital apparatus in scorpions]. *Trudy Leningradskogo Obshchestva Yestestvoispytatelei (Transactions of the Leningrad Society of Naturalists)*, 53 (2): 17–86.
- PAVLOVSKY, E. N. 1924b. Studies on the organization and development of Scorpions. *Quarterly Journal of Microscopical Science*, 68: 615–640.
- PARINS-FUKUCHI, C. 2018. Use of continuous traits can improve morphological phylogenetics. *Systematic Biology*, 67 (2): 328–339.
- PIKE, T.W. 2011. Using digital cameras to investigate animal colouration: estimating sensor sensitivity functions. *Behavioral Ecology and Sociobiology*, 65: 849–858.
- PLATNICK, N. I. & W. J. GERTSCH. 1976. The suborders of spiders: a cladistic analysis (Arachnida, Araneae). *American Museum Novitates*, 2607: 1–15.
- PLATNICK, N. & P. A. GOLOBOFF. 1985. On the monophyly of the spider suborder Mesothelae (Arachnida: Araneae). *Journal of the New York Entomological Society*, 93 (4): 1265–1270.
- POCOCK, R. I. 1889a. Notes on some Buthidae, new and old. *Annals and Magazine of Natural History*, 3: 334–351.
- POCOCK, R. I. 1889b. Another new species of scorpion from Madagascar. *Annals and Magazine of Natural History*, 3: 461–463.
- POCOCK, R. I. 1890. A revision of the genera of scorpions of the family Buthidae, with descriptions of some South-African species. *Proceedings of the Zoological Society*, 1890: 114–141.
- POCOCK, R. I. 1893. Notes on the classification of Scorpions, followed by some observations upon synonymy, with descriptions of new genera and species. *Annals and Magazine of Natural History*, 6 (12): 303–330.
- POCOCK, R. I. 1896. A further revision of the species of Scorpions belonging to the South- African genera *Uroplectes*, *Lepreus* and *Tityolepreus*. *Annals and Magazine of Natural History*, 6 (16): 377–393.
- POCOCK, R. I. 1897. Descriptions of two new species of scorpions from East Africa. *Annals and Magazine of Natural History*, 6 (19): 116–119.
- POLIS, G. A. & W. D. SISSOM. 1990. Life History. Pp. 161–223 in: POLIS, G. A. (Ed.) *The Biology of Scorpions*. Stanford University Press, Stanford, California.
- PRENDINI, L. 2001. Phylogeny of *Parabuthus* (Scorpiones, Buthidae). *Zoologica Scripta*, 30: 13–35.
- PRENDINI, L. 2004a. Systematics of the genus *Pseudolychas* Kraepelin (Scorpiones: Buthidae). *Annals of the Entomological Society of America*, 97 (1): 37–63.
- PRENDINI L. 2004b. The systematics of southern African *Parabuthus* Pocock (Scorpiones, Buthidae): revisions to the taxonomy and key to the species. *Journal of Arachnology*, 32 (1): 109–187.
- PRENDINI, L. 2015a. A remarkably small species of *Uroplectes* Peters, 1861 (Scorpiones: Buthidae), endemic to the Succulent Karoo of South Africa. *African Invertebrates*, 56 (2): 499–513.

- PRENDINI, L. 2015b. Three new *Uroplectes* (Scorpiones: Buthidae) with punctate metasomal segments from tropical central Africa. *American Museum Novitates*, 3840: 1–32.
- PRENDINI, L., V. I. EHRENTHAL & S. F. LORIA. 2021. Systematics of the relictual Asian scorpion family Pseudochactidae Gromov, 1998, with a review of cavernicolous, troglobitic, and troglomorphic scorpions. *Bulletin of the American Museum of Natural History*, 453: 1–149.
- PRENDINI, L. & S. F. LORIA. 2020. Systematic revision of the Asian forest scorpions (Heterometrinae Simon, 1879), revised suprageneric classification of Scorpionidae Latreille, 1802, and revalidation of Rugodentidae Bastawade et al., 2005. *Bulletin of the American Museum of Natural History*, 442: 1–481.
- PRENDINI, L., E. S. VOLSCHENK, S. MAALIKI & A. V. GROMOV. 2006. A ‘living fossil’ from Central Asia: The morphology of *Pseudochactas ovchinnikovi* Gromov, 1998 (Scorpiones: Pseudochactidae), with comments on its phylogenetic position. *Zoologischer Anzeiger*, 245 (3–4): 211–248.
- PRENDINI, L. & W. C. WHEELER. 2005. Scorpion higher phylogeny and classification, taxonomic anarchy, and standards for peer review in online publishing. *Cladistics*, 21: 466–494.
- PRPIC, N.-M. 2019. Limb development. A lesson in homology. *eLife* 2019;8:e48335, doi.org/10.7554/eLife.48335
- PURCELL, W. F. 1901. On some South African Arachnida belonging to the orders Scorpiones, Pedipalpi and Solifugae. *Annals of South African Museum*, 2: 137–225.
- REISSLAND, A. & P. GÖRNER. 1985. VIII. Trichobothria. Pp. 139–161 in: BARTH, F. G. (Ed.). *Neurobiology of Arachnids*. Springer-Verlag Berlin, Heidelberg.
- RUBIN, M., J. C. LAMSDELL, L. PRENDINI & M. J. HOPKINS. 2017. Exocuticular hyaline layer of sea scorpions and horseshoe crabs suggests cuticular fluorescence is plesiomorphic in chelicerates. *Journal of Zoology*, 303: 245–253.
- SANTIBÁÑEZ-LÓPEZ, C. E., S. AHARON., J. A. BALLESTEROS, G. GAINETT, C. M. BAKER, E. GONZÁLEZ-SANTILLÁN, M. S. HARVEY, M. K. HASSAN, A. H. ABU-ALMAATY, S. M ALDEYARBI, L. MONOD, A. OJANGUREN-AFFILASTRO, R. J. RAVEN, R. PINTO-DA-ROCHA, Y. ZVIK, E. GAVISH-REGEV & P. P. SHARMA. 2022. Phylogenomics of scorpions reveal contemporaneous diversification of scorpion mammalian predators and mammal-active sodium channel toxins. *Systematic Biology*, doi.org/10.1093/sysbio/syac021
- SHARMA, P. P., C. M. BAKER, J. G. COSGROVE, J. E. JOHNSON, J. T. OBERSKI, R. J. RAVEN, M. S. HARVEY, S.J. BOYER & G. A. GIRIBET. 2018. A revised dated phylogeny of scorpions: Phylogenomic support for ancient divergence of the temperate Gondwanan family Bothriuridae. *Molecular Phylogenetics and Evolution*, 122: 37–45.
- SHARMA, P. P., R. FERNÁNDEZ, L. A. ESPOSITO, E. GONZÁLEZ-SANTILLÁN & L. MONOD. 2015. Phylogenomic resolution of scorpions reveals multilevel discordance with morphological phylogenetic signal. *Proceedings of the Royal Society, B* 282: 20142953, doi.org/10.1098/rspb.2014.2953.
- SHRIVASTAVA, S. C. 1954. On the dermal glands of some Indian scorpions. *Current Science*, 23: 363–364.
- SIGERNES, F., M. DYRLAND, N. PETERS, D. A. LORENTZEN, T. SVENØE, K. HEIA, S. CHERNOUSS, C. S. DEEHR & M. KOSCH. 2009. The absolute sensitivity of digital colour cameras. *Optics Express*, 17 (22): 20211–20220.
- SIMON, E. 1880. Études arachnologiques 12e Mémorie (1). XVIII. Descriptions de genres et espèces de l’ordre des Scorpiones. *Annales de la Société Entomologique de France*, (5), 10: 377–398.
- SIMONNET, F., J. DEUTSCH & E. QUÉINNEC. 2004. hedgehog is a segment polarity gene in a crustacean and a chelicerate. *Development, Genes and Evolution*, 214: 537–545.
- SISSOM, W. D. 1990. Systematics, biogeography and paleontology. Pp. 64–160 in: POLIS, G. A. (Ed.). *The Biology of Scorpions*. Stanford, California: Stanford University Press.
- SISSOM, W. D. 1991. Systematic studies on the nitidulus group of the genus *Vaejovis*, with descriptions of seven new species (Scorpiones, Vaejovidae). *Journal of Arachnology*, 19 (1): 4–28.
- SISSOM, W. D. 2000. Family Vaejovidae Thorell, 1876. Pp. 503–553 in: FET, V., W. D. SISSOM, G. LOWE & M. E. BRAUNWALDER (Eds.). *Catalog of the Scorpions of the World (1758–1998)*. New York: The New York Entomological Society, 689 pp.
- SISSOM, W. D., G. A. POLIS & D. D. WATT. 1990. Field and laboratory methods. Pp. 445–461 in: POLIS, G. A. (Ed.). *The Biology of Scorpions*. Stanford University Press, Stanford, CA.
- SISSOM, W. D. & S. A. STOCKWELL. 1991. The genus *Serradigitus* in Sonora, Mexico, with descriptions of four new species (Scorpiones, Vaejovidae). *Insecta Mundi*, 5 (3–4): 197–214.

- SEITER, M., F. D. SCHRAMM & A. BARTHEL. 2016. The South African scorpion *Pseudolychas ochraceus* (Hirst, 1911) (Scorpiones: Buthidae) can reproduce by parthenogenesis. *Journal of Arachnology*, 44: 85–87.
- SMITH, U. E. & J. R. HENDRICKS. 2013. Geometric morphometric character suites as phylogenetic data: extracting phylogenetic signal from gastropod shells. *Systematic Biology*, 62 (3): 366–385.
- SOLEGLAD, M. E. 1974. *Vejovis calidus*, a new species of scorpion from Coahuila, Mexico (Scorpionida: Vejovidae). *Entomological News*, 85: 109–115.
- SOLEGLAD, M. E. & V. FET. 2001. Evolution of scorpion orthobothriotaxy: a cladistic approach. *Euscorpius*, 1: 1–38.
- SOLEGLAD, M. E. & V. FET. 2003a. The scorpion sternum: structure and phylogeny (Scorpiones: Orthosterni). *Euscorpius*, 5: 1–34.
- SOLEGLAD, M. E. & FET, V. 2003b. High-level systematics and phylogeny of the extant scorpions (Scorpiones: Orthosterni) *Euscorpius*, 11: 1–175.
- SOLEGLAD, M. E. & FET, V. 2006. Contributions to scorpion systematics. II. Stahnkeini, a new tribe in scorpion family Vaejovidae (Scorpiones: Chactoidea). *Euscorpius*, 40: 1–34.
- SOLEGLAD, M. E. & V. FET. 2008. Contributions to scorpion systematics. III. Subfamilies Smerringurinae and Syntropinae (Scorpiones: Vaejovidae). *Euscorpius*, 71: 1–115.
- SPINNER, M., A. KOVALEV, S. N. GORB & G. WESTHOFF. 2013. Snake velvet black: hierarchical micro- and nanostructure enhances dark colouration in *Bitis rhinoceros*. *Scientific Reports*, 3: 1846, doi: 10.1038/srep01846.
- SPRING, K. R. 2003. Cameras for digital microscopy. Pp. 87–102 in: SLUDER, G. & WOLF, D.E. (Eds.). *Methods in Cell Biology*, 72. *Digital Microscopy: A second edition of video microscopy*. Elsevier Academic Press, San Diego.
- STAHNKE, H. L. 1972a. UV light, a useful field tool. *Bioscience*, 22 (10): 604–607.
- STAHNKE, H. L. 1972b. A key to the genera of Buthidae (Scorpionida). *Entomological News*, 83(5): 121–133.
- STAHNKE, H. L. 1974. Revision and keys to the higher categories of Vejovidae (Scorpionida). *Journal of Arachnology*, 1: 107–141.
- STAPORNWONGKUL, K. S. & J.-P. VINCENT. 2021. Generation of extracellular morphogen gradients: the case for diffusion. *Nature Reviews Genetics*, doi: 10.1038/s41576-021-00342-y.
- STATHI, I. & W. R. LOURENCO. 2003. Description of a new scorpion species of the genus *Birulatus* Vachon, 1974 (Scorpiones, Buthidae) from Syria. *Zoology in the Middle East*, 30: 105–110.
- STEVENS, M., C. A. PÁRRAGA, I. C. CUTHILL, J. C. PARTRIDGE & T. S. TROSCIANKO. 2007. Using digital photography to study animal coloration. *Biological Journal of the Linnean Society*, 90: 211–237.
- ŠTUNDLOVÁ, J., F. ŠŤÁHLAVSKÝ, V. OPATOVA, J. STUNDL, F. KOVARÍK, P. DOLEJŠ & J. ŠMÍD. 2022. Molecular data do not support the traditional morphology-based groupings in the scorpion family Buthidae (Arachnida: Scorpiones). *Molecular Phylogenetics and Evolution*, 173(2022) 107511.
- TAMURA, K., G. STECHER & S. KUMAR. 2021. MEGA11: Molecular Evolutionary Genetics Analysis Version 11. *Molecular Biology and Evolution*, 38 (7):3022–3027. doi:10.1093/molbev/msab120
- TIKADER, B. K. & D. B. BASTAWADE. 1983. *The fauna of India: Scorpions. Scorpionida, Arachnida*. Vol III. Zoological Survey of India, Calcutta, 668 pp.
- VACHON, M. 1950. Subsidios para o estudo da biologia na Lunda. Remarques sur les scorpions de l'Angola (Premiere note). *Publicacoes Culturais da Companhia de Diamantes Angola (Luanda)*, 1950: 5–18.
- VACHON, M. 1963. De l'utilité, en systématique, d'une nomenclature des dents de chélicères chez les scorpions. *Bulletin du Muséum National d'Histoire Naturelle, Paris*, (2), 35(2): 161–166.
- VACHON, M. 1969. *Grosphus griveaudi*, nouvelle espèce de Scorpion Buthidae malgache. *Bulletin du Muséum national d'Histoire naturelle, Paris*, (2), 41: 476–483
- VACHON, M. 1974. Études des caractères utilisés pour classer les familles et les genres des scorpions (Arachnides). 1. La trichobothriotaxie en arachnologie. Sigles trichobothriaux et types de trichobothriotaxie. chez les Scorpions. *Bulletin du Muséum national d'Histoire naturelle (Paris)*, 3e série, 140, *Zoologie* 104: 857–958.
- VACHON, M. 1975. Sur l'utilisation de la trichobothriotaxie du bras des pédipalpes des Scorpions (Arachnides) dans le classement des genres de famille des Buthidae Simon. *Comptes Rendus Hebdomadaires des Séances de l'Académie des Sciences, (D)*, 281 (21): 1597–1599.

- VACHON, M. 1986. Etude de la denture des doigts des pedipalpes chez les Scorpions du genre *Lychas* C. L. Koch, 1845 (Arachnida, Scorpiones, Buthidae). *Bulletin du Museum National d'Histoire Naturelle, Paris*, (A), 8(4): 835–850.
- VISSEER, J. H. & S. GEERTS. 2021. Static allometry and sexual dimorphism in the Striped Lesser-thicktail Scorpion *Uroplectes lineatus*. *Arachnology*, 18 (7): 700–707.
- VOLSCHENK, E. S., C. I. MATTONI & L. PRENDINI. 2008. Comparative anatomy of the mesosomal organs of scorpions (Chelicerata, Scorpiones), with implications for the phylogeny of the order. *Zoological Journal of the Linnean Society*, 154 (4): 651–675.
- VUKUSIC, P., J. R. SAMBLES & C. R. LAWRENCE. 2004. Structurally assisted blackness in butterfly scales. *Proceedings of the Royal Society of London. B: Biological Sciences (Supplement)*, 271: S237–S239.
- WERNER, F. 1934. Scorpiones, Pedipalpi. Pp. 1–316 in: H. G. BRONNS *Klassen und Ordnungen des Tierreichs. Akademische Verlagsgesellschaft*, Leipzig. 5, IV, 8, Lief. 1–2 (Scorpiones).
- WHEELER, W. C., J. A. CODDINGTON, L. M. CROWLEY, D. DIMITROV, P. A. GOLOBOFF, C. E. GRISWOLD, G. HORMIGA, L. PRENDINI, M. J. RAMÍREZ, P. SIERWALD, L. ALMEIDA-SILVA, F. ALVAREZ-PADILLA, M. A. ARNEDO, L. R. BENAVIDES SILVA, S. P. BENJAMIN, J. E. BOND, C. J. GRISMADO, E. HASAN, M. HEDIN, M. A. IZQUIERDO, F. M. LABARQUE, J. LEDFORD, L. LOPARDO, W. P. MADDISON, J. A. MILLER, L. N. PIACENTINI, N. I. PLATNICK, D. POLOTOW, D. SILVA-DÁVILA, N. SCHARFF, T. SZÜTS, D. UBICK, C. J. VINK, H. M. WOOD & J. ZHANG. 2017. The spider tree of life: phylogeny of Araneae based on target-gene analyses from an extensive taxon sampling. *Cladistics*, 33 (6): 574–616.
- WIENS, J. J. 2006. Missing data and the design of phylogenetic analyses. *Journal of Biomedical Informatics*, 39: 34–42.
- WILEY, E. O. & H. LIEBERMAN. 2011. *Phylogenetics. Theory and Practice of Phylogenetic Systematics*. Second Edition. Wiley-Blackwell.
- WILLIAMS, S. C. 1968. Scorpion preservation for taxonomic and morphological studies. *The Wasmann Journal of Biology*, 26 (1): 133–136.
- WILLIAMS, S. C. 1970. New scorpions belonging to the eusthenura group of *Vejovis* from Baja California, Mexico (Scorpionida, Vejovidae). *Proceedings of the California Academy of Sciences*, ser. 4, 37 (12): 395–418.
- WILLIAMS, S. C. 1971. New and little known scorpions belonging to the punctipalpi group of the genus *Vaejovis* from Baja California, Mexico, and adjacent areas (Scorpionida, Vejovidae). *Wasmann Journal of Biology*, 29 (1): 37–63.
- WILLIAMS, S. C. 1980. Scorpions of Baja California, Mexico, and adjacent islands. *Occasional Papers of the California Academy of Sciences*, 135: 1–127.
- WILLIAMS, S. C. & B. T. BERKE. 1986. A new species of *Serradigitus* from Central California (Scorpiones: Vejovidae). *Pan-Pacific Entomologist*, 62 (4): 350–354.
- WOLFF, C., J.-Y. TINEVEZ, T. PIETZSCH, E. STAMATAKI, B. HARICH, L. GUIGNARD, S. PREIBISCH, S. SHORTE, P. J. KELLER, P. TOMANCAK & A. PAVLOPOULOS. 2018. Multi-view light-sheet imaging and tracking with the MaMuT software reveals the cell lineage of a direct developing arthropod limb. *eLife* 2018;7:e34410. doi.org/10.7554/eLife.34410.
- YAN, R., M. CHEN, H. ZHOU, T. LIU, X. TANG, K. ZHANG, H. ZHU, J. YE, D. ZHANG & T. FAN. 2016. Bio-inspired plasmonic nanoarchitected hybrid system towards enhanced far red-to-near infrared solar photocatalysis. *Scientific Reports*, 6: 20001, doi: 10.1038/srep20001.
- YOSHIMOTO, Y., M. TANAKA, M. MIYASHITA, M. ABDEL-WAHAB, A. M. A. MEGALY, Y. NAKAGAWA & H. MIYAGAWA. 2020. A fluorescent compound from the exuviae of the scorpion, *Liocheles australasiae*. *Journal of Natural Products*, 83: 542–546.
- ZAMBRE, A., R. V. SANAP & Z. A. MIRZA. 2014. A new high-elevation scorpion species of the genus *Scorpions* Peters, 1861 (Scorpiones: Euscorpiidae: Scorpioninae) from the Himalayas, India. *Comptes Rendus Biologies*, 337: 399–404.
- ZEMEL, R. S. & D. HOUGHTON. 2017. The ability of specific-wavelength LED lights to attract night-flying insects. *The Great Lakes Entomologist*, 50 (2): 79–85.
- ZHANG, C., D. CHEN, S. NIU, J. ZHANG, X. MENG, L. LIU, T. SUN, S. WEN, Y. ZHOU, Y. SHI, Z. HAN & L. REN. 2020. High-aspect-ratio deflection transducers inspired by the ultra-sensitive cantilever configuration of scorpion trichobothria. *Journal of Materials Chemistry C*, 8: 6093–6101.

